STRONG AND WEAK INTERLAYER INTERACTIONS OF TWO-DIMENSIONAL MATERIALS AND THEIR ASSEMBLIES

Tyler William Farnsworth

A dissertation submitted to the faculty at the University of North Carolina at Chapel Hill in partial fulfillment of the requirements for the degree of Doctor of Philosophy in the Department of Chemistry.

Chapel Hill
2018

Approved by:

Scott C. Warren

James F. Cahoon

Wei You

Joanna M. Atkin

Matthew K. Brennaman

ABSTRACT

Tyler William Farnsworth: Strong and weak interlayer interactions of two-dimensional materials and their assemblies
(Under the direction of Scott C. Warren)

The ability to control the properties of a macroscopic material through systematic modification of its component parts is a central theme in materials science. This concept is exemplified by the assembly of quantum dots into 3D solids, but the application of similar design principles to other quantum-confined systems, namely 2D materials, remains largely unexplored. Here I demonstrate that solution-processed 2D semiconductors retain their quantum-confined properties even when assembled into electrically conductive, thick films. Structural investigations show how this behavior is caused by turbostratic disorder and interlayer adsorbates, which weaken interlayer interactions and allow access to a quantum-confined but electronically coupled state. I generalize these findings to use a variety of 2D building blocks to create electrically conductive 3D solids with virtually any band gap.

I next introduce a strategy for discovering new 2D materials. Previous efforts to identify novel 2D materials were limited to van der Waals layered materials, but I demonstrate that layered crystals with strong interlayer interactions can be exfoliated into few-layer or monolayer materials. The strategy relies on a mechanistic similarity between mechanical exfoliation and scratching in layered materials: both involve crack propagation between layers. I therefore use the Mohs hardness scale, a measure of scratch resistance, to identify promising layered materials, and I test these predictions using mechanical exfoliation. We find that a Mohs hardness of five is a threshold below which mechanical

exfoliation occurs. To understand why, we examined 1,000 crystals and find an intuitive correlation between Mohs hardness and the nature of interlayer bonding. Finally, we show how our approach can be extended to computational searches of large databases of material properties to find additional 2D materials that can be used as building blocks for new 3D solids with custom-designed properties.

To my wife, Katie – my constant encouragement,
biggest supporter, and love of my life.

ACKNOWLEDGEMENTS

I would like to thank my advisor, Professor Scott Warren, for his guidance, mentoring, and support during my PhD research. I owe my ability to think critically and carefully about scientific ideas to him, and I'm grateful for his pushing me to be the best that I can be.

Thank you to my committee members, Professor Wei You, Professor Jim Cahoon, Professor Joanna Atkin, and Dr. Matthew (Kyle) Brennaman, for taking the time to serve on my committee. Each of them has provided stimulating discussions about my research at various points over the past five years, and I'm thankful for each of their contributions.

I would also like to thank the Warren Lab for the thought-provoking discussions of scientific research and the fun we have had over the years. You are each so very gifted and talented in your abilities as scientists and I know that each of you have a bright future ahead. I'm looking forward to hearing about your upcoming accomplishments! Special shout-out here to Adam – aka my Chess coach – I couldn't have asked for a better partner in crime as we built up the lab, and now we are "exit buddies" as we move on to our next paths. Best of luck in all your endeavors! I would also be remiss to not mention the many undergraduate students who worked with me over the years. Thank you to Emily, Jon, Elle, and Rebekah for your hard work and uncanny ability to give me a hard time.

I extend a special thanks to my wife, Katie, for her constant encouragement and support as I've completed this dissertation. You mean the world to me and I honestly wouldn't have made it to the end of this PhD without you. I'm grateful as well to my family

and friends who have encouraged me throughout the PhD. You are each so important to me and I'm grateful for your support. Thank you, Mom, for the time and energy that you invested into my homeschool education, K5-12th. Thank you for teaching me to work hard and well and that I could accomplish anything if I put my mind to it.

Thank you also to my former advisor, Professor Christopher Bender at the University of South Carolina Upstate, who showed me how cool chemistry is and convinced me to become a Chemistry major.

I am grateful to the National Science Foundation for their support over the past three years through the Graduate Research Fellowship Program. It is a privilege to be called an NSF Fellow, and I will strive to live up to the honor of this award during my scientific career.

Finally, I give thanks to God for his faithfulness to me. All that I have is a gift from God, and I continue to be amazed that I have an opportunity to study and learn more about the complexity of our world and its reflection of the Creator. To Him be the glory.

TABLE OF CONTENTS

LIST OF TABLES

LIST OF FIGURES

LIST OF ABBREVIATIONS

AFM: atomic force microscope

DAC: diamond anvil cell

DMPU: 1,3-dimethyltetrahydropyrimidin-2(1*H*)-one

eDRA: external diffuse reflectance accessory

iDRA: internal diffuse reflectance accessory

IPA: isopropanol

NMP: *n*-methyl-2-pyrrolidone

SEM: scanning electron microscope

TEM: transmission electron microscope

CHAPTER ONE – INTRODUCTION

1.1 2D nanomaterials as unique material class

The discovery of graphene[1] unlocked a class of two-dimensional materials that exhibit extraordinary electronic, mechanical, and optoelectronic properties. Because material properties depend on symmetry, dielectric environment, and boundary conditions, most layered materials exhibit significant changes in properties as they transition from bulk to monolayer (2D). Graphene is the most well-known example, with the monolayer exhibiting metallic character and high mobility despite being only one atom thick (Figure (1.1A). The transition metal dichalcogenides (Figure 1.1B) such as molybdenum disulfide (MoS_2) exhibit tunable band gaps that widen from an indirect band gap of *ca.* 1.2 eV in the bulk to *ca.* 1.8 eV direct gap in the monolayer[2]. Black phosphorus (Figure 1.1C) exhibits the largest known band gap tunability for any 2D material with a widening of its direct band gap from 0.3 eV in the bulk to *ca.* 2 eV for the monolayer[3-4], exceeding the tunability of most quantum dots[5-7].

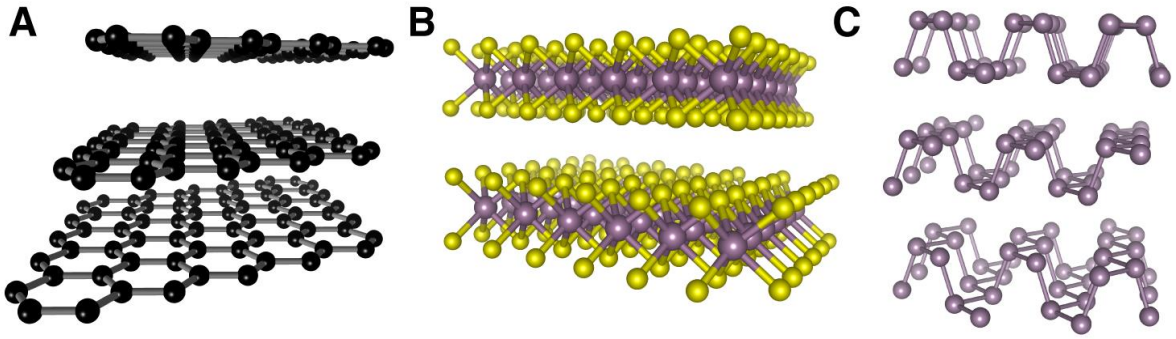

Figure 1.1 | Bulk layered precursors of common 2D materials. (A) graphite, **(B)** transition metal dichalcogenide (TMD) – MoS_2. Purple = Mo, Yellow = S. **(C)** black phosphorus. Structures plotted with VESTA[8] software.

The tunable band gaps of 2D semiconductors have sparked interest in their use for optoelectronics, especially in transistor and photovoltaic applications[9-11]. In several cases, 2D materials have demonstrated absorption or charge transport properties that exceed the limits of current technologies. As just one example, a single monolayer of MoS_2 (~0.7 nm) absorbs the same amount of light as 15 nm of GaAs or 50 nm of silicon[12], which are common materials found in modern-day solar cells. The incorporation of MoS_2 into photovoltaics shows potential as a lightweight and flexible alternative to current technology.

Despite their promise, the widespread use of 2D materials, especially in industry, is limited by the lack of scalable synthetic protocols. For MoS_2 to be a viable alternative material for solar cells, the lateral size of the nanomaterial must be dramatically increased beyond current methods of production. Most studies on 2D materials use the "Scotch tape" exfoliation method to produce single crystals of pristine quality, but this method has exceedingly low yields and produces flakes with limited lateral sizes. Efforts to synthesize 2D materials with larger lateral dimensions via chemical vapor deposition (CVD) have successfully produced large-area films of graphene and smaller flakes of transition metal dichalcogenides. However, these films tend to have high defect concentrations and exhibit many grain boundaries that negatively affect their properties[10]. Furthermore, CVD growth has, so far, been demonstrated for only a small number of 2D materials.

Liquid phase exfoliation (LPE) is an alternative synthetic approach that can produce large quantities of 2D nanoflakes of varying thickness[13-17]. The technique has shown viability across a broad spectrum of layered materials and offers a gateway to create thin film assemblies of 2D nanoflakes[18-21]. If the quantum-confined properties of individual 2D semiconductors can be harnessed in a large-area film, there is enormous potential to design

three-dimensional structures that exhibit the properties of their 2D building blocks. By designing films from the bottom-up using 2D semiconductors as building blocks, materials could be engineered with virtually any band gap.

1.2 Extension of confined-yet-coupled design to 2D materials

This ability to control the properties of a macroscopic material based on its underlying building blocks is at the core of structure-property relationships within materials science. Quantum dot solids (QDS) have provided a compelling demonstration of this concept through their "confined-yet-coupled" design[22-28], which enables the creation of quantum dot films that retain their quantum-confined absorption edge despite being assembled into electrically conductive films. The balance between quantum confinement and electronic coupling is tuned based on the ligand spacers between the individual quantum dots. The longer the ligand, the greater the distance between nanocrystals, and the balance favors quantum confinement over electronic coupling. Shorter ligands result in higher mobilities but a decrease in the quantum confinement.

Two-dimensional semiconductors are an interesting point of comparison to QDS because of the similar emergence of quantum-confined, size-dependent properties. If the electronic coupling between flakes of 2D assemblies can be controlled, there may be an opportunity to create a 2D material analogue of the QDS confined-yet-coupled design. The creation of "quantum 2D solids" will require an understanding of the extent to which quantum-confined properties are retained or lost when 2D flakes are stacked together. To this end, there have been several studies that have investigated the charge transport, absorption, and photoluminescence properties of individual nanoflakes and 2D heterostructures[29-38], revealing that quantum confinement is lost when flakes are restacked in orientations that

have interlayer distances similar to that of the bulk layered material. These studies have yet to be fully extended to large-area assemblies of 2D materials. Although charge transport studies on thick assemblies of vacuum-filtered or inkjet-printed LPE 2D flakes have been performed[39-41], the extent to which quantum-confinement is retained or lost in these thick films remains an open question. Exploring these fundamental interactions will be crucial for the implementation of 2D materials as quantum-confined solids for optoelectronics, sensors, and energy applications.

To design a confined-yet-coupled 2D material system with tunable flake-to-flake interactions, it is helpful to first consider the intrinsic interlayer coupling of a 3D layered structure. The majority of 2D materials are exfoliated from layered solids held together by weak van der Waals (vdW) interactions, and the quantum-confined property is a result of the decreased electronic coupling as the layers are separated. The relationship between quantum confinement and electronic coupling should therefore be related to the interlayer spacing between two stacked flakes. If two monolayers of a 2D material were brought back into contact, we should expect to see a decrease in quantum confinement (i.e. reversion to a "bulk-like" state) when the flakes are electronically coupled. This is, in fact, what is observed experimentally, so long as the two monolayers are in direct contact with no interlayer contaminants[29-30, 36, 42-44]. However, the slightest degree of rotation between the top and bottom MoS_2 flakes reduces the electronic coupling due to a slightly increased interlayer distance. Although the properties do not match those of the monolayer, rotated bilayers do exhibit properties intermediate between non-rotated bilayers and monolayers—i.e., there is partial re-emergence of quantum-confined properties. These studies demonstrate that interlayer distance can be used to control the electronic coupling between 2D flakes and

could provide a handle for tuning the confined-yet-coupled properties of 2D material assemblies.

To this end, the first part of my thesis (Chapters 3 and 4 with corresponding methods 2.1–2.6) is devoted to the investigation of the fundamental flake-to-flake interactions within 2D material assemblies and the design of large-area films that retain the quantum-confined properties of the 2D material building blocks. I have developed protocols to (1) synthetically scale-up 2D materials through liquid phase exfoliation, (2) deposit well-ordered assemblies of 2D material thin films via interfacial assembly, and (3) investigate the quantum-confined properties of 2D assemblies using a variety of optical and structural characterization techniques.

1.3 Opportunities to advance the discovery of new 2D materials

The allure of a confined-yet-coupled "2D solid" that harnesses the properties of 2D materials in a three-dimensional structure motivates the search for novel 2D material building blocks with new and exotic properties. The current library of 2D materials is limited to just a few crystal types (graphene, transition metal dichalcogenides, metal oxides, black phosphorus, etc.), with the majority of known 2D materials characterized by vdW interlayer interactions. The discovery of new layered crystals beyond vdW structures would open the door to exciting new physics and phenomena and provide additional building blocks for the design of confined-yet-coupled solids. Two examples of non-vdW layered crystals that have recently been discovered are 2D electrides[45-46], which have an electron gas between layers that result in metallic properties at the nanoscale and the production of 2D hematene[47], a form of iron oxide that demonstrates ferromagnetic properties as a 2D material. The discovery of new 2D materials beyond vdW layered crystals promises a wide array of new and exciting properties.

Efforts to diversify 2D materials via computational search algorithms[48-54] have shown promise in revealing an extended group of layered parent compounds that are potential candidates for 2D exfoliation. However, the full diversification of the 2D material library to include non-vDW structures with a variety of chemical structure and composition types remains a challenge due to the complexity of such structures[51] and the computational power[49] that is required to assess hundreds of thousands of crystal structures. To circumvent these challenges, many searches rely on arbitrary cut-off values of the interlayer distance or interlayer binding energy[48, 55] to determine whether a given material can be exfoliated into 2D form. Although the searches have resulted in several promising candidates, most of these

studies are limited to weakly bound systems that are dominated by vdW interlayer binding forces. There remains a need to experimentally confirm the relationship between the interlayer binding energy and the exfoliation probability of materials with strong interlayer interactions to enable the successful expansion of the 2D material library to include crystals beyond vdW layered structures.

In Chapter Five, I present a heuristic to experimentally study the interlayer interaction energy of a layered crystal and demonstrate how this assessment correlates well with the exfoliation likelihood of a given crystal. Using this approach, I expand the library of current 2D materials and provide a framework for understanding the mechanism of 2D material exfoliation, paving the way for new 2D material discovery.

REFERENCES

1. Novoselov, K. S.; Geim, A. K.; Morozov, S. V.; Jiang, D.; Zhang, Y.; Dubonos, S. V.; Grigorieva, I. V.; Firsov, A. A., Electric field effect in atomically thin carbon films. *Science* **2004,** *306* (5696), 666-9.

2. Mak, K. F.; Lee, C.; Hone, J.; Shan, J.; Heinz, T. F., Atomically Thin MoS2. A New Direct-Gap Semiconductor. *Phys. Rev. Lett.* **2010,** *105* (13), 136805/1-136805/4.

3. Tran, V.; Soklaski, R.; Liang, Y.; Yang, L., Layer-controlled band gap and anisotropic excitons in few-layer black phosphorus. *Physical Review B* **2014,** *89* (23).

4. Woomer, A. H.; Farnsworth, T. W.; Hu, J.; Wells, R. A.; Donley, C. L.; Warren, S. C., Phosphorene: Synthesis, Scale-Up, and Quantitative Optical Spectroscopy. *ACS Nano* **2015,** *9* (9), 8869-8884.

5. Gorer, S.; Albu-Yaron, A.; Hodes, G., Quantum Size Effects in Chemically Deposited, Nanocrystalline Lead Selenide Films. *J. Phys. Chem.* **1995,** *99* (44), 16442-8.

6. Kang, I.; Wise, F. W., Electronic structure and optical properties of PbS and PbSe quantum dots. *J. Opt. Soc. Am. B* **1997,** *14* (7), 1632-1646.

7. Pietryga, J. M.; Schaller, R. D.; Werder, D.; Stewart, M. H.; Klimov, V. I.; Hollingsworth, J. A., Pushing the Band Gap Envelope: Mid-Infrared Emitting Colloidal PbSe Quantum Dots. *J. Am. Chem. Soc.* **2004,** *126* (38), 11752-11753.

8. Momma, K.; Izumi, F., VESTA 3 for three-dimensional visualization of crystal, volumetric and morphology data. *Journal of applied crystallography* **2011,** *44* (6), 1272-1276.

9. Jariwala, D.; Sangwan, V. K.; Lauhon, L. J.; Marks, T. J.; Hersam, M. C., Emerging device applications for semiconducting two-dimensional transition metal dichalcogenides. *ACS nano* **2014,** *8* (2), 1102-1120.

10. Bhimanapati, G. R.; Lin, Z.; Meunier, V.; Jung, Y.; Cha, J.; Das, S.; Xiao, D.; Son, Y.; Strano, M. S.; Cooper, V. R., Recent advances in two-dimensional materials beyond graphene. *Acs Nano* **2015,** *9* (12), 11509-11539.

11. Wang, Q. H.; Kalantar-Zadeh, K.; Kis, A.; Coleman, J. N.; Strano, M. S., Electronics and optoelectronics of two-dimensional transition metal dichalcogenides. *Nature nanotechnology* **2012,** *7* (11), 699.

12. Bernardi, M.; Palummo, M.; Grossman, J. C., Extraordinary sunlight absorption and one nanometer thick photovoltaics using two-dimensional monolayer materials. *Nano Lett* **2013,** *13* (8), 3664-70.

13. Hernandez, Y.; Nicolosi, V.; Lotya, M.; Blighe, F. M.; Sun, Z.; De, S.; McGovern, I.; Holland, B.; Byrne, M.; Gun'Ko, Y. K., High-yield production of graphene by liquid-phase exfoliation of graphite. *Nature nanotechnology* **2008,** *3* (9), 563.

14. Nicolosi, V.; Chhowalla, M.; Kanatzidis, M. G.; Strano, M. S.; Coleman, J. N., Liquid exfoliation of layered materials. *Science* **2013,** *340* (6139), 1226419.

15. Cunningham, G.; Lotya, M.; Cucinotta, C. S.; Sanvito, S.; Bergin, S. D.; Menzel, R.; Shaffer, M. S.; Coleman, J. N., Solvent exfoliation of transition metal dichalcogenides: dispersibility of exfoliated nanosheets varies only weakly between compounds. *ACS nano* **2012,** *6* (4), 3468-3480.

16. O'Neill, A.; Khan, U.; Coleman, J. N., Preparation of High Concentration Dispersions of Exfoliated MoS2with Increased Flake Size. *Chemistry of Materials* **2012,** *24* (12), 2414-2421.

17. Coleman, J. N.; Lotya, M.; O'Neill, A.; Bergin, S. D.; King, P. J.; Khan, U.; Young, K.; Gaucher, A.; De, S.; Smith, R. J.; Shvets, I. V.; Arora, S. K.; Stanton, G.; Kim, H. Y.; Lee, K.; Kim, G. T.; Duesberg, G. S.; Hallam, T.; Boland, J. J.; Wang, J. J.; Donegan, J. F.; Grunlan, J. C.; Moriarty, G.; Shmeliov, A.; Nicholls, R. J.; Perkins, J. M.; Grieveson, E. M.; Theuwissen, K.; McComb, D. W.; Nellist, P. D.; Nicolosi, V., Two-dimensional nanosheets produced by liquid exfoliation of layered materials. *Science* **2011,** *331* (6017), 568-71.

18. Yu, X.; Prévot, M. S.; Guijarro, N.; Sivula, K., Self-assembled 2D WSe 2 thin films for photoelectrochemical hydrogen production. *Nature communications* **2015,** *6*, 7596.

19. Coleman, J. N.; Lotya, M.; O'Neill, A.; Bergin, S. D.; King, P. J.; Khan, U.; Young, K.; Gaucher, A.; De, S.; Smith, R. J., Two-dimensional nanosheets produced by liquid exfoliation of layered materials. *Science* **2011,** *331* (6017), 568-571.

20. De, S.; King, P. J.; Lotya, M.; O'Neill, A.; Doherty, E. M.; Hernandez, Y.; Duesberg, G. S.; Coleman, J. N., Flexible, Transparent, Conducting Films of Randomly Stacked

Graphene from Surfactant-Stabilized, Oxide-Free Graphene Dispersions. *Small* **2010,** *6* (3), 458-464.

21. Chen, H.; Müller, M. B.; Gilmore, K. J.; Wallace, G. G.; Li, D., Mechanically strong, electrically conductive, and biocompatible graphene paper. *Advanced Materials* **2008,** *20* (18), 3557-3561.

22. Baumgardner, W. J.; Whitham, K.; Hanrath, T., Confined-but-connected quantum solids via controlled ligand displacement. *Nano Lett* **2013,** *13* (7), 3225-31.

23. Choi, J.-H.; Wang, H.; Oh, S. J.; Paik, T.; Sung, P.; Sung, J.; Ye, X.; Zhao, T.; Diroll, B. T.; Murray, C. B.; Kagan, C. R., Exploiting the colloidal nanocrystal library to construct electronic devices. *Science* **2016,** *352* (6282), 205.

24. Whitham, K.; Yang, J.; Savitzky, B. H.; Kourkoutis, L. F.; Wise, F.; Hanrath, T., Charge transport and localization in atomically coherent quantum dot solids. *Nat Mater* **2016,** *15* (5), 557-63.

25. Sargent, E. H., Infrared photovoltaics made by solution processing. *Nature Photonics* **2009,** *3* (6), 325-331.

26. Hanrath, T., Colloidal nanocrystal quantum dot assemblies as artificial solids. *Journal of Vacuum Science & Technology A: Vacuum, Surfaces, and Films* **2012,** *30* (3), 030802.

27. Kim, J. Y.; Voznyy, O.; Zhitomirsky, D.; Sargent, E. H., 25th anniversary article: Colloidal quantum dot materials and devices: a quarter-century of advances. *Adv Mater* **2013,** *25* (36), 4986-5010.

28. Kagan, C. R.; Murray, C. B., Charge transport in strongly coupled quantum dot solids. *Nat Nanotechnol* **2015,** *10* (12), 1013-26.

29. Huang, S.; Ling, X.; Liang, L.; Kong, J.; Terrones, H.; Meunier, V.; Dresselhaus, M. S., Probing the interlayer coupling of twisted bilayer MoS2 using photoluminescence spectroscopy. *Nano Lett* **2014,** *14* (10), 5500-8.

30. Cao, B.; Li, T., Interlayer Electronic Coupling in Arbitrarily Stacked MoS2Bilayers Controlled by Interlayer S–S Interaction. *The Journal of Physical Chemistry C* **2015,** *119* (2), 1247-1252.

31. Wang, Z.; Chen, Q.; Wang, J., Electronic Structure of Twisted Bilayers of Graphene/MoS2and MoS2/MoS2. *The Journal of Physical Chemistry C* **2015,** *119* (9), 4752-4758.

32. Rigosi, A. F.; Hill, H. M.; Li, Y.; Chernikov, A.; Heinz, T. F., Probing Interlayer Interactions in Transition Metal Dichalcogenide Heterostructures by Optical Spectroscopy: MoS2/WS2 and MoSe2/WSe2. *Nano Lett* **2015,** *15* (8), 5033-8.

33. Puretzky, A. A.; Liang, L.; Li, X.; Xiao, K.; Sumpter, B. G.; Meunier, V.; Geohegan, D. B., Twisted MoSe(2) Bilayers with Variable Local Stacking and Interlayer Coupling Revealed by Low-Frequency Raman Spectroscopy. *ACS Nano* **2016,** *10* (2), 2736-44.

34. Yu, J. H.; Lee, H. R.; Hong, S. S.; Kong, D.; Lee, H. W.; Wang, H.; Xiong, F.; Wang, S.; Cui, Y., Vertical heterostructure of two-dimensional MoS(2) and WSe(2) with vertically aligned layers. *Nano Lett* **2015,** *15* (2), 1031-5.

35. Bradley, A. J.; Ugeda, M. M.; da Jornada, F. H.; Qiu, D. Y.; Ruan, W.; Zhang, Y.; Wickenburg, S.; Riss, A.; Lu, J.; Mo, S. K.; Hussain, Z.; Shen, Z. X.; Louie, S. G.; Crommie, M. F., Probing the role of interlayer coupling and coulomb interactions on electronic structure in few-layer MoSe(2) nanostructures. *Nano Lett* **2015,** *15* (4), 2594-9.

36. Zheng, S.; Sun, L.; Zhou, X.; Liu, F.; Liu, Z.; Shen, Z.; Fan, H. J., Coupling and Interlayer Exciton in Twist-Stacked WS2Bilayers. *Advanced Optical Materials* **2015,** *3* (11), 1600-1605.

37. Cai, Y.; Zhang, G.; Zhang, Y.-W., Electronic Properties of Phosphorene/Graphene and Phosphorene/Hexagonal Boron Nitride Heterostructures. *The Journal of Physical Chemistry C* **2015,** *119* (24), 13929-13936.

38. Li, Y.; Xu, C.-Y.; Qin, J.-K.; Feng, W.; Wang, J.-Y.; Zhang, S.; Ma, L.-P.; Cao, J.; Hu, P. A.; Ren, W.; Zhen, L., Tuning the Excitonic States in MoS2/Graphene van der Waals Heterostructures via Electrochemical Gating. *Advanced Functional Materials* **2016,** *26* (2), 293-302.

39. Kelly, A. G.; Hallam, T.; Backes, C.; Harvey, A.; Esmaeily, A. S.; Godwin, I.; Coelho, J.; Nicolosi, V.; Lauth, J.; Kulkarni, A., All-printed thin-film transistors from networks of liquid-exfoliated nanosheets. *Science* **2017,** *356* (6333), 69-73.

40. Tomašević-Ilić, T.; Pešić, J.; Milošević, I.; Vujin, J.; Matković, A.; Spasenović, M.; Gajić, R., Transparent and conductive films from liquid phase exfoliated graphene. *Optical and Quantum Electronics* **2016,** *48* (6).

41. Matković, A.; Milošević, I.; Milićević, M.; Tomašević-Ilić, T.; Pešić, J.; Musić, M.; Spasenović, M.; Jovanović, D.; Vasić, B.; Deeks, C.; Panajotović, R.; Belić, M. R.; Gajić, R., Enhanced sheet conductivity of Langmuir–Blodgett assembled graphene thin films by chemical doping. *2D Materials* **2016,** *3* (1), 015002.

42. van der Zande, A. M.; Kunstmann, J.; Chernikov, A.; Chenet, D. A.; You, Y.; Zhang, X.; Huang, P. Y.; Berkelbach, T. C.; Wang, L.; Zhang, F.; Hybertsen, M. S.; Muller, D. A.; Reichman, D. R.; Heinz, T. F.; Hone, J. C., Tailoring the electronic structure in bilayer molybdenum disulfide via interlayer twist. *Nano Lett* **2014,** *14* (7), 3869-75.

43. Castellanos-Gomez, A.; van der Zant, H. S. J.; Steele, G. A., Folded MoS2 layers with reduced interlayer coupling. *Nano Research* **2015,** *7* (4), 572-578.

44. Liu, K.; Zhang, L.; Cao, T.; Jin, C.; Qiu, D.; Zhou, Q.; Zettl, A.; Yang, P.; Louie, S. G.; Wang, F., Evolution of interlayer coupling in twisted molybdenum disulfide bilayers. *Nat Commun* **2014,** *5*, 4966.

45. Druffel, D. L.; Kuntz, K. L.; Woomer, A. H.; Alcorn, F. M.; Hu, J.; Donley, C. L.; Warren, S. C., Experimental Demonstration of an Electride as a 2D Material. *Journal of the American Chemical Society* **2016,** *138* (49), 16089-16094.

46. Druffel, D. L.; Woomer, A. H.; Kuntz, K. L.; Pawlik, J. T.; Warren, S. C., Electrons on the surface of 2D materials: from layered electrides to 2D electrenes. *Journal of Materials Chemistry C* **2017,** *5* (43), 11196-11213.

47. Balan, A. P.; Radhakrishnan, S.; Woellner, C. F.; Sinha, S. K.; Deng, L.; de los Reyes, C.; Rao, B. M.; Paulose, M.; Neupane, R.; Apte, A., Exfoliation of a non-van der Waals material from iron ore hematite. *Nature nanotechnology* **2018**, 1.

48. Mounet, N.; Gibertini, M.; Schwaller, P.; Campi, D.; Merkys, A.; Marrazzo, A.; Sohier, T.; Castelli, I. E.; Cepellotti, A.; Pizzi, G.; Marzari, N., Two-dimensional materials from high-throughput computational exfoliation of experimentally known compounds. *Nature Nanotechnology* **2018,** *13* (3), 246-252.

49. Choudhary, K.; Kalish, I.; Beams, R.; Tavazza, F., High-throughput Identification and Characterization of Two-dimensional Materials using Density functional theory. *Scientific Reports* **2017,** *7* (1), 5179-5179.

50. Cheon, G.; Duerloo, K. A. N.; Sendek, A. D.; Porter, C.; Chen, Y.; Reed, E. J., Data Mining for New Two- and One-Dimensional Weakly Bonded Solids and Lattice-Commensurate Heterostructures. *Nano Letters* **2017,** *17* (3), 1915-1923.

51. Revard, B. C.; Tipton, W. W.; Yesypenko, A.; Hennig, R. G., Grand-canonical evolutionary algorithm for the prediction of two-dimensional materials. *Physical Review B* **2016,** *93* (5), 054117-054117.

52. Ashton, M.; Sinnott, S. B.; Hennig, R. G., Computational discovery and characterization of polymorphic two-dimensional IV-V materials. *Applied Physics Letters* **2016,** *109* (19).

53. Zhuang, H. L.; Hennig, R. G., Computational discovery, characterization, and design of single-layer materials. *JOM* **2014,** *66* (3), 366-374.

54. Lebègue, S.; Björkman, T.; Klintenberg, M.; Nieminen, R. M.; Eriksson, O., Two-dimensional materials from data filtering and Ab Initio calculations. *Physical Review X* **2013,** *3* (3), 1-7.

55. Björkman, T.; Gulans, A.; Krasheninnikov, A. V.; Nieminen, R. M., Van der Waals bonding in layered compounds from advanced density-functional first-principles calculations. *Physical Review Letters* **2012,** *108* (23), 1-5.

CHAPTER TWO – METHODS

Introduction

During the course of my Ph.D., I have gained expertise in numerous techniques. An overview of experimental procedures and analytical techniques used throughout my work will be given in this chapter. First, I discuss the procedures that I developed for the preparation of scaled-up quantities of 2D black phosphorus and molybdenum disulfide. These procedures are generalizable and can be used to produce a variety of 2D materials. Second, I present a discussion on the various methods of thin film deposition of 2D materials and detail the protocols that I developed to create large-area, well-ordered films. Third, I provide an introduction to the optical absorption and light scattering of 2D material dispersions and thin films and highlight the utility of an integrating sphere geometry for absorption measurements. Fourth, I introduce the diamond anvil cell as a useful tool for high pressure spectroscopic and diffraction measurements and provide a detailed procedure for its use. The remaining sections detail additional techniques or methods that I developed for sample preparation and data mining.

2.1 2D phosphorus preparation

2.1.1 Black phosphorus synthesis

Black phosphorus crystals were prepared using a vapor-phase transport procedure adapted from the Nilges[1] method. First, one end of a quartz tube (14 mm outer diameter and 9.6 mm inner diameter) was sealed with an oxygen–hydrogen torch. Once sealed, the quartz tube was pumped into a glove box. 0.420 g red phosphorus, 0.020 g tin (Sn), and 0.010 g

tin(IV) iodide (SnI_4, Alfa Aesar 99.998%, a light-sensitive powder) was added to the quartz tube. Because 10 mg is difficult to accurately weigh out and transfer, the SnI_4 and Sn were mixed together in-house in a scaled-up 2:1 ratio. Thirty mg of this mixture was added to the red phosphorus in the quartz tube.

Once the powders were loaded, the open end of the quartz tube was capped with parafilm, removed from the glovebox, and immediately connected to the vacuum line of an oxygen–hydrogen torch setup. The vacuum needle valve was opened slowly to prevent powder from being sucked into the vacuum line. The top end of the quartz tube was melted to create a seal, targeting a final tube length of 20 cm. During the sealing process, a band of red and/or yellow sometimes appeared halfway up the tube (Figure 2.1A). This was a result of SnI_4 or red phosphorus depositing on the inner quartz wall. After sealing the quartz tubes, they were placed inside a long quartz tube in a programmable three-zone furnace. The three-zone furnace was operated inside a fume hood because of the risks of the quartz tube over-pressurizing during heating. Warning: do not change these ratios or tube volumes because of risk of explosion.

Figure 2.1B shows the series of 8 temperature gradients with associated temperatures and times that was used for each zone of the three-zone furnace. The entire synthesis required a minimum of 23 hours, but often took longer because the final cool-down was slower than the programmed rate. The evacuated tubes were placed in the three-zone furnace such that the mixture of red phosphorus, Sn, and SnI_4 was in zone 2 and the empty end of the evacuated tube lied in zone 1 or 3. An insulating sleeve was placed around the middle of the tube (Figure 2.1C). Zone 2 was the “hot zone” and zones 1 and 3 were the “cold zones”. It is possible to heat two tubes at once using the three-zone furnace as shown in Figure 2.1C.

Successful reactions resulted in 0.25 – 0.35 g of black phosphorus crystals (Figure 2.1E, F). The crystals were deposited at the "cold" end of each evacuated tube (zone 1 or 3). Once at room temperature, the quartz tubes were pumped into a glove box and smashed open using a wrench or heavy object such as this dissertation. The black phosphorus crystals were stored in a sealed vial in the glove box. The quartz tubing was cleaned by soaking in DI water and treating with 1M $CuSO_4$ to quench any residual white phosphorus.

If the evacuated tubes are not properly sealed, or if too much red phosphorus is placed into the evacuated tube, it is possible that the vapor pressure may exceed the threshold pressure limit of the quartz tube and cause the tube to explode (Figure 2.1D). If such an explosion occurs, wait several hours to allow any white phosphorus vapor to be evacuated via the fume hood before clean-up. Wear a face mask to prevent inhalation of insulation powder from the furnace. Note: the mask will NOT prevent exposure to white phosphorus vapor – keep sash at recommended height to prevent accidental exposure to vapors. Large broken pieces of quartz may be picked up with tweezers and placed into a large beaker with DI water. Treat the beaker of DI water and quartz with 1M $CuSO_4$ solution to quench any residual white phosphorus. Residual quartz and insulation may be vacuumed up with a shop-vac with HEPA filter.

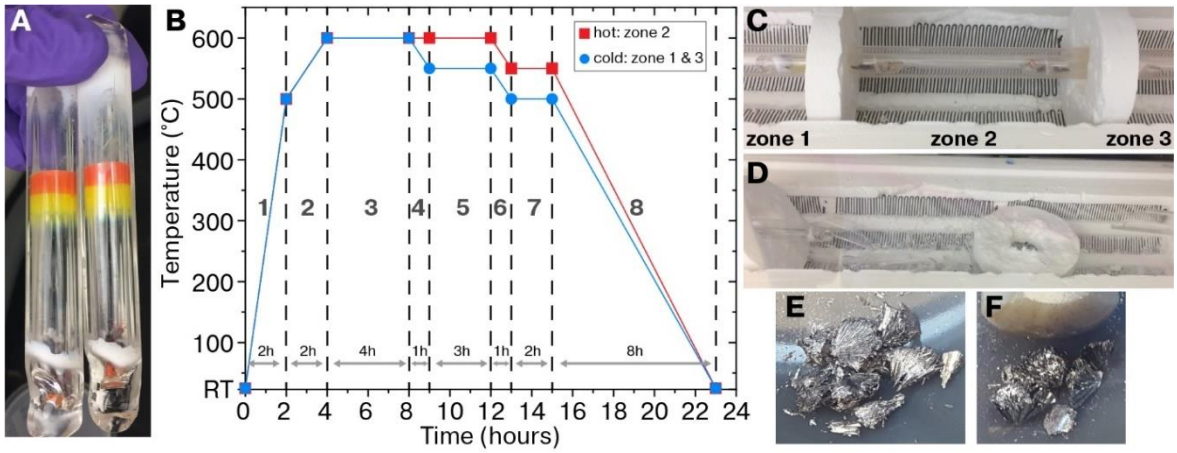

Figure 2.1 | Black phosphorus synthesis. (A) Sealed, evacuated quartz tubes containing red phosphorus, tin, and tin(IV) iodide prior to heating. **(B)** Temperature settings and time (hours) to program into the zone controllers of the three-zone furnace. The dark gray numbers in the center represent 8 sequential temperature/time settings. The gray arrows at the base of the plot represent the time at each ramp. For example, setting #1 for all three zones should be 500°C/2h and setting #5 would be zone 2: 600°C/3h and zone1/3: 550°C/3h. **(C)** loading of two quartz tubes inside a larger quartz tube in the three-zone furnace prior to heating. The powder should be in the end of the tube located in zone 2. Insulating sleeves are placed around the sample tubes between each zone. **(D)** aftermath of explosion from black phosphorus reaction. **(E) & (F)** Representative crystals of black phosphorus synthesis after grinding with mortar & pestle.

The black phosphorus crystals usually contained unreacted SnI_4. To remove this impurity, the crystals were refluxed with acetone in a Soxhlet extractor (Figure 2.2) under nitrogen gas for 12-24 hours. The below procedure details the washing process:

1) Collect the following materials: large Soxhlet extractor, 2- or 3- neck 500 mL round bottom flask (RBF), condenser, Whatman extraction thimble 603 (cat .no. 10350226), oil bath, hot plate, thermometer.
2) Wash and dry the Soxhlet and RBF. Place in an oven for 1 hour before using.
3) Dry 500 mL certified ACS-grade acetone and set aside. This can be accomplished by distilling over the Schlenk line or by allowing to sit overnight over activated Linde 4A sieves. Note that the sieves require extremely high temperatures (> 300 °C) to initially activate and must be kept in an oven to maintain activation.

4) Pump the Soxhlet extractor and Whatman thimble into the glovebox with the black phosphorus crystals.
5) Crush the black phosphorus crystals with a mortar & pestle and place them into the Whatman thimble. Load the thimble with crystals into the Soxhlet extractor. It will be necessary to crush the thimble slightly to enable it to fit inside the Soxhlet. Multiple black phosphorus samples can be washed simultaneously. If it is desired to keep the crystals separated during the wash, wrap them in a Kimwipe before loading in the thimble.
6) After placing the thimble with black phosphorus crystals in the Soxhlet, cover both ends with parafilm.
7) Setup the RBF in a hood with an oil bath and hotplate. Add a stir bar to the RBF. Plug all but one of the openings with rubber septa. The open port is for the Soxhlet attachment. Add ~200 – 300 mL dry acetone to the RBF (enough acetone needs to be in the RBF to fully enclose the thimble in the Soxhlet during reflux), and bubble N_2 through the acetone for 30 minutes. It will be useful to have the N_2 needle piercing one of the septa rather than being placed in the opening.
8) Cap the condenser with a rubber septum and insert an outlet needle that leads to a N_2 bubbler.
9) After 30 minutes of N_2 bubbling, bring the Soxhlet/thimble/black phosphorus setup out of the glovebox (with parafilm!) and immediately attach to the RBF. Continue bubbling N_2 through the RBF + Soxhlet and allow it to escape out of the top of the Soxhlet.

10) Attach the condenser (with the septum/N_2 outlet) to the top of the Soxhlet and purge system with N_2 for several minutes.
11) Remove the N_2 inlet and outlet needles to conduct reflux in a closed system.
12) Set the white ThermoFisher hot plate to a temperature of 150 °C – this should result in an oil bath temperature of ~100 °C. Monitor temperature of oil bath with a thermometer to ensure that the temperature reaches > 56 °C (boiling point of acetone) so that the acetone refluxes continuously.
13) Let reflux for 12-24 hours. The acetone will turn yellow as it dissolves the SnI_4 impurity.
14) Turn off heat and use long needle and 50-mL syringe to remove the yellow-tinted acetone from the RBF.
15) Reinsert the N_2 inlet and outlet needles and purge the system overnight with N_2 flow to dry the black phosphorus and Whatman filter.
16) After purging, separate Soxhlet from RBF and condenser. Cover both ends with KimWipe (fastened with rubber band) and pump into glovebox (3 x 20 minute cycle). The KimWipe prevents black phosphorus powder from being sucked up by vacuum.
17) Confirm the structure of the black phosphorus crystals using powder XRD (Figure 2.2C).

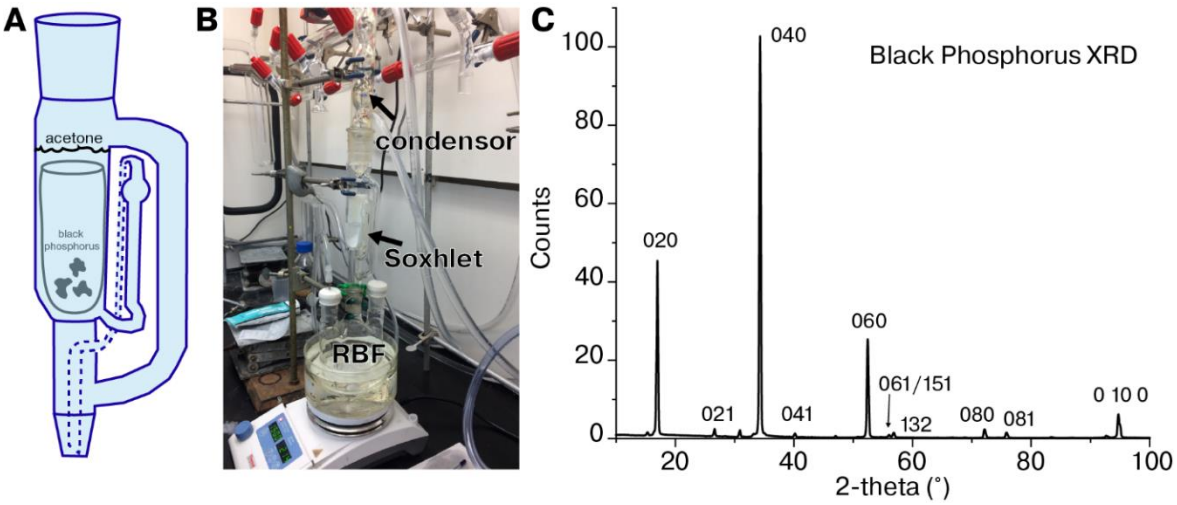

Figure 2.2 | Purification of black phosphorus crystals. (A) Cartoon of black phosphorus crystals loaded in Whatman thimble inside a Soxhlet extractor. **(B)** Full setup with RBF, Soxhlet, and condenser. **(C)** powder XRD spectrum of black phosphorus crystal.

2.1.2 2D phosphorus exfoliation

Black phosphorus crystals were slightly crushed using a mortar and pestle in a nitrogen glove box. For typical experiments, 10 mg was weighed into a 20-mL scintillation vial. Twenty milliliters of solvent was added to give a concentration of 0.5 mg/mL. Vials were tightly capped and wrapped with parafilm to prevent air exposure before placing into a Branson 5800 bath sonicator. The bath sonicator was outfitted with a test tube rack to allow for controlled placement of vials. Vials were systematically moved through several locations during the course of sonication to minimize vial-to-vial variations in phosphorus dispersion. The samples were subjected to eight to ten cycles of sonication, each lasting 99 minutes. Bath water was changed after each cycle to maintain a temperature between 22 and 30 °C (during sonication, bath temperature increased dramatically). During the sonication process, the black phosphorus crystals dispersed into the solution and the suspension acquired a brown appearance. After sonication, the vials were returned to the glove box.

To fractionate phosphorus suspensions and isolate narrow thickness distributions of 2D phosphorus, we employed a three-step centrifugation protocol. First, solutions were transferred

to Nalgene Oak Ridge FEP 10- or 50-mL centrifuge tubes. The solutions were centrifuged in a Sorvall RC-5B superspeed refrigerated centrifuge (rotor radius 10.7 cm). Second, the supernatant from the centrifuge tubes was collected and transferred to a clean centrifuge tube. Third, the supernatant was centrifuged at a speed higher than the first run. The sediment was collected and typically re-dispersed in fresh solvent. Depending on choice of centrifugation speeds, these fractionated suspensions contained 2D phosphorus with narrow and systematically varying thicknesses distributions (see chapter 3).

As a typical example, a distribution could be collected at RCF values between 17,200*g* and 23,400*g*. The tube would first be spun at 17,200*g* for 30 minutes. The resulting supernatant would then be removed and re-centrifuged at 23,400*g* for 30 minutes. The sediment from the second centrifuge would then contain a distribution of sheets that could then be re-dispersed into any solvent (often we chose IPA) for further analysis; for simplicity, we label this new suspension as 20,200g, the average RCF between the two sequential centrifugation steps. Table 2.1 lists the average RCF value for each suspension. Note that all solution transfers between centrifuge tubes were performed inside a glove box. High speed centrifugations (>12,000*g*) were performed at 4 °C to lengthen tube lifetime.

Table 2.1 | Labeling of centrifugation fractions containing 2D phosphorus suspensions

Sequential RCF (g)	Label (1,000g)
30 to 480	0.12
480 to 1,900	1.1
1,900 to 4,300	3.0
7,700 to 12,000	9.7
17,200 to 23,400	20.2

Inductively coupled-mass spectroscopy (ICP-MS) was correlated with UV-vis-nIR spectroscopy to make a standard curve that we used to measure the concentration of liquid-exfoliated black phosphorus. Black phosphorus was exfoliated in NMP, centrifuged at 3,000*g*, and dialyzed into fresh NMP under inert conditions to remove possible molecular phosphorus byproducts caused by sonication (Millipore Biotech RC membranes, 8-10 kDa). The dialyzed samples were serially diluted and analyzed by ICP-MS and UV-vis-nIR spectroscopy at 450, 500, and 550 nm to create three calibration curves. The equations governing the relationship between absorbance (see section 2.4.1 for a description of UV-vis-nIR methods) for 2D phosphorus supernatants collected after centrifugation at 3,000*g* were:

$$A_{450\text{-nm}} = 3.4\text{ E-}6 \times (\text{phosphorus concentration in parts per billion}) \quad (2\text{-}1)$$

$$A_{500\text{-nm}} = 2.5\text{ E-}6 \times (\text{phosphorus concentration in parts per billion}) \quad (2\text{-}2)$$

$$A_{550\text{-nm}} = 1.8\text{ E-}6 \times (\text{phosphorus concentration in parts per billion}) \quad (2\text{-}3)$$

The results of our liquid exfoliation study are summarized in Table 2.2.

Table 2.2 | Liquid exfoliation of black phosphorus and Hansen solubility parameters[2]

Solvent	Ave. Conc. (ug/mL)	Std. Dev. (ug/mL)	Hildebrand ($MPa^{1/2}$)	Hansen ($MPa^{1/2}$)		
			δ	δ_d	δ_p	δ_h
N-methyl-2-pyrrolidone (NMP)	44.12	11.23	23	18	12.3	7.2
Cyclopentanone	37.05	17.30	22.1	17.9	11.9	5.2
1-Cyclohexyl-2-pyrrolidone (CHP)	25.08	7.54	20.5	18.2	6.8	6.5
1-Dodecyl-2-pyrrolidinone (N12P)	22.81	6.26	18.3	17.5	4.1	3.2
Benzyl benzoate	32.05	16.69	21.3	20	5.1	5.2
1-Octyl-2-pyrrolidone (N8P)	37.47	15.72	19.1	17.4	6.2	4.8
1-Vinyl-2-pyrrolidinone (NVP)	61.74	20.75	19.8	16.4	9.3	5.9
Benzyl ether	3.31	3.88	20.6	19.6	3.4	5.2
1,3-Dimethyl-2-imidazolidinone	65.63	10.20	23	18	10.5	9.7
Cyclohexanone	3.54	2.28	20.3	17.8	8.4	5.1
Chlorobenzene	0.76	1.02	19.6	19	4.3	2
Dimethylsulfoxide (DMSO)	29.06	2.19	26.7	18.4	16.4	10.2
Benzonitrile	110.82	16.63	22.5	18.8	12	3.3
N-methylformamide	50.91	17.61	30.1	17.4	18.8	15.9
Dimethylformamide	40.82	4.72	24.9	17.4	13.7	11.3
Benzaldehyde	16.12	13.52	21.4	19.4	7.4	5.3
Isopropylalcohol (IPA)	38.65	7.60	23.6	15.8	6.1	16.4

2.2 2D MoS_2 preparation

Thin flakes of MoS_2 were prepared by one of two methods, described below. Method 1 can be easily translated to other 2D materials using almost identical conditions. The exfoliation solvent may differ, but Table 2.2 (above) can provide a helpful starting point to find a good solvent for the layered material. Method 2 has viability for other transition metal dichalcogenides, but exact experimental parameters may differ and I recommend searching the literature for additional insight before attempting.

2.2.1 Method 1: Scaled-up MoS_2 liquid-phase exfoliation

Bulk flakes of 2H MoS_2 (Sigma Aldrich 69860-100G or Acros 215785000) were placed into four 100-mL vials with 100-mL *n*-methyl-2-pyrrolidone (NMP, VWR) at concentrations ranging from 1–2 mg/mL. The vials were tightly capped, wrapped with electrical tape, and suspended using copper wire in a Branson 5800 bath sonicator for six consecutive cycles of 99 minutes at high power. The water bath was emptied, refilled with tap water, and de-gassed between cycles in order to prevent excessive heating of the bath. In order to help disperse and exfoliate "bulk" flakes that settled to bottom of vial during sonication, I vigorously shook each vial to re-disperse flakes between cycles. Upon completion of the cycles, the dispersions contained a polydisperse thickness distribution of exfoliated MoS_2 flakes ranging from bulk to monolayers. The dispersions were transferred into eight 50-mL Oak Ridge FEP centrifuge tubes (nominal volume: 40-mL) using a 10-mL automatic pipet (4 pipet transfers = one 50-mL tube; one 100-mL vial = 2.5 tubes). The vials were shaken prior to tube transfer in order to collect both exfoliated and unexfoliated flakes. The tubes were centrifuged in a Sorvall RC-5B superspeed refrigerated centrifuge (rotor radius 10.7 cm; # tubes: 8) at 4 °C in order to fractionate the starting dispersion into isolated

volume fractions of various thickness distributions. The typical centrifuge protocol involves three separate centrifuge spins and are as follows:

1) 40 minutes @ 1,000 rpm, "1k", to remove unexfoliated flakes; keep top ~35 mL of supernatant for step (2) – the supernatants can be transferred to disposable centrifuge tubes for intermediary holding; discard sediment.
2) Transfer supernatant from holding tubes to Oak Ridge FEP tubes and fill to top with NMP. Centrifuge supernatant for 68 minutes @ 8k rpm. Separate top ~35 mL of supernatant and place in disposable holding tubes for step (3). Keep sediment if desired and label as "1-8k".
3) Transfer supernatant of (2) into Oak Ridge FEP tubes and fill to top with NMP. Centrifuge for 45 minutes @ 19,000 rpm, "19k" (Note that 19k is the maximum speed of our centrifuge before automatic shutoff. Earlier protocols specified 40 minutes at 20,000 rpm). Discard supernatant (~40 mL) and combine sediments from each tube into a newly labeled "8-20k" fraction, which contains predominately nanoflakes with estimated thickness of 1-15 layers. The supernatant is discarded because it will contain very small fragments of the nanoflakes that are nearly impossible to remove from the supernatant, despite repeated centrifugation at high rpm. If it desired to completely remove *all* nanoflakes, regardless of size, it will be necessary to combine the supernatant with a poor solvent (see 2.2.2 step 9) to successfully crash out all nanoflakes.

Note that earlier centrifuge protocols specified fractions of 1-3k, 3-6k, 6-8k, and 8-20k to isolate other flake thickness distributions (each centrifuge run = 40 minutes). This updated protocol enables rapid preparation of large quantities of thin MoS_2 flakes in reduced

time. For example, a 40-minute centrifuge time at 3,000 rpm (3k) is equivalent to 5 minutes at 8,000 rpm according to the centrifuge equations (Appendix 1). Therefore, fractions 1-3k, 3-6k, and 6-8k were consolidated into 1-8k by centrifuging @ 8k rpm for 68 minutes rather than 40 minutes. *Note that this protocol is tuned to the preparation of MoS_2 dispersions for a specific application. If other materials (i.e. graphite, 2D phosphorus, etc.) are prepared using this method, the centrifugation fractions can be modified based on desired application. For example, the 8-20k fraction can be divided into several, such as 8-10k, 10-14k, etc.*

The use of NMP as an exfoliation solvent is not always useful if the desired application of flakes requires a lower boiling point solvent (i.e. film deposition). Unfortunately, many low boiling point solvents are not well-suited for exfoliating layered materials into their nanoflake counterparts. Therefore, the below procedure may be followed to transfer flakes from the original exfoliation solvent into a new solvent (labeled "new solvent") by following the below centrifugation procedure of three solvent washes.

2.2.2 Solvent transfer procedure

1) Fill 50-mL Oak Ridge FEP tube halfway with isolated volume fraction (i.e. "8-20k") in original solvent.
2) Add new solvent to each tube – fill to top.
3) Centrifuge @ 19,000 rpm ("19k") for 1 hour. If supernatant is nearly colorless, proceed to step 4. If supernatant has color, the flakes have not fully crashed out, and an additional step is required (see step 9).
4) Discard supernatant of (3) using automatic 10-mL pipet. Be careful not to disturb sediment. If sediment is disturbed, there is a risk of removing sediment with discarded supernatant. There is typically 2-5 mL of solvent that cannot be removed due to re-dispersion.

5) Once supernatant is removed, use automatic pipet to transfer sediments into a 10-mL Oak Ridge FEP tube – divide sediments equally between tubes, with targeted volume of 5-mL (half-full). I recommend a 10-mL tube for this second wash in order to prevent waste.
6) Fill 10-mL tube to top with transfer solvent.
7) Centrifuge 10-mL tubes in the Sorvall RC-5B @ 19k for 25 minutes. Discard supernatant *(remove solvent using long-necked plastic disposable pipets…NOT a glass pipet, as this will scratch and damage tubes)*, add new solvent, and sonicate briefly (2-5 seconds) to resuspend sediment. Repeat step (7) until confident that original solvent is completely removed (typical washes require 2 centrifuge runs in 10-mL tube).
8) After final 19k run in 10-mL tube (step 7), add 1-5 mL new solvent to sediment. Transfer to scintillation vial and sonicate briefly (2-5 seconds) before using.
9) If color remains in the supernatant after step 3, the new solvent is too much of a "good" solvent for material and the flakes will not successfully crash out of the solvent. In order to fully wash the flakes of the original solvent, a "poor" solvent (such as methanol, ethanol, or toluene) must be used in an intermediary washing step before transferring to the new solvent. Follow steps 1-7 using the intermediary solvent. After one centrifuge run at step 7, the new solvent can then be added for final transfer. Step 7 may be repeated as many times as needed to ensure complete intermediary solvent removal.

Note that the exfoliated flakes may crash out over time, so it is wise to briefly sonicate any prepared dispersion before using.

2.2.3 Method 2: *n*-butyllithium MoS_2 exfoliation

The *n*-butyllithium (*n*BuLi) intercalation method of MoS_2 exfoliation was first developed by Joensen, Frindt, and Morrison in 1986[3]. The intercalation process is used to create aqueous dispersions comprised of predominantly monolayer MoS_2 flakes, which has distinct advantages to the exfoliation technique of method 1, which produces polydisperse distributions of MoS_2 nanoflakes. While promising, the disadvantages of the *n*BuLi method must also be considered. First, the use of *n*BuLi is hazardous, as it reacts strongly in the presence of water and requires extreme caution. It must be used under inert conditions, such as in a glovebox or using a Schlenk line. Second, the *n*BuLi method produces MoS_2 monolayers that are of the metallic (1T) phase rather than the semiconducting (2H) phase of method 1. The 2H phase has been shown to be recovered in *films* after an annealing step at 200 – 300 °C under inert conditions.

My method relies heavily on that of Eda, G. and co-workers[4], with the caveat that the method reported in their original paper is incorrect as they later published a correction[5] to their methods section. I also modified their method to reinstate the semiconducting 2H phase of the monolayer MoS_2. My revised procedure for Method 2 is as follows:

Add 3 mL of 1.6 M *n*-butyllithium hexanes solution (Sigma Aldrich) to 0.3 g of MoS_2 powder (Acros Organics) in a 5-mL round bottom flask (RBF) topped with a rubber stopper and purged with N_2(g). Let flask sit for 2 days under a closed N_2 atmosphere. The powder will noticeably expand upon intercalation. After 2 days, purge the flask with N_2, and add fresh hexanes from a bottle stored under ambient conditions. The ambient storage conditions will result in hexanes that contain a small amount of water/oxygen that will help scavenge any unreacted *n*BuLi. After adding the hexanes, uncap the 5-mL RBF and wash the *n*BuLi-MoS_2 with 100-mL hexanes using a filter flask (ambient conditions) to remove excess *n*BuLi.

It will most likely be necessary to add additional hexanes to the RBF and scrape the sides with a spatula to collect all of the powder. After washing, place the *n*BuLi-MoS_2 into a 100-mL scintillation vial and add 100-mL DI water. The water reacts exothermically with the *n*BuLi to create butane(g), LiOH (aq), and possibly H_2(g) that literally blows apart the layers of MoS_2. Bubbles will be noticeable at the top of the opaque dispersion. Next, cap the vial, wrap with electrical tape to help seal, and bath sonicate in a Branson 5800 bath sonicator for 1 hour at max power (use copper wire to suspend vial in the bath). After sonicating, measure the pH of the dispersion using pH strips. It should be ~12-14 due to presence of LiOH.

After sonicating, wash the flakes with DI water via several centrifugation cycles to remove the residual LiOH. Follow the below steps to complete the washing cycle and monitor the removal of LiOH using pH strips. Washing is complete when pH ≈ 7.

1) Using the 50-mL Oak Ridge FEP centrifuge tubes, centrifuge at 3,000 rpm (3k) at 4 °C for 40 minutes to remove any unexfoliated flakes. Collect 38 mL of supernatant and proceed to step (2); discard sediment.
2) Wash 1: Add DI water to supernatant of (1) until FEP tube is filled to top. Centrifuge at 19,000 rpm for 2 hours. Remove supernatant, place in disposable tube, and measure pH (~10-11). Add fresh DI water to the sediment and re-suspend nanoflakes using the Vortex.
3) Wash 2: Centrifuge at 19k for 1 hour. Remove supernatant, place in disposable tube, and measure pH. Add fresh DI water to the sediment and re-suspend nanoflakes using the Vortex.

4) Wash 3: Centrifuge at 19k for 1 hour. Remove supernatant, place in disposable tube, and measure pH. If pH ≈ 6-7, washing is complete. Otherwise, repeat step 4 until pH is neutral.

2.2.4 Conversion of 1T *n*BuLi-MoS_2 to 2H phase

Because the *n*BuLi exfoliation method results in flakes of the 1T phase, it is necessary to induce a phase change back to the 2H phase for experiments that rely on the semiconducting nature of MoS_2. Eda and coworkers[4] demonstrated that annealing films of *n*BuLi-MoS_2 at temperatures above 200 °C for 1 hour resulted in a greater than 90% conversion of 1T to 2H phase. However, their method annealed flakes that were deposited in a film, which is not amenable to processing of the nanoflakes for future use. The following steps detail my modified protocol for the conversion of the metallic 1T phase of *n*BuLi-MoS_2 into the semiconducting 2H phase by refluxing in 1,3-dimethyltetrahydropyrimidin-2(1*H*)-one (DMPU) under N_2 at ~250 °C. Note the use of a Variac and heating mantle rather than a hotplate/oil bath to achieve the high temperatures required.

1) After the DI water washing of *n*BuLi-MoS_2 (section 2.2.3) to remove LiOH, add a total of 50 mL 1,3-dimethyltetrahydropyrimidin-2(1*H*)-one (DMPU) to the remaining sediment of 1T MoS_2/DI water. Don't worry about removing residual water, as this will be evaporated off during reflux. Set aside 0.2–2 mL for UV-vis transmittance measurement. (Volume is concentration-dependent; set aside enough dispersion to achieve good S/N in a 3 mL cuvette.)
2) Transfer the dispersion of step (1) into a 100-mL single-neck RBF. Bubble N_2 through the dispersion with stirring (football-shaped stir bar) for 20 minutes to remove oxygen.

3) After 20 minutes, immediately remove needle and connect flask to a long condenser (~1.5 feet) that is outfitted with a rubber septum at its top. Insert N_2 purge needle and needle connected to a bubbler in the septum on top of the condenser.
4) Place a heating mantle filled with sand under the RBF and connect to a Variac. Continue stirring by placing stir plate under the Variac. Be sure that sand uniformly surrounds the dispersion of MoS_2/DMPU and insert a high-temp thermometer or thermocouple into the sand to monitor the temperature. Slowly ramp temperature by incrementally increasing the Variac setpoint voltage to a final value of 55V. In the author's experience, the appropriate setpoint value was found by ramping the temperature over the course of 2 hours until boiling was observed. The 2 hours can be decreased with the knowledge of the final setpoint of 55V, but still use caution as the final setpoint may vary based on experimental conditions.
5) Heat @ ~250 °C (boiling) for minimum of 4 hours. Shut off heat and continue stirring while cooling overnight.
6) Once cool, measure UV-vis (300-800 nm) of the refluxed dispersion to confirm conversion to 2H phase. Compare to the UV-vis spectrum of the 1T dispersion that was set aside in step (1). The emergence of a peak (exciton C) at ~400 – 450 nm is direct evidence of successful conversion to the 2H phase (Figure 2.3B). There will also be two smaller humps (excitons A and B) that emerge at 600 – 700 nm. Photoluminescence is also a measure of successful conversion to the 2H semiconducting phase (Figure 2.3B, inset).
7) If 2H conversion successful, transfer MoS_2 nanoflakes to solvent of choice using the solvent transfer procedure of 2.2.2 with 10-mL or 50-mL Oak Ridge FEP tubes. Note

that the use of toluene as an intermediary solvent will be necessary because DMPU is a good solvent for *n*BuLi-MoS_2. After solvent transfer, the flakes have a very high tendency to aggregate in solution. It will be necessary to sonicate briefly (2-5 seconds) before using the dispersion.

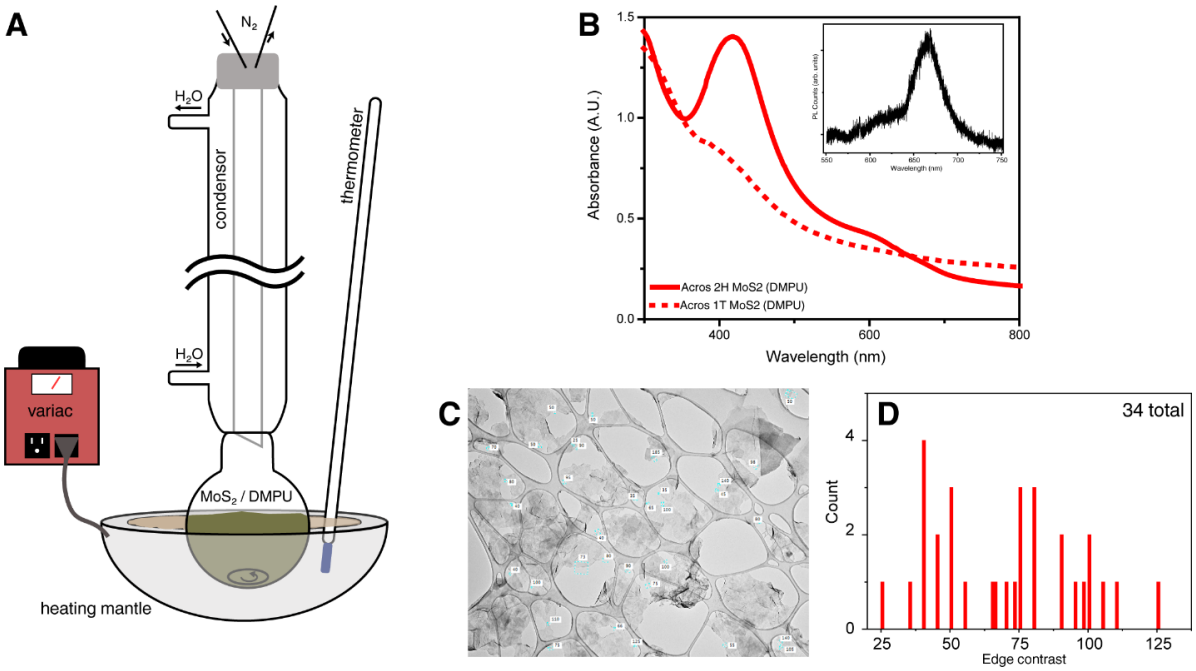

Figure 2.3 | Conversion of 1T metallic MoS_2 to 2H semiconducting phase. (A) Reflux setup for the thermal conversion of MoS_2 from metallic 1T to semiconducting 2H phase. DMPU = 1,3-dimethyltetrahydropyrimidin-2(1*H*)-one, boiling point = ~240 °C. **(B)** UV-Vis demonstrates emergence of C exciton at ~420 nm upon 2H conversion. Inset shows photoluminescence of 2D MoS_2 flakes, which further confirms 2H phase. **(C)** Low-resolution TEM of nBuLi-MoS_2 after refluxing in DMPU (A). **(D)** Edge contrast analysis of flakes in (C) show that flakes are in the range of 1-4 layers in thickness.

2.3 Thin film deposition of 2D materials

2.3.1 Vial interface method

The interfacial assembly of 2D materials utilizes oil-water interface energy differences to form well-ordered films of 2D materials. When two immiscible non-solvents (poor solvents for the 2D material) are mixed together, the 2D material self-assembles at their interface in order to minimize the free energy of the system. This process results in highly uniform films that can be easily transferred to a hydrophilic substrate by simply pulling the substrate vertically through the interface (Figure 2.4). My methods are based on the work of Divigalpitiya and coworkers[6-7], who assembled monolayers of *n*BuLi-exfoliated MoS_2[3] (see section 2.2.3) at the interface of hexanes (or 1-hexene) and water.

As shown in Figure 2.4, a concentrated 2D material suspension in isopropanol (IPA) (see sections 2.2.1 and 2.2.2) is mixed with 1–2 mL hexanes or 1-hexene and placed into a scintillation vial. IPA is used to suspend the flakes and prevent aggregation/crashing out of solution. The hexanes/1-hexene serve as the immiscible phase. Distilled water is added to the vial, forming an immiscible layer below the organic solvent (Figure 2.4A). The water depth should be greater than the substrate length. Cap and shake the vial vigorously until the 2D material migrates from the organic phase to the interface (Figure 2.4B). You may notice emulsions of 2D materials that encapsulate an organic or water droplet, but most of the 2D material should eventually migrate to the interface. The packing of 2D nanoflakes at the interface is highly dependent on the concentration of the starting dispersion in relation to the surface area of the interface. The thin film may be transferred to a hydrophilic substrate (e.g. glass slide) by inserting the substrate through the non-polar upper phase into the water phase and slowly pulling it through the interfacial film (Figure 2.4C). The hydrophilic nature of the substrate enables the water + 2D material to "spread" up the slide to deposit a thin film

(Figure 2.4D). The mechanism of spreading and deposition is not compatible with hydrophobic substrates. If a hydrophobic substrate were used, the film would pre-maturely deposit onto the slide as it was inserted into the water and would be washed away when removed through the organic upper layer. Examples of MoS_2 films created via this approach are shown in Figure 2.4E. Notice the distinct color progression from left to right as the films go from bulk material to thin (2D) flakes with volume fractions 1-3k, 3-6k, 6-8k, and 8-20k (see section 2.2.1 for a description of liquid phase exfoliation).

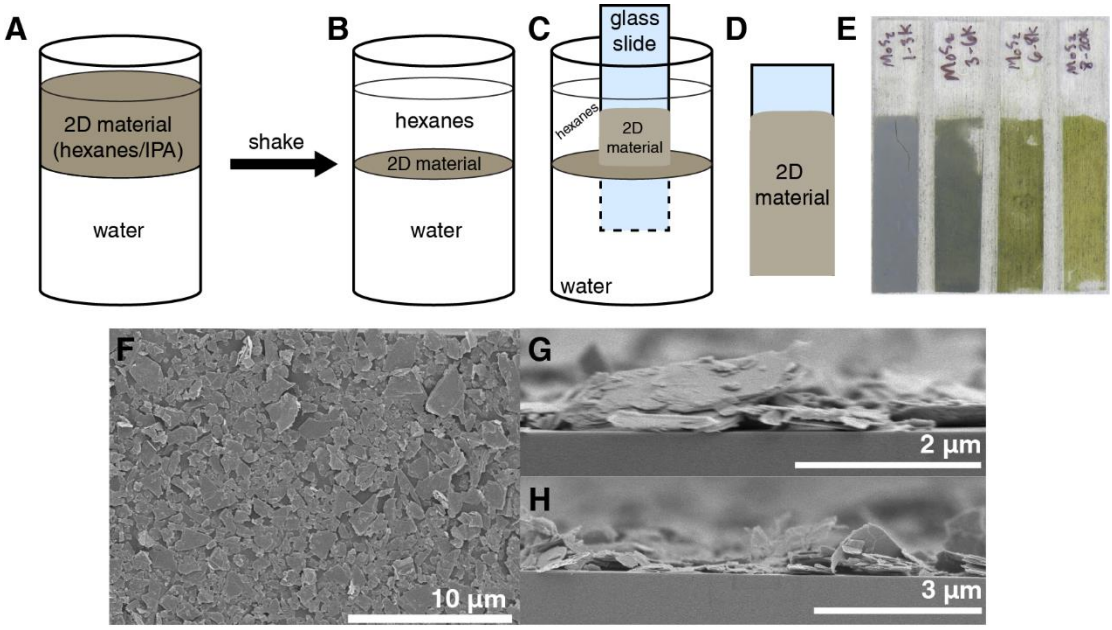

Figure 2.4 | Interface films of 2D materials. (A) 2D material suspended in organic solvent that is immiscible with water subphase. **(B)** Shaking the vial results in a self-assembled 2D thin film at the interface. **(C–D)** transfer of thin film to hydrophilic substrate. **(E)** Films of MoS_2 nanoflakes ranging from thick flakes (1-3k) to thin (8-20k). **(F)** top-down SEM image of thick flakes of MoS_2 prepared by vial interface method. **(G-H)** cross-section images of film in (F).

2.3.2 Buchner interface method

Impressed with the results of this simple technique, I began to explore other interfacial methods for self-assembly of 2D materials. My first attempt to scale up my film interface work is modeled after the methods of Yu et.al.[8-9] to self-assemble MoS_2 at the interface of hexanes and water, but without the shaking requirement of the Divigalpitiya

method[6-7] (Figure 2.5). In this approach, the resulting film may be deposited on a horizontal substrate using a Buchner funnel, enabling a layer-by-layer deposition of 2D material assemblies that is otherwise not possible with the interface method.

The Buchner interface method utilizes a similar approach to the vial interface method, but the 2D dispersion is added directly to the organic-water interface rather than mixing with the organic upper phase and shaking to induce self-assembly. A key difference between my work and the work of Yu et. al. is that I am not using any type of surfactant to stabilize my flake dispersions. Surfactant can be troublesome to completely remove and we wanted to avoid trace contaminants in our films. However, the surfactant can be useful in preventing flake-to-flake aggregation of the 2D material dispersion and may enhance the spreading and ordering of the nanoflakes into a thin film.

The deposition procedure for the Buchner interface method is shown in Figure 2.5. Place the substrate of choice (hydrophilic or hydrophobic) at the bottom of a fine-fritted Buchner funnel. Add ~10 mL of deionized water to the funnel followed by ~5 mL hexanes. Be careful not to disturb the water surface when adding the hexanes to prevent the formation of emulsions. The 2D material dispersion is then added via glass pipet in a continuous flow directly at the interface of the immiscible fluids. When the nanoflakes are first added, they may aggregate slightly, but the interfacial energy mismatch between the hexanes and the water forces the flakes to spread out to minimize the surface energy. Excess hexanes are then removed with a pipet and any residual hexanes are left to evaporate before proceeding. It may be helpful to flow a steady stream of air or N_2 (g) over the surface of the film to speed evaporation. Once the hexane layer is removed, the water is pulled through the bottom of the

Buchner funnel via vacuum pump, lowering the interface film onto the substrate. The mechanism of the deposition enables its applicability for a variety of substrates.

As shown in Figure 2.5C–E, the interfacial film is comprised of highly packed flakes that is transparent to visible light when deposited onto a glass substrate (E). Multiple depositions can be achieved by annealing under inert or vacuum conditions between each step to remove excess solvent. The results of this method were promising, enabling semi-controlled deposition of thin films in a timely manner. However, the lack of control over material packing density hindered reproducibility and often resulted in non-uniform films.

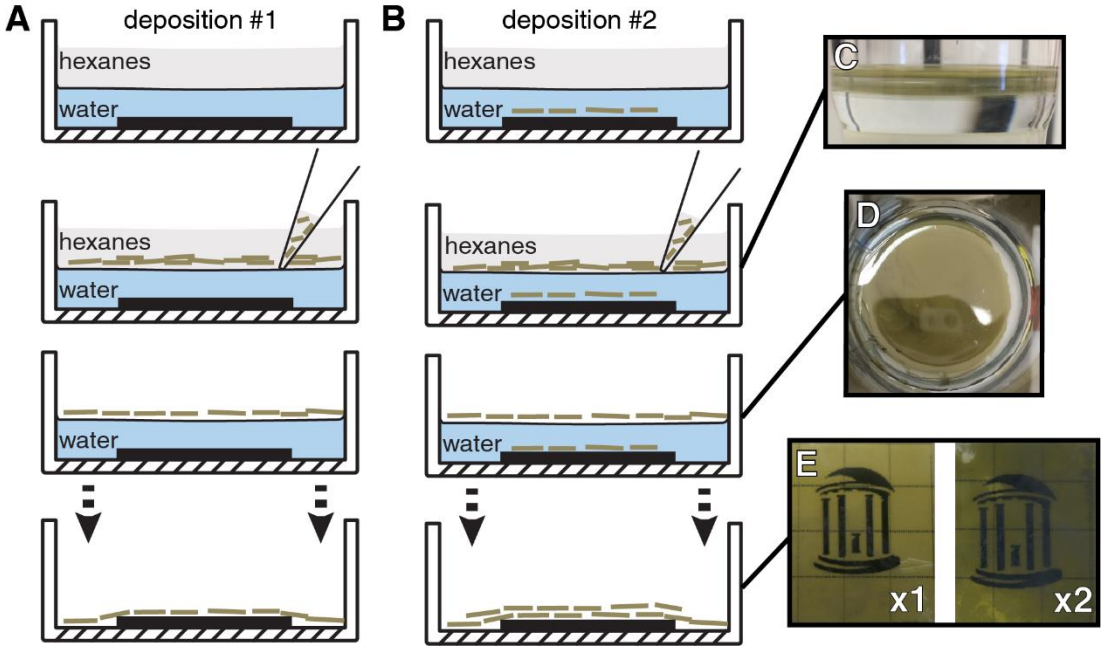

Figure 2.5 | Buchner funnel interface film. (A) Hexanes/water interface with a substrate (black box) laying on top of Buchner glass frit in water phase. The 2D material suspension is deposited at the interface, the hexanes are evaporated, and the water is removed from the bottom of the glass frit to deposit the film onto the substrate. **(B)** After annealing at 150 °C under N_2, it is possible to achieve multiple depositions. **(C-E)** 1-layer and 2-layer 6-8k MoS_2 interface film deposited on a glass slide.

2.3.3 Langmuir-Blodgett assembly

The general success of these methods led to my pursuit of Langmuir-Blodgett (LB) assembly, which has received recent interest as a tool to create ordered assemblies of 2D

materials[10-27]. The LB method relies on an air-water interface for self-assembly, where the 2D material is deposited on a water subphase via carrier solvent that evaporates and leaves a thin film floating on the water surface. Langmuir-Blodgett assembly was originally designed to study the mechanics of molecular packing and spreading of a surfactant on a water subphase[28]. A droplet of molecules would immediately spread out on the water surface upon impact, forming a monolayer film. Molecular packing is controlled via movable barriers on the outside edge of the trough: by moving the barriers inward, the molecules would become more tightly packed. Other dynamics that influence packing density can also be controlled with the LB system, including pH and water temperature.

The packing of 2D nanoflakes at an air-water interface is a different mechanism of self-assembly than the organic-water interface methods previously described. The LB apparatus offers several distinct advantages over the above approaches, including (1) large-area substrate compatibility, (2) software-controlled packing densities of 2D nanoflakes with surface pressure monitoring, (3) dipping rate control at a variety of angles, (4) temperature control of the water subphase, and (5) adaptability to air-water or oil-water interfaces. Most of the early work on the LB trough for 2D materials focused on graphene[10, 12-13, 15, 19, 24], with a few papers demonstrating the application to MoS_2[29-30] and metal oxides[11, 31]. In the case of the metal oxides, the material is not deposited on the surface of the water but is rather mixed directly with the water subphase and allowed to migrate to the air-water interface (typically by pH control) for thin film formation. There have also been attempts to deposit phosphorene[32] as a large-area film using an LB trough.

The Langmuir-Blodgett trough in the Warren Lab is a Biolin Scientific KSV NIMA Medium trough with Delrin barriers (see Figure 2.6) on a standard frame. Additional

accessories include a temperature sensor, injection port, and Teflon barriers which have a slightly different hydrophobicity than the Delrin barriers. A pH sensor is also available for purchase and is compatible with our system. The trough is housed in an enclosed cabinet to prevent dust contaminants and unwanted air circulation and is located on an isolation table to dampen vibrations from the surroundings. The barriers, dipper, surface pressure, and trough temperature are controlled via software on a laptop computer, and there is also an external control unit with an LCD display that enables simple control over the compression/decompression of the barriers or raising/lowering of the dipper head.

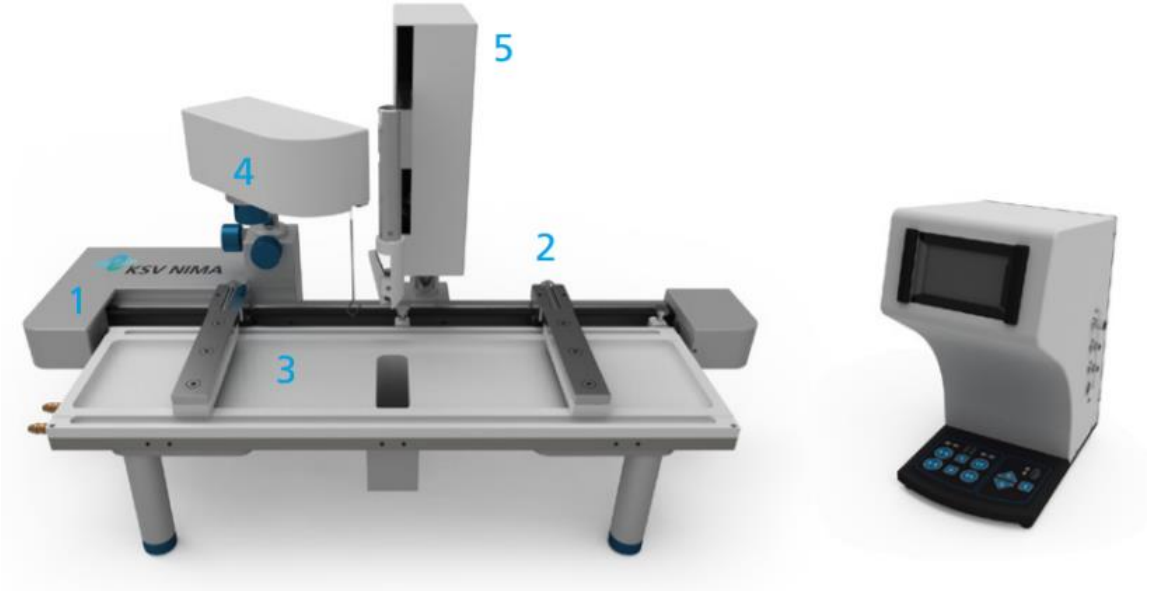

Figure 2.6 | KSV NIMA Langmuir-Blodgett Medium Trough with external control unit. (1) Standard Frame, (2) Barrier, (3) Trough, (4) Force sensor (i.e. balance), (5) Dip Coater. Image credit: https://www.biolinscientific.com/

The packing density of the deposited material is monitored with a force sensor and controlled by compressing or decompressing barriers at the edges of the trough. Measured as a force-per-area, the surface pressure (Π) is here defined as the difference between the final surface tension of water + "surfactant" (γ_s) and the initial surface tension of a clean water surface (γ_w):

$$\Pi\ (\frac{\mathrm{mN}}{\mathrm{m}}) = \ -\Delta\gamma = \ -\ [\gamma_s - \gamma_w] \tag{2-4}$$

The surface tension of water + surfactant (γ_s) will always be less than that of pure water (γ_w). As the concentration of surfactant (i.e. 2D material) increases at the water surface, the surface tension will decrease and result in an increase in the measured surface pressure (Π). High aggregation of surfactant will decrease γ_s, while low aggregation and high spreading of surfactant over the water surface will increase γ_s. In an ideal system, the surfactant will spread until $\Delta\gamma = 0$, with γ_w as the upper limit. The surface tension can be directly measured by monitoring the force exerted on a Wilhelmy plate (Figures 2.7 and 2.8B):

$$F\ (mN) = \rho_p g l_p w_p t_p + 2\gamma\left(t_p w_p\right)(cos\theta) - p_l g t_l w_l h_l \tag{2-5}$$

where the first term and second terms capture the net downward force of the plate and the third term represents the counterforce (buoyancy) of the water. The symbols are defined as: ρ_p = density of plate, g = gravitational constant, l_p = length of plate, w_p = width of plate, t_p = thickness of plate, γ = surface tension of the water, θ = wetting angle (Figure 2.7B), ρ_l = density of water, and $t_l w_l h_l$ represents the volume of the plate submerged under water.

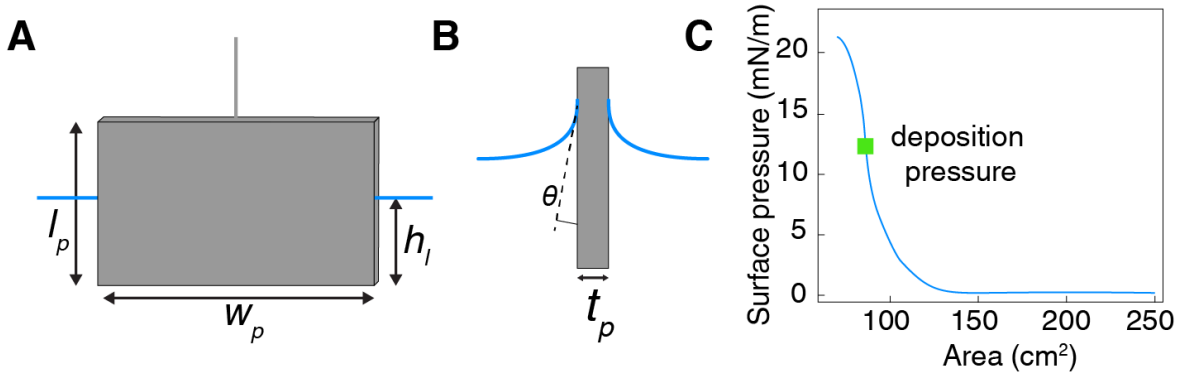

Figure 2.7 | Wilhelmy plate pressure sensor. (A) Front-view of platinum Wilhelmy plate with the length (l_p), width (w_p), and height/depth of submersion (h_l). **(B)** Side view of Wilhelmy plate with thickness (t_p) and wetting angle (θ). **(C)** Typical isotherm measurement depicting increase in surface pressure (mN/m) as the area of the trough decreases when the barriers are compressed.

Because the first and third terms of equation (2-6) cancel each other out, the force is a direct measurement of the surface tension of the water. When $\cos(\theta) = 1$ and $\omega_p >> t_p$, the surface pressure is determined by measuring the difference in the force before and after surfactant addition/compression:

$$\Pi\left(\frac{mN}{m}\right) = -\Delta\gamma = -\frac{\Delta F}{2(w_p + t_p)} = -\frac{\Delta F}{2w_p} \quad (\text{when } t_p \ll w_p) \tag{2-6}$$

An isotherm (Figure 2.7C) gives a visual depiction of surfactant packing. As the area of the trough decreases, the surface pressure will increase as a result of the decreased surface tension (γ_s). The inflection point near the top of the curve is an indication that the surfactant has "buckled" and is no longer assembled in monolayer form[26]. The ideal surface pressure of deposition is therefore a point on the isotherm that is before the inflection, or buckling, point but at a high enough pressure to exhibit good packing density.

The traditional method of thin film transfer for a LB system is via vertical dipping and withdrawal of a substrate through the thin film through use of a dipping well (Figure 2.8A). The surfactant thin film is transferred to the substrate through hydrophilic, hydrophobic, or ionic interactions. Many of the early molecules of study were lipids, characterized by a polar head and non-polar tail that could be harnessed for varying deposition procedures. The Langmuir–Shaefer (LS) method of deposition is nearly identical to that of the LB design, but the substrate does not travel through the film. Instead, it is lowered horizontally to just touch the film surface and lift away with the transferred molecules. This transfer method requires a special dipper design that holds the substrate via suction and we do not have one with our system. Figure 2.8A shows the LB trough with freshly-deposited 2D MoS_2 nanoflakes and Figure 2.8B shows the reflective film of highly

compressed nanoflakes at the air-water interface. The packing density is controlled by monitoring the surface pressure of the interface.

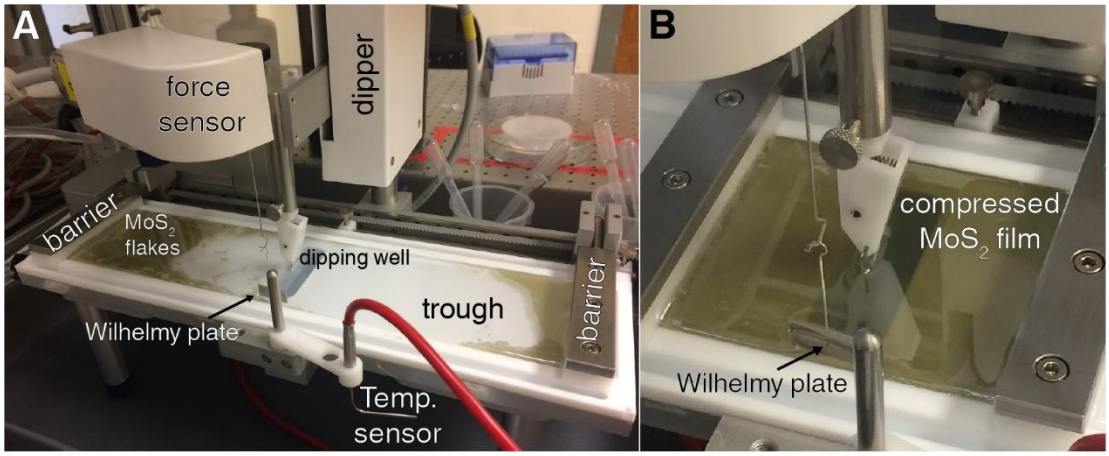

Figure 2.8 | KSV NIMA Langmuir Blodgett medium trough with MoS_2 2D flakes deposited on the water surface**(A)**. **(B)** Compressed film of highly-packed 2D MoS_2 flakes with a vertical dipping geometry.

The LS method is similar to the method that I have developed for 2D material deposition in that the substrate is geometrically positioned horizontally in relation to the water subphase rather than vertically. A key difference between the LS and my approach is that the substrate in my method physically travels through the thin film rather than resting on the top surface. My approach is very similar to that of the Buchner interface method mentioned above but utilizes an air–water interface rather than hexanes–water and offers more control over flake packing and film transfer. If a vertical deposition is desired, the LB system will function in a similar fashion to the vial interface method (above) that relies on the spreading of solvent up the substrate to deposit flakes. The utility of the horizontal deposition is that flakes may be deposited on a variety of substrates and are not limited to hydrophilic substrates as in a vertical deposition.

I now present a generalized procedure for the deposition of 2D materials using the Langmuir-Blodgett trough. The approach has been successfully applied to create films of

MoS_2, WSe_2, graphene, and phosphorene with multiple layers of deposition on substrate sizes of ~16 cm^2 (Figure 2.9). Larger substrates approaching 40 cm^2 have also been accommodated.

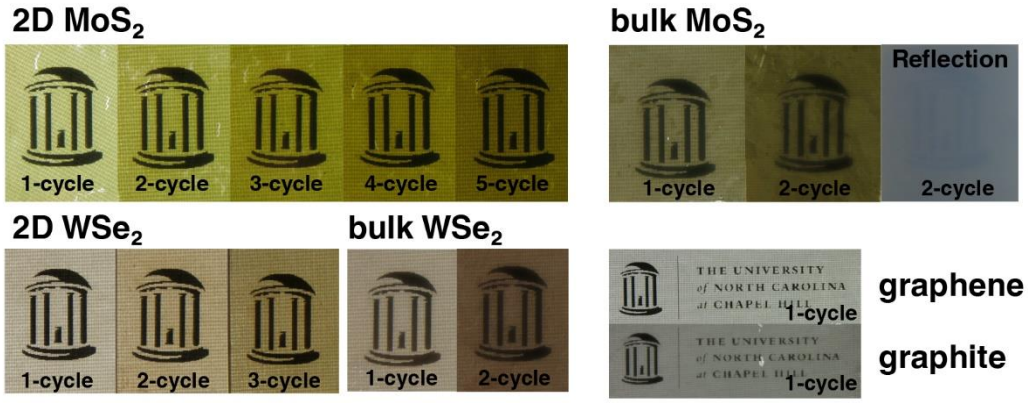

Figure 2.9 | Transparent films of 2D materials via LB trough deposition. Scale: the "Old Well" = 1 cm wide. All 2D materials were prepared via method 1 protocol of section 2.2.

Single layer deposition

1) Turn on the laptop and external control unit (switch on back). Push red button on Chiller unit to power on. Open LB trough software and click "Manual Control" from top menu to open the controls for the LB trough. Click on temperature and select "On" and "Bath". Typical temperature set point is 20 °C. If "Control" is selected rather than "Bath", the temperature sensor (connected to red cord) will be used instead.
2) Clean the trough and barriers thoroughly before using. Rinse with ethanol and use paintbrush to thoroughly coat trough and barriers. Next, rinse with DI water (~18 MΩ-cm) to dissolve ethanol and use vacuum pump to remove all liquid. A KimWipe may be useful to wipe off tough stains during the ethanol rinse that the brush is not able to remove. If a deep cleaning is needed, remove trough from stand and carefully wash with soap and water. Be careful not to scratch or dent the Teflon surfaces.

3) After cleaning, place barriers into their slots on the trough. Fill trough with DI water (~18 MΩ-cm) such that the water forms a curved surface ~3-5 mm above trough edge.
4) Use reverse tweezers to remove platinum Wilhelmy plate from the ethanol soak bath. Rinse with water and hang plate from force sensor hook. The plate should be halfway submerged into the water subphase and be positioned perpendicular to the barriers (see Figure 2.6B).
5) Using the software, zero the balance (force sensor) when the barriers are fully opened. Close the barriers (either with the software or using the external control unit) and monitor the surface pressure (Π, mN/m). If $\Pi \leq 0.3$ mN/m, the water surface is clean and you can proceed to step 7. If it is above 0.3 mN/m, proceed to step 6.
6) If $\Pi > 0.3$ mN/m, vacuum off any dust particles from the surface. Be sure to turn vacuum pump to low power so that you don't remove the trough water. The dust particles are easiest to see with reflected light. Once particles are removed, close the barriers and monitor Π. Repeat cleaning/vacuuming until $\Pi < 0.3$ mN/m.
7) Insert the substrate of choice into the water subphase. Previous substrates have included glass, quartz, silicon, silicon oxide, FTO, Teflon, and silicone. There are two options available for mounting, including a vertical mount where the substrate is clipped directly to the dipper head and an angled mount, which utilizes a metal piece that clips to the dipper head and the substrate is held in place by magnets (for large or heavy substrates, use strong magnets). There are several different angled metal brackets available, but the most commonly used angle is 90°. Note that the metal brackets are coated with a hydrophobic polymer coating to prevent rusting.

8) IMPORTANT STEP: When inserting the substrate, stop the dipper when the substrate comes in contact with the water surface. ZERO THE DIPPER POSITION on the software. If the dipper is not zeroed, it could wreak havoc during the dipping step later on because the software may lower the substrate into the trough rather than raising it.
9) After the substrate is inserted below the surface of the water, zero the balance sensor using the software and repeat step 6 to remove excess particulates that accumulated during substrate insertion.
10) Preparation of 2D material dispersion: for detailed procedures for 2D material preparation and solvent transfer, see sections 2.1.2 and 2.2. n-butanol is chosen as a carrier solvent due to its relatively low boiling point (118 °C), immiscibility with water, and ability to disperse 2D flakes well. Other solvent carriers can certainly be considered and common examples included hexanes and DCM.
11) Addition of 2D materials to the water subphase: *The total amount of material added will depend on the starting concentration of the dispersion. Add enough sample so that the total area coverage is 2 – 3 times larger than the area of the substrate.* Add the 2D material sample suspended in n-butanol dropwise to the water subphase using a glass Pasteur pipet. Hold the tip close to the water surface to prevent large ripples of the water subphase. Add a second drop after the n-butanol is no longer moving over the water subphase. If the trough is too full, the addition of 2D material can cause the water and 2D material to spill out the sides of the trough. If this occurs, remove excess water by vacuuming water from outside of barrier.

12) When adding the 2D material dispersion dropwise, focus the droplets on one side of the trough. The flakes will self-assemble at the opposite side of the trough due to the surface tension mismatch between n-butanol and water. If material gets stuck toward the center of the trough, add a few droplets of n-butanol/2D material near the stuck material to force it to migrate to the opposite end of the trough. The goal is to achieve uniform packing density and no gaps in coverage prior to compression.
13) After flake deposition, the Π will likely be ~20 – 24 mN/m. The large increase is a combination of the 2D material and residual n-butanol that has not yet evaporated. Turn on the fan (Figure 2.10) and fasten it so that it blows air *away* from the trough to help facilitate n-butanol evaporation from the water surface. Let sit for 20–30 minutes to allow the 2D flakes to relax as the n-butanol finishes evaporating. Note that if left for too long, the water subphase will begin to evaporate, resulting in a change in the surface pressure.

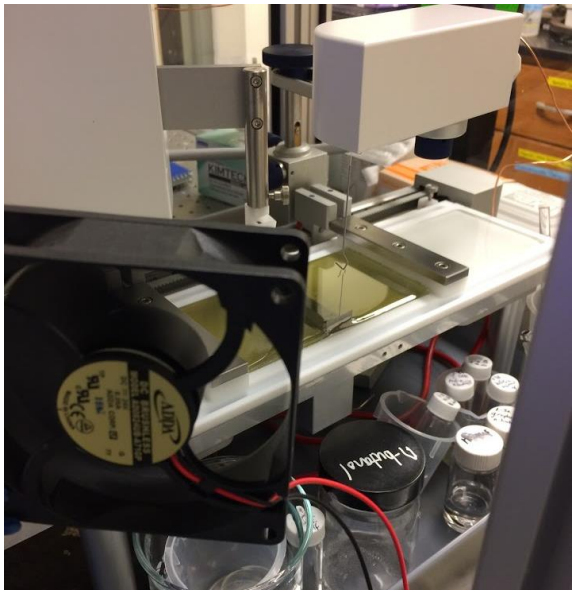

Figure 2.10 | Optimized LB trough setup. The fan is blowing air away from the trough to increase rate of n-butanol evaporation. Notice the compressed film in the background.

14) After 20 – 30 minutes, Π will be in the range 15 – 20 mN/m.

15) Open the dipping control from the main software window. Click “dip”. On the pop-up “trough” window, set the surface pressure to 22 mN/m (this may vary based on material used and trial-and-error) and the barrier rate to 10 mm/min. The forward and reverse barrier rates after reaching the Π set point are typically set between 3 – 5 mm/min. Press Go/Hold. The barriers will move inward over the water surface until the Π set point is reached.
16) Once the set point is reached, increase Π by 1 mN/m until the target pressure of ~24 mN/m using the trough control window (you will need to click Window > Trough Control to re-open). A target of 24 mN/m is a good starting place. Your actual target pressure will vary depending on material and desired packing density. For 2D material systems, the self-assembly induced with the n-butanol/water surface tension mismatch results in decently packed flakes from the start. Therefore, the surface pressure increase mostly enables the created film to be moved over top of the horizontal substrate.
17) After the target pressure is reached, ensure that the substrate lies entirely beneath the thin film and that there are no gaps in surface coverage. If there is a gap above the film, try to rotate the dipping head so that the substrate avoids the gap. If this doesn’t work, it is possible to increase the surface pressure to close the gap, but note that Π > 25 mN/m may result in stress lines parallel to the barriers due to flakes buckling and aggregating together.
18) Click on the dip control window (it will have already popped up when the target pressure was first reached. If not, access it through Window > Dip control.

19) CLICK BOX TO SET LOWER LIMIT ON DIPPER. It should be negative if you zeroed the dipper in step 8. If this is not checked, the dipper will lower instead of raise when you press go! Set dipping rate to 0.5 mm/min. Click Start. Check that the table in the window that pops up says “up” (Small letters). The trough will maintain the set pressure during the dipping by moving the barriers forward or backward to maintain the constant pressure.
20) Once the substrate fully emerges from the water subphase, press “stop” on the dipper window and press the up button on the external control unit. When film is dry, remove from clamp and anneal under vacuum at 120 – 150 °C for 20 minutes to remove excess water and n-butanol.
21) Remove the Wilhelmy plate with reversible self-closing tweezers and rinse with water then ethanol. Place carefully in the vial filled with ethanol for storage. The plate will get dirty over time. Periodically clean it using a Bunsen burner to burn off residual material.
22) With the barriers still closed, vacuum off nanoflakes from water surface. Next, remove the barriers and rinse with ethanol, wipe off material residue with KimWipe, rinse with ethanol again, and rinse with water followed by vacuum pump suction to remove liquid.
23) Remove water from trough with vacuum pump. Clean the trough using the ethanol–water combo mentioned several times previously. It will be necessarily to wipe down the dirty areas of the trough with a KimWipe soaked in ethanol.
24) Once clean, replace the cover on the trough to prevent dust accumulation.

Multiple layer deposition

If you wish to deposit multiple layers of a thin film on a substrate, the procedure is essentially identical to the single layer deposition described above. Here I provide a couple of recommendations for multiple layer deposition based on personal experience:

- Anneal the sample at 120–150 °C for 20 minutes in a vacuum oven between depositions to prevent film delamination.
- Overfill the trough with water before inserting the film + substrate into the water. After film insertion, the water level can be readjusted to normal height using the vacuum pump. Explanation: the film is likely to be more hydrophobic than the substrate and the water will not flow as easily over the film. Overfilling the trough allows the water to easily glide over the film + substrate without delamination. If the trough is not overfilled, the water may only partially cover the film at the lowest dipper point, resulting in film delamination at the water edge.

General advice and comments on the LB method:

- Consider the surface tension mismatch of carrier solvent and water subphase. The spreading coefficient[33-36] can play a large factor in the aggregation, spreading, and packing of films during deposition.
- The Wilhelmy plate can be made out of paper rather than platinum, but it is imperative that the paper is thoroughly wetted with water before using as a force sensor to prevent wicking effects and inaccurate measurements.
- If attempting a deposition on a hydrophobic substrate, it is likely that the water may simple roll off the substrate and not deposit any flakes when the substrate is lifted through the thin film. I recommend mounting the hydrophobic substrate onto a

slightly larger hydrophilic substrate for the deposition. Leave room around the edges of hydrophobic substrate to allow the hydrophilic area to act as a "barrier" of sorts to prevent the water subphase from easily sliding away from the hydrophobic section and preventing good flake deposition. This approach has enabled me to deposit well-ordered films of 2D MoS_2 on both silicone and Teflon.

- KSV NIMA also sells a liquid-liquid trough which would enable the organic-water utility of the Buchner interface method (section 2.3.2) along with the pressure, temperature, and dipping control of the LB trough. The basic idea is that the liquid-liquid interface forces flakes to de-aggregate and form more well-ordered films than the air-water interface. At the time of the dissertation submission, KSV NIMA sent the Warren Lab a demo setup of the liquid-liquid trough to determine the feasibility with our materials.
- There are several other methods of sample deposition techniques that I began to experiment with toward the end of my dissertation research but was not able to fully optimize. These include syringe pump[30] and electrospray deposition[37].

2.4. Spectroscopy of 2D dispersions and thin films

This section will introduce the theory of light absorption and light scattering and describe the utility of an integrating sphere to capture scattered light and measure a sample's true absorption. This description will be reinforced with examples of MoS_2 dispersions and films.

Light incident on a sample may be represented by the ideal model of light absorption, given by:

$$I = T + A \tag{2-7}$$

where I = incident light, T = transmitted light, and A = absorbed light. Transmittance is defined as the ratio of the light intensity after passing through a sample (I) to the incident beam (I_0):

$$T = \frac{I}{I_0} \tag{2-8}$$

Absorbance is related to transmittance through the following equations:

$$A = -\log_{10}(T) \tag{2-9}$$

$$A = 2 - \log_{10}(\%T) \tag{2-10}$$

This relationship is not valid in a non-ideal system where light scattering occurs. In this case, a scattering term (S) is introduced on the right side of equation (2-7), resulting

$$I = T + A + S \tag{2-11}$$

Both transmitted and scattered light are measured by the detector as light *not* absorbed by the sample, and these components would not be separable in a typical spectrometer geometry. Equation (2-10) can be modified to better incorporate the scattered light component that will influence the measured absorbance spectrum:

$$A = 2 - \log_{10}(\%T + \%S) \tag{2-12}$$

where %S represents the scattered light. Based on this equation, an increase in %S would result in an increase in the measured absorbance. Therefore, a sample that is highly scattering will exhibit a measured absorbance that is higher than the true absorption of the sample. This inclusion of a scattering component within the absorbance measurement is also known as the concentration-dependent extinction coefficient (k), which includes a scattering component (σ) based on a particle's scattering cross-section in addition to the absorption coefficient (α), yielding the equation:

$$k = \alpha + \sigma \tag{2-13}$$

The extinction coefficient makes up the imaginary component of a material's complex index of refraction ($\tilde{n}$):

$$\tilde{n} = n + ik \tag{2-14}$$

where n = index of refraction and i = imaginary unit. A non-zero n contribution in the wavelength range of interest may result in a non-trivial interpretation of a material's extinction or absorption coefficient, as will be demonstrated in the analysis of thin films of 2D MoS_2.

The scattering component is dependent on particle size. For particles smaller than the wavelength (λ) of the incoming radiation, the wavelength-dependent Rayleigh scattering mechanism dominates, with scattering occurring in all directions proportional to λ^{-4}. As the particle size approaches the wavelength of the incident light, Mie scattering dominates, with scattering occurring predominantly in the forward direction (Figure 2.11). Earlier work demonstrated that light scattering by 2D sheets that are suspended in liquids can be modeled by Mie theory,[38] and this influenced how we designed the optical measurements of 2D phosphorus dispersions for band edge analysis[39] (see appendix 2).

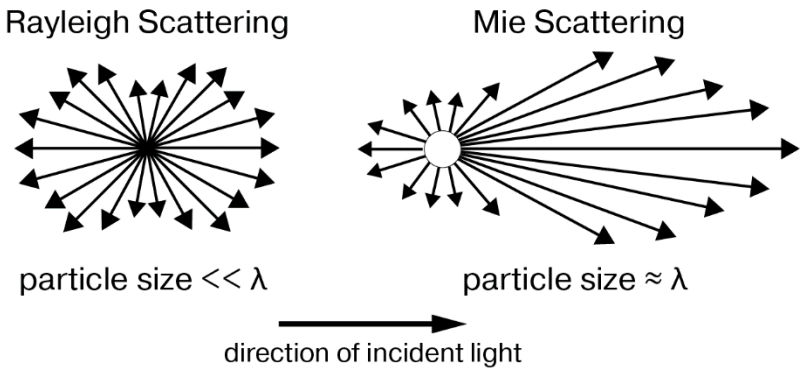

Figure 2.11 | Angular distributions of Rayleigh and Mie scattered light.

The spectroscopic study of MoS_2 dispersions and thin films utilized an integrating sphere (external diffuse reflectance accessory, eDRA) in conjunction with a Cary 5000 double beam spectrometer. This sphere is an upgrade to the integrating sphere (internal diffuse reflectance accessory, iDRA) utilized in chapter 3 and appendix 2 for the spectroscopic analysis of 2D phosphorus dispersions. In contrast to the iDRA, the eDRA allows samples to be placed *inside* the sphere rather than on the outside edge (yes, the name "external" is confusing w.r.t. sample placement inside the sphere). The geometry of the eDRA sphere enables the theoretical collection of all scattered light as well as provides opportunity to separate out different angular components of the scattered light through a variety of sample positions (see Figure 2.12). Additional features of the sphere include a rotating center mount (position 2) and an angled rear mount (position 3) that, when coupled with a light trap, enable the parsing of the diffuse and specular components of thin film reflectance.

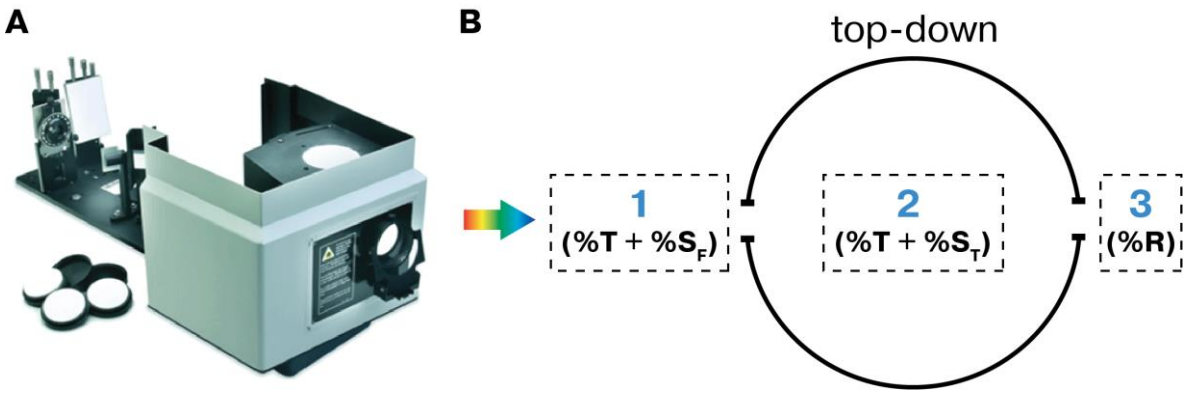

Figure 2.12 | eDRA integrating sphere (A); (B) Top-down sketch of integrating sphere with simplistic representation of light collected by the detector. Position (1) collects transmitted light (%T) and forward-scattered light (%S_F), position (2) collects %T and total-scattered light (%S_T), and position (3) is predominantly used to collect reflected light (%R) of films and powders.

The integrating sphere offers a pronounced advantage over a spectrometer's traditional linear transmission geometry in mitigating the influence of light scattering. To demonstrate this, I show the absorbance spectra of a dispersion of MoS_2 flakes in isopropanol (1-3k fraction, see 2.2.1) measured in the linear geometry as well as two different integrating sphere positions in Figure 2.13. The linear spectrum in Figure 2.13D exhibits a much higher absorbance than the eDRA spectra due to the pronounced scattering background induced by Mie scattering. A careful assessment of the directionality of the light that is collected by each geometry enables the determination of which angular components of the scattered light are screening an accurate measurement of MoS_2 flake absorption. For the linear geometry, only light in direction [1] reaches the detector (dashed line in Figure 2.13A), resulting in the "linear" absorbance spectrum in 2.13D. For the eDRA(1) and eDRA(2) positions (Figure 2.13B and C), light in directions [1] + [2] and [1] + [2] + [3], respectively, are collected by the detector.

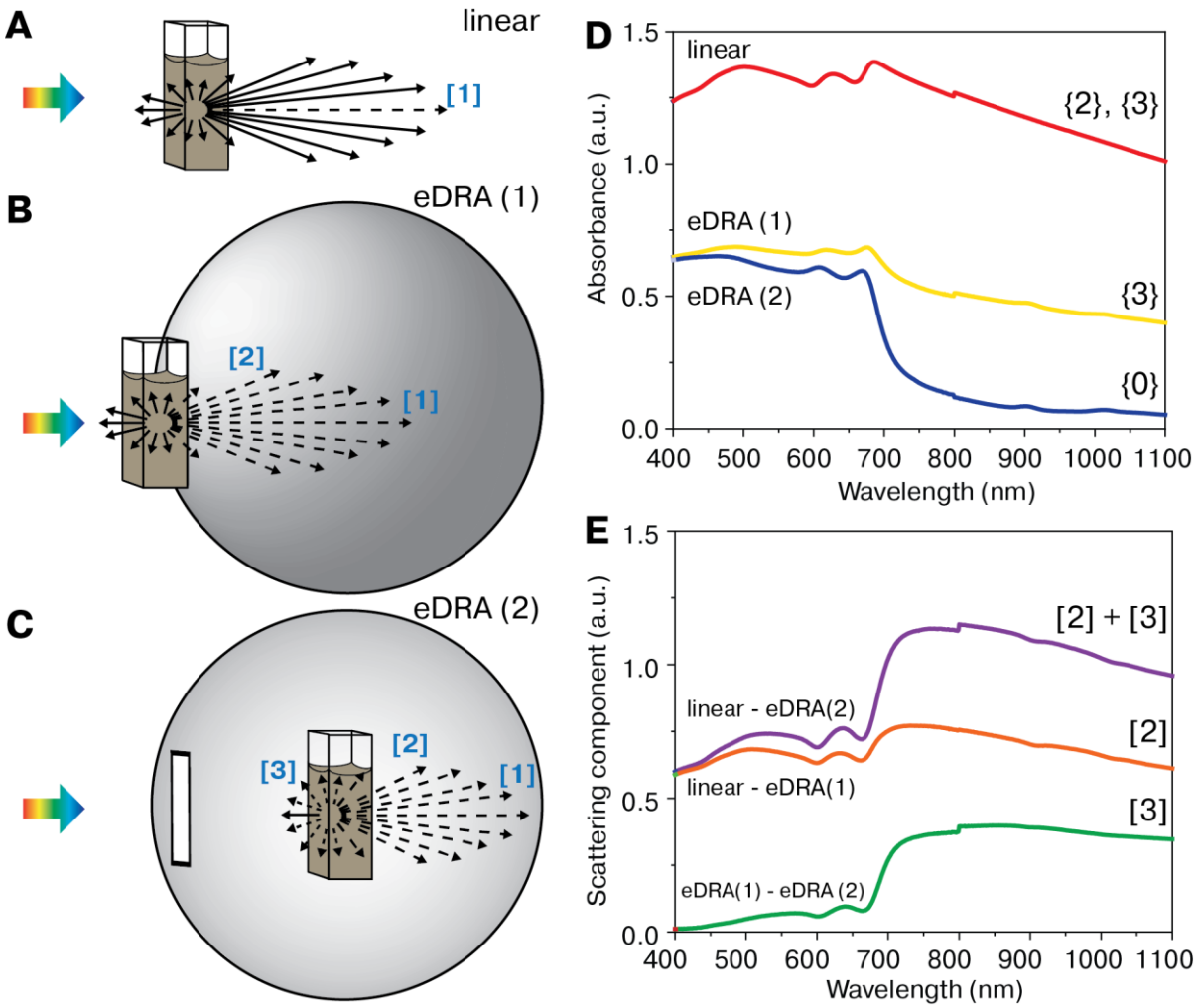

Figure 2.13 | eDRA geometries for light transmission measurements. (A) is the traditional linear geometry of a spectrometer, and **(B), (C)** represent positions 1 and 2 of the integrating sphere Figure 2.12. **(D)** The absorbance spectra of a 1-3k MoS_2 dispersion collected at each of the sample positions of A-C. Curly brackets represent the directional scatter component that screens the true absorption edge. **(E)** The calculated scattering component of the flake dispersion along with the angular components that contribute to the scattered light in brackets, [].

Direction [2] represents forward-scattered light and [3] is comprised of back- and side-scattered light. The associated absorbance spectra are shown in 2.13D, eDRA(1) and eDRA(2). The scattering contributions (Figure 2.13E) are calculated through simple subtraction of the absorbance spectra in D. The directional contributions are also shown in 2.13D as curly brackets to highlight their role in screening the true absorption edge. Figure 2.13E reveals that the MoS_2 dispersion of relatively thick flakes scatters more light in the

forward- than back-direction with [2] > [3]. Note that thick flakes (>50 nm thick) will scatter light more strongly than 2D flakes (< 50 nm thick), as shown in Figure 2.14A. Figure 2.14B demonstrates that thick flakes (1-3k) have a higher scattering component than a dispersion comprised of 2D MoS_2 (8-20k). This observation that 2D flakes scatter light most strongly in the forward direction with negligible back-scatter is in agreement with previous reports[38-39]. In order to measure the forward-scattered component, [2], of the 8-20k MoS_2 dispersion as is done for 1-3k MoS_2 in Figure 2.13, an additional measurement would need to be performed on a spectrometer with the linear transmission geometry. It is also worth noting that the 1-3k MoS_2 dispersion used in Figure 2.13 is in a different solvent and at a lower concentration than the 1-3k dispersion in Figure 2.14.

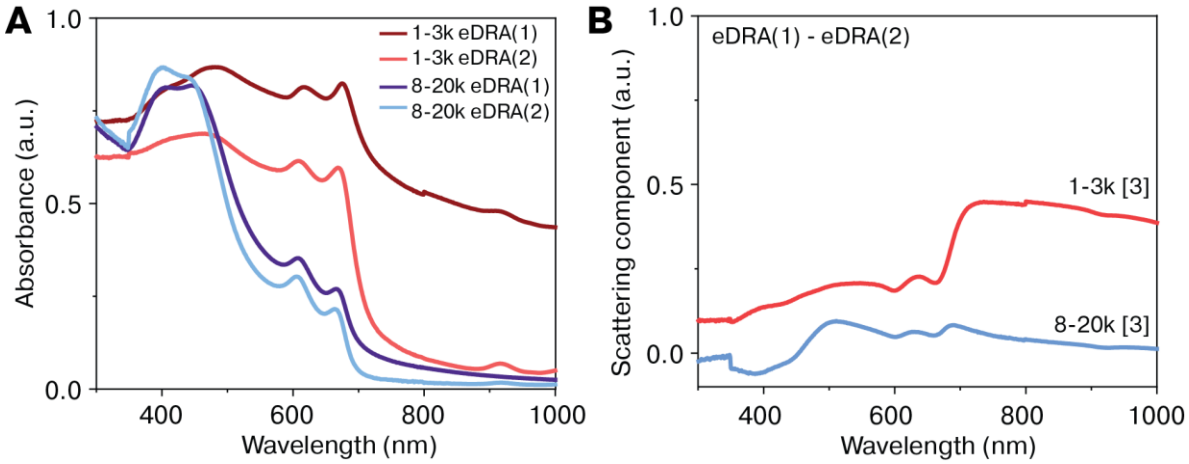

Figure 2.14 | Light scattering of thick (1-3k fraction) versus 2D (8-20k fraction) flakes of MoS_2 suspended in n-butanol. (A) Absorbance spectra of each fraction in the eDRA(1) and eDRA(2) positions. (B) Calculated back- & side- scattering component (direction [3] in Figure 2.13C) of each dispersion.

These measurements demonstrate that the integrating sphere may be used to mitigate significant contributions from light scattering to enable a proper assessment of the fundamental absorption edge of MoS_2 dispersions. We now turn to the study of thin films of MoS_2 nanoflakes using the eDRA. Thin films interact with light in a fundamentally different manner than dispersions of small particles and the absorbance spectra will be dominated by a

reflectance component (Figure 2.15) rather than by the light scattering mechanism described above. Specular reflectance (R_S) obeys Snell's law where the angle of reflection is equal to the angle of incidence. A material that exhibits high R_S will appear mirror-like. Diffuse reflectance (R_D) is rather characterized by angles of reflection that are not equal to the angle of incidence and exit the material in a diverse array of directions, resulting in a matte-like finish. The eDRA is a useful tool for separating out the specular and diffuse components of a thin film's reflectance properties. If the thin film does not absorb or reflect 100% of the incoming light, we may also gain information regarding the transmitted (T) and forward-scattered (S_F) light. For a thin film, forward-scattered light is defined as diffusely reflected light that is transmitted through the sample at an angle of reflection that is different than the incident angle.

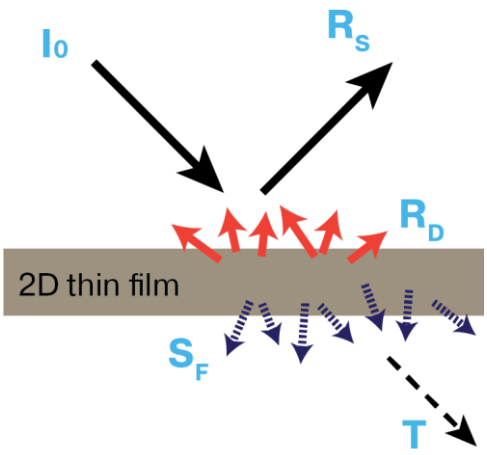

Figure 2.15 | Reflectance of a thin film. I_0: incident light, R_S: specular reflectance, R_D diffuse reflectance, S_F forward-scattered light, T: transmitted light.

There are four sample positions available on the eDRA for the study of thin films and powders, three of which are shown in Figure 2.16A–C. A fourth position at the rear of the eDRA collects only reflected light, but I did not use it in my studies because the other three sample positions provided the needed information. If you decide to use the fourth position at the rear of the eDRA, note that it is difficult to properly collect a baseline if the sample is not

100% opaque. All of my thin films studies with the eDRA utilized a small spot kit (SSK) that enabled precise control over the beam size and ensured that the beam spot was smaller than the sample width. As shown in Figure 2.16A, the eDRA(1) position rejects R_S and R_D light and captures S_F and T, while eDRA(2) (Figure 2.16B) captures all components of reflected, scattered, and transmitted light. If a light trap is added to eDRA(2) (Figure 2.16C), R_S is rejected. Figure 2.16D shows the spectra for a 1-3k MoS_2 thin film at each sample position of the eDRA in Figure 2.16A–C. The absorbance is calculated using equation 2-9, with %R replacing the %S. Note the increase in measured absorbance when the specular and diffuse reflectance components are rejected from sphere and are not collected by the detector. The specular and diffuse components of the reflected light may be calculated through simple subtraction of the absorbance spectra in Figure 2.16D. For the example of the 1-3k MoS_2 thin film, the diffuse reflectance is much stronger than the specular component (Figure 2.16E).

Figure 2.17 shows the absorbance spectra for an 8-20k MoS_2 thin film at different positions of the eDRA (Figure 2.16 A–C). The films were prepared via the interface method of section 2.3, and several different cycles (1L, 3L) of thin flake deposition were characterized, where 1L refers to "1-layer", or 1 cycle of thin film deposition and 3L refers to three layers of deposition. The calculated diffuse reflectance for these MoS_2 thin films is shown in Figure 2.17B, which reveals that R_D increases with increasing layers of deposition. The inset of Figure 2.17B shows the calculated R_S of the films, which is much smaller than R_D. The spectra of a 1-layer 1-3k MoS_2 film (red, dashed line) is included in 2.17B for comparison. At higher energies, the R_D of the 1L 1-3k film is greater than a 2L 8-20k film, but much less than that of the 3L 8-20k film while R_S is much more similar for all samples.

The 1L 1-3k film exhibits a higher diffuse and specular component than the 8-20k films at longer wavelengths.

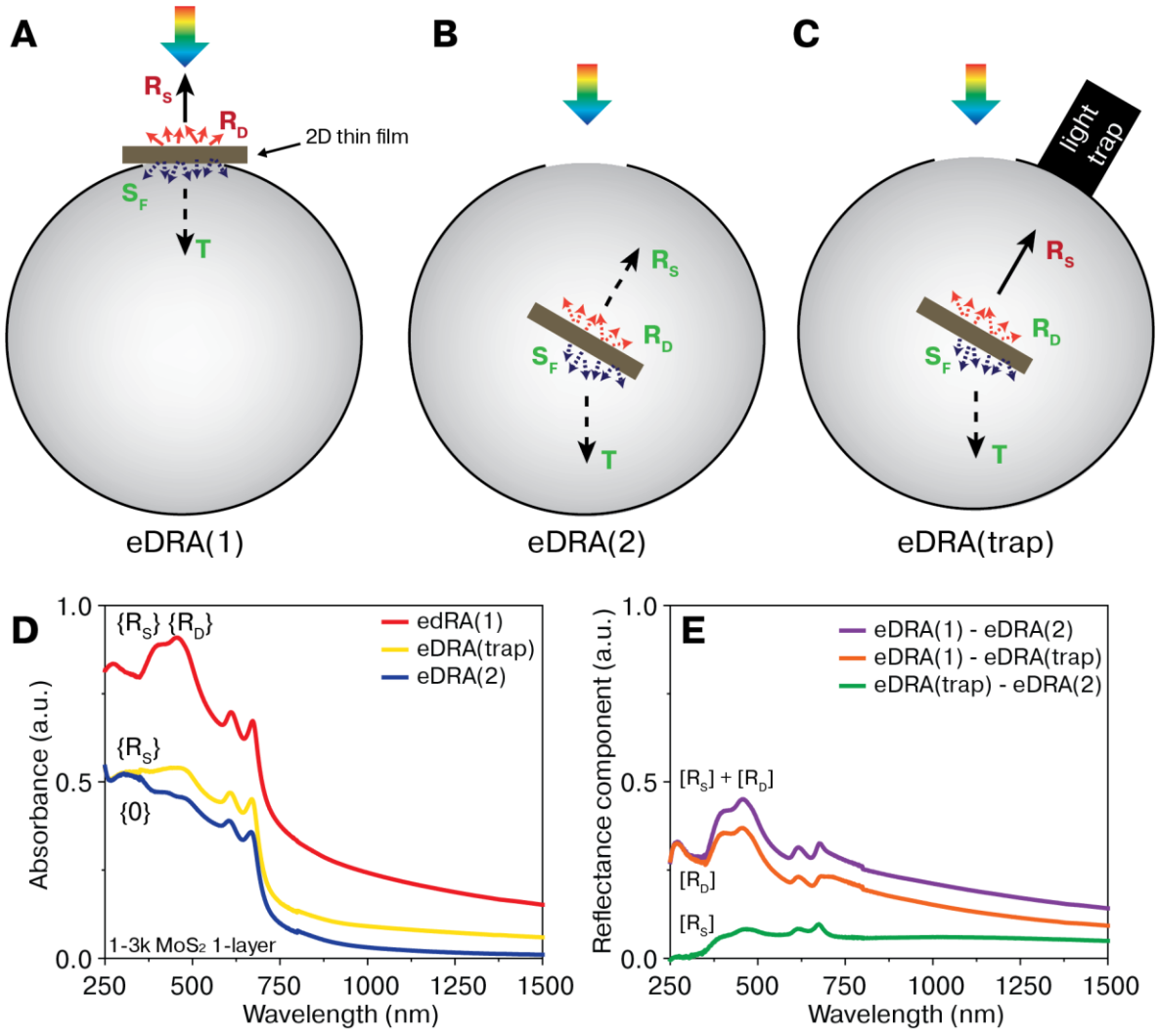

Figure 2.16 | Sample positions for thin film analysis by eDRA. (A) eDRA(1) captures forward-scattered (S_F) and transmitted (T) light. **(B)** eDRA (2), ~15° rotation, captures S_F, T, diffuse-reflected (R_D) and specular-reflected (R_S) light. **(C)** addition of a light trap to eDRA(2) rejects R_S and captures S_F, T, and R_D. **(D)** absorbance spectra of a 1-3k MoS_2 thin film collected at eDRA(1), eDRA(2), and eDRA(trap). Curly brackets represent the reflected light component that screens the true absorption. **(E)** calculated reflectance spectra of the thin film. Brackets, [], indicate whether R_S or R_D contribute to the reflectance spectrum.

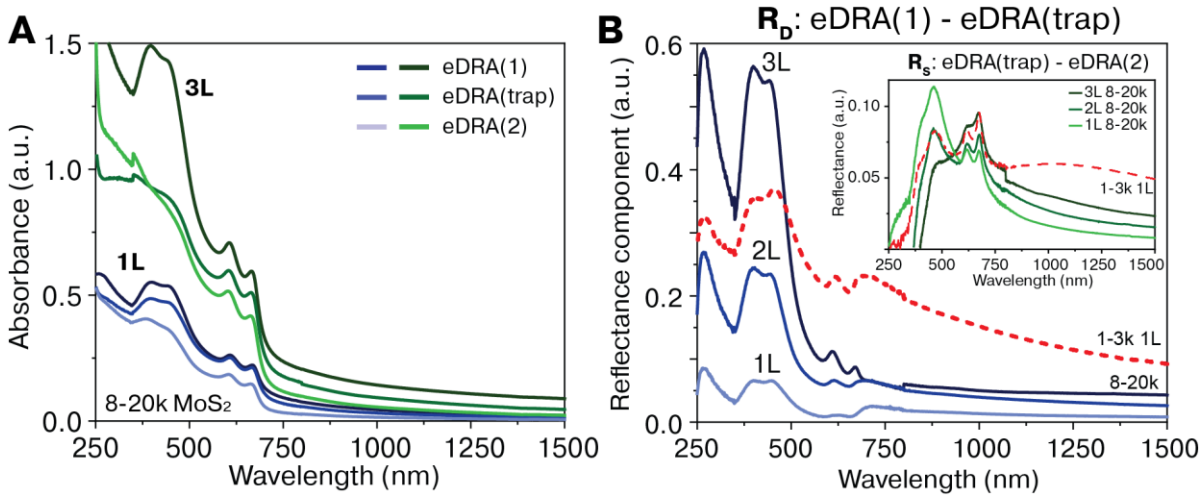

Figure 2.17 | MoS_2 thin film absorbance and reflectance. (A) 8-20k MoS_2 thin film absorbance for 1 and 3-layered Buchner interface film (see section 2.3.2) at different eDRA positions. **(B)** Diffuse reflectance of 8-20k (1L, 2L, 3L) in blue, 1-3k (1L) in red; inset: specular reflectance.

General advice for use of the eDRA

- The eDRA user manual created by Kyle Brennaman is a good start when first operating the integrating sphere. He condensed and clarified the information from the original manual quite well and also provides a good explanation of the theory of light absorption and scattering.
- The 0° position for eDRA(2) does not actually correspond to 100% rejection of specular-light. A series of control measurements indicates that the rotation angle is off by ~3°. If concerned with rejecting 100% of the specular light at the 0° setting, I recommend to first run a control experiment to measure %T at various angles of rotation.
- Rotate the center port, eDRA(2), to 15–18° (rather than the 8° recommended by the user manual) when collecting specular-reflected light of a thin film so that all light is captured by the sphere. If you elect to run a control experiment in the above point,

compare the %T measurement at 15–18 degrees as well to determine the optimal rotation angle.

- The small spot kit (SSK) for the eDRA is incredibly useful for thin film analysis as it enables the narrowing of the beam for small film sizes. Despite this utility, it may result in a lower S/N, so keep this in mind when running experiments.
- Use caution when utilizing the eDRA(2) position for liquid dispersions. The detector is located directly below the sample, and any spill of liquid could be disastrous. Use screw-top cuvettes or tightly fitted push caps with normal cuvettes for all analysis.

2.5 Diamond anvil cell high pressure measurements

The diamond anvil cell (DAC) is a useful apparatus for conducting spectroscopic and structural studies of materials under high pressure (1 to >100 GPa). This section will focus on several key points with regard to the DAC preparation and use, and highlight challenges the user must consider when considering the DAC for their experiments. I am indebted to several handbooks[40-45] on the diamond anvil cell for much of the information that will be included, and I will attempt to highlight key points from each as well as include my own self-taught tips and tricks for the use of the DAC. As you begin to work with the diamond anvil cell, you may find that you agree with the musings of Sherman and Stadtmuller[44], who say, "It is not a trivial problem for an inexperienced worker to load a gasketed DAC with a crystalline sample, a ruby chip, and a liquid-pressure transmitter… As with many high-pressure techniques, the best advice is to serve a short apprenticeship in a laboratory that has considerable past experience with that technique". I suppose that you can consider graduate school to be your "short apprenticeship" as you learn to use the diamond anvil cell, and with any luck this methods section will ease some of the burden on you as you learn to perform high pressure measurements.

The DAC owned by the Warren Laboratory at UNC-Chapel Hill is a Diacell Bragg Mini (Figure 2.18A) purchased from Almax EasyLab in June 2017 for $6,850. The specifications of our cell are listed in Table 2.3. We chose an "x-ray" cell with a wide-angle aperture (85°) to ensure maximum compatibility across spectroscopic and x-ray diffraction instruments. The Type IIas label refers to the diamond's purity and is addressed in section 2.5.1. Note the working distance (WD) of 7.5 mm and be sure to use an appropriate long WD objective when performing microscopic and spectroscopic measurements. Working

distance is defined as the distance between the edge of a lens objective and the sample when the sample is in focus.

Table 2.3 | Merrill-Bassett diamond anvil cell specifications

- Screw-drive pressure mechanism
- Tungsten Carbide support
- 85° conical x-ray top and bottom angle
- Boehler-Almax design: Type IIas Diamonds
- Max pressure: 10 GPa
- DAC height: 15 mm
- Working distance: 7.5 mm
- 0.85 numerical aperture (NA)
- Diamond specs: 3.3 mm/85 degree, 16-sided, Culet = 1mm, (100)-oriented

The diamond anvil cell is comprised of two diamond anvils mounted on tungsten carbide supports and assembled in the geometry shown in Figure 2.18. The sample is placed between the inverted anvils, and pressure is applied through use of a force-generation mechanism, such as the screw-drive pressure mechanism of the bolts in Figure 2.18B.

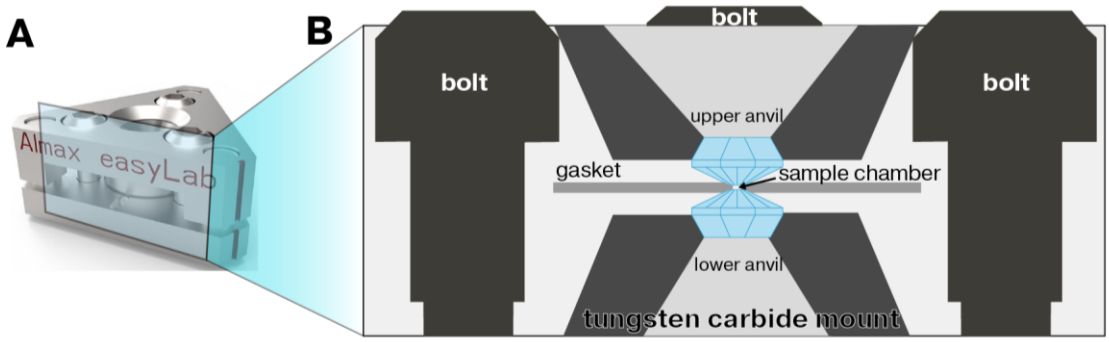

Figure 2.18 | Diamond anvil cell. (A) Diacell Bragg Mini diamond anvil cell (DAC). **(B)** Cartoon cross-section of DAC

There are four key components of the DAC to consider when preparing a high-pressure measurement: the diamond anvils, the gasket, the pressure medium, and the pressure measurement. The following subsections address the background of each subject and provide step-by-step procedures for the DAC sample preparation. Unless otherwise stated, the procedures presented here is adapted from the procedures within *High pressure techniques in chemistry and physics* by Holzapfel and Isaacs[41]. There is also a manual from Almax

EasyLab that came with the DAC, but it is not all that helpful for beginners in the field. When using the DAC, it is *highly recommended* to use a stereoscope (Figure 2.19A) for all alignment and sample loading procedures. In contrast to an optical microscope, a stereoscope (such as the one in CHANL) provides a "3D" depth-of-field that helps tremendously in diamond aligning and sample loading.

2.5.1 The diamond anvils

The high strength and visible transparency of diamond makes it a great material for high pressure spectroscopic studies, but it comes at a cost. At the time of purchase, an individual diamond anvil in the DAC cost ~$1500. With this price tag, it is important to ALWAYS USE CAUTION when handling the DAC. I will note here that I may use "anvil" and "diamond" interchangeably. The diamond anvils should never come into direct contact with each other. Despite their high strength, they are very brittle and the slightest force with diamond-on-diamond contact can cause an anvil to fracture. The DAC comes with a plastic red protective ring that must always be placed between the two diamonds when it is not being used for an experiment.

Before first use of the DAC, it is necessary to check for proper anvil alignment, which will require diamond-on-diamond contact. This is a necessary, yet painstaking, exception to the rule of no contact because mis-alignment of the diamonds could result in anvil fracture during the application of pressure. The DAC should be checked for anvil alignment every ~10 – 15 experiments. The following instructions detail the procedure for proper diamond anvil alignment. USE EXTREME CAUTION when sliding the top half of the DAC onto the supporting lower half and beware of sudden, jarring movements that could cause the two anvils to knock together. In addition to this written procedure, look up Weldon MacDonald on YouTube, "Diamond anvil, preparing the gasket"[46] for tips on diamond anvil

alignment in video form. The video provides a hands-on approach to the diamond alignment and preparation that a handbook cannot match.

1) Clean the DAC diamonds with a cotton Q-tip moistened with ethanol. Be careful not to use excess solvent as this may dissolve the cement that holds the diamond to the tungsten carbide support. (this advice was taken from a handbook[41], it is unclear if the cement of our DAC is actually soluble in ethanol). If any dust remains, use a dry-air dust can to remove.
2) Check the alignment of the diamonds after cleaning using a stereoscope (Figure 2.19). If a beginner, insert a thin, transparent plastic sheet (~100-200 micron thick) between the two diamond anvils to avoid direct contact. Rotate the top half of the DAC so that the red line on the corner matches the red line of the bottom half. ALWAYS MAKE SURE THE LINES MATCH. When lowering the top diamond anvil to make contact with the plastic, try to keep the top anvil as parallel to the bottom anvil as possible to avoid uneven contact/pressure between the diamonds. Beware of friction on the support rods as you lower the top half of the DAC onto the bottom. The friction may cause sudden jarring that could force hard contact of the anvils. The allowed contact should be even across the anvil face and cause minimal deformation of the plastic. NO BOLTS SHOULD BE INSERTED IN THIS PROCEDURE.
3) If the anvils are misaligned in the lateral direction, adjust the alignment with the *tiny* set screws (bottom half) and the supplied Allen wrench. DO NOT ADJUST WHILE DIAMONDS ARE IN DIRECT CONTACT. Lift up top half before adjusting *tiny* set screws. Lower the top anvil and check alignment again. Repeat step 3 until diamonds are aligned. Note that tilt alignment is not possible with the Diacell Bragg-Mini.

4) After aligning, raise top half and remove plastic. CAREFULLY bring anvils into direct contact to check for edge alignment as shown in Figure 2.19B (if the Diacell Bragg-Mini had tilt alignment capabilities, you would also adjust tilt to eliminate Newtonian fringes). DO NOT APPLY ANY TYPE OF LOAD TO DIAMONDS WHEN IN DIRECT CONTACT. If not aligned, repeat step 3. Otherwise, the alignment is complete.

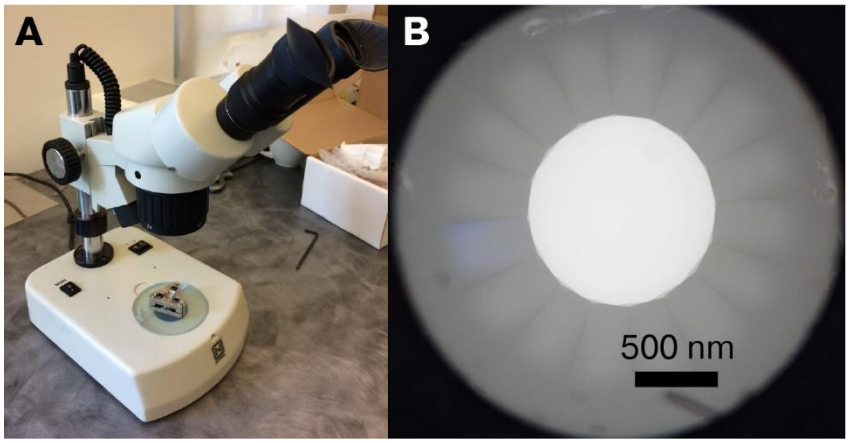

Figure 2.19 | Visualization and alignment of diamonds. (A) Stereoscope and DAC. **(B)** top-down view of anvil alignment. The view is looking down through the upper anvil toward the lower anvil. The large white space is called the culet, or the diamond face where sample is placed.

The maximum pressure that a DAC can achieve is directly related to the diameter of an anvil's culet[41] (equation 2-15), or the face of the diamond where the sample is placed.

$$P_{max} = (10/d)\ \text{GPa mm}^{-1} \qquad (2\text{-}15)$$

The culet size of the Warren Lab's DAC is 1 mm, which is larger than traditional culet diameters and limits the maximum attainable pressure to 10 GPa. The diamonds are type IIas and are described as conical low-birefringence of Boehler-Almax design, exhibiting low fluorescence and Raman backgrounds (Figure 2.20) for optical spectroscopy and X-ray experiments.

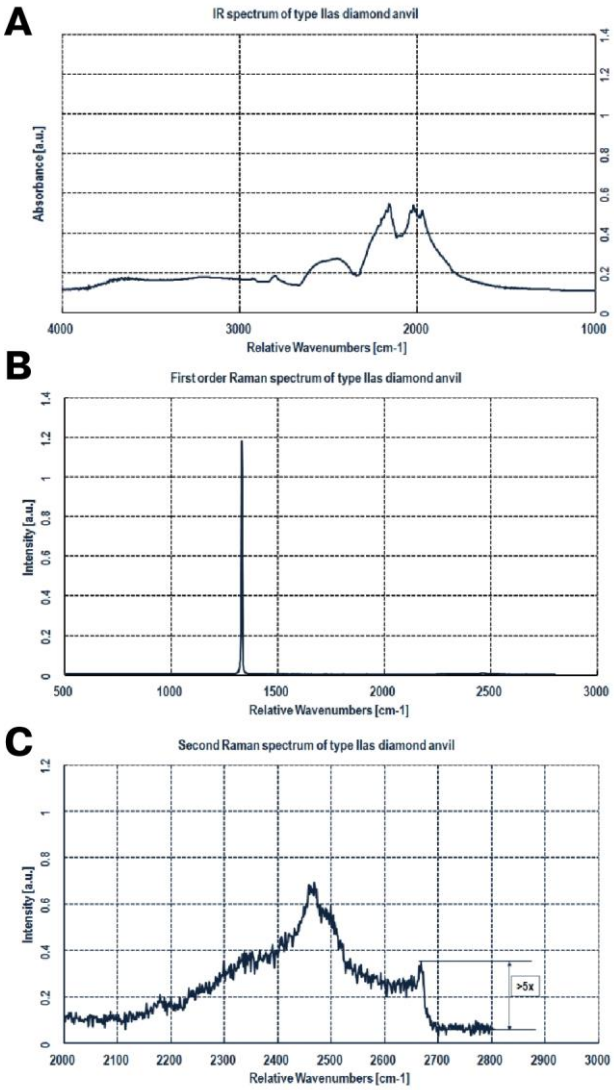

Figure 2.20 | Spectroscopic purity of diamonds. (A) FT-IR spectrum of type IIas diamond anvil. **(B)** 1st order Raman spectrum of type IIas anvil. **(C)** 2nd order Raman spectrum of IIas anvil depicting low fluorescence.

2.5.2 The gasket

The metal gasket acts as a barrier between the diamond anvils to provide lateral support and serve as the pressure chamber for a high-pressure experiment. Before the introduction of the metal gasket, experiments were performed by squeezing samples directly between two diamond anvils. Naturally, this increased the likelihood of fracture during high-pressure experiments due to diamond-on-diamond contact[47]. This method also resulted in a pressure gradient between the center of the anvil and the edge, resulting in a non-hydrostatic

pressure environment[48]. The gasket helps to overcome these challenges by providing a hydrostatic pressure chamber in the center of the diamond anvils. In addition, the gasket prevents diamond-on-diamond contact, extending the lifetime of the anvils.

The gasket can be made out of a variety of different metals[41], including stainless steel, beryllium copper, tungsten, molybdenum, or rhenium. Rhenium[41] is a common gasket material for experiments requiring both high pressure and high temperature. Stainless steel[49] is cheap, easy-to-use, exhibits good flow under pressure, and is the only metal that I used in my studies. Other metals can certainly be considered, but it is not clear whether others (i.e. copper) would have benefits over stainless steel. In order to serve as a pressure chamber, a hole must be created in the center of the gasket. Practically, the gasket hole diameter should be targeted to 1/3 – 1/2 of the culet diameter so that there remains a metal seal around the outer edge of the culet face. The hole must be as cylindrical and symmetrical as the drilling allows. As the gasket is squeezed between the diamond anvils, the metal will flow under the applied pressure, causing the drilled hole diameter to decrease and therefore increase pressure on the sample within (see Figure 2.21). In order to prevent "gasket failure", where the metal deteriorates under pressure and causes the pressure chamber to leak, it is necessary to pre-indent the gaskets using the DAC to a thickness of 30 – 50 μm prior to drilling a hole.

The gaskets used in all experiments were prepared from a 0.01" thick Stainless Steel 301 grade sheet[49] bought from McMaster Carr. I borrowed a punch set and hammer from the Physics Machine Shop (ref. Philip Thompson) to punch out 10 mm discs (Figure 2.21E). Using the DAC, each disc was then pre-indented to a thickness of ~ 50 μm (Figure 2.21A). Follow this step-by-step procedure in conjunction with Figure 2.21 to pre-indent a gasket.

1) De-assemble the DAC and place the bottom half on the work space (Figure 2.21B). Set aside the upper half.
2) Place the gasket "holder" (Figure 2.21C) on top of the bottom anvil (Figure 2.21B) and insert the 10 mm punched disc (Figure 2.21E–F). The gasket holder is a part that was custom-made by the Physics Machine Shop (ref. Cliff Tysor).
3) Carefully re-assemble the DAC with the gasket still in place. Carefully tighten the three bolts with an Allen wrench until "snug". This definition of "snug" may appear ambiguous, but I define it as the point at which the bolts are just barely tight and do not wiggle. Do not overtighten one bolt at the expense of the other two, but rather tighten each bolt in a clockwise manner where one bolt is rotated once, followed by the 2^{nd} bolt, then the 3^{rd} bolt until X number rotations achieves a "snug" fit of all bolts. Note that the first bolt will loosen after tightening the other two and will need to tightened again to achieve a snug fit, and so on. The goal is to achieve a uniform pressure distribution over the anvil surface by targeting a parallel contact between the two anvil surfaces. A non-parallel contact may cause anvil failure.
4) After each bolt is "snug", use the long-handled Allen wrench to tighten each bolt by a 3/8 turn (Figure 2.21G). Typically, I achieved the 3/8 turn in one continuous rotation for each bolt and did not worry with sequential steps as I did when tightening snug. It will be necessary to strongly grip the DAC on the bench with one hand in order to tighten the Allen wrench. USE CAUTION WHEN TIGHTENING AND DO NOT BEND THE BOLTS – maintain a perpendicular angle between the wrench and bolts.

5) After tightening, you should be able to observe where the metal has “bent” around the edge of the anvil culets (Figure 2.21J) when viewed under a microscope. Upon disassembly, the disc should be puckered (Figure 2.21H). The indentation thickness is measured by taking the difference between the thickness of the starting gasket and the thickness of the indented region, measured by a micrometer (Physics Machine Shop). The “indentation thickness” of a 3/8 turn is ~ 50 μm, which has been repeatedly confirmed through a series of tests. Figures 2.21 I and K depict the differences in metal flow around the culet edge with bolt rotations of 1/4 and 1/2 turn, respectively. A greater degree of rotation will result in a higher pressure and an increase in the indented thickness.

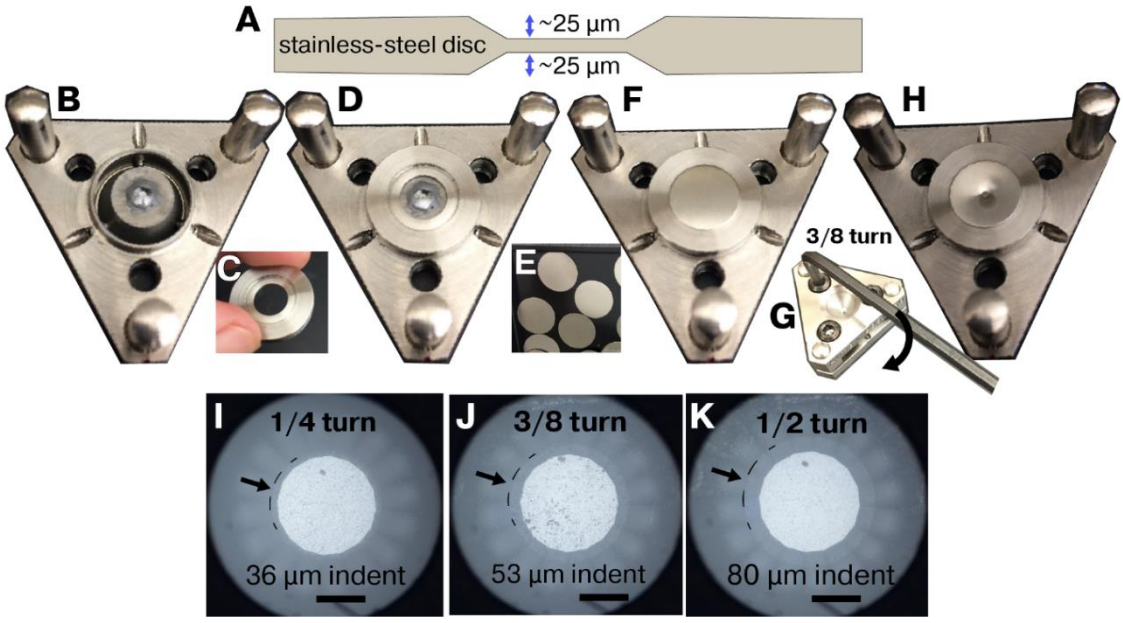

Figure 2.21 | Procedure to create indented gasket. (A) Pre-indented stainless-steel disc with a 50-μm indentation thickness (25 μm + 25 μm). **(B–H)** Visual depiction of gasket pre-indentation steps described in the main text. **(I–K)** Top-down view of indented disc at three different bolt rotation degrees, 1/4, 3/8, and 1/2. The indentation thickness of 36, 53, and 80 microns correspond to the difference in thickness between the starting gasket and the new indented region (shown in **A**). Notice the different widths of the shaded regions at the edge of the culet face (marked by dashed line) that correspond to the metal flow around the anvil face/culet. Scale bars = 500 nm.

Several methods have been documented to create the hole in the gasket disc, including a hammer and nail (primitive), an electric microdrill, or an electric discharge machine (homemade[50-52] or industrial[53]). Almax Easy Labs, the maker of our DAC, sells a bench-top micro-drilling machine for ~$20,000, so I originally attempted to build my own spark erosion device as detailed by Lorenzana et. al.[51] to avoid excessive cost. Building off the work of Anginelle Alabanza, a previous graduate student in the Warren Lab, I achieved limited success with creating sparks and small holes in copper metal (easier proof-of-concept than stainless-steel). The stainless-steel discs presented further challenges, as the tungsten electrode used for spark erosion was prone to weld to the steel surface. Because of these and other difficulties, I set the homemade spark erosion device aside, and looked at other methods for hole creation in the pre-indented discs.

I ultimately settled on an electric discharge machine (EDM), which is an industrial-grade spark erosion instrument (Figure 2.22A) available in the Physics Machine Shop (ref. Cliff Tysor). The EDM uses a graphite electrode to generate sparks between the electrode and the metal disc, burning a hole in the process. Once calibrated, the EDM produced consistent results for every disc, and several discs could be burned in a relatively short period of time (Figure 2.22B). It is worth noting that the bulkiness of the EDM makes it difficult to burn small holes in the exact center of the disc, so it is necessary to perform calibration tests to determine proper alignment. These calibration tests may result in off-center holes (Figure 2.22C) in the pre-indented gaskets which cannot be used in the DAC. I suggest providing five additional discs for the alignment process with the expectation that they will be discarded. After the holes are burned, I sanded off any residual metal burrs within the hole using Mitchell's Abrasive Cords & Tapes No. 66S crocus cord.

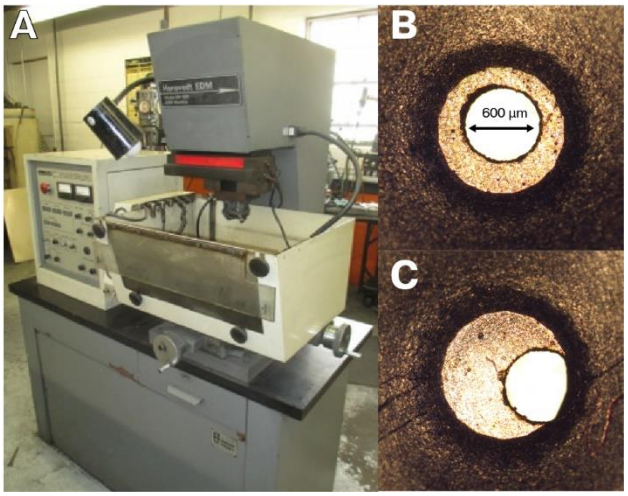

Figure 2.22 | Electric discharge machine for hole burning. (A) Electric discharge machine (EDM) in the Physics Machine Shop in Phillips Hall. **(B)** on-center hole burned via spark erosion using the EDM. **(C)** off-center hole that is not usable for the DAC but may be typical of trial-and-error alignment.

While the EDM produced good results, it is limited to burning holes of just one diameter. If smaller holes could be created, other experimental possibilities could be opened, such as multiple sample chambers within one pre-indent. To explore this possibility, I attempted hole creation using a laser ablation system located in the Chapel Hill Analytical and Nanofabrication Laboratory (CHANL) at UNC (Figure 2.23A). I was able to ablate holes of varying diameters in the stainless-steel discs in a relatively short period of time. However, they were characterized by excessive charring and asymmetry in the lateral and z-direction of the laser etch (Figure 2.23B-C). Therefore, I decided to forgo further testing of the laser ablation and use the EDM for all future gasket preparation.

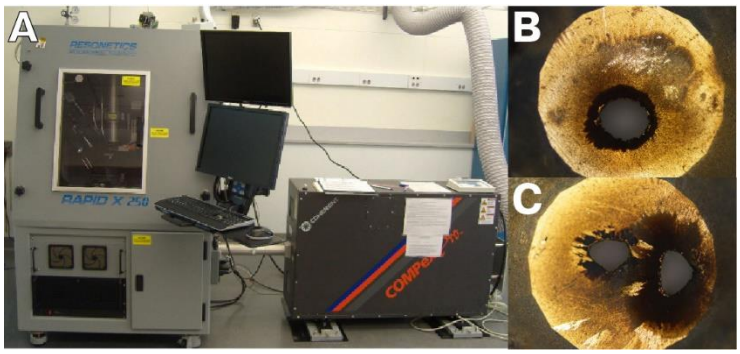

Figure 2.23 | Laser ablation for hole burning. (A) Laser ablation instrument in CHANL. **(B, C)** examples of holes burned using a laser. High charring and asymmetry are characteristic of all holes burned.

2.5.3 The pressure medium

The choice of pressure medium is critical for its role as a pressure-transmitter within the DAC. Sherman and Stadtmuller[44] define the role of the pressure-transmitting medium as the ability to "transform pressure-generating thrust into an adequately uniform pressure upon a sample" and recommend the following properties for the ideal medium: (1) zero shear strength, (2) chemically inert, (3) zero penetration into the sample or the materials used in construction of high-pressure apparatus, (4) zero compressibility, (5) easy to handle, (6) easy to seal within high-pressure enclosure, (7) cheap and readily available. Soignard and McMillan[47] also highlight the importance of hydrostatic pressure conditions to ensure uniform pressure distribution across a sample. The ability to achieve hydrostatic pressure is sample-dependent; for example, powders will behave differently than single crystals. Several examples of liquids that have been used as pressure media within the DAC include[43-45, 47-48]: 4:1 methanol–ethanol, other alcohol–water mixtures, glycerin, hydrocarbons such as pentane/isopentane, heavy hydrocarbon oils such as Octoil-S, Plexol 201, Shell Tellus mineral oil, and silicone grease. The most common liquid pressure medium is a solution of 4:1 methanol – ethanol[41, 43, 47] which remains viscous up to 10 GPa[41]. Above 10 GPa, the

solution turns into glass, resulting in non-hydrostatic conditions. If high pressures are required, silicone oil is preferred.

When preparing the sample chamber, the medium is applied to the sample chamber through use of a thin syringe after the sample is in place. It will take practice to perfect the technique, as the solvent tends to evaporate very quickly. One suggestion[47] is to place the drop of liquid on the edge of the pre-indent/hole and then drive or drag the droplet into the hole with a sharp needle before quickly closing the DAC to avoid evaporation. In practice, this is extremely difficult, as the solvent evaporates quickly, and it is easy to trap air bubbles between the anvils.

Solids can also be used as pressure-transmitting media, but they will not produce the same hydrostatic conditions associated with fluid media. However, soft solid media have the distinct advantage of low compressibility. There are several examples of soft solids as pressure media in the literature, including sodium chloride[41, 47], cesium iodide[41, 47], pyrophyllite[44-45], silver chloride[40, 44], talc[44], and indium[44]. When loading samples with a soft solid as the pressure medium, first place the solid medium in the bottom of the gasket hole, then place the sample directly on top. It is better to underfill the hole with medium than to overfill it[47], as the gasket hole will collapse with increased pressure.

Newer DAC designs have used gases such as argon as the pressure medium, as they provide the best possible quasi-hydrostatic conditions[41] and enable extremely accurate control over the applied pressure. These designs are completely different than the Diacell Bragg-Mini (Figure 2.18A) and are much more expensive.

2.5.4 The pressure measurement

It is desirable to have an *in-situ* pressure measurement while conducting a high-pressure experiment. This is accomplished through use of materials that exhibit pressure-

sensitive peak shifts in the Raman, IR or visible region. The most common *in-situ* pressure manometer is the (Al_2O_3:Cr^{3+}) fluorescence peak of a ruby microsphere that is calibrated against the lattice compression of NaCl using the Decker isothermal equation of state[54]. The calibration was created by measuring the peak shift of the ruby R_1 fluorescent line in relation to the NaCl lattice parameter shift with pressure via x-ray diffraction. The ruby pressure shift has also been verified against several different metals[55]. There have been multiple sources[41-42, 48, 54-57] detailing the utility of the ruby pressure calibrant and confirming its linear pressure dependence up to ~30 GPa. Above 30 GPa, there is debate in the literature regarding the reliability of ruby as a pressure sensor, but this is well beyond the 10 GPa limit of our DAC. The Mao and Bell calibration[55] provides the most-used equation by which to relate pressure to the shift in ruby R_1 fluorescence peak.

$$P = \frac{A}{B}\left\{\left[1 + \left(\frac{\Delta\lambda}{\lambda_o}\right)\right]^B - 1\right\} \quad (2\text{-}16)$$

where P = pressure (Mbar), λ = wavelength (nm) of ruby R_1 line (shifted), λ_o = wavelength (nm) of ruby R_1 line at zero pressure, A = 19.04 (Mbar) and B = 7.665 (unitless). The calibration curve based on this equation and an example of the ruby R_1 fluorescence shift are plotted in Figure 2.24.

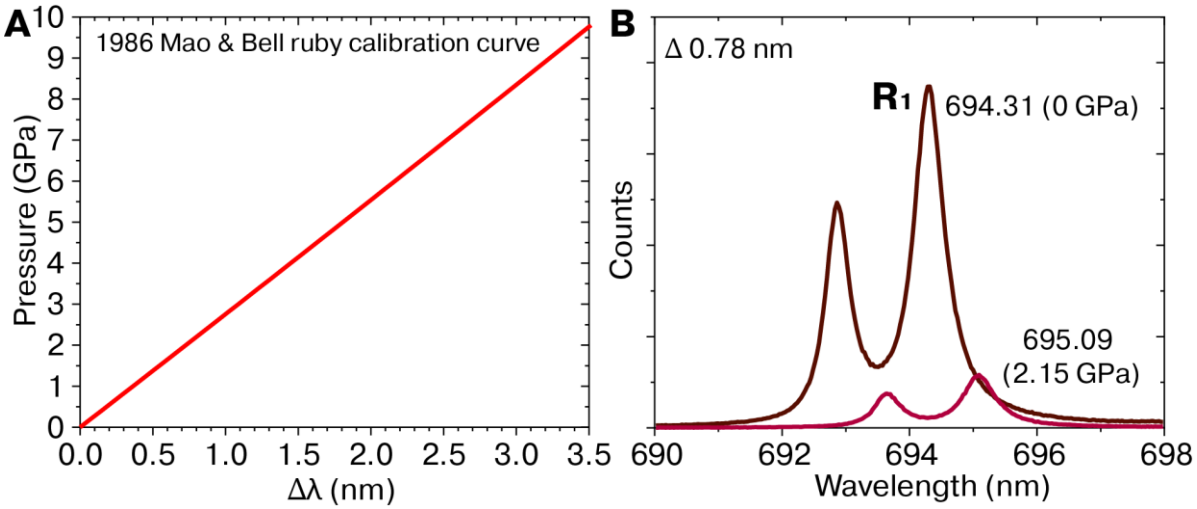

Figure 2.24 | Ruby as an in-situ pressure manometer. (A) Ruby calibration curve based on equation 2-16. **(B)** Ruby R_1 red-shift and corresponding pressure.

Figure 2.25 shows an example of a 4:1 methanol – ethanol pressure medium with several ruby spheres fluorescing. Notice that the gasket hole diameter shrinks due to metal flow as the degree of bolt rotation increases from frame A to frame E of Figure 2.25. The applied pressure is measured by examining the red-shift of the ruby R1 fluorescence peak in Figure 2.25B and determining the pressure using equation (2-16). Although the gasket hole diameter decreases with increased bolt rotation, the actual measured pressure of the sample chamber (based on ruby shift) does not increase until frame F. This is most likely due to gasket failure and leakage of the 4:1 methanol–ethanol pressure medium. Frame F corresponds to Figure 2.24B, with a ruby peak shift of 0.78 nm and calculated pressure of 2.15 GPa.

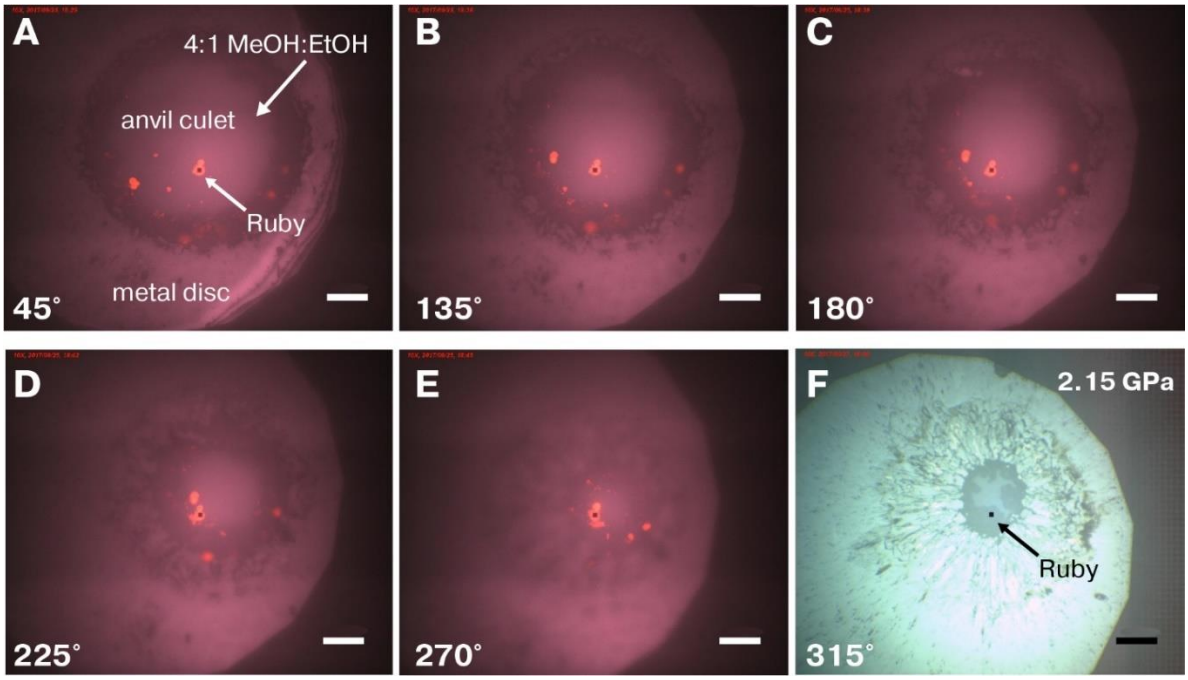

Figure 2.25 | Demonstration of ruby fluorescence and gasket shrinkage in a 4:1 methanol–ethanol pressure medium. (A) 45° rotation of DAC bolts. Red dots = ruby microspheres fluorescing. **(B-E)** Gasket hole diameter decreases as bolt rotation increases from 135° to 270° **(F)** Transmission image showing the gasket hole diameter at the point where the ruby R_1 peak red-shifted (see Figure 2.24B). Gasket failure caused the solvent pressure medium to leak out of the sample chamber, requiring a high degree of bolt rotation to achieve a noticeable R_1 shift. Scale bars = 100 microns.

While ruby is the most popular of the *in-situ* pressure sensors, it may not always be the most viable option depending on the sample, targeted pressure range, and other experimental conditions. It can also be difficult to directly relate the pressure experienced by the ruby sphere to the sample because of differences in geometry. There are several additional materials cited in the literature, and many are based on a pressure-sensitive Raman or IR peak shift in contrast to the visible region shift of ruby fluorescence. Several noteworthy materials include $BaSO_4$[58], quartz[47, 58-59], $NaNO_3$[47], $MgCO_3$[47], methanol[42, 60], NaCl[44, 61], KCl[61], KBr[61], KI[61], TlBr[27], and nickel dimethylglyoxime[44, 62-64]. While these materials could be viable alternatives to ruby fluorescence, note that most of them have not undergone the rigorous testing associated with the ruby calibration. There are also additional

materials that are not listed here that can be found by searching the associated references above. It is interesting to note that several of these materials could serve a dual purpose as both a pressure medium *and* sensor, which may be useful if you are worried that the ruby sphere does not provide a direct pressure comparison to the sample of interest, such as a powder. Though I never tried this myself, I imagine that a material like KBr would be interesting because of its well-known utility in making pellets of solid samples for FTIR analysis.

2.5.5 General advice

Use a stereoscope rather than a traditional optical microscope for sample loading. It provides the depth-of-field that is necessary for sample manipulation. You will also find several items to be useful to include in a "DAC toolkit": eyelash (TedPella prod. No. 113) and/or deer hair (TedPella prod. No. 119) brush, fine-tipped tweezers (x2), ethanol and Q-tips to clean the anvils, surgical microknife (Electron Microscopy Sciences, cat no. 72047-45) and core sampler (Electron Microscopy Sciences, cat no. 69039-05) for sample cutting and preparation.

2.5.6 Sample preparation of LB Trough Film for DAC

One of our motivations to purchase a diamond anvil cell was the ability to measure the absorbance and photoluminescence properties of 2D material assemblies (i.e. Langmuir-Blodgett thin films) at high pressure. There were two key factors to consider when designing this experiment: (1) the pressure medium and (2) the sample loading. In the ideal scenario, the pressure medium would enable unilateral pressure transmission in the z-direction. Because the thin films were comprised of thin nanomaterials, we also needed to avoid solvents and other polymers with low molecular weight to mitigate solvent/medium

penetration between the flakes. Other factors included optical transparency in the visible region and stability up to pressures of 10 GPa. The second factor was the challenge of transferring the film from the LB trough to the DAC. We opted to use a polydimethylsiloxane (PDMS) doctor-bladed film on a glass slide. The choice of PDMS is rooted in the literature precedent (see section 2.5.3) of silicone-based oils for DAC pressure media. PDMS met all of the requirements for the pressure medium listed above and can be easily cut away from the glass slide for transfer to the DAC. We used commercially available JB Weld Clear Silicone (Figure 2.26A) for our measurements. To prepare a substrate, the JB Weld was doctor-bladed onto a glass slide. The thickness of the JB Weld silicone layer could be controlled by varying the number of stacked tape pieces (Figure 2.26B). The optimal thickness that was compatible with the metal gasket chambers of section 2.5.2 was two tape layers. The silicone films were air-cured for 24 hours and then annealed on a hot plate in air at 150 °C for 2 hours in order to prevent polymer flow during later annealing steps.

Take note that a small portion of the glass was left exposed around the edges of the cured silicone film (Figure 2.26C). The hydrophilic nature of glass helps with flake deposition on the LB trough by acting as a “barrier” to the water and preventing the water from immediately flowing off the hydrophobic silicone without depositing material.

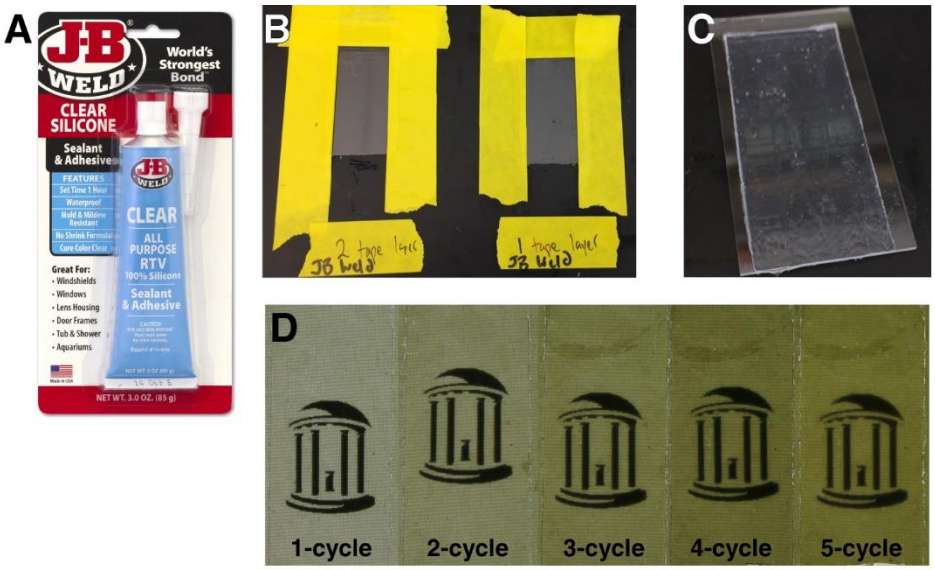

Figure 2.26 | Silicone substrate for LB to DAC transfer. (A) Commercially available JB Weld PDMS. **(B)** doctor-bladed JB Weld on a glass slide. Thickness is controlled by varying the number of tape layers. **(C)** 4-tape layer JB Weld silicone film on glass slide. Note exposed glass around edge to aid flake deposition via LB trough. **(D)** Sequential depositions of nBuLi-exfoliated MoS_2 on JB Weld silicone. The film was annealed at 120 °C under vacuum for 20 minutes between depositions.

Figure 2.26D shows five sequential depositions of nBuLi-exfoliated MoS_2 (sections 2.2.3 and 2.2.4) deposited onto the silicone-glass substrate via the methods described in section 2.3.3. The film was vacuum-annealed at 120 °C between deposition cycles. As previously highlighted, it can be challenging to deposit sequential cycles of flakes onto a hydrophobic surface. First described in section 2.3.3, it is imperative that the LB trough is overfilled with water before lowering the film into the subphase. If the trough is not overfilled, the water may not completely "collapse" over the top of the film, resulting in an air pocket/bubble directly over the film that causes flake delamination.

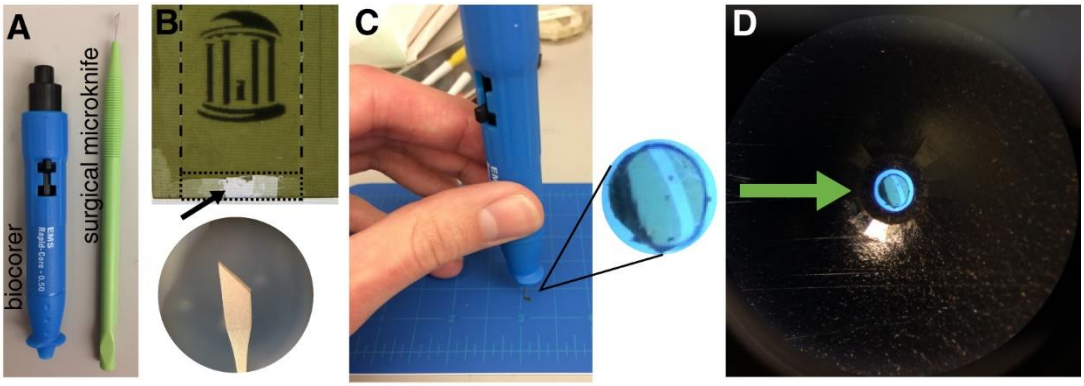

Figure 2.27 | MoS_2–silicone film transfer to DAC. (A) 0.5 μm diameter biocorer and 45° angle microsurgical knife. **(B)** 5-cycle nBuLi-MoS_2 (Figure 2.26D). The dotted box shows where silicone squares were cut away using the microsurgical knife. Silicone is outlined with a dashed line. **(C)** The corer is pressed firmly into the piece cut off in (B) to produce a cylinder of MoS_2 film + silicone. **(D)** Silicone cylinder is transferred to DAC gasket chamber with fine-tipped tweezers.

Once the film is prepared, use a 45° angle microsurgical knife to cut slits in the film in order to remove a small square for the DAC sample. This operation is easiest when performed using a stereoscope. Note that the upper and lower surfaces of the silicone should be parallel for the DAC pressure experiment, and care must be taken with the knife to prevent jagged edges on the bottom of the cut surface. To achieve this clean cut, I recommend holding the knife perpendicular to the substrate with the beveled blade flush with the glass substrate. Slowly, but forcefully, slide the blade flush against the glass to cut the underside of the silicone away from the glass. The cut piece can be easily handled with fine-tipped tweezers.

Once the sample is prepared, transfer to a cutting mat (Figure 2.27C) with the MoS_2 side up and use the 0.5 μm diameter biocorer (Figure 2.27A) to cut a cylinder from the sample. The biocorer should be pressed firmly into the sample such that the cutting edge penetrates the cutting mat. Give a slight twist while pressing to cleanly cut the silicone. Remove the biocorer and eject the “pellet” onto the DAC. Using a stereoscope, fine-tipped

tweezers can be used to position the sample in the gasket chamber. Once positioned, a ruby sphere can be loaded as a pressure manometer.

2.6. Preparation of KBr pellet for FTIR solid sample analysis

KBr pellets are used to analyze the light transmission properties of solid samples in the IR or visible region. Only spectroscopic grade KBr should be used, and it should be kept in a desiccator when not in use. The KBr is extremely sensitive to humidity. If you are attempting to make a KBr pellet on a rainy NC day, it will be challenging to produce pellets that are not plagued by cloudiness. The following procedure details my recommendations on how to prepare a KBr pellet using an evacuable die and pellet press. The exact masses, times, and pressures required will change based on experimental conditions and will certainly require a series of trial-and-error measurements to determine exact parameters.

1) Grind 200 – 300 mg spectroscopic grade KBr with 2–3 wt-% of the solid sample using a mortar and pestle. The finer the grind, the better the final pellet. The ratio of KBr to solid will depend on the sample and will require trial-and-error to determine the appropriate masses.
2) Assemble the two large halves of the pellet die with an O-ring between them. Insert one of the small cylinders into the die and then add the KBr ground mixture on top.
3) Use the plunger to gently flatten the powder. Once smooth, remove the plunger and drop the 2nd small cylinder on top of the powder.
4) Insert the plunger with beveled side up into the die. Add an O-ring around the plunger to create a seal at the point where the plunger meets the die.
5) Place assembled die with powder onto a hydraulic press. Apply just enough pressure to hold die in place, then attach a vacuum hose to the barbed fitting.
6) Pull vacuum for ~5 minutes before pressing. The KBr pellets are extremely sensitive to humidity, and pulling vacuum helps dry out the powder.

7) Compress the sample to the 4 or 5-ton mark on the scale (1/2 inch diameter plunger = 8 to 10 ton force on die). Wait 5 to 10 minutes then release pressure.
8) Break the vacuum by pulling the hose off of the barbed fitting. Remove the upper half of the die, including the plunger, and invert on the hydraulic press. Set aside the lower half. Place a PVC end cap overtop of the assembly and compress. The plunger will push the sample that is sandwiched between the two small cylinders out of the die.
9) Check to see if the KBr pellet is transparent. If not, repeat the entire procedure.

2.7 Data mining of minerals

The randomized 1,000 mineral subset for the layered versus non-layered analysis was compiled from a larger list of 2,232 minerals that were cross-listed between the databases associated with the American Mineralogist Crystal Structure Database (AMCSD)[65] and Handbook of Mineralogy (HoM)[66] by the Mineralogical Society of America (MSA). The majority of the Mohs hardness values and all of the cleavage plane information were collected from the HoM. If needed, any missing Mohs hardness values were collected from www.webmineral.com. The AMCSD and the Crystallography Open Database (COD, www.crystallography.net) were used to find and download the CIF files for structure analysis. The Handbook of Inorganic Compounds[67] and the United States Geological Survey Bulletin 2131[68] provided the melting point data unless otherwise noted. Decomposition or phase transition temperatures were not included in the melting point analysis unless otherwise noted.

The elastic stiffness tensor dataset was determined by analyzing approximately 200 minerals that were cross-listed across the AMCSD and the Materials Project Database (materialsproject.org). Each database records the crystal structures in a different manner, so a Python script was generated to search and match structure files based on identical chemical composition. This matched dataset was used to compare the Mohs experimental values with calculated elastic tensors. I am indebted to Jack Sundberg for his help in creating the Python code and analyzing the results.

2.8 Mechanical exfoliation and characterization of layered minerals

Scotch tape or Nitto tape exfoliation was used to prepare and isolate 2D nanoflakes of various minerals. The flakes were deposited on a UV-ozone cleaned silicon or aluminum oxide substrate with a 90 or 300 nm oxide layer. The substrates were first washed with acetone followed by 2-propanol and dried with a N_2 gun before placing in the UV-ozone chamber. The substrates must be used within ~10 – 15 minutes of cleaning in order to prevent the re-agglomeration of hydrocarbons.

To exfoliate the layered crystal, a piece of tape was placed sticky-side-up and secured to the working surface using tape. A small piece of the mineral of study was placed on the sticky-side-up tape. The adhesive side of a second piece of tape was pressed against the mineral and then peeled away. This process was repeated 12-20 times until the tape was covered with small specks of the mineral.

To transfer the exfoliated flakes to the cleaned substrate (above), press the 2^{nd} tape piece against the substrate and carefully smooth the tape over the substrate to ensure uniform contact. Slowly peel away to transfer the 2D materials. The substrate with transferred flakes will undoubtedly have polymer residue from the Scotch tape. Nitto tape has much lower residue but is also characterized by a lower adhesion. To attempt removal of the Scotch tape residue, the substrates were placed in a bath of 3:1 acetone–toluene for 20 – 30 minutes with high stirring. After 20 – 30 minutes, the substrates were removed and washed with acetone followed by 2-propanol and dried with a N_2 gun.

The 90 or 300 nm oxide layer of the substrates aids the identification of nanoflakes via color contrast under an optical microscope. The optical contrast follows ROY–G–BV, where flakes with colors on the red side of the spectrum will be thicker in the z-direction than

flakes on the blue or violet end of the spectrum. Blue and violet colors were almost always associated with few-layer or monolayer flakes, which was confirmed with an Asylum Atomic Force Microscope (AFM), with scan rates less than or equal to 12 microns/second.

A numbered block shape pattern was patterned onto silicon/aluminum oxide wafers to aid the finding of flakes between the microscope and AFM. The pattern is shown in Figure 2.28 and the blue shapes and block numbers are patterned in a repeated fashion with the # increasing left to right and the letter increasing from A to Z from top-to-bottom. If a flake of interest was discovered, it will be given a code based on its location, such as D26-03, T5-NE, etc. Note that the black letters and numbers are *not* included in the pattern but are written here to designate location. Special thanks to Bob Geil in CHANL for his help with the patterning; the pattern is currently under his care in CHANL's cleanroom.

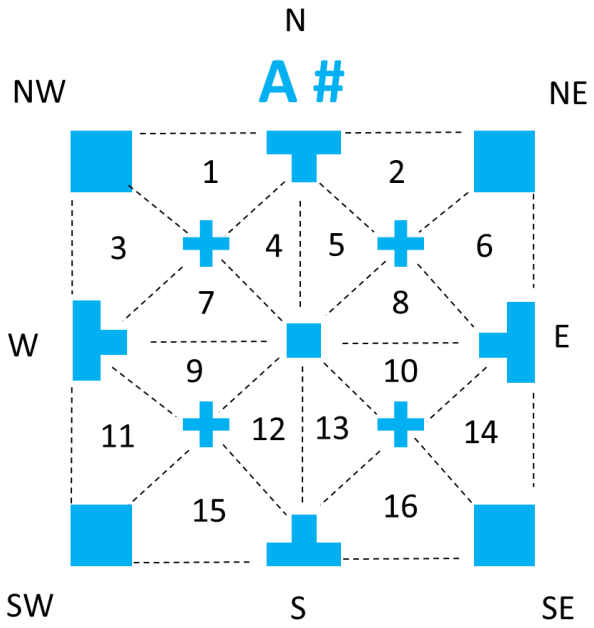

Figure 2.28 | Identification pattern for mechanical exfoliation. Gold pattern (blue) that is patterned onto a silicon or aluminum oxide wafer. The black numbers and letters are not patterned but rather serve as a location guide.

REFERENCES

1. Koepf, M.; Eckstein, N.; Pfister, D.; Grotz, C.; Krueger, I.; Greiwe, M.; Hansen, T.; Kohlmann, H.; Nilges, T., Access and in situ growth of phosphorene-precursor black phosphorus. *J. Cryst. Growth* **2014,** *405*, 6-10.

2. Hansen, C. M., *Hansen solubility parameters : a user's handbook.* CRC Press: Boca Raton, Fla., 2000; p 208 p.

3. Joensen, P.; Frindt, R. F.; Morrison, S. R., Single-layer MoS2. *Materials Research Bulletin* **1986,** *21* (4), 457-461.

4. Eda, G.; Yamaguchi, H.; Voiry, D.; Fujita, T.; Chen, M.; Chhowalla, M., Photoluminescence from chemically exfoliated MoS_2. *Nano Letters* **2011,** *11* (12), 5111-6.

5. Eda, G.; Yamaguchi, H.; Voiry, D.; Fujita, T.; Chen, M.; Chhowalla, M., Correction to Photoluminescence from Chemically Exfoliated MoS_2. *Nano Letters* **2012,** *12* (1), 526-526.

6. Divigalpitiya, W. M. R.; Frindt, R. F.; Morrison, S. R., Spread films of single molecular transition-metal sulphides. *Applied Surface Science* **1991,** *48/49*, 572-575.

7. Divigalpitiya, W. M. R.; Morrison, S. R.; Frindt, R. F., Thin Oriented Films of Molybdenum Disulphide. *Thin Solid Films* **1990,** *186*, 177-192.

8. Yu, X.; Prevot, M. S.; Guijarro, N.; Sivula, K., Self-assembled 2D WSe2 thin films for photoelectrochemical hydrogen production. *Nat Commun* **2015,** *6*, 7596.

9. Yu, X.; Rahmanudin, A.; Jeanbourquin, X. A.; Tsokkou, D.; Guijarro, N.; Banerji, N.; Sivula, K., Hybrid Heterojunctions of Solution-Processed Semiconducting 2D Transition Metal Dichalcogenides. *ACS Energy Letters* **2017,** *2* (2), 524-531.

10. Li, X.; Zhang, G.; Bai, X.; Sun, X.; Wang, X.; Wang, E.; Dai, H., Highly conducting graphene sheets and Langmuir-Blodgett films. *Nat Nanotechnol* **2008,** *3* (9), 538-42.

11. Akatsuka, K.; Haga, M.-a.; Ebina, Y.; Osada, M.; Fukuda, K.; Sasaki, T., Construction of highly ordered lamellar nanostructures through Langmuir-Blodgett deposition of molecularly thin titania nanosheets tens of micrometers wide and their excellent dielectric properties. *ACS Nano* **2009,** *3* (5), 1097-1106.

12. Zhu, Y.; Cai, W.; Piner, R. D.; Velamakanni, A.; Ruoff, R. S., Transparent self-assembled films of reduced graphene oxide platelets. *Applied Physics Letters* **2009,** *95* (10), 103104.

13. Zheng, Q.; Ip, W. H.; Lin, X.; Yousefi, N.; Yeung, K. K.; Li, Z.; Kim, J.-K., Transparent conductive films consisting of ultralarge graphene sheets produced by Langmuir-Blodgett Assembly. *ACS Nano* **2011,** *5* (7), 6039-6051.

14. Zheng, Q.; Zhang, B.; Lin, X.; Shen, X.; Yousefi, N.; Huang, Z.-D.; Li, Z.; Kim, J.-K., Highly transparent and conducting ultralarge graphene oxide/single-walled carbon nanotube hybrid films produced by Langmuir–Blodgett assembly. *Journal of Materials Chemistry* **2012,** *22* (48), 25072.

15. Zheng, Q.-b.; Shi, L.-f.; Yang, J.-h., Langmuir-Blodgett assembly of ultra-large graphene oxide films for transparent electrodes. *Transactions of Nonferrous Metals Society of China* **2012,** *22* (10), 2504-2511.

16. Jia, B.; Zou, L., Langmuir–Blodgett assembly of sulphonated graphene nanosheets into single- and multi-layered thin films. *Chemical Physics Letters* **2013,** *568-569*, 101-105.

17. Kim, H.; Mattevi, C.; Kim, H. J.; Mittal, A.; Mkhoyan, K. A.; Riman, R. E.; Chhowalla, M., Optoelectronic properties of graphene thin films deposited by a Langmuir-Blodgett assembly. *Nanoscale* **2013,** *5* (24), 12365-74.

18. Jia, B.; Wang, Q.; Zhang, W.; Lin, B.; Yuan, N.; Ding, J.; Ren, Y.; Chu, F., A new oil/water interfacial assembly of sulphonated graphene into ultrathin films. *RSC Adv.* **2014,** *4* (65), 34566-34571.

19. Ahn, S. I.; Kim, K.; Jung, J.; Choi, K. C., Large and pristine films of reduced graphene oxide. *Sci Rep* **2015,** *5*, 18799.

20. Benito, J.; Fenero, M.; Sorribas, S.; Zornoza, B.; Msayib, K. J.; McKeown, N. B.; Téllez, C.; Coronas, J.; Gascón, I., Fabrication of ultrathin films containing the metal organic framework Fe-MIL-88B-NH2 by the Langmuir–Blodgett technique. *Colloids and Surfaces A: Physicochemical and Engineering Aspects* **2015,** *470*, 161-170.

21. Nie, H. L.; Dou, X.; Tang, Z.; Jang, H. D.; Huang, J., High-Yield Spreading of Water-Miscible Solvents on Water for Langmuir-Blodgett Assembly. *J Am Chem Soc* **2015,** *137* (33), 10683-8.

22. Yang, T.; Yang, J.; Shi, L.; Mäder, E.; Zheng, Q., Highly flexible transparent conductive graphene/single-walled carbon nanotube nanocomposite films produced by Langmuir–Blodgett assembly. *RSC Adv.* **2015,** *5* (30), 23650-23657.

23. Kaur, H.; Yadav, S.; Srivastava, A. K.; Singh, N.; Schneider, J. J.; Sinha, O. P.; Agrawal, V. V.; Srivastava, R., Large Area Fabrication of Semiconducting Phosphorene by Langmuir-Blodgett Assembly. *Sci Rep* **2016,** *6*, 34095.

24. Tomašević-Ilić, T.; Pešić, J.; Milošević, I.; Vujin, J.; Matković, A.; Spasenović, M.; Gajić, R., Transparent and conductive films from liquid phase exfoliated graphene. *Optical and Quantum Electronics* **2016,** *48* (6).

25. Zhang, H.; Jeon, K. W.; Seo, D. K., Equipment-Free Deposition of Graphene-Based Molybdenum Oxide Nanohybrid Langmuir-Blodgett Films for Flexible Electrochromic Panel Application. *ACS Appl Mater Interfaces* **2016,** *8* (33), 21539-44.

26. Silverberg, G. J.; McClelland, A. A.; Griesse-Nascimento, S.; Girabawe, C.; Kadow, J. P.; Mahadevan, L.; Vecitis, C. D., Controlling the Roughness of Langmuir-Blodgett Monolayers. *J Phys Chem B* **2017,** *121* (19), 5078-5085.

27. Zhang, Y.; Xu, L.; Walker, W. R.; Tittle, C. M.; Backhouse, C. J.; Pope, M. A., Langmuir films and uniform, large area, transparent coatings of chemically exfoliated MoS2 single layers. *J. Mater. Chem. C{Zhang, 2017 #1747}* **2017**.

28. Ariga, K.; Yamauchi, Y.; Mori, T.; Hill, J. P., 25th anniversary article: what can be done with the Langmuir-Blodgett method? Recent developments and its critical role in materials science. *Adv Mater* **2013,** *25* (45), 6477-512.

29. Taguchi, Y.; Kimura, R.; Azumi, R.; Tachibana, H.; Koshizaki, N.; Shimomura, M.; Momozawa, N.; Sakai, H.; Abe, M.; Matsumoto, M., Fabrication of hybrid layered films of MoS2 and an amphiphilic ammonium cation using the Langmuir− Blodgett technique. *Langmuir* **1998,** *14* (22), 6550-6555.

30. Zhang, Y.; Xu, L.; Walker, W. R.; Tittle, C. M.; Backhouse, C. J.; Pope, M. A., Langmuir films and uniform, large area, transparent coatings of chemically exfoliated MoS 2 single layers. *Journal of Materials Chemistry C* **2017,** *5* (43), 11275-11287.

31. Muramatsu, M.; Akatsuka, K.; Ebina, Y.; Wang, K.; Sasaki, T.; Ishida, T.; Miyake, K.; Haga, M.-a., Fabrication of Densely Packed Titania Nanosheet Films on Solid Surface by

Use of Langmuir− Blodgett Deposition Method without Amphiphilic Additives. *Langmuir* **2005,** *21* (14), 6590-6595.

32. Kaur, H.; Yadav, S.; Srivastava, A. K.; Singh, N.; Schneider, J. J.; Sinha, O. P.; Agrawal, V. V.; Srivastava, R., Large area fabrication of semiconducting phosphorene by Langmuir-Blodgett assembly. *Scientific reports* **2016,** *6*, 34095.

33. Afsar-Siddiqui, A. B.; Luckham, P. F.; Matar, O. K., The spreading of surfactant solutions on thin liquid films. *Advances in Colloid and Interface Science* **2003,** *106* (1-3), 183-236.

34. von Bahr, M.; Tiberg, F.; Zhmud, B. V., Spreading dynamics of surfactant solutions. *Langmuir* **1999,** *15* (20), 7069-7075.

35. Dussaud, A. D.; Troian, S. M., Dynamics of spontaneous spreading with evaporation on a deep fluid layer. *Physics of Fluids* **1998,** *10* (1), 23-38.

36. Majumder, M.; Rendall, C. S.; Eukel, J. A.; Wang, J. Y.; Behabtu, N.; Pint, C. L.; Liu, T.-Y.; Orbaek, A. W.; Mirri, F.; Nam, J., Overcoming the "coffee-stain" effect by compositional Marangoni-flow-assisted drop-drying. *The Journal of Physical Chemistry B* **2012,** *116* (22), 6536-6542.

37. Nie, H.-L.; Dou, X.; Tang, Z.; Jang, H. D.; Huang, J., High-Yield Spreading of Water-Miscible Solvents on Water for Langmuir–Blodgett Assembly. *Journal of the American Chemical Society* **2015,** *137* (33), 10683-10688.

38. Coleman, J. N.; Lotya, M.; O'Neill, A.; Bergin, S. D.; King, P. J.; Khan, U.; Young, K.; Gaucher, A.; De, S.; Smith, R. J.; Shvets, I. V.; Arora, S. K.; Stanton, G.; Kim, H. Y.; Lee, K.; Kim, G. T.; Duesberg, G. S.; Hallam, T.; Boland, J. J.; Wang, J. J.; Donegan, J. F.; Grunlan, J. C.; Moriarty, G.; Shmeliov, A.; Nicholls, R. J.; Perkins, J. M.; Grieveson, E. M.; Theuwissen, K.; McComb, D. W.; Nellist, P. D.; Nicolosi, V., Two-dimensional nanosheets produced by liquid exfoliation of layered materials. *Science* **2011,** *331* (6017), 568-71.

39. Woomer, A. H.; Farnsworth, T. W.; Hu, J.; Wells, R. A.; Donley, C. L.; Warren, S. C., Phosphorene: Synthesis, Scale-Up, and Quantitative Optical Spectroscopy. *ACS Nano* **2015,** *9* (9), 8869-84.

40. Paul, W.; Warschauer, D. M., *Solids under pressure*. McGraw-Hill: New York, 1963.

41. Holzapfiel, W. B.; Isaacs, N. S., *High pressure techniques in chemistry and physics: a practical approach*. Oxford University Press: Oxford; New York, 1997.

42. Ferraro, J. R., *Vibrational spectroscopy at high external pressures: the diamond anvil cell*. Academic Press: New York, 1984.

43. Hazen, R. M.; Finger, L. W., *Comparative crystal chemistry: temperature, pressure, composition, and the variation of crystal structure*. Wiley: Chichester; New York, 1982.

44. Sherman, W. F.; Stadtmuller, A. A., *Experimental techniques in high-pressure research research*. Wiley: Chichester; New York, 1987.

45. Tsiklis, D. S., *Handbook of techniques in high-pressure research and engineering*. Plenum Press: New York, 1968.

46. MacDonald, W., Diamond anvil, preparing the gasket. YouTube: https://youtu.be/XxIGoJ-fJro, 2015.

47. Soignard, E.; McMillan, P. F., An introduction to DACs and loading techniques. In *High Pressure Crystallography*, Katrusiak, A.; McMillan, P., Eds. Kluwer Academic Publishers: Netherlands, 2004; Vol. Nato Science Series, pp 81-100.

48. Piermarini, G. J.; Block, S.; Barnett, J. D., Hydrostatic limits in liquids and solids to 100 kbar. *Journal of Applied Physics* **1973,** *44* (12), 5377-5382.

49. Bassett, W., The diamond cell and the nature of the earth's mantle. *Ann. Rev. Earth Planet Sci.* **1979,** *7*, 357-384.

50. Katrusiak, A., Facilitating preparation of gaskets for routine high-pressure diffraction studies. *Journal of Applied Crystallography* **1999,** *32*, 1021-1023.

51. Lorenzana, H. E.; Bennahmias, M.; Radousky, H.; Kruger, M. B., Producing diamond anvil cell gaskets for ultrahigh-pressure applications using an inexpensive electric discharge machine. *Review of Scientific Instruments* **1994,** *65* (11), 3540-3543.

52. Pugh, E.; Thompson, H. E.; Balsod, R. B.; Brown, S. V., Automatic spark drill for high pressure experiments. *Review of Scientific Instruments* **2006,** *77* (5), 055109.

53. Lonappan, D.; Shekar, N. V. C.; Sundaram, L. M.; Edwin, T.; Sahu, P. C.; Garg, A. B.; Mittal, R.; Mukhopadhyay, R., EDM Machine Modified For Micro Drilling In DAC Experiments. *AIP Conference Proceedings* **2011,** *1349*, 461-462.

54. Piermarini, G. J.; Block, S.; Barnett, J. D.; Forman, R. A., Calibration of the pressure dependence of theR1ruby fluorescence line to 195 kbar. *Journal of Applied Physics* **1975,** *46* (6), 2774-2780.

55. Mao, H. K.; Xu, J.; Bell, P. M., Calibration of the ruby pressure gauge to 800 kbar under quasi-hydrostatic conditions. *Journal of Geophysical Research* **1986,** *91* (B5), 4673.

56. Mao, H. K.; Bell, P. M.; Shaner, J. W.; Steinberg, D. J., Specific volume measurements of Cu, Mo, Pd, and Ag and calibration of the rubyR1fluorescence pressure gauge from 0.06 to 1 Mbar. *Journal of Applied Physics* **1978,** *49* (6), 3276-3283.

57. Jaffe, A.; Lin, Y.; Mao, W. L.; Karunadasa, H. I., Pressure-Induced Metallization of the Halide Perovskite (CH3NH3)PbI3. *J Am Chem Soc* **2017,** *139* (12), 4330-4333.

58. Wong, P. T. T.; Moffatt, D. J., A new internal pressure calibrant for high-pressure IR spec of aqueous systems. *Applied Spectroscopy* **1989,** *43* (7), 1279-1281.

59. Wong, P. T. T.; Moffatt, D. J.; Baudais, F. L., Crystalline quartz as an internal pressure calibrant for high-pressure infrared spectroscopy. *Applied Spectroscopy* **1985,** *39* (4), 733-735.

60. Christian, S. D.; Grundnes, J.; Klaboe, P., High Pressure Infrared Studies of Liquids with the Diamond Anvil Cell. *Applied Spectroscopy* **1976,** *30* (2), 227-229.

61. Drickamer, H. G., The Effect of High Pressure on the Electronic Structure of Solids. **1965,** *17*, 1-133.

62. Lippincott, E. R.; Duecker, H. C., Pressure Distribution Measurements in Fixed-Anvil High-Pressure Cells. *Science* **1964,** *144* (3622), 1119.

63. Zahner, J. C.; Drickamer, H. G., Pressure Effects in Nickel Dimethylglyoxime and Related Chelates. *The Journal of Chemical Physics* **1960,** *33* (6), 1625-1628.

64. Decker, D. L.; Bassett, W. A.; Merrill, L.; Hall, H. T.; Barnett, J. D., High-Pressure Calibration: A Critical Review. *Journal of Physical and Chemical Reference Data* **1972,** *1* (3), 773-836.

65. Downs, R. T.; Hall-Wallace, M., The American Mineralogist crystal structure database. *American Mineralogist* **2003,** *88*, 247-250.

66. Anthony, J., W.; Bideaux, R. A.; Bladh, K., W.; Nichols, M. C., *Handbook of Mineralogy*. Mineralogical Society of America: Chantilly, VA 20151-1110, USA.

67. Perry, D. L., *Handbook of inorganic compounds [electronic resource]*. CRC Press: Boca Raton, 2011.

68. Robie, R.; Hemingway, B., US Geological Survey Bulletin 2131. *US Geological Survey: Reston, VA* **1995**.

CHAPTER THREE – PHOSPHORENE: SYNTHESIS, SCALE-UP, AND QUANTITATIVE OPTICAL SPECTROSCOPY[1]

Adam H. Woomer[#], Tyler W. Farnsworth[#], Jun Hu, Rebekah A. Wells, Carrie L. Donley, and Scott C. Warren

Introduction

Solution-processable nanomaterials with tunable optoelectronic properties are being considered as potential building blocks for numerous technologies, such as photovoltaics,[1] transistors,[2] and light-emitting diodes.[3] Among these nanomaterials, quantum dots have attracted broad interest because of their size-dependent electronic structure and controllable physical properties; for example, band gaps can be increased by as much as 2 eV as particle size decreases.[4–7] With the advent of two-dimensional (2D) semiconductors,[8] new opportunities have emerged for designing materials and devices, although the size-dependent variation of electronic properties like band gaps are, in general, smaller: transition metal dichalcogenides have band gaps that can only be tuned by 0.7 eV[9,10] while, for example, PbSe quantum dots can be tuned from 0.27 to 1.5 eV.[11–13] Toward increasing the library of solution-processable materials, here we show that black phosphorus can be liquid exfoliated to yield a family of 2D flakes with tunable optical properties that rival those of quantum dots.

Black phosphorus,[14] a layered 3D crystal of elemental phosphorus (Figure 3.1A), and its 2D derivative, termed phosphorene[15,16] (Figure 3.1B), have recently attracted renewed[17]

---

[1] Reprinted (adapted) with permission from (Woomer, A. H., Farnsworth, T. W., Hu, J. et. al. Phosphorene: Synthesis, Scale-Up, and Quantitative Optical Spectroscopy, *ACS Nano*, **2015,** *9*, 8869-8884). Copyright (2015) American Chemical Society; [#]authors contributed equally

attention. In the last few months, there have been exciting demonstrations of the material's application to transistors,[16,18,19] photovoltaics,[20,21] photodetectors,[22,23] and batteries.[24,25] As a 2D material with an intriguing corrugated or accordion-like structure, phosphorene has captured significant theoretical interest with numerous predictions of the material's anisotropic[16,26] and thickness-dependent optoelectronic properties,[27,28] mechanical properties,[29] and chemical reactivity.[30–32] Most predictions have gone untested, however, because there is still no reliable method to make or purify monolayer or few-layer phosphorus. When monolayers have been observed, they are typically situated at the edges of thicker sheets and are typically too small to characterize. Underlying these practical challenges are the inherent problems associated with phosphorus: the phosphorus-phosphorus bonds are significantly weaker than carbon-carbon bonds and several studies have noted the material's tendency to oxidize[14,33] or form other allotropes.[34,35] In addition, interlayer interactions may be stronger in black phosphorus than in other 2D materials.[36,37] These strong interlayer interactions would inhibit exfoliation and, consequently, black phosphorus may be harder to exfoliate and more likely to fragment than other 2D materials. In fact, this is consistent with reports of mechanical exfoliation in which sheets of fewer than six layers have seldom been observed.[16,18,19,38,39]

Our own attempts to mechanically exfoliate black phosphorus confirmed the results of other groups. We prepared and analyzed samples under an inert atmosphere, using scotch tape for exfoliation and a Bruker Dimension FastScan atomic force microscope (AFM) to rapidly analyze sheet thickness over macroscopic areas (see Supporting Information for additional details). We randomly surveyed large areas and assessed the structure of over 3,000 flakes. Our survey revealed that the yield of sheets thinner than 10 layers is less than

0.06%; in addition, no sheets thinner than 6 layers were found. Given the low odds for identifying and characterizing 2D materials prepared in this way, we began exploring liquid exfoliation[40,41] as an alternative route for material preparation. Here we provide evidence that liquid exfoliation, when carefully executed under an inert atmosphere, produces macroscopic (milligram-to-gram scale) quantities of monolayer and few-layer phosphorene.[42] We note that this is a considerable improvement over state-of-the-art methods of liquid exfoliation,[43–45] which have so-far produced flakes with thicknesses that are 10 to 20 times thicker than those described here. We characterize the material's structure, stability, and thickness-dependent optical properties and compare these properties to theoretical predictions. In addition, we perform the first quantitative optical absorption measurements on 2D phosphorus, allowing us to determine the thickness-dependent optical transitions and band gaps.

3.1 Liquid exfoliation of black phosphorus

Black phosphorus crystals (Figure 3.1A) were acquired from Smart Elements between December 2012 and March 2014 or grown in our laboratory by SnI_2 vapor transport.[46] (Smart Elements modified its method of manufacture in the summer of 2014 and the microstructures of materials acquired after this date may differ.) Black phosphorus was ground in a mortar and pestle and sonicated in anhydrous, deoxygenated organic liquids using low-power bath sonication under an inert atmosphere. In our initial experiments, black phosphorus was sonicated in electronic grade isopropanol for sixteen hours. During sonication, the phosphorus was suspended in solution and its color changed from black to reddish-brown to yellow (Figure 3.1C), indicating a profound change in the electronic structure of the material. We quantified this change in appearance by ultraviolet-visible-near

IR (UV-vis-near IR) absorption spectroscopy (see discussion below for further details). Over several weeks, there was limited reaggregation and no further change in color, suggesting that these suspensions were comprised of small phosphorus particulates. To examine the morphology of the particulates, suspensions were drop-cast onto a silicon wafer for analysis by scanning electron microscopy (SEM, Figure 3.1D). These images confirmed the presence of thin phosphorus flakes with lateral dimensions between 50 nm and 50 μm. From these results, we concluded that a more extensive study was required to identify conditions that maximized the yield of thin phosphorus flakes.

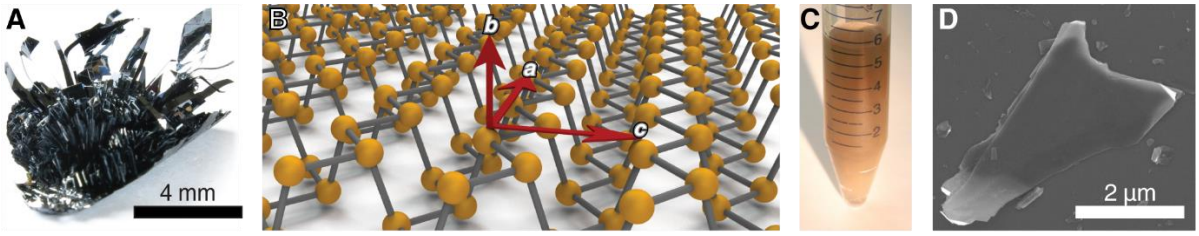

Figure 3.1 | Liquid exfoliation of black phosphorus. (A) Photograph of black phosphorus grown by chemical vapor transport. **(B)** Illustration of a phosphorene monolayer showing the conventional crystallographic axes. The zig-zag direction is 'a', the armchair direction is 'c', and the 'b' direction is normal to the flake. **(C)** Photograph of a liquid-exfoliated suspension of 2D phosphorus in isopropanol. **(D)** SEM image of liquid-exfoliated 2D phosphorus.

We surveyed[42] eighteen solvents for their ability to exfoliate black phosphorus (see Supporting Information for full experimental details). Black phosphorus (10 mg) was added to 20 mL of each solvent and sonicated for thirteen hours under anhydrous and air-free conditions. The suspensions were centrifuged at 3,000*g* for 30 minutes to remove unexfoliated black phosphorus. The supernatant was further purified *via* dialysis to remove small (< 2.5 nm) phosphorus fragments. These suspensions were characterized with inductively coupled plasma-mass spectroscopy (ICP-MS) and UV-vis transmission spectroscopy to measure a dispersed concentration. We found that the best solvent was benzonitrile, which achieved a mean concentration of 0.11 ± 0.02 mg/mL. Plots of

phosphorus concentration *vs*. the Hansen solubility parameters of each solvent (Figure 3.2A-D) allow us to estimate that the Hildebrand parameter for 2D phosphorus is 22 ± 3 $MPa^{1/2}$. Although there is significant solvent-to-solvent variability—a feature common to graphene, boron nitride, and transition metal dichalcogenides[41]—we find that the optimal solvents for 2D phosphorus are similar to those for other 2D materials. An essential difference, however, is that 2D phosphorus must be handled and sonicated under an inert atmosphere, as we demonstrate below.

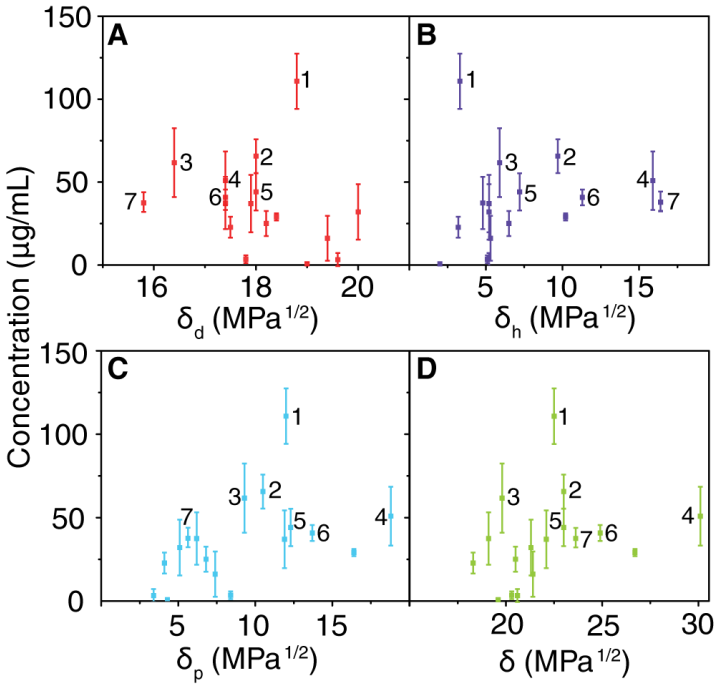

Figure 3.2 | Survey of organic liquids, showing 2D phosphorus concentrations *vs*. Hansen **(A-C)** and Hildebrand **(D)** solubility parameters for 18 solvents. The Hansen plots depict the energy due to dispersion forces (A), hydrogen bonding (B), and dipolar intermolecular forces (C). Numbers 1 through 7 rank the best liquids: (1) benzonitrile, (2) 1,3-dimethyl-2-imidazolidinone, (3) 1-vinyl-2-pyrrolidinone, (4) *N*-methylformamide, (5) *N*-methyl-2-pyrrolidone, (6) *N*,*N*-dimethylformamide, (7) 2-propanol. Each data point is an average of three trials; the error bars correspond to the standard deviation.

3.2 Characterization of 2D phosphorus

In order to examine the structure of the suspended material, we used transmission electron microscopy (TEM) to quantify shape, size, and thickness as well as high resolution

TEM (HR-TEM) to assess crystallinity. We imaged and measured thousands of phosphorus flakes; Figure 3.3A-C shows TEM images of several representative samples. As before, a broad distribution of flake sizes was found. Single pieces typically had uniform contrast, suggesting that they had a planar morphology. All of the pieces examined in HR-TEM exhibited lattice fringes, showing that the crystallinity of phosphorus flakes was preserved (Figure 3.3D). We analyzed HR-TEM images by performing fast Fourier transforms (FFT), allowing us to observe the expected {200} and {002} plane families of black phosphorus. In addition, some flakes exhibited strong 101 intensities (Figure 3.33E), which are forbidden sets of diffracting planes in bulk black phosphorus. To understand the origin of the 101 spots, we used multi-slice calculations (JEMS[47]) to simulate HR-TEM images of 2D phosphorus sheets with varying thicknesses from four common microscopes (see Supporting Information for additional details). Fast Fourier transforms were applied to the HR-TEM images to determine the intensities of spots corresponding to plane families. In agreement with a previous analysis of electron diffraction patterns,[28] we found that a large 101:200 intensity ratio in FFTs is a unique characteristic of monolayers (Figure 3.3F) when imaged at or near Scherzer defocus, thus confirming their presence in our suspensions. We attribute the diffuse background of the FFT (Figure 3.3E) to the likely presence of absorbed organics, which has been observed previously for other 2D materials that were not degassed at elevated temperatures prior to imaging.[48,49]

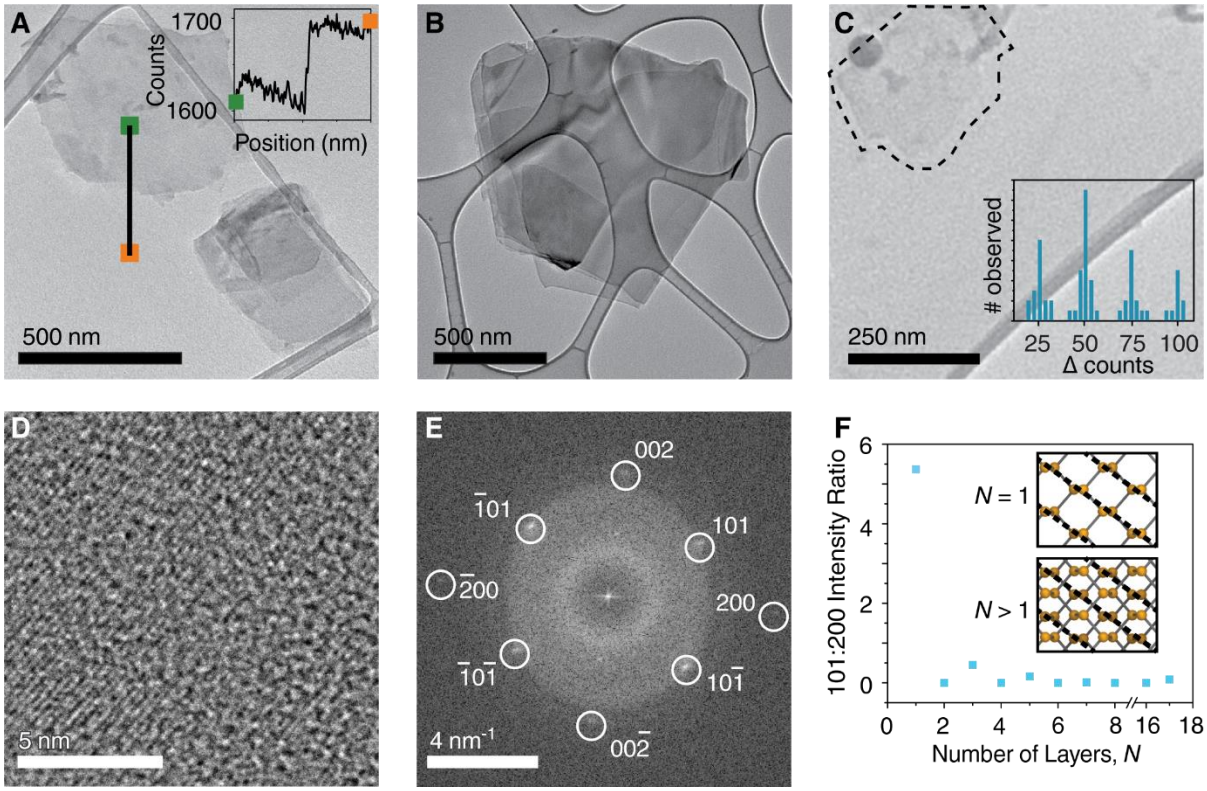

Figure 3.3 | TEM characterization of liquid-exfoliated 2D phosphorus. (A-C) TEM images of 2D phosphorus. **(C)** TEM image of a monolayer of 2D phosphorus. The inset in **(A)** shows the contrast change (*ca.* 75 counts) from a line profile drawn across a flake that is three layers thick. The inset in **(C)** provides a histogram of contrast changes from one hundred flakes. The changes in intensity (25, 50, *etc*.) correspond to monolayers, bilayers, *etc*. **(D)** HR-TEM image of phosphorene, a monolayer. **(E)** FFT of the HR-TEM image in (D). **(F)** Intensity ratios of 101 and 200 spots in FFT HR-TEM images and their relation to layer thickness, as calculated from multi-slice simulations in JEMS.[47] Insets show that constructive interference from {101} plane families (dashed lines) occur in monolayers but have low or no intensity in multilayer flakes.

To quantify the thickness of all flakes in our suspensions, we used our real-space TEM images—all acquired under identical imaging conditions including exposure time, aperture selection, lens currents, magnification and defocus value—to measure the change in intensity across sheet edges for hundreds of flakes (Figure 3.3A, line and inset). Flake edges were suspended over either vacuum or carbon film (see Supporting Information for additional details). The smallest intensity change was 25 ± 3 counts and all other intensity changes were multiples of 25 counts (Figure 3.3C, inset). We therefore assigned an intensity change of 25, 50, 75, and 100 counts to monolayers, bilayers, trilayers, and four-layered 2D

phosphorus flakes, respectively. Further confirming this assignment, we found that only those flakes with a contrast change of *ca.* 25 counts had the intense 101 spots that are a hallmark of monolayers. Although this method is simple and fast, we do note that the linear relationship breaks down for flakes that are thicker than *ca.* 40 layers.

With the goal of isolating 2D flakes with well-defined thicknesses and optical properties, we used centrifugation to fractionate the phosphorus suspensions. We centrifuged at a rotational centrifugal force (RCF) as low as 120*g* and then centrifuged the supernatant at a slightly greater RCF, reaching values of up to 48,000*g*. The sediment from the second centrifugation was collected and re-dispersed in pure solvent. This new suspension is labeled by the average centrifugal force between the two RCFs; for example, a suspension labeled 20,200*g* has been centrifuged at 17,200*g* and 23,400*g* (see Supporting Information for full experimental details). Using TEM, we analyzed the thicknesses (Figure 3.4A) lateral size (Figure 3.4B) and of the suspended 2D phosphorus flakes. We found that this centrifugation approach could systematically isolate flakes with varying size and thickness distributions. When centrifuging at high speeds, for example, we collected macroscopic quantities of flakes with size distributions centered near one-layer and two-layer thicknesses (Figure 3.4A) in which monolayers comprised up to 45% of the sample. Phosphorene—a material that has been sought after but rarely observed—is now easily accessible.

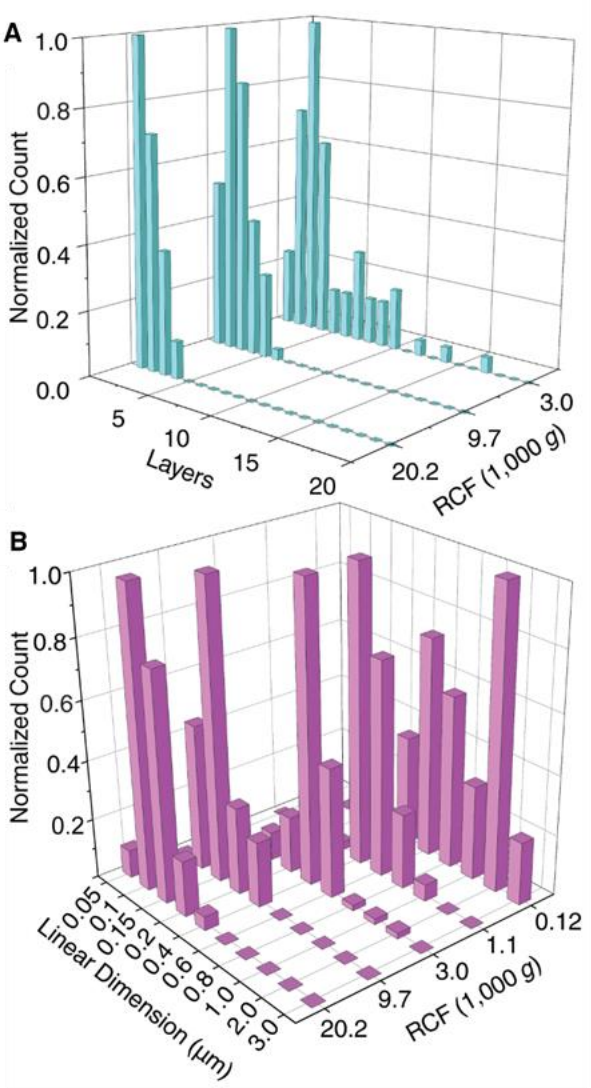

Figure 3.4 | Selective variation of the centrifugation rate allows for control over flake thickness **(A)** and flake lateral size **(B)**.

3.3 Stability of phosphorene and 2D phosphorus

As first recognized by Bridgman in 1914,[ref. 14] black phosphorus oxidizes and converts to phosphoric acid under humid atmospheric conditions. More recent studies have also shown that mechanically-exfoliated phosphorus degrades in air.[19,28,32] We used x-ray photoelectron spectroscopy (XPS) and measurements of apparent pH to assess the oxidation. We performed XPS both on bulk black phosphorus to obtain a reference spectrum (Figure 3.5A) and on 2D phosphorus to test whether oxidation accompanies liquid exfoliation

(Figure 3.5B). In addition to performing all exfoliation and centrifugation under an inert atmosphere, we constructed a transfer chamber that excluded oxygen and water during sample transfer to and from the XPS instrument (see SI for experimental details). Pristine black phosphorus had $2p_{1/2}$ and $2p_{3/2}$ peaks that are characteristic of unoxidized elemental phosphorus.[50] We exposed the same sample to air and re-acquired XPS spectra at later time intervals. A broad peak at 134 eV emerged, which can be attributed to several types of phosphorus-oxygen bonds.[51] Lacking an oxidation mechanism, we cannot yet identify the type or types of P-O species that may be present in our samples. We performed similar experiments on thin 2D phosphorus (< 6 layers). The pristine sample exhibited no signs of oxidation (Figure 3.5B, black). Upon exposure to oxygen gas that contained some water (not dried) and 460 nm light, a broad peak appeared at 133 eV, characteristic of oxidized phosphorus. In this modified material, *ca.* 5% of the phosphorus was oxidized, as estimated by peak integration software. Collectively, our analyses demonstrate that liquid exfoliation successfully yields high-quality, unoxidized 2D phosphorus.

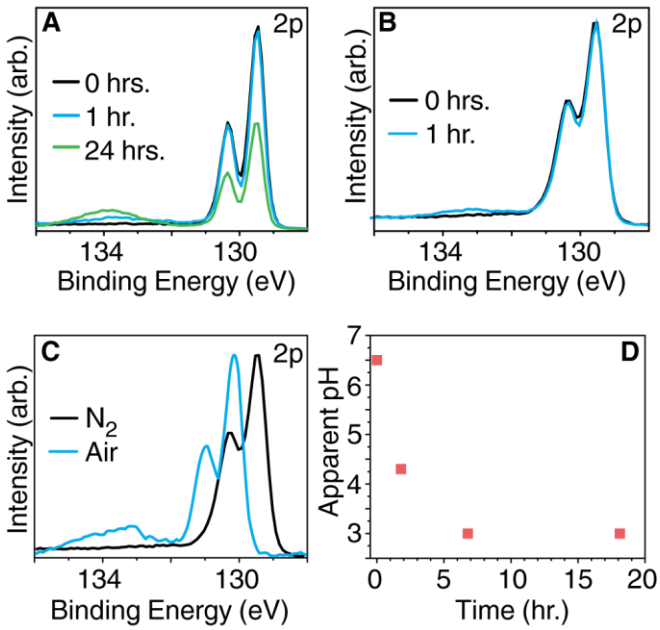

Figure 3.5 | XPS of freshly cleaved bulk black phosphorus. (A) after exposure to ambient air and room light for 0 (black), 1 (blue), and 24 (green) hours. **(B)** XPS analysis of few-layer 2D phosphorus showing that the material prepared by liquid exfoliation was unoxidized (black). The few-layer sheets were controllably oxidized by exposure to light (λ = 460 nm) and oxygen with some water (blue). **(C)** Exfoliation of black phosphorus in a sealed vial with N_2 (black) or air (blue) in the head space of the vial shows that the presence of air causes 28% of the phosphorus to become oxidized. Binding energies also increase, although the origin of this effect—whether sample charging, doping, or both—is not yet clear. **(D)** When few-layer 2D phosphorus (< 6 layers) is suspended in isopropanol and exposed to light and air (λ = 460 nm), the apparent pH (recorded by a pH meter) decreases because of acid production.

In order to evaluate whether handling under an inert atmosphere is important, we sonicated black phosphorus in a sealed vial, with either nitrogen or air in the vial's headspace. Analysis of the air-exposed material by XPS (Figure 3.5C) shows substantial oxidation, with 28% of the phosphorus no longer in the unoxidized form. In addition, we monitored the pH of a solution of few-layer phosphorus that was suspended in isopropanol and exposed to light and air (Figure 3.5D). We found that the solution rapidly acidifies, consistent with Bridgman's prediction[14] that phosphoric acid is produced upon exposure to air. When higher phosphorus concentrations are used, the apparent change in pH is larger. On the basis of these and prior findings,[43] we conclude that although liquid exfoliation in the

presence of air may produce some crystalline, thin material, its surfaces and interior[52] are oxidized, acid is present, and its overall quality is low.

3.4 Exfoliation of black phosphorus at the 10-gram scale

We explored shear mixing[42,53] as a method for the scaled-up production of 2D phosphorus. We used a Silverson L5M-A shear mixer with either a 0.75-inch or 1.385-inch rotor with square holes for our work at the 1-gram and 10-gram scales, respectively. All experiments were performed under oxygen-free and water-free conditions by bubbling nitrogen gas into the mixing container. In addition, we used a water bath to keep the solutions at room temperature during mixing. We used several different grades of NMP, as it was disclosed to us by the Coleman group that only certain types of NMP may work for shear mixing of graphene.[54] Ultimately, we selected NMP from Sigma Aldrich (99.5% purity, anhydrous) for our scaled-up exfoliation. Black phosphorus was ground in a mortar and pestle prior to its use in shear mixing. We used two different grades of black phosphorus, both of which we produced in our laboratory. The first, "high quality" black phosphorus, was highly crystalline with millimeter-sized crystals and was difficult to grind; the second, "low quality" black phosphorus, was highly polycrystalline, had trace amounts of red phosphorus, and was easy to grind. In our experiments, we found that only the low-quality material could be successfully exfoliated by shear mixing alone, regardless of the type of NMP or the conditions of shear mixing. This observation is consistent with a mechanism in which the separation of layers is nucleated at grain boundaries or other defects in the material. In order to exfoliate the higher-quality starting material, we had to rely on a combination of shear mixing and bath sonication.

For our scaled-up synthesis, we dispersed 6 grams of pulverized, high-quality black phosphorus into 100 mL of NMP and bath sonicated the suspension for 2 hours. Next, we added 700 mL of NMP and shear mixed the sample at 5,000 rpm for 4 hours. The dispersion was sonicated again for 3 hours and then shear mixed again for 1 hour at 5,000 rpm. The resulting suspension is shown in Figure 3.6A. The material was then centrifuged at 20,200*g* to yield a highly concentrated suspension of very thin, fractionated material (Figure 3.6A, small vial). In this suspension, nearly 25% of the sample was monolayers (Figure 3.6B) and the lateral size (Figure 6c) was similar to the material produced using bath sonication at a smaller scale (Figure 3.4). This demonstration reveals that the production of high quality 2D phosphorus—including phosphorene—can be readily accomplished using simple and scalable approaches.

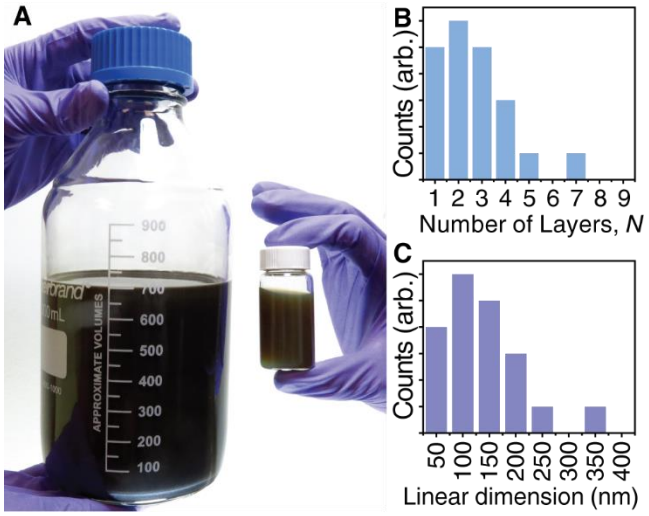

Figure 3.6 | Scaled-up production of 2D phosphorus. (A) Photograph of solutions that were exfoliated using a combination of shear mixing and sonication. In our scale-up, we used six grams of black phosphorus and 800 mL of NMP (left). We centrifuged 40 mL of this mixture at 20,200*g* to isolate a highly concentrated suspension containing thin pieces (right). The size distribution of 2D phosphorus in this fraction is shown in **(B)** and **(C)**.

3.5 Optical absorption in 2D phosphorus: background

The optoelectronic properties of black phosphorus and 2D phosphorus—high mobility, anisotropy and the extreme variation in band structure with flake thickness—have provoked intense interest and debate. In 1981, a calculation first proposed the idea of a monolayer of black phosphorus[55] (*i.e.*, phosphorene) and calculated a band gap of 1.8 eV, which is significantly larger than the bulk value of 0.33 ± 0.02 eV (see below for discussion). This remarkable prediction was dormant until several months ago, when the possibility of making phosphorene began to emerge. Despite this interest, the synthesis of monolayers has remained a challenge and, consequently, the majority of recent studies have been theoretical. These studies have essentially confirmed the 1981 prediction—that the band gap is tunable—although they have also introduced considerable uncertainty as to the actual size of the gap: values for monolayers typically range from 1.0 to 2.2 eV (see Table 3.1). Nevertheless, theory consistently predicts that the band gap is direct for all thicknesses of 2D phosphorus, which has driven further interest because most other 2D semiconductors have indirect band gaps.

These predictions are compelling and need to be systematically examined but, so far, only a few experiments have been reported. Photoluminescence measurements have shown that these predictions are qualitatively correct, but with a varying exciton binding energy of 0.01 to 0.9 eV in phosphorene, this technique will underestimate the band gap of black phosphorus by a similar amount, which depends on the static dielectric constant of the surrounding medium.[56–58] In addition, surface defects, contamination, and oxidation of samples may introduce further experimental uncertainty. In fact, results so far are quite varied: in one study, a trilayer photoluminesced at 1.60 eV, while, in another, the measured

value was 0.97 eV (see optical gaps, Table 3.1). Electrical measurements have also been performed and the reported mobility gaps were smaller than those found by photoluminescence (see mobility and optical gaps, Table 3.1), a result that is surprising because the mobility gap should be larger than the optical gap in a semiconductor with few interband states.[59,60] However, the study did provide a detailed analysis of many flake thicknesses, and revealed that bulk properties begin to transition towards quantum-confined properties at flake sizes as large as 30 layers.

Table 3.1 | Reported optical, mobility, and band gaps of 2D phosphorus

Thickness (layers)	1	2	3	4	Bulk	Source
Photoluminescence (optical gap, eV)	1.75	1.29	0.97	0.84		Yang, J.[61]
	1.45					Liu, H.[16]
	1.31					Wang, X.[62]
		1.29	0.98	0.88		Zhang, S.[63]
			1.60			Castellanos-Gomez, A.[28]
Electrical (mobility gap, eV)	0.98	0.71	0.61	0.56	0.30	Das, S.[64]
Computation (band gap, eV)	2.15	1.70	1.48	1.36	1.08	Castellanos-Gomez, A.[28]
	2.0	1.30	1.06		0.30	Tran, V.[37]
	1.94	1.7	1.3	0.8	0.43	Liang, L.[65]
	1.60	1.01	0.68	0.46	0.10	Rudenko, A.[66]
	1.52	1.01	0.79	0.67	0.36	Qiao, J.[67]
	1.01	0.66	0.52	0.47	0.31	Liu, H.[16]
		1.02	0.79	0.68		Zhang, S.[63]
Absorbance (band gap, eV)		1.88	1.43	1.19	0.33	This work, see Table 3.2.

In this section, we report our experiments on the optical absorbance of black phosphorus and fractionated suspensions of 2D phosphorus. We also report our analyses of these spectra, from which we estimate the absorption edge and band gap in black phosphorus and 2D phosphorus. Some of our analysis uses Elliot's theory of light absorption[68] by delocalized, Wannier-type excitons,[69] and we implement Elliot's theory in the form of Tauc plots.[70] Tauc plots determine the band-to-band transition energy as well as the nature of the

transition—whether it is phonon-mediated (indirect) or not (direct), and whether it is dipole-mediated (allowed) or not (forbidden). A proper Tauc plot yields a linear relationship between $(\alpha h\nu)^n$ and hν, where α is the absorption coefficient, hν is the photon energy, and n describes the nature of the transition. Although Tauc plots have been criticized because of their simplistic assumptions about band structure and their poor treatment of excitonic effects,[56] they have been used to analyze the absorption edge of many semiconductors, including black phosphorus.[71] In a reported Tauc analysis of black phosphorus, a room-temperature band gap of 0.31 eV was found.[71] This agrees with previously reported electrical measurements,[17,72–76] which we have averaged to calculate a room-temperature band gap of 0.33 ± 0.02 eV. Although this agreement is promising, there are important differences between our 2D samples and bulk black phosphorus that may prevent the application of Tauc's method to our materials. Next, we consider these differences and the corresponding limitations of Elliot's theory.

We have identified five possible reasons why a Tauc analysis could fail to apply to our 2D phosphorus suspensions.

(1) *Light scattering:* A Tauc analysis requires an accurate measurement of the absorption coefficient, α, *versus* wavelength. We measured light that is absorbed by our suspensions of 2D phosphorus using a transmission geometry, but in a traditional transmission geometry, most scattered light is not captured by the detector. To account for forward-scattered light, we placed samples near the opening aperture of an integrating sphere. This measurement showed that the amount of forward-scattered light was relatively small. In addition, because there is less back-scattered light than forward-scattered light,[77] we estimated that our measurements that capture both the

transmitted and forward-scattered but neglect back-scattered light have less than a 3% error (see Supporting Information for complete details). Consequently, we have reported an absorption coefficient rather than an extinction coefficient.

(2) *Exciton binding energy:* Elliot's theory is only applicable to Wannier excitons, which have an exciton binding energy (EBE) of less than 100 meV. Bulk black phosphorus has an EBE of 8 meV and the excitonic features in absorbance spectra are only apparent at low temperature.[17] The predicted EBE of phosphorene (a monolayer) depends on the static dielectric constant of the surrounding medium, and can be as large as 900 meV in a vacuum.[28,37] We performed most optical absorbance experiments in NMP, which has a high dielectric constant (32.17) and yields a small EBE (15 meV, see Supporting Information). The small EBEs, combined with the measurement of our absorbance spectra at room temperature and low light intensities, allows Elliot's theory to be applied because excitons will not obscure the absorption edge as they do in MoS_2 and other transition metal chalcogenides.

(3) *Urbach tail:* In materials with significant structural disorder, a pronounced absorption extends below the absorption edge.[78] This absorption, called an Urbach tail, could be present in 2D phosphorus because of the loss of periodicity and presence of defects at the edge of sheets. Urbach tails give a non-linear contribution to Tauc plots. To avoid misinterpreting our spectra, we only extracted an estimate of the band gap when a linear fit of the Tauc plot was obtained at energies above the Urbach tail.

(4) *Anisotropic optical properties:* The nature of black phosphorus' band gap depends on direction: it is direct and allowed in the ***c*** direction but direct and forbidden in the ***a*** direction (see Figure 3.1B).[17] In principle, this would prevent a Tauc plot from

distinguishing either transition. Fortunately, the forbidden transition is relatively weak and its contribution to light absorption is negligible;[17] thus, it does not obscure the Tauc analysis of the direct, allowed band gap.

(5) *Variation in band gap:* Tauc analyses are typically applied to materials with a single band gap. If multiple gaps are present and they span a narrow range of energies, it is not possible to distinguish each gap. The superposition of multiple absorption edges of similar strength leads to non-linearity in the Tauc plot, preventing one from determining the nature of the absorption edge or from extracting an accurate band gap energy. Of the five limitations, we found that this consideration is the most important. Our suspensions contain flakes of several thicknesses and therefore several band gaps. Because the absorption coefficients from flakes of different thicknesses are similar and because their band gaps fall across a range of energies, we found that it is not always possible to use a Tauc analysis (see below). In those instances, we have developed and applied a different method for estimating the absorption edge.

3.6 Optical absorption in 2D phosphorus: measurement and Tauc analysis

In this section, we report our measurement and Tauc analyses of the optical absorbance of 2D phosphorus suspensions. In order to interpret these measurements, we first established reference spectra of bulk black phosphorus. We performed UV-vis-nIR (175 nm to 3,300 nm) and FT-IR measurements on a polycrystalline sample (KBr pellet, Figure 3.7A, black) and used a CRAIC microspectrophotometer on single flakes of mechanically cleaved bulk crystals (Figure 3.7A, gray). All spectra were acquired under an inert atmosphere. Fractionated suspensions of 2D phosphorus (Figure 3.4) were analyzed using an integrating

sphere to capture both transmitted and scattered light (see Supporting Information in Appendix 2 for full experimental details).

The polycrystalline black phosphorus within the KBr pellet had a high optical density, which allowed us to quantify light absorption near the band gap threshold. We observed an onset of absorption at *ca.* 0.4 eV (Figure 3.7A, black), characteristic of bulk black phosphorus. The analysis of cleaved phosphorus flakes (20 to 40 nm thick) with low optical density revealed an additional absorption edge at *ca*. 1.95 eV (Figure 3.7A, gray). We attribute this absorption event to a higher energy transition. We will see that these two absorption thresholds—the low-energy band gap transition and the high-energy transition (see band diagram in Figure 3.8B)—are also present in suspensions of 2D phosphorus.

The fractionated suspensions of 2D phosphorus varied significantly in their appearance: in transmitted light, dilute suspensions of thick pieces appeared black or brown while those containing primarily thin pieces appeared red or yellow (Figure 3.7B, inset). These observations were consistent with the corresponding optical absorbance spectra of the suspensions (Figure 3.7B) in which we observed a spectral blue-shift as the flake thickness decreased. There are two notable features in these spectra: a sharply rising absorption within the visible region and a slowly rising absorption that extends into the near-IR. In the following analysis, we will attribute these spectral features to the same high- and low-energy transitions observed in the bulk material.

We sought to quantify these absorption features by using a Tauc analysis. The high-energy transition achieved an excellent fit to a Tauc model when $n = 2$, indicating that this transition is direct and allowed (Figure 3.7C). We assigned the high-energy transition energies to values of 1.95 eV in bulk black phosphorus and 3.15 eV in a suspension

containing primarily monolayers, the thinnest fraction analyzed. The fact that the Tauc models fit our data may suggest that the five experimental challenges outlined above—light scattering, high exciton binding energy, Urbach tail, anisotropic optical properties, and variation in band gap—have a negligible effect on our Tauc analyses of the high-energy transition.

When we applied the direct Tauc model to the low-energy transition, we measured a value of 0.40 eV for bulk black phosphorus (Figure 3.7D, bulk) which is slightly larger than previous estimates of its band gap. The method of sample preparation—grinding bulk black phosphorus with KBr to make a pellet—may have exfoliated some thin sheets, yielding a slightly larger band gap. We found that the band gap is direct and allowed, which is consistent with earlier findings. Because theory consistently predicts that the band gap is direct for all thicknesses of 2D phosphorus, we attempted to apply direct Tauc models (both allowed and forbidden) to the low-energy, band gap transition of 2D phosphorus. For all Tauc models that we explored, we never found a linear region of the Tauc plot, which prevented us from determining the band gap using this method (Figure 3.7D shows the direct, allowed Tauc plot). We attribute the non-linearity of the Tauc plot to several causes. First, the low-energy transition has a lower absorption coefficient than the high-energy transition. The weak absorbance is more likely to be obscured by other optical processes, such as light absorption from Urbach tails or light scattering. Second, the polydispersity of our samples gives a broader distribution of absorption edges for the low-energy absorption than the high-energy absorption. This is because the high-energy transition is less sensitive to flake thickness than the low energy transition, as will become apparent in the following analysis. Because of these experimental challenges in applying a Tauc analysis to the absorption edge

of 2D phosphorus, we introduce a new analytical method that can supplant the Tauc method when analyzing families of bulk and quantum-confined semiconductors.

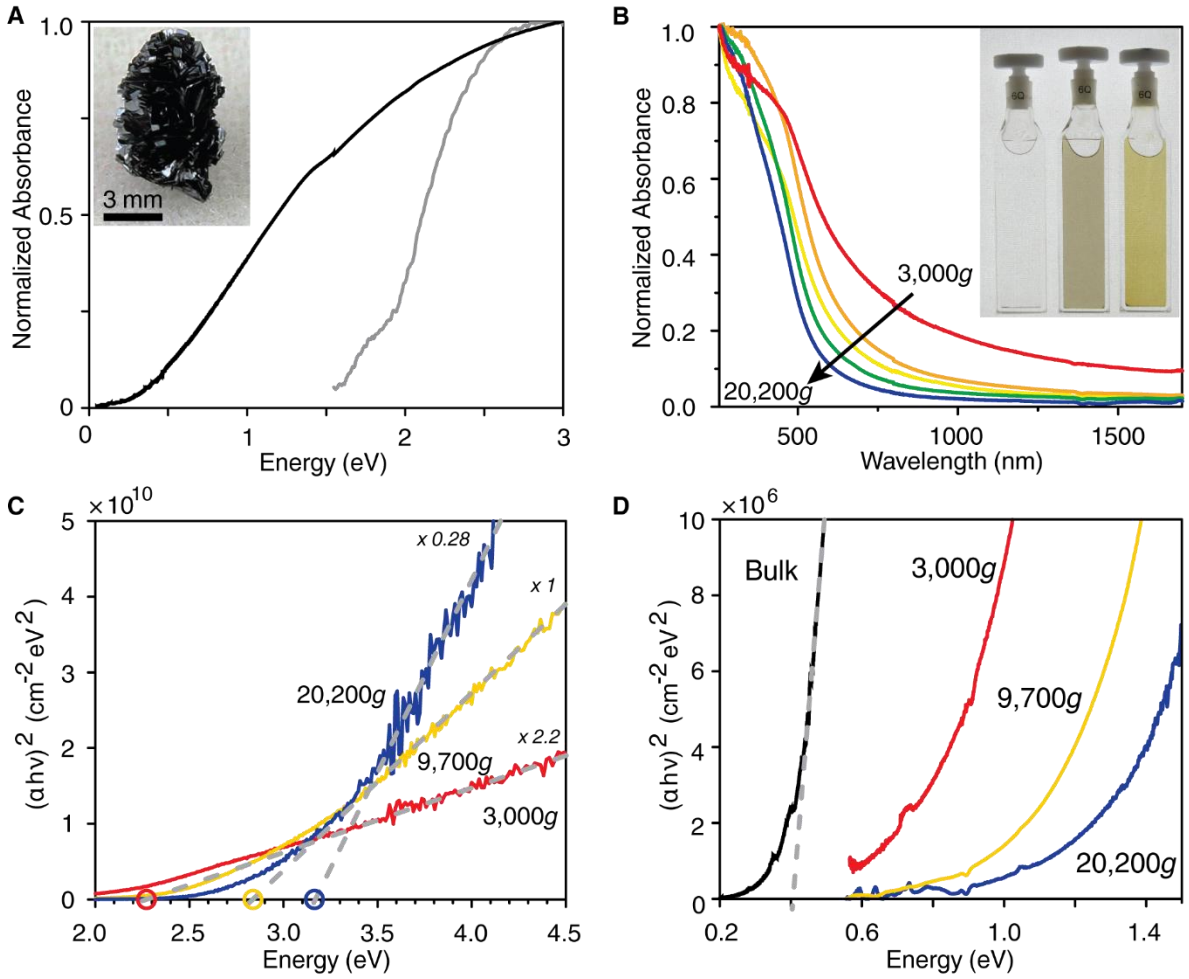

Figure 3.7 | UV-vis-nIR spectroscopy of black phosphorus and its liquid-exfoliated few-layer flakes. (A) Optical absorbance of bulk phosphorus measured at two different optical densities (black = high; gray = low) to reveal two distinct optical transitions (*ca.* 0.4 eV and 1.95 eV). **(B)** Absorbance of 2D phosphorus suspensions that were prepared by fractionation at RCFs near 3.0, 5.9, 9.7, 14.5, and 20.2 thousand *g*'s (red to blue). **(C)** Representative direct Tauc plots used to determine the band-to-band transition. **(D)** Representative direct Tauc plots of the low-energy optical transition. The fit to Tauc models is poor, consistent with the wider range of optical absorption edges that are present in these suspensions.

3.7 A method for determining absorption edges in quantum-confined semiconductors

In our suspensions of 2D phosphorus, sample polydispersity has prevented a straightforward application of Elliot's theory. Indeed, this is an extremely common problem and the liberal application of the Tauc method often causes large errors in the measurement

of band gaps.[56] To circumvent these challenges, we now introduce an alternate method that can be applied to families of bulk and quantum-confined semiconductors such as black and 2D phosphorus. We validated our method using simulated absorption spectra of monodisperse and polydisperse suspensions of 2D phosphorus. Our tests demonstrate that the method is robust: it can determine absorption edges of semiconductors in polydisperse samples and has several advantages over the Tauc method, such as providing an estimate of uncertainty in the absorption edge energy (usually less than a few percent). Crucially, the measurement of an absorption edge (also called the optical gap) also allows us to determine the band gap because the optical and band gaps differ in energy by the exciton binding energy, which is <15 meV in our experiments and therefore negligible.

Our analytical method, which we call the "alpha method", utilizes the similarities that often exist between the electronic structures of quantum-confined semiconductors and the corresponding bulk semiconductor. As an example, numerous studies of black phosphorus and 2D phosphorus show that the band gaps of bulk and 2D phosphorus are always direct with both allowed and forbidden contributions, that their lowest energy transition is always located at the Z-point (in a 3D Brillouin zone), and that the conduction and valence bands are always comprised primarily of p_z orbitals.[17,37,55] In the case of the black phosphorus family, these similarities result in joint densities of states near the absorption edge that are virtually unchanged among members of the family, except for an effective scissoring of the band gap energy. In general, the absorption coefficient increases with increasing quantum confinement,[79] but we hypothesized that the change in the absorption coefficient at the absorption edge (α_{AE}) with confinement would be small and could therefore be treated as being unchanged from the bulk to the monolayer. While this is an oversimplification, we

will show that this introduces only a small error in the determination of optical/band gap energies.

The step-wise analytical method that follows from this hypothesis is illustrated in Figure 3.8A. Using black phosphorus as an example, we exploit the fact that the band gap of the bulk material has been measured many times and has a well-defined value (0.33 ± 0.02 eV). First, we measure the absorption spectrum of the bulk material to determine the value of α_{AE}. Second, we measure the absorption spectra of a series of samples of 2D phosphorus. Finally, we assign the band gap of each sample as the energy at which the absorption coefficient equals α_{AE} (see Figure 3.8A). Note that this process is equating the absorption edge (optical gap) and the fundamental absorption edge (band gap), which is an accurate approximation in our experiments but is not necessarily true in all cases.

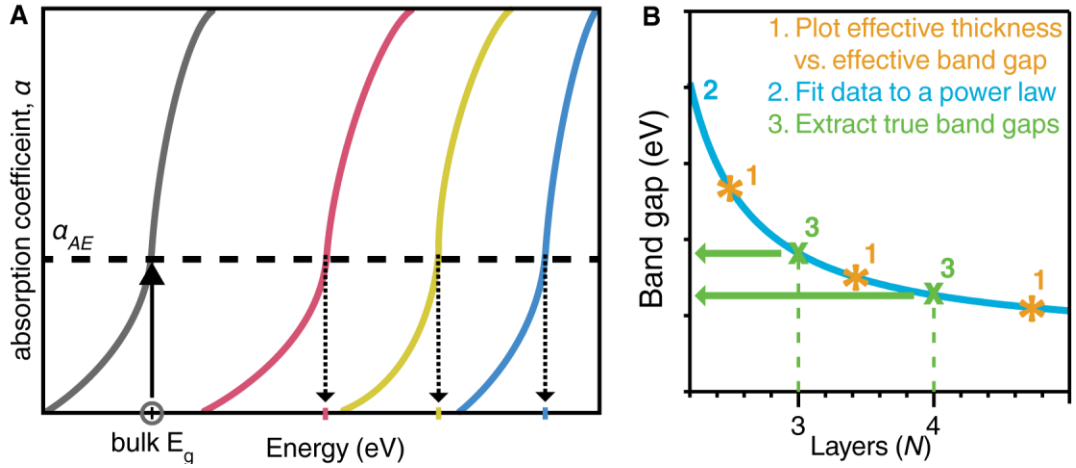

Figure 3.8 | "Alpha method" for band gap determination. (A) The absorption coefficient at the absorption edge (α_{AE}) is measured for the bulk material. We use this α_{AE} to estimate the band gap energy for the quantum-confined 2D flakes. If the 2D flakes are not monodisperse in thickness, the band gap that we have determined is an effective band gap. **(B)** To convert an effective band gap into a real band gap, we (1) plot the effective band gap *vs.* effective thickness for a series of polydisperse samples. Next (2), we fit the data to a power law, see equation [1] in the text. Lastly (3), we use the power law fit to extract the band gap for 2D flakes with real thicknesses.

To validate the alpha method, we used four calculated (G_0W_0) absorption spectra—the spectra that come from bulk, trilayer, bilayer, and monolayer phosphorus.[37] For each

spectrum, we used the reported band gaps, acquired by measuring the energy difference between the conduction and valence bands. We then applied the alpha method to the same data to obtain a second estimate. Across this family of materials, we found that the maximum difference between the methods was 1.85%—an amount that is essentially negligible for most purposes (see Supporting Information for a complete analysis). Although the central assumption—that α_{AE} is the same in all members of the family—is not true, the error due to this assumption is small. This is because α rises steeply near the band gap ($d\alpha/dE$ is large as the energy E approaches the band gap energy E_g). Consequently, even if large differences in α_{AE} exist among the members of a semiconductor family, these produce small differences in the estimated band gap energy.

With this set of results for monodisperse samples in hand, we then tested whether the alpha method could be applied to polydisperse samples. We constructed a series of 24 different artificial mixtures of 2-, 3-, 4-, and 5-layer pieces by taking linear combinations of the calculated absorption spectra of the individual flakes. For these mixtures, Tauc plots were often unusable: the plots either contained several linear regions or did not contain any linear region at all. On the other hand, when we applied the alpha method to each suspension, we always obtained an estimate of an "effective band gap". We found that the effective band gap increased monotonically as the sample distributions shifted from containing a majority of thicker flakes (4- or 5-layers) to a majority of thinner flakes (2- or 3-layers) and that, as expected, the effective band gap always fell between the band gaps of the thinnest (2-layer) and thickest (5-layer) flakes. This example shows that the effective band gap does not necessarily correspond to the band gap of any real material but rather represents the contributions from various-sized flakes in a given mixture. Nevertheless, if this effective

band gap is properly correlated with an "effective thickness" and these band gap-thickness correlations are performed on multiple samples, then it would be possible, at least in principle, to interpolate between these data points to obtain the band gap of 2D materials with real thicknesses (*e.g.*, a bilayer or a trilayer) as illustrated in Figure 3.8B.

The challenge with this approach is that it is not obvious whether the interpolated values are correct. We addressed this challenge by applying a robust mathematical approach to determine an effective thickness for each simulated mixture that, when paired with the effective band gap (alpha method), would lead to correct values of the band gap for real flake thicknesses. We compared our effective thicknesses and effective band gaps to those predicted by a power-law fit of the true thickness and true band gaps for the individual flakes in our simulated mixtures. A power-law fit was selected because, as suggested by numerous calculations, it appears to correctly describe the variation in band gap with flake thickness.[16,28,37,67,80] The power law model yields a band gap for the N_{th} layer as:

$$E_{g_N} = \frac{E_{g_1} - E_{g\infty}}{N^x} + E_{g_\infty} \tag{3-1}$$

where E_{g_1} is the band gap of phosphorene (a monolayer), E_{g_∞} is the band gap of bulk black phosphorus and x is a parameter describing the nature of quantum confinement in the system. Values of x are usually between 0 and 2, where the variation is due in large part to the extent of Coulomb interactions[79,81] and therefore depends on the material geometry (quantum dot *vs*. nanowire *vs*. 2D flake). In the present case, the power law fit is useful because it provides an excellent fit to the calculated G_0W_0 spectra and because it allows us to make direct comparisons of the real band gaps to the effective band gaps at non-real (*i.e.*, non-integer) thicknesses.

In these calculations, we considered the same series of mixtures as above. The skewness of these 24 distributions was systematically varied to capture the full range of likely skews that may be observed experimentally, which, as seen in Figure 3.4, typically have a log-normal shape. For each artificial mixture, we employed the alpha method to determine an effective band gap and we tested five different statistical approaches to extract effective thicknesses. The approaches that we tested were a number-averaged mean (analogous to $\overline{M_n}$ in polymer physics), a weight-averaged mean (analogous to $\overline{M_w}$ in polymer physics), and the mean, median and mode that were derived from a log-normal fit to each distribution. We note that the weight-averaged mean is not equivalent to a weight fraction, which is defined as the weight of material per total weight of solvent and material (see Supporting Information, Section 11, for a complete description of these statistical measures).

From these 24 mixtures comprising realistic skews, we found that the best two averages were the log-normal mean and the number-averaged mean. When paired with the effective thickness as calculated by the log-normal mean, the calculated band gap (power law) was 0.3 ± 1.5% above the effective band gap (alpha method). When paired with the effective thickness from the number-averaged mean, the calculated band gap was 0.2 ± 2.6% below the effective band gap. The next two closest measures of thickness were the log-normal median (2.3 ± 1.6% above the effective band gap) and the weight-averaged mean (3.6 ± 3.5% below the effective band gap). In general, we found that the extent to which these statistical measures over- or underestimated the true bandgap varied systematically with the skewness of the distribution. For distributions with low skewness, the band gap was systematically overestimated by about 1.5%, while distributions with high skewness, such as those obtained in our experiments (Figure 3.4), the band gap was systematically

underestimated by about 1%, although there were a small number of outliers with errors up to 6%. A table and graphs that summarize these calculations are provided in Appendix 2.

The central conclusion from these simulations is that the alpha method, when combined with an appropriate flake thickness, yields band gaps that are reliable. As noted above, the maximum difference between the reported band gap and the alpha band gap was 1.85%. In addition, the maximum error in using either the number-averaged mean or the log-normal mean was 6%. We emphasize that these are maximum errors and the typical errors will be less. However, these estimates of error only describe those errors due to data analysis and do not include systematic or non-systematic errors that are inherent to the experimental measurements.

3.8 Thickness-dependent absorption edges of black and 2D phosphorus

In this section, we compile the results of our experimental determination of the absorption edge of 2D phosphorus. As we described above, the absorption edge probed by our experiments (the optical gap) is indistinguishable from the band gap because the exciton binding energy is extremely small (8 to 15 meV) and exciton fission is rapid. When discussing the energy associated with a particular transition, we will use "absorption edge", "optical gap" and "band gap" interchangeably.

From the absorption spectrum of bulk black phosphorus, we measured α_{AE} to be 0.24 μm^{-1}, which is equivalent to a light penetration depth of 4 μm. (We note that the absorption coefficient determined by us is similar to the one reported previously,[73] $\alpha_{AE} = 0.17\ \mu m^{-1}$.) We then used this absorption coefficient to determine the effective band gap of each 2D phosphorus suspension. The thickness distribution of each phosphorus suspension was analyzed by TEM and this distribution was converted into effective thicknesses using the

four most accurate statistical averages (log-normal mean, number-averaged mean, log-normal median and weight-averaged mean). For each of these averages, a power law (Equation 1) was fit to the thickness-band gap data set. The same process was repeated for the high-energy transition, with the only difference being that the band-to-band transition energy was taken from a Tauc analysis rather than the alpha method (see justification, above).

Figure 3.9 summarizes our most important findings: the experimental quantification of the band-to-band transitions of 2D phosphorus. Figure 3.9a displays the band gaps (orange curves, "low energy") and high-energy transitions (blue curves, "high energy"). The low energy and high energy transitions show the most probable values (dark orange, dark blue) and a maximum likely range of values (light orange, light blue). The four curves that define the most probable and maximum likely boundaries come from the power-law fits to the four types of effective thicknesses, with the most probable boundaries defined by the log-normal and number-averaged means and with the maximum likely boundaries defined by the log-normal median and weight-averaged mean. The average exponent x of the power law (Equation 1) calculated from our data is 0.81. Earlier theoretical predictions suggest that the value may between 0.7 and 1.0, with an average value of 0.80 ± 0.11 reported across six studies.[16,28,37,66,82,83]

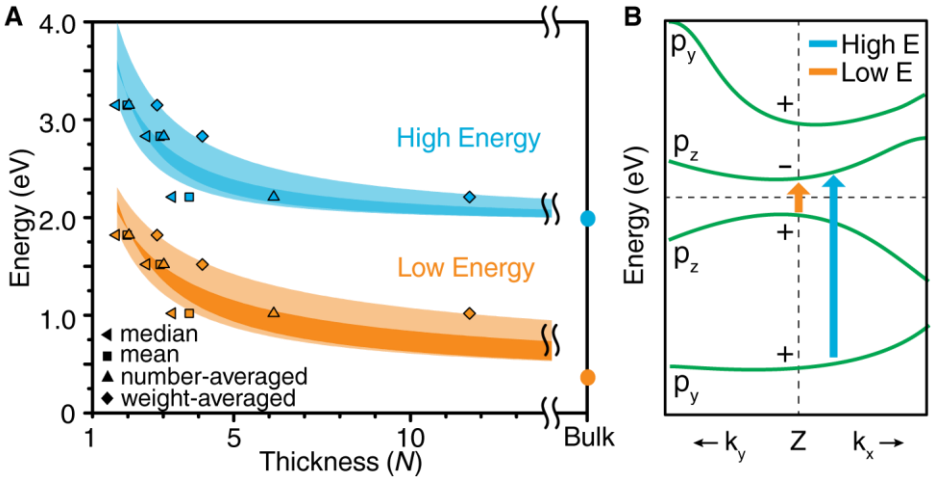

Figure 3.9 | Experimentally determined band gap (low energy) and high-energy transitions of 2D and bulk black phosphorus. (A) The band gap (orange, "low energy") and high-energy band-to-band (blue, "high energy") transitions are plotted with respect to flake thickness. The dark blue and dark orange regions define the most probable energy values and the light orange and light blue define the maximum likely range. **(B)** Band structure of bulk black phosphorus at the Z point of the first Brillouin zone. The orange arrow represents the band gap transition (VB → CB) while the blue arrow represents the high energy transition (VB-1 → CB). The plot also shows the parity of bands near the Z point (+, -) and the nature of orbitals that primarily contribute to each band (p_y, p_z). The valence bands come from angle-resolved photoelectron spectroscopy measurements[18,85] and the conduction bands come from calculations.[18,84] The horizontal dashed line shows the Fermi level.

Our measurements provide direct experimental evidence that the band gap and the high-energy transitions undergo extreme changes as flakes approach monolayer thickness. The band gap can be tuned from 0.33 ± 0.02 eV in bulk to 1.88 ± 0.24 eV in bilayers. The higher energy transition can be tuned from 1.95 ± 0.06 eV in bulk to 3.23 ± 0.39 eV in bilayers. These ranges surpass all known 2D materials and are as large as the most tunable quantum dots. The most important band gaps and high-energy transitions are reported in Figure 3.9a and Tables 3.1 and 3.2. Our estimates of error (*e.g.*, ± 0.24 eV for the band gap of bilayers) are the same as the maximum ranges in Figure 9A (light blue and light orange regions). These estimates of error do not include the 1.85% maximum error between the alpha method and reported gaps or experimental error. We have not extrapolated our power law to a monolayer thickness because of the errors associated with such an extrapolation: the

smallest effective thickness of our samples was 1.71 layers and it has also been suggested that a phosphorene monolayer does not lie on the power-law curve.[37]

Table 3.2 | Electronic band-to-band transitions in 2D phosphorus.

Layers	Band gap (eV)	High-energy (eV)
2	1.88 ± 0.24	3.23 ± 0.39
3	1.43 ± 0.28	2.68 ± 0.32
4	1.19 ± 0.28	2.44 ± 0.27
5	1.04 ± 0.27	2.31 ± 0.23
6	0.94 ± 0.26	2.23 ± 0.20
7	0.87 ± 0.26	2.18 ± 0.17
8	0.81 ± 0.25	2.14 ± 0.16
9	0.77 ± 0.24	2.11 ± 0.14
10	0.73 ± 0.23	2.09 ± 0.13
15	0.62 ± 0.20	2.03 ± 0.09
20	0.56 ± 0.18	2.01 ± 0.07
∞	0.33 ± 0.02	1.95 ± 0.06

In order to place these measurements in context, we compare our band gaps to prior optical gap measurements (see Table 3.1). We focus, in particular, on the optical gaps of Yang[61] and Zhang[63] because these studies surveyed the largest range of flake thicknesses and because these studies are the only two that are in agreement. When the optical gap and band gap are measured in the same dielectric environment, the band gap is expected to be larger than the optical gap by an amount equal to the exciton binding energy. This relationship only holds true for measurements that are performed in media with the same dielectric constant, since the exciton binding energy, optical gap, and band gap all depend on the medium's dielectric constant. This sensitivity to the medium's dielectric constant disappears as flakes become thicker and in the limit of thick flakes, the optical gaps and band gaps converge because the exciton binding energy is 8 meV in bulk black phosphorus.[17] To see whether the electrical gap and optical gap do converge, we focus on four- and five-layer thicknesses,

which are the thickest flakes that have been studied in the photoluminescence (optical gap) experiments. The four-layer optical gap was reported as 0.86 eV and the five-layer optical gap was 0.80 eV. We measured a four-layer band gap as 1.19 ± 0.28 eV and a five-layer band gap as 1.04 ± 0.27 eV. It is apparent that the difference between the band gap in our experiments and the optical gap in the photoluminescence experiments is decreasing (0.33 eV for four-layer, 0.24 eV for five-layer), as expected. Although the extent to which we can make comparisons is limited by the available data, it appears that there is reasonable agreement between our measurements and some previous photoluminescence measurements.

Next, we turn our attention to the high-energy band-to-band transition. Although this transition has been neglected in earlier studies, we suggest two reasons that understanding this transition will be important. First, the changes in the color of 2D phosphorus with decreasing thickness (Figure 3.7B, inset) are due, in large part, to changes in the high-energy band-to-band transition rather than the band gap. As a result, the ability to modulate the material's color requires an understanding of the high energy transition. Second, the high-energy transition has a substantially larger absorption coefficient (3.3 μm^{-1} at 3 eV) and a smaller light penetration depth (300 nm at 3 eV) than the band gap transition. This feature will be important in designing 2D phosphorus for applications that require high light absorption. From our Tauc analyses of the high-energy transition, we found that the bulk material has a transition energy of 1.95 eV, increasing up to 3.23 ± 0.39 eV in bilayers (Figure 3.9B, blue). From these measurements, it is also apparent that the high-energy transition is less sensitive to flake thickness as compared to the low-energy band gap transition: from bulk to bilayers, the band gap changes by 1.55 eV while the high-energy transition changes by 1.28 eV. This difference in sensitivity may be why Tauc plots appear

to work well for the high-energy transition while they do not work for the low-energy transition.

Finally, we describe four key observations that allow us to determine the nature of the high-energy transition. First, the Tauc plots show that there is a linear relationship between $(\alpha h\nu)^2$ and the photon energy (Figure 3.7C), which is characteristic of a direct, allowed transition. Second, the high-energy transition is sensitive to material thickness, varying from 1.95 eV in bulk to 3.23 eV in bilayers. These changes follow a power law and therefore appear to be driven by quantum confinement.[79,81] As such, it is plausible that the high-energy transition occurs at or near the Z-point of the Brillouin zone, since Z is perpendicular to the plane of flakes. In examining the band structure near the Z-point (Figure 3.9B), it is clear that there are two likely candidates for a direct optical transition at or near the Z-point: a transition between the valence band (VB) and the second lowest unoccupied band (CB+1) or between the second highest occupied band (VB-1) and the conduction band (CB). Third, the energy of the transition for the bulk material (1.95 eV) can be compared to previous measurements of the band structure of bulk black phosphorus.[15,84] From these comparisons, it is clear that only the VB-1 → CB transition provides the right energy. Fourth, the absorption coefficient of the high-energy optical transition is considerably larger (about ten times larger) than that of the low-energy optical transition. This observation is consistent with an assignment of the optical transition to VB-1 → CB: this transition is direct, allowed in the *c*-direction, and leads to a change in parity (+ → -).[17] These selection rules favor strong optical absorption. Figure 3.9B summarizes this assignment and also identifies the low-energy transition.

Conclusions

In this work, we have described our method[42] for preparing and isolating large quantities of monolayers, bilayers, and few-layer flakes and we identified benzonitrile as the best solvent of those we surveyed. Although shear mixing provides insufficient force for exfoliating high-quality samples of black phosphorus, it is possible to combine shear mixing and sonication to exfoliate black phosphorus at the 10-gram scale. Using XPS, TEM, and multi-slice TEM simulations, we observed that monolayers, bilayers, and few-layer flakes of 2D phosphorus are crystalline and unoxidized. Our work also demonstrates a rapid and simple TEM-based method for measuring the thickness of 2D phosphorus.

Using a method that we introduced here for quantifying the optical absorbance spectra, we showed that it is possible to measure the optical gap of polydisperse 2D phosphorus samples and to extract an accurate estimate of the material's band gap. Our results may go some ways towards resolving the long-standing question of how the band gap of black phosphorus changes with thickness. We expect that the methodology presented here will be broadly applicable as it provides a robust approach for optical or band gap measurement in mixtures of complex semiconductors and can extract useful information even when the Tauc analysis fails.

Of central importance for future applications of 2D phosphorus, we have performed the first accurate measurements of the thickness-dependent band gap. Although there are a large number of theoretical predictions, these predictions have not yet been tested, until now, by careful experiments. We found that the band gap can be tuned from 0.33 ± 0.02 eV in bulk black phosphorus to 1.88 ± 0.24 eV in bilayer phosphorus. It is important to note that the band gap will likely depend on the surrounding medium but, in any case, the range of

optical transitions for black and 2D phosphorus is relatively large compared to that of other quantum-confined nanomaterials such as MoS_2 (1.2 to 1.9 eV),[9,85] CdSe quantum dots (2.0 to 3.0 eV)[86] or PbSe quantum dots (0.27 to 1.5 eV).[11–13,86] This suggests that the electronic coupling between layers is stronger than in most other van der Waals layered solids but a complete description of this unusual property is still needed. Looking toward future applications of this material, we suggest that the astounding range of band gaps that can be achieved by 2D phosphorus, with tunable absorption thresholds from the infrared to the visible, will provide a new material platform for the design and development of solar cells, photodetectors, photocatalysts, transistors, and batteries.

REFERENCES

1. Thompson, B. C.; Fréchet, J. M. J. Polymer-Fullerene Composite Solar Cells. *Angew. Chem. Int. Ed.*, **2008**, *47*, 58–77.

2. Talapin, D. V; Murray, C. B. PbSe Nanocrystal Solids for N- and P-Channel Thin Film Field-Effect Transistors. *Science* **2005**, *310*, 86–89.

3. Wu, J.; Agrawal, M.; Becerril, H. A.; Bao, Z.; Liu, Z.; Chen, Y.; Peumans, P. Organic Light-Emitting Diodes on Solution-Processed Graphene Transparent Electrodes. *ACS Nano* **2010**, *4*, 43–48.

4. Rossetti, R.; Nakahara, S.; Brus, L. E. Quantum Size Effects in the Redox Potentials, Resonance Raman Spectra, and Electronic Spectra of CdS Crystallites in Aqueous Solution. *J. Chem. Phys.* **1983**, *79*, 1086.

5. Brus, L. Electronic Wave Functions in Semiconductor Clusters: Experiment and Theory. *J. Phys. Chem.* **1986**, *90*, 2555–2560.

6. Rossetti, R.; Hull, R.; Gibson, J. M.; Brus, L. E. Excited Electronic States and Optical Spectra of ZnS and CdS Crystallites in the ~15 to 50 Å Size Range: Evolution from Molecular to Bulk Semiconducting Properties. *J. Chem. Phys.* **1985**, *82*, 552.

7. Dannhauser, T.; Johansson, K.; Whitten, D. Photophysics of Quantized Colloidal Semiconductors. Dramatic Luminescence Enhancement by Binding of Simple Amines. **1986**, *90*, 6074–6076.

8. Novoselov, K. S.; Jiang, D.; Schedin, F.; Booth, T. J.; Khotkevich, V. V; Morozov, S. V; Geim, A. K. Two-Dimensional Atomic Crystals. *Proc. Natl. Acad. Sci. U. S. A.* **2005**, *102*, 10451–10453.

9. Mak, K. F.; Lee, C.; Hone, J.; Shan, J.; Heinz, T. F. Atomically Thin MoS_2: A New Direct-Gap Semiconductor. *Phys. Rev. Lett.* **2010**, *105*, 136805.

10. Yun, W. S.; Han, S.; Hong, S. C.; Kim, I. G.; Lee, J. Thickness and Strain Effects on Electronic Structures of Transition Metal Dichalcogenides: 2H-MX_2 Semiconductors (M = Mo, W; X = S, Se, Te). *Phys. Rev. B*, **2012**, *85*, 033305.

11. Gorer, S.; Albu-Yaron, A.; Hodes, G. Quantum Size Effects in Chemically Deposited, Nanocrystalline Lead Selenide Films. J. Phys. Chem. 1995, 99, 16442–16448.

12. Kang, I.; Wise, F. W. Electronic Structure and Optical Properties of PbS and PbSe Quantum Dots. J. Opt. Soc. Am. B, 1997, 14, 1632.

13. Pietryga, J. M.; Schaller, R. D.; Werder, D.; Stewart, M. H.; Klimov, V. I.; Hollingsworth, J. A. Pushing the Band Gap Envelope: Mid-Infrared Emitting Colloidal PbSe Quantum Dots. J. Am. Chem. Soc. 2004, 126, 11752–11753.

14. Bridgman, P. W. Two New Modifications of Phosphorus. J. Am. Chem. Soc. 1914, 36, 1344–1363.

15. Li, L.; Yu, Y.; Ye, G. J.; Ge, Q.; Ou, X.; Wu, H.; Feng, D.; Chen, X. H.; Zhang, Y. Black Phosphorus Field-Effect Transistors. Nat. Nano. 2014, 9, 372–377.

16. Liu, H.; Neal, A. T.; Zhu, Z.; Luo, Z.; Xu, X.; Tománek, D.; Ye, P. D. Phosphorene: An Unexplored 2D Semiconductor with a High Hole Mobility. ACS Nano 2014, 8, 4033–4041.

17. Morita, A. Semiconducting Black Phosphorus. Appl. Phys. A 1986, 39, 227–242.

18. Li, L.; Yu, Y.; Ye, G. J.; Ge, Q.; Ou, X.; Wu, H.; Feng, D.; Chen, X. H.; Zhang, Y. Black Phosphorus Field-Effect Transistors. Nat. Nano. 2014, 9, 372–377.

19. Koenig, S. P.; Doganov, R. A.; Schmidt, H.; Castro Neto, A. H.; Özyilmaz, B. Electric Field Effect in Ultrathin Black Phosphorus. Appl. Phys. Lett. 2014, 104, 103106.

20. Buscema, M.; Groenendijk, D. J.; Steele, G. A.; van der Zant, H. S. J. Photovoltaic Effect in Few-Layer Black Phosphorus PN Junctions Defined by Local Electrostatic Gating. Nat. Comm. 2014, 5, 4651.

21. Deng, Y.; Luo, Z.; Conrad, N. J.; Liu, H.; Gong, Y.; Najmaei, S.; Ajayan, P. M.; Lou, J.; Xu, X.; Ye, P. D. Black Phosphorus-Monolayer MoS2 van Der Waals Heterojunction P-N Diode. ACS Nano 2014, 8, 8292-8298.

22. Engel, M.; Steiner, M.; Avouris, P. A Black Phosphorus Photo-Detector for Multispectral, High-Resolution Imaging. Nano Lett. 2014, 14, 6414–6417.

23. Low, T.; Engel, M.; Steiner, M.; Avouris, P. Origin of Photoresponse in Black Phosphorus Phototransistors. Phys. Rev. B 2014, 90, 081408.

24. Park, C.-M.; Sohn, H.-J. Black Phosphorus and Its Composite for Lithium Rechargeable Batteries. Adv. Mater. 2007, 19, 2465–2468.

25. Cunningham, G.; Lotya, M.; Cucinotta, C. S.; Sanvito, S.; Bergin, S. D.; Menzel, R.; Shaffer, M. S. P.; Coleman, J. N. Solvent Exfoliation of Transition Metal Dichalcogenides: Dispersibility of Exfoliated Nanosheets Varies Only Weakly Between Compounds. ACS Nano 2012, 6, 3468–3480.

26. Fei, R.; Yang, L. Strain-Engineering the Anisotropic Electrical Conductance of Few-Layer Black Phosphorus. Nano Lett. 2014, 14, 2884–2889.

27. Low, T.; Rodin, A. S.; Carvalho, A.; Jiang, Y.; Wang, H.; Xia, F.; Neto, A. H. C. Tunable Optical Properties of Multilayers Black Phosphorus. Phys. Rev. B 2014, 90, 075434.

28. Castellanos-Gomez, A.; Vicarelli, L.; Prada, E.; Island, J. O.; Narasimha-Acharya, K. L.; Blanter, S. I.; Groenendijk, D. J.; Buscema, M.; Steele, G. A; Alvarez, J. V; et al. Isolation and Characterization of Few-Layer Black Phosphorus. 2D Mater. 2014, 1, 025001.

29. Jiang, J.-W.; Park, H. S. Mechanical Properties of Single-Layer Black Phosphorus. J. Phys. D. Appl. Phys. 2014, 47, 385304.

30. Kou, L.; Frauenheim, T.; Chen, C. Phosphorene as a Superior Gas Sensor: Selective Adsorption and Distinct I - V Response. J. Phys. Chem. Lett. 2014, 5, 2675–2681.

31. Zhang, R.; Li, B.; Yang, J. First-Principles Study of the Interactions of Electron Donor and Acceptor Molecules with Phosphorene. arXiv 2014, 1409.7190.

32. Favron, A.; Gaufrès, E.; Fossard, F.; Phaneuf-L'Heureux, A.-L.; Tang, N. Y.-W.; Lévesque, P. L.; Loiseau, A.; Leonelli, R.; Francoeur, S.; Martel, R. Photooxidation and Quantum Confinement Effects in Exfoliated Black Phosphorus. Nat. Mater. 2015, 826–832.

33. Ziletti, A.; Carvalho, A.; Campbell, D. K.; Coker, D. F.; Neto, A. H. C. Oxygen Defects in Phosphorene. Phys. Rev. Lett. 2014, 046801.

34. Carvalho, A.; Rodin, A. S.; Neto, A. H. C. Phosphorene Nanoribbons. EPL-Europhys. Lett. 2014, 108, 47005.

35. Xie, J.; Si, M. S.; Yang, D. Z.; Zhang, Z. Y.; Xue, D. S. A Theoretical Study of Blue Phosphorene Nanoribbons Based on First-Principles Calculations. J. Appl. Phys. 2014, 116, 073704.

36. Guan, J.; Zhu, Z.; Tomanek, D. High Stability of Faceted Nanotubes and Fullerenes of Multi-Phase Layered Phosphorus: A Computational Study. Phys. Rev. Lett. 2014, 113, 226801.

37. Tran, V.; Soklaski, R.; Liang, Y.; Yang, L. Layer-Controlled Band Gap and Anisotropic Excitons in Few-Layer Black Phosphorus. Phys. Rev. B 2014, 89, 235319.

38. Xia, F.; Wang, H.; Jia, Y. Rediscovering Black Phosphorus as an Anisotropic Layered Material for Optoelectronics and Electronics. Nat. Commun. 2014, 5, 4458.

39. Buscema, M.; Groenendijk, D. J.; Blanter, S. I.; Steele, G. A.; van der Zant, H. S. J.; Castellanos-Gomez, A. Fast and Broadband Photoresponse of Few-Layer Black Phosphorus Field-Effect Transistors. Nano Lett. 2014, 14, 3347–3352.

40. Hernandez, Y.; Nicolosi, V.; Lotya, M.; Blighe, F. M.; Sun, Z.; De, S.; McGovern, I. T.; Holland, B.; Byrne, M.; Gun'Ko, Y. K.; et al. High-Yield Production of Graphene by Liquid-Phase Exfoliation of Graphite. Nat. Nano. 2008, 3, 563–568.

41. Coleman, J. N.; Lotya, M.; O'Neill, A.; Bergin, S. D.; King, P. J.; Khan, U.; Young, K.; Gaucher, A.; De, S.; Smith, R. J.; et al. Two-Dimensional Nanosheets Produced by Liquid Exfoliation of Layered Materials. Science 2011, 331, 568–571.

42. Warren, S. C.; Woomer, A. H.; Wells, R. A.; Farnsworth, T. W. Two Dimensional Materials Produced by the Liquid Exfoliation of Black Phosphorus. 62/031,184, 2014.

43. Brent, J. R.; Savjani, N.; Lewis, E. A.; Haigh, S. J.; Lewis, D. J.; O'Brien, P. Production of Few-Layer Phosphorene by Liquid Exfoliation of Black Phosphorus. Chem. Commun. 2014, 50, 13338–13341.

44. Yasaei, P.; Kumar, B.; Foroozan, T.; Wang, C.; Asadi, M.; Tuschel, D.; Indacochea, J. E.; Klie, R. F.; Salehi-Khojin, A. High-Quality Black Phosphorus Atomic Layers by Liquid-Phase Exfoliation. Adv. Mater. 2015, 27, 1887–1892.

45. Kang, J.; Wood, J. D.; Wells, S. A.; Lee, J.-H.; Liu, X.; Chen, K.-S.; Hersam, M. C. Solvent Exfoliation of Electronic-Grade, Two-Dimensional Black Phosphorus. ACS Nano 2015, 9, 3596–3604.

46. Köpf, M.; Eckstein, N.; Pfister, D.; Grotz, C.; Krüger, I.; Greiwe, M.; Hansen, T.; Kohlmann, H.; Nilges, T. Access and In Situ Growth of Phosphorene-Precursor Black Phosphorus. J. Cryst. Growth 2014, 405, 6–10.

47. Stadelmann, P. JEMS - EMS Java Version http://cimewww.epfl.ch/people/stadelmann/jemsWebSite/jems.html.

48. Ci, L.; Song, L.; Jin, C.; Jariwala, D.; Wu, D.; Li, Y.; Srivastava, A.; Wang, Z. F.; Storr, K.; Balicas, L.; et al. Atomic Layers of Hybridized Boron Nitride and Graphene Domains. Nat. Mater. 2010, 9, 430–435.

49. Gass, M. H.; Bangert, U.; Bleloch, A. L.; Wang, P.; Nair, R. R.; Geim, A. K. Free-Standing Graphene at Atomic Resolution. Nat. Nano. 2008, 3, 676–681.

50. Favron, A.; Gaufrès, E.; Fossard, F.; Lévesque, P. L.; Heureux, P.; Tang, N. Y.; Loiseau, A.; Leonelli, R. Exfoliating Black Phosphorus down to the Monolayer: Photo-Induced Oxidation and Electronic Confinement Effects. arXiv 2014, 1408.0345.

51. Goodman, N. B.; Ley, L.; Bullett, D. W. Valence-Band Structures of Phosphorus Allotropes. Phys. Rev. B 1983, 27, 7440–7450.

52. Moulder, J. F.; Stickle, W. F.; Sobol, P. E.; Bomben, K. D. Handbook of X-Ray Photoelectron Spectroscopy; 1979; Vol. 3.

53. Wood, J. D.; Wells, S. A.; Jariwala, D.; Chen, K.-S.; Cho, E.; Sangwan, V. K.; Liu, X.; Lauhon, L. J.; Marks, T. J.; Hersam, M. C. Effective Passivation of Exfoliated Black Phosphorus Transistors against Ambient Degradation. Nano Lett. 2014, 14, 6964–6970.

54. Paton, K. R.; Varrla, E.; Backes, C.; Smith, R. J.; Khan, U.; O'Neill, A.; Boland, C.; Lotya, M.; Istrate, O. M.; King, P.; et al. Scalable Production of Large Quantities of Defect-Free Few-Layer Graphene by Shear Exfoliation in Liquids. Nat. Mater. 2014, 13, 624–630.

55. Paton, K. Personal Communication.

56. Takao, Y.; Asahina, H.; Morita, A. Electronic Structure of Black Phosphorus in Tight Binding Approach. J. Phys. Soc. Jpn. 1981, 50, 3362–3369.

57. Klingshirn, C. Semiconductor Optics; 2007.

58. Degoli, E.; Cantele, G.; Luppi, E.; Magri, R.; Ninno, D.; Bisi, O.; Ossicini, S. Ab Initio Structural and Electronic Properties of Hydrogenated Silicon Nanoclusters in the Ground and Excited State. Phys. Rev. B 2004, 69, 155411.

59. Choi, J. H.; Strano, M. S. Solvatochromism in Single-Walled Carbon Nanotubes. Appl. Phys. Lett. 2007, 90.

60. Jackson, W. B.; Kelso, S. M.; Tsai, C. C.; Allen, J. W.; Oh, S.-J. Energy Dependence of the Optical Matrix Element in Hydrogenated Amorphous and Crystalline Silicon. Phys. Rev. B 1985, 31, 5187–5198.

61. Mott, N. F. Electronic Processes in Non-Crystalline Materials; Davis, E. A., Ed.; 2nd Ed.; Clarendon Press: Oxford, 1979.

62. Yang, J.; Xu, R.; Pei, J.; Myint, Y. W.; Wang, F.; Wang, Z.; Yu, Z.; Lu, Y. Unambiguous Identification of Monolayer Phosphorene by Phase-Shifting Interferometry. arXiv 2014, 1412.6701.

63. Wang, X.; Jones, A. M.; Seyler, K. L.; Tran, V.; Jia, Y.; Wang, H.; Yang, L.; Xu, X.; Xia, F. Highly Anisotropic and Robust Excitons in Monolayer Black Phosphorus. Nat. Nano. 2014, 10, 517-521.

64. Zhang, S.; Yang, J.; Xu, R.; Wang, F. Extraordinary Photoluminescence and Strong Temperature/Angle-Dependent Raman Responses in Few-Layer Phosphorene. ACS Nano 2014, 8, 9590–9596.

65. Das, S.; Zhang, W.; Demarteau, M.; Hoffmann, A.; Dubey, M.; Roelofs, A. Tunable Transport Gap in Phosphorene. Nano Lett. 2014, 14, 5733–5739.

66. Liang, L.; Wang, J.; Lin, W.; Sumpter, B. G.; Meunier, V.; Pan, M. Electronic Bandgap and Edge Reconstruction in Phosphorene Materials. Nano Lett. 2014, 14, 6400–6406.

67. Rudenko, A. N.; Katsnelson, M. I. Quasiparticle Band Structure and Tight-Binding Model for Single- and Bilayer Black Phosphorus. Phys. Rev. B - Condens. Matter Mater. Phys. 2014, 89, 1–5.

68. Qiao, J.; Kong, X.; Hu, Z.-X.; Yang, F.; Ji, W. High-Mobility Transport Anisotropy and Linear Dichroism in Few-Layer Black Phosphorus. Nat. Commun. 2014, 5, 4475.

69. Elliott, R. Intensity of Optical Absorption by Excitons. Phys. Rev. 1957, 108, 1384–1389.

70. Wannier, G. The Structure of Electronic Excitation Levels in Insulating Crystals. Phys. Rev. 1937, 52, 191–197.

71. Tauc, J. Optical Properties and Electronic Structure of Amorphous Ge and Si. Mater. Res. Bull. 1968, 3, 37–46.

72. Baba, M.; Nakamura, Y.; Shibata, K.; Morita, A. Photoconduction of Black Phosphorus in the Infrared Region. Jpn. J. Appl. Phys. 1991, 30, L1178.

73. Keyes, R. The Electrical Properties of Black Phosphorus. Phys. Rev. 1953, 92, 580

74. Warschauer, D. Electrical and Optical Properties of Crystalline Black Phosphorus. J. Appl. Phys. 1963, 34, 1853–1860.

75. Maruyama, Y.; Suzuki, S.; Kobayashi, K.; Tanuma, S. Synthesis and Some Properties of Black Phosphorus Single Crystals. Physica B+C, 1981, 105, 99–102.

76. Irotani, I. S. H.; Physics, S. Growth of Large Single Crystals of Black Phosphorus at High Pressures and Temperatures, and Its Electrical Properties. Mol. Cryst. Liq. Cryst. 1982, 86, 203–211.

77. Akahama, Y.; Endo, S.; Narita, S. I. Electrical Properties of Black Phosphorus Single Crystals. J. Phys. Soc. Japan 1983, 52, 2148–2155.

78. Hecht, E.; Ganesan, A. R. Optics; 4th Ed.; Dorling Kindersley, 2008.

79. Urbach, F. The Long-Wavelength Edge of Photographic Sensitivity and of the Electronic Absorption of Solids. Phys. Rev. 1953, 92, 1324.

80. Brus, L. E. Electron–Electron and Electron-Hole Interactions in Small Semiconductor Crystallites: The Size Dependence of the Lowest Excited Electronic State. J. Chem. Phys. 1984, 80, 4403.

81. Rudenko, A. N.; Katsnelson, M. I. Quasiparticle Band Structure and Tight-Binding Model for Single- and Bilayer Black Phosphorus. Phys. Rev. B 2014, 89, 201408.

82. Perebeinos, V.; Tersoff, J.; Avouris, P. Scaling of Excitons in Carbon Nanotubes. Phys. Rev. Lett. 2004, 92, 257402–1.

83. Qiao, J.; Kong, X.; Hu, Z.-X.; Yang, F.; Ji, W. High-Mobility Transport Anisotropy and Linear Dichroism in Few-Layer Black Phosphorus. Nat Commun 2014, 5.

84. Wang, V.; Kawazoe, Y.; Geng, W. T. Native Point Defects in Few-Layer Phosphorene. Phys. Rev. B 2015, 91, 45433.

85. Yuan, H.; Liu, X.; Afshinmanesh, F.; Li, W.; Xu, G.; Sun, J.; Lian, B.; Ye, G.; Hikita, Y.; Shen, Z.; et al. Polarization-sensitive broadband photodetector using a black phosphorus vertical p–n junction. Nat. Nano. 2015, AOP.

86. Splendiani, A.; Sun, L.; Zhang, Y.; Li, T.; Kim, J.; Chim, C.-Y.; Galli, G.; Wang, F. Emerging Photoluminescence in Monolayer MoS2. Nano Lett. 2010, 10, 1271–1275.

87. Murray, C. B.; Norris, D.; Bawendi, M. G. Synthesis and Characterization of Nearly Monodisperse CdE (E= S, Se, Te) Semiconductor Nanocrystallites. J. Am. Chem. Soc. 1993, 115, 8706–8715.

.

CHAPTER FOUR – ENGINEERED 3D SEMICONDUCTORS WITH QUANTUM-CONFINED 2D PROPERTIES

Tyler W. Farnsworth, Adam H. Woomer, Jon R. Thompson, Scott C. Warren

Quantum confinement has resulted in some of the most exciting properties within chemistry, materials science, and physics. The size-dependent electronic structure of quantum confined materials have made them candidates for a wide variety of applications, from electronic displays[1-2] to photovoltaics[3-4] to medical imaging[5-6] to sensors[7-8]. Many applications, especially those in optics and electronics, require that quantum-confined building blocks retain their properties, even when in an aggregated, electronically conductive state. This requirement has led to numerous efforts in, for example, quantum dot solids, to identify methods of reducing the distance between dots while maintaining their quantum confined properties[9-13]. With the relatively recent emergence of 2D quantum-confined semiconductors, a similar challenge has now emerged: is it possible to control the separation between adjacent 2D flakes to produce highly conductive 3D solids that retain the quantum-confined optoelectronic properties of their 2D building blocks?

The emergence of quantum confinement in 2D semiconductors has been heralded as a significant advance towards enabling fascinating new materials. One of the outstanding examples of such quantum confined semiconductors is 2D MoS_2, which transitions to a direct band gap material with strong photoluminescence only at monolayer thickness[14-15]. Another exciting advance has been the development of quantum confined 2D phosphorus, which has a band gap that can be tuned from 0.3 eV (bulk) to 2.1 eV (monolayer)[16]. Numerous studies have examined the optoelectronic properties of 2D materials when they are restacked into

solids. Such studies consistently show that the quantum confined properties are lost when two 2D solids are stacked on top of each other, regardless of the orientation between the two flakes[17].

Here we introduce a strategy to maintain quantum confinement in highly conductive 3D solids comprised of 2D materials. Our strategy relies on the entrapment of a monolayer of small molecules between adjacent layers, which lead to a small (ca. 4 Å) increase in interlayer spacing between adjacent flakes. This distance is large enough to maintain full quantum confinement—as judged by, for example, the photoluminescence of our 3D films of MoS_2—but is small enough to achieve among the highest electrical conductivities yet reported for 3D assemblies of 2D materials. Compared to quantum dots, which are challenged by trap state passivation, our 3D films have low trap state densities due to the intrinsic lack of surface states on all but the edges of 2D flakes. Furthermore, our results indicate that the conductivity of solids are at least the same order of magnitude, if not greater, than those of quantum dots. By using 2D materials as building blocks, we show that we can engineer 3D architectures that remain quantum-confined even in "bulk" form, allowing the integration of 2D materials into a wider range of technologies than were previously accessible and the fabrication of materials with a wide range of desirable colors and properties.

2D flakes of various TMDCs and black phosphorus were prepared by liquid exfoliation by sonication in N-methyl 2-pyrrolidone (NMP). These were centrifuged to isolate 2D materials with well-defined thickness distributions. Samples containing monolayers of MoS_2 were prepared by n-butyl lithium-assisted chemical exfoliation, and transformed back into the 2H phase via refluxing in 1,3-dimethyl-3,4,5,6-tetrahydro-2(1H)-

pyrimidinone (DMPU) under an inert atmosphere. Samples of 2D flakes were transferred into n-butanol for deposition in a Langmuir-Blodgett (LB) trough. Films of varying thicknesses were deposited onto glass, silicon, or polymer substrates through repeated LB film formation and deposition. Thicker films were prepared by vacuum filtration of suspensions of 2D flakes in isopropanol onto a 0.1 μm PVDF membrane.

The liquid suspensions of 2D flakes in solvents exhibited variable colors depending on their thickness owing to varying degrees of quantum confinement. Most samples transitioned from a grey/black color in thick flakes towards yellow or red in monolayers. When these flakes were deposited as thick films, either via LB deposition or vacuum filtration, we observed that the color of the films matched that of the starting 2D suspension (Figure 4.1A). When we measured the electrical conductivity of one such film of thin 2D phosphorus, we were surprised to observe that the electrical conductivity, ca. 10^{-4} S/cm, exceeded that of many high quality films of 2D materials[18]. This suggested that, in spite of the quantum confinement, the flakes within these materials were in good electrical contact.

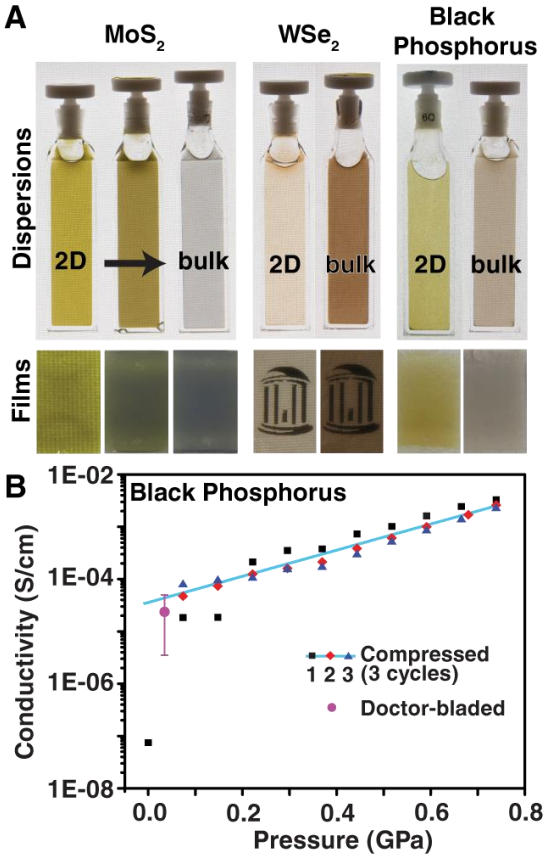

Figure 4.1 | Dispersions and films of 2D materials. (A) 2D materials of MoS_2, WSe_2, and black phosphorus dispersed in solvent. Each film was prepared from the dispersion directly above. **(B)** Electrical conductivity of films of 2D black phosphorus at atmospheric pressure and under uniaxial pressure. After uniaxial pressure is released, the films retain quantum confinement and have an electrical conductivity of 10^{-5} to 10^{-4} S/cm.

To understand the origin of this surprising combination of quantum confinement and electrical conductivity, we examined the structure of the vacuum-filtered and Langmuir-Blodgett films. Scanning electron microscopy of the vacuum filtered films (A) revealed densely packed layers of 2D materials with a preferential co-facial alignment of adjacent 2D flakes. The Langmuir-Blodgett films were thinner, slightly rough, but individual flakes were difficult to distinguish (B). The lack of well defined features suggested a relatively dense packing of the 2D flakes. The co-facial alignment of adjacent flakes, as seen in (A) for MoS_2, was observed in all vacuum filtered films, and could partially explain the high electrical conductivity observed in these films.

To provide deeper insight into the structure of these films, we performed several x-ray diffraction techniques. To confirm whether most flakes shared a similar oriention, we mapped the orientation of the (002) plane in a film made from few-layer MoS_2 using the pole figure technique (Figure 4.2C). The (002) plane is parallel to the plane of each 2D flake. A randomly oriented film would show equal intensities at all angles; instead, we observed strong intensities within 15 degrees of the film's normal. This indicated that most flakes were oriented with their normal nearly parallel to the film's normal, similar to the SEM image in Figure 4.2A. Next, to measure the spacing between flakes, we prepared a LB multilayer film made of monolayer MoS_2. Near room temperature, we observed strong diffraction at 8.9° 2-theta, corresponding to an interlayer distance of 7.0 Å (Figure 4.2D-E). Upon heating above 240 °C, the peak at 8.9° disappeared and a new peak at 14.1° appeared, corresponding to an interlayer distance of 3.3 Å (the bulk interlayer distance is 3.2 Å). Upon returning to room temperature, the peak at 14.1° remained. This behavior suggested the presence of a molecule trapped between adjacent layers that evaporated upon heating. To assess if a molecule was present, we performed secondary ion mass spectroscopy (SIMS) on the same film. Indeed, we observed a large signal from the cyanide ion, which is a decomposition product from the DMPU solvent used to prepare the MoS_2 film. The boiling point of DMPU, 240 °C, agreed with the temperature at which the interlayer spacing decreased. These structural investigations indicate, therefore, that the 2D flakes are largely stacked parallel to each other (i.e., in a co-facial orientation) with a small, planar molecule holding apart adjacent layers.

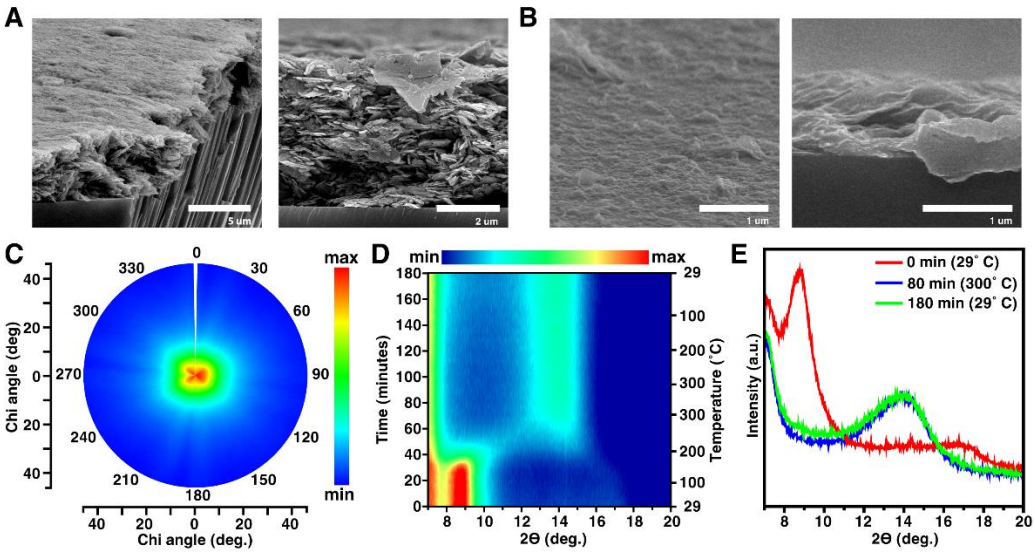

Figure 4.2 | Structural analysis of MoS_2 films. (A) SEM images of a vacuum-filtered film of few-layer MoS_2. **(B)** Top and side-view SEM images of a LB film of monolayer MoS_2. **(C)** Pole figure analysis of the (002) plane of a film of few-layer MoS_2. **(D, E)** 2-theta analysis of monolayer MoS_2 as a function of temperature; scale bar shows intensity of diffracted x-rays.

To further understand the electronic coupling between individual flakes that have been reassembled into a film, we measured their electrical properties using uniaxially pressure- and temperature-dependent van der Pauw resistivity measurements (Figure 4.3). We use MoS_2 films as a model system because we can control the average number of layers per flake by choice of preparation technique: intercalation of n-butyllithium (nBuLi) yields primarily monolayer MoS_2 flakes while normal liquid exfoliated suspensions can be centrifuged to get polydisperse fractions of thin (3–10 layers) and thick (10 layers to bulk-like) flakes.

We first measured the conductivity of the films of monolayer MoS_2 (Figure 4.3A). We found that conductivity of films prior to pressurization (Figure 4.3A., black) is 3.2×10^{-8} S/cm at 30° C. When the pressure was increased to 0.1 GPa (Figure 4.3A., red), there was a dramatic increase in the conductivity to 6.1×10^{-6} S/cm at 30° C. It has been shown that for polycrystalline 2H-MoS_2, there is a 0.448 log (σ)/GPa dependence up to 10.0 GPa with

hydrostatic pressure[19]. For 0.1 GPa applied pressure, this corresponds to a 10% increase in conductivity. Given the 1000-fold increase in conductivity with applied pressure, we therefore conclude that the increase in conductivity with compression is due to an improvement in the percolative network for electrical transport. Increasing the pressure further to 0.2 GPa (Figure 4.3A., blue) only slightly improved the conductivity of the film, to 9.8×10^{-6} S/cm at 30° C.

For all pressures, there is a $\log \sigma \sim 1/T$ dependence. This dependence has also been observed in analogous systems, such as nanoparticle arrays, in which charge transport proceeds *via* hopping events across the array[20]. We measured an activation energy (E_a) for charge transport of 1.2 eV, which is larger than the reported in-plane E_a of 0.417 eV for 2H-MoS_2 at room temperature[21]. We therefore expect the measured activation energy to be the energy required for an electron to hop from one 2D flake to the next, thereby making one flake positively charged and the other negatively charged. This is called a charging energy, and is the work required to charge a capacitor to the elementary charge of an electron (Eqn. 1):

$$E_a = \int^{e} \frac{q}{C} dq = \frac{e^2}{2C} \tag{4-1}$$

where q is charge and C is the capacitance. For spherical nanoparticle systems, it has been shown that E_a is proportional to s/r , where s and r are nanoparticle separation and radius, respectively[20].

We expect a similar dependence of E_a on flake thickness and separation. To investigate this dependence, we measured the electrical properties of vacuum filtered films with thick (10 layers to bulk-like) and thin (3 to 10 layers) MoS_2 flakes (Figure 4.3B-C). Consistent with our findings above, there was at least an order of magnitude increase in

conductivity upon compression of the vacuum filtered films. Additionally, we find that $E_a \sim 1/t$, where t is the thickness of MoS_2 flakes and that pressurizing the film has a minimal effect on E_a. These experiments demonstrate that compression does increase the proportion of flake area that is situated at the point of closest contact (an interlayer distance of 7.0 Å), where the rate of electron transfer is the highest.

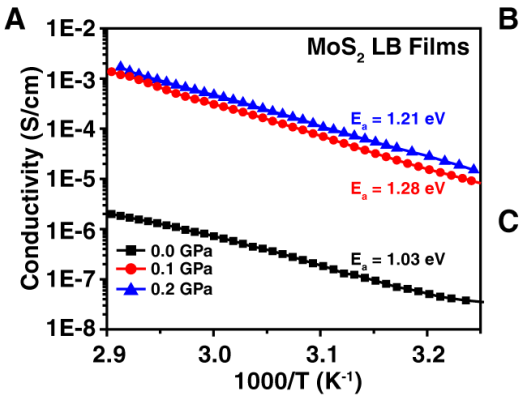

B

MoS_2 VF, 2k-4k RPM, 'thick' flakes

P (GPa)	σ, 23° C (S/cm)	σ, 66° C (S/cm)	E_a (eV)
0.00	3.44×10^{-5}	1.62×10^{-4}	0.321 ± 0.030
0.99	1.16×10^{-3}	5.24×10^{-3}	0.312 ± 0.006

C

MoS_2 VF, 12k-20k RPM, 'thin' flakes

P (GPa)	σ, 23° C (S/cm)	σ, 83° C (S/cm)	E_a (eV)
0.00	7.83×10^{-6}	1.16×10^{-4}	0.560 ± 0.016
0.49	3.11×10^{-5}	3.64×10^{-4}	0.545 ± 0.032

Figure 4.3 | Electrical properties of MoS_2 films with varying flake thickness. (A) Conductivity of MoS_2 films prepared from nBuLi exfoliation and Langmuir-Blodgett trough deposition. Tables of conductivity and activation energy values for vacuum filtered (VF) films of 'thick' (~10–40 layers) MoS_2 flakes **(B)** and thin (~3–10 layers) MoS_2 flakes **(C)**.

With these conductivity measurements in hand, we next explored the quantum confinement of Langmuir-Blodgett films of various 2D materials via UV-vis-nIR, fluorescence, and Raman spectroscopies. We found that the dispersions of both bulk-like and few-layer (2D) MoS_2 flakes exhibited similar spectral shapes to the as-deposited films, and that the 2D films retained the same absorption edge as the 2D dispersions rather than reverting to the bulk-like film absorption edge. This suggests the retention of the quantum confined properties of the 2D building blocks (Figure 4.4A). The exciton absorption peaks of MoS_2 provide useful indicators of the degree of quantum confinement in these films[22-24], and the blue-shifted exciton A peak of the 2D MoS_2 film as compared to the bulk-like flakes (Figure 4.4A, inset) confirms the retention of quantum confinement.

We further probed the dependence of quantum confinement on flake-to-flake interlayer distance by performing photoluminescence measurements on films of nBuLi-exfoliated monolayer MoS_2 under an applied pressure. The monolayer photoluminescence (PL) peak of MoS_2 is known to quench and slightly red-shift when two flakes are brought into direct contact[17, 25-26], indicative of the increase in interlayer electronic coupling as the flake thickness increases. By measuring the PL peak of monolayer MoS_2 under pressure, we can obtain a quantitative measure of the quantum confinement of our 2D material films and compare it directly to the conductivity studies under unilateral pressure.

An MoS_2 film was created via Langmuir-Blodgett assembly on a silicone substrate with five sequential depositions and the pressure was applied using a diamond anvil cell. The pressure was measured in-situ by monitoring the Ruby R_1 fluorescence peak and comparing to known calibration curves[27]. At 0 GPa pressure (Figure 4.4B), we observe a PL peak at ~664 nm, consistent with previous reports of monolayer and bilayer photoluminescence[28-31]. With applied pressure, the PL peak is quenched and blue-shifted with respect to the peak at 0 GPa but returns to its original position upon pressure release. This pressure-induced blue-shift and quenching has been previously observed for monolayer and bilayer flakes of MoS_2[31], suggesting that our assemblies of monolayer flakes are acting independently despite the applied pressure and are, in fact, not coupled. This agrees well with the pressure–conductivity and activation energy measurements that suggest that the increase in conductivity is due to the improved percolation network with compression rather than a decrease in flake-to-flake distance.

The A_{1g} and E^1_{2g} Raman modes of MoS_2 provide further evidence that the flakes remain confined under compression (Figure 4.4C). The peak frequency difference (cm^{-1}) of

the A_{1g} and E^1_{2g} phonon modes is known to widen with increased flake thickness as a result of interlayer coupling[32-34], with frequency differences of 19-20 cm^{-1} for the monolayer and ~25 cm^{-1} in bulk. The peak frequency differences for our sample (Figure 4.4D) at 0 GPa agree well with the reported values for monolayer and bilayer flakes of MoS_2 (see supporting information). Under applied pressure, the peak frequency difference for our MoS_2 film increases slightly, but returns to the 0 GPa value after pressure release. The peak frequency differences at 0 and 2.70 GPa are both within the range of observed peak frequency differences for monolayer and bilayer flakes, and suggests that the flakes are not strongly coupled.

The slight widening of the peak frequency differences of the A_{1g} and E^1_{2g} modes with pressure could also be attributed to a pressure-induced effect on an individual crystal[19, 35-37] rather than interlayer flake-to-flake coupling. We can test this theory by examining the direction of peak shift for the phonon modes. For individual crystals of MoS_2, the A_{1g} mode stiffens (blue-shifts) and the E^1_{2g} softens (red-shifts) during the transition from monolayer to bulk. Under pressure, however, both of the Raman modes are known to stiffen and the peak frequency difference would widen. The data in Figure 4.4C clearly shows a stiffening of both the A_{1g} and E^1_{2g} modes for our MoS_2 films, allowing us to attribute the observed peak frequency widening to a pressure-induced effect of an individual flake. The collective results from the absorbance, photoluminescence, and Raman data unequivocally confirm that the MoS_2 flakes remain quantum confined when assembled as a thick film, despite being electronically coupled.

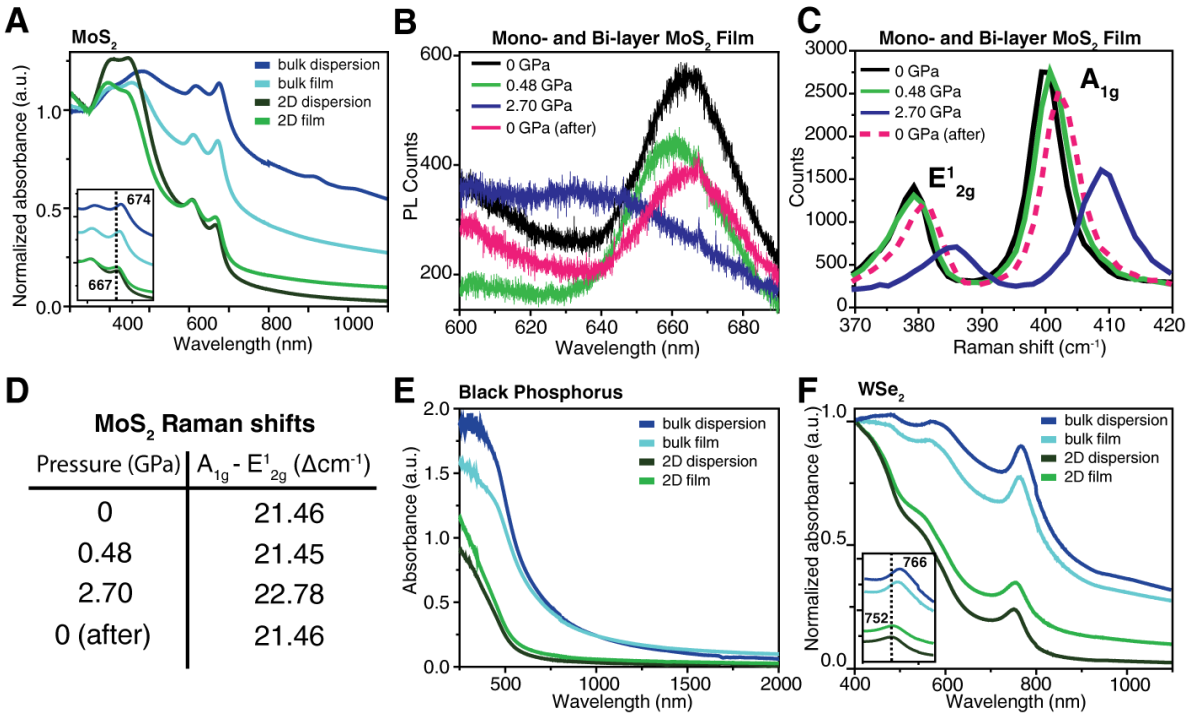

Figure 4.4 | Quantum confinement of 2D material films. (A) Absorbance spectra of bulk-like and 2D MoS_2 dispersions and corresponding films. Inset: blue-shift of exciton A with decrease in flake thickness. **(B–C)** Photoluminescence (B) and Raman shifts (C) of monolayer MoS_2 films as a function of unilateral pressure. **(D)** Peak frequency difference as a function of pressure for the Raman spectra in (C). **(E), (F)** Absorbance spectra of bulk-like and 2D Black Phosphorus (E) and WSe_2 (F) dispersions and corresponding films. Inset (F): blue-shift of exciton with decrease in flake thickness demonstrates retention of quantum confinement.

Based on this new understanding of the quantum confinement of MoS_2 flakes deposited as films, we wondered whether we could extend our findings to films of other 2D materials. To test this, we deposited films of bulk and 2D black phosphorus (Figure 4.4E) and tungsten diselenide (Figure 4.4F) and measured the absorbance spectra of the dispersions and films. In each case, the dispersions and films of the 2D flakes are both blue-shifted as compared to the bulk-like flakes, indicating the retention of the quantum confined properties of the 2D building blocks.

Our successful demonstration that films of 2D materials can be designed to retain their quantum confined properties while remaining electronically coupled provides a new

strategy for the design of 3D materials whose properties can be tuned based on the underlying building blocks. This would allow the creation of 3D materials with arbitrary combinations of absorption, conductivity, metallic, and insulating characteristics and will advance development, not only for semiconductors but other 2D materials and their mixtures.

REFERENCES

1. Kim, T.-H.; Cho, K.-S.; Lee, E. K.; Lee, S. J.; Chae, J.; Kim, J. W.; Kim, D. H.; Kwon, J.-Y.; Amaratunga, G.; Lee, S. Y.; Choi, B. L.; Kuk, Y.; Kim, J. M.; Kim, K., Full-colour quantum dot displays fabricated by transfer printing. *Nature Photonics* **2011,** *5*, 176.

2. Eunjoo, J.; Shinae, J.; Hyosook, J.; Jungeun, L.; Byungki, K.; Younghwan, K., White-Light-Emitting Diodes with Quantum Dot Color Converters for Display Backlights. *Advanced Materials* **2010,** *22* (28), 3076-3080.

3. Pattantyus-Abraham, A. G.; Kramer, I. J.; Barkhouse, A. R.; Wang, X.; Konstantatos, G.; Debnath, R.; Levina, L.; Raabe, I.; Nazeeruddin, M. K.; Grätzel, M.; Sargent, E. H., Depleted-Heterojunction Colloidal Quantum Dot Solar Cells. *ACS Nano* **2010,** *4* (6), 3374-3380.

4. Nozik, A. J., Quantum dot solar cells. *Physica E: Low-dimensional Systems and Nanostructures* **2002,** *14* (1), 115-120.

5. Gao, X.; Cui, Y.; Levenson, R. M.; Chung, L. W. K.; Nie, S., In vivo cancer targeting and imaging with semiconductor quantum dots. *Nature Biotechnology* **2004,** *22*, 969.

6. Medintz, I. L.; Uyeda, H. T.; Goldman, E. R.; Mattoussi, H., Quantum dot bioconjugates for imaging, labelling and sensing. *Nature Materials* **2005,** *4*, 435.

7. Medintz, I. L.; Clapp, A. R.; Mattoussi, H.; Goldman, E. R.; Fisher, B.; Mauro, J. M., Self-assembled nanoscale biosensors based on quantum dot FRET donors. *Nature Materials* **2003,** *2*, 630.

8. McDonald, S. A.; Konstantatos, G.; Zhang, S.; Cyr, P. W.; Klem, E. J. D.; Levina, L.; Sargent, E. H., Solution-processed PbS quantum dot infrared photodetectors and photovoltaics. *Nature Materials* **2005,** *4*, 138.

9. Talapin, D. V.; Murray, C. B., PbSe Nanocrystal Solids for n- and p-Channel Thin Film Field-Effect Transistors. *Science* **2005,** *310* (5745), 86.

10. Tang, J.; Kemp, K. W.; Hoogland, S.; Jeong, K. S.; Liu, H.; Levina, L.; Furukawa, M.; Wang, X.; Debnath, R.; Cha, D.; Chou, K. W.; Fischer, A.; Amassian, A.; Asbury, J. B.; Sargent, E. H., Colloidal-quantum-dot photovoltaics using atomic-ligand passivation. *Nat. Mater.* **2011,** *10*, 765.

11. Baumgardner, W. J.; Whitham, K.; Hanrath, T., Confined-but-Connected Quantum Solids via Controlled Ligand Displacement. *Nano Lett.* **2013,** *13* (7), 3225-3231.

12. Kagan, C. R.; Murray, C. B., Charge transport in strongly coupled quantum dot solids. *Nat. Nanotechnol.* **2015,** *10*, 1013.

13. Whitham, K.; Yang, J.; Savitzky, B. H.; Kourkoutis, L. F.; Wise, F.; Hanrath, T., Charge transport and localization in atomically coherent quantum dot solids. *Nat. Mater.* **2016,** *15*, 557.

14. Splendiani, A.; Sun, L.; Zhang, Y.; Li, T.; Kim, J.; Chim, C.-Y.; Galli, G.; Wang, F., Emerging Photoluminescence in Monolayer MoS2. *Nano Lett.* **2010,** *10* (4), 1271-1275.

15. Eda, G.; Yamaguchi, H.; Voiry, D.; Fujita, T.; Chen, M.; Chhowalla, M., Photoluminescence from Chemically Exfoliated MoS2. *Nano Lett.* **2011,** *11* (12), 5111-5116.

16. Woomer, A. H.; Farnsworth, T. W.; Hu, J.; Wells, R. A.; Donley, C. L.; Warren, S. C., Phosphorene: Synthesis, Scale-Up, and Quantitative Optical Spectroscopy. *ACS Nano* **2015,** *9* (9), 8869-8884.

17. Liu, K.; Zhang, L.; Cao, T.; Jin, C.; Qiu, D.; Zhou, Q.; Zettl, A.; Yang, P.; Louie, S. G.; Wang, F., Evolution of interlayer coupling in twisted molybdenum disulfide bilayers. *Nature Communications* **2014,** *5*, 4966.

18. Kelly, A. G.; Hallam, T.; Backes, C.; Harvey, A.; Esmaeily, A. S.; Godwin, I.; Coelho, J.; Nicolosi, V.; Lauth, J.; Kulkarni, A.; Kinge, S.; Siebbeles, L. D. A.; Duesberg, G. S.; Coleman, J. N., All-printed thin-film transistors from networks of liquid-exfoliated nanosheets. *Science* **2017,** *356* (6333), 69.

19. Chi, Z.-H.; Zhao, X.-M.; Zhang, H.; Goncharov, A. F.; Lobanov, S. S.; Kagayama, T.; Sakata, M.; Chen, X.-J., Pressure-Induced Metallization of Molybdenum Disulfide. *Physical Review Letters* **2014,** *113* (3), 036802.

20. Zabet-Khosousi, A.; Dhirani, A.-A., Charge transport in nanoparticle assemblies. *Chem. Rev.* **2008,** *108* (10), 4072-4124.

21. El-Mahalawy, S.; Evans, B., Pressure dependence of the electrical conductivity in 2H-MoS2 and 2H-WSe2. *physica status solidi (b)* **1978,** *86* (1), 151-157.

22. Backes, C.; Smith, R. J.; McEvoy, N.; Berner, N. C.; McCloskey, D.; Nerl, H. C.; O'Neill, A.; King, P. J.; Higgins, T.; Hanlon, D.; Scheuschner, N.; Maultzsch, J.; Houben, L.; Duesberg, G. S.; Donegan, J. F.; Nicolosi, V.; Coleman, J. N., Edge and confinement effects allow in situ measurement of size and thickness of liquid-exfoliated nanosheets. *Nature Communications* **2014,** *5*, 4576.

23. Castellanos-Gomez, A.; Quereda, J.; van der Meulen, H. P.; Agraït, N.; Rubio-Bollinger, G., Spatially resolved optical absorption spectroscopy of single-and few-layer MoS2 by hyperspectral imaging. *Nanotechnology* **2016,** *27* (11), 115705.

24. Shi, H.; Yan, R.; Bertolazzi, S.; Brivio, J.; Gao, B.; Kis, A.; Jena, D.; Xing, H. G.; Huang, L., Exciton dynamics in suspended monolayer and few-layer MoS2 2D crystals. *ACS nano* **2013,** *7* (2), 1072-1080.

25. Huang, S.; Ling, X.; Liang, L.; Kong, J.; Terrones, H.; Meunier, V.; Dresselhaus, M. S., Probing the interlayer coupling of twisted bilayer MoS2 using photoluminescence spectroscopy. *Nano letters* **2014,** *14* (10), 5500-5508.

26. Castellanos-Gomez, A.; van der Zant, H. S.; Steele, G. A., Folded MoS 2 layers with reduced interlayer coupling. *Nano Research* **2014,** *7* (4), 572-578.

27. Mao, H. K.; Xu, J.; Bell, P. M., Calibration of the ruby pressure gauge to 800 kbar under quasi-hydrostatic conditions. *Journal of Geophysical Research* **1986,** *91* (B5), 4673.

28. Eda, G.; Yamaguchi, H.; Voiry, D.; Fujita, T.; Chen, M.; Chhowalla, M., Photoluminescence from chemically exfoliated MoS_2. *Nano Letters* **2011,** *11* (12), 5111-6.

29. Mak, K. F.; Lee, C.; Hone, J.; Shan, J.; Heinz, T. F., Atomically thin MoS 2: a new direct-gap semiconductor. *Physical review letters* **2010,** *105* (13), 136805.

30. Dou, X.; Ding, K.; Jiang, D.; Fan, X.; Sun, B., Probing Spin-Orbit Coupling and Interlayer Coupling in Atomically Thin Molybdenum Disulfide Using Hydrostatic Pressure. *ACS Nano* **2016,** *10* (1), 1619-24.

31. Dou, X.; Ding, K.; Jiang, D.; Sun, B., Tuning and identification of interband transitions in monolayer and bilayer molybdenum disulfide using hydrostatic pressure. *ACS nano* **2014,** *8* (7), 7458-7464.

32. Zhan, Y.; Liu, Z.; Najmaei, S.; Ajayan, P. M.; Lou, J., Large-area vapor-phase growth and characterization of MoS2 atomic layers on a SiO2 substrate. *Small* **2012,** *8* (7), 966-971.

33. Lee, C.; Yan, H.; Brus, L. E.; Heinz, T. F.; Hone, J.; Ryu, S., Anomalous lattice vibrations of single-and few-layer MoS2. *ACS nano* **2010,** *4* (5), 2695-2700.

34. Li, H.; Zhang, Q.; Yap, C. C. R.; Tay, B. K.; Edwin, T. H. T.; Olivier, A.; Baillargeat, D., From bulk to monolayer MoS2: evolution of Raman scattering. *Advanced Functional Materials* **2012,** *22* (7), 1385-1390.

35. Livneh, T.; Sterer, E., Resonant Raman scattering at exciton states tuned by pressure and temperature in 2 H-MoS 2. *Physical review B* **2010,** *81* (19), 195209.

36. Sugai, S.; Ueda, T., High-pressure Raman spectroscopy in the layered materials 2 H-Mo S 2, 2 H-Mo Se 2, and 2 H-Mo Te 2. *Physical Review B* **1982,** *26* (12), 6554.

37. Bagnall, A.; Liang, W.; Marseglia, E.; Welber, B., Raman studies of MoS2 at high pressure. *Physica B+ C* **1980,** *99* (1-4), 343-346.

CHAPTER FIVE – MECHANICAL EXFOLIATION OF NON-VAN DER WAALS SOLIDS INTO 2D MATERIALS

Tyler W. Farnsworth, Eleanor L. Brightbill, Patrick C. O'Brien, Kaci L. Kuntz, Adam H. Woomer, Jack Sundberg, Scott C. Warren

Exfoliation has played a central role in the discovery of 2D materials, yielding many new materials with fascinating properties for catalysis[1], energy storage[2], electronics[3], and separations[4]. The first 2D materials were exfoliated from van der Waals layered solids, and this naturally led to experiments on other van der Waals layered solids. Building on these experimental observations, computational searches have used a large interlayer spacing as the most common criterion for exfoliation.[5-11] As a result of these focused efforts, most[12-14] known or predicted 2D materials are derived from van der Waals layered solids. Van der Waals layered solids, however, represent just 5% of all solids[6], whereas non-van der Waals layered solids—i.e., those with a low density of covalent, ionic, or hydrogen bonds that bridge layers—constitute 25% (see Appendix 4, Table A4-1). Few experiments have examined the exfoliation of non-van der Waals solids[14], and the principles that could guide the search for promising layered solids are not yet known.

In addition to interlayer distance, a second common criterion for exfoliation is that the interlayer binding energy should be small[5-7, 15-16]. The binding energy is equivalent to a surface energy—i.e., it is the energy needed per unit area to cleave a material on a crystallographic plane. The limits of binding energy were recently demonstrated, however, with the exfoliation of hematite into 2D hematene[14]. Hematite exfoliated on the (001) and (010) planes, even though ab-initio[17] and molecular dynamics[18-19] reveal that the (102)

surface energy is significantly lower. More generally, the observation that many crystals easily cleave on high energy surfaces[20] demonstrates the limitations of binding energy in non-van der Waals solids. Presumably, these limitations arise because binding energy does not account for the mechanism by which atomic layers separate and the resulting in- and out-of-plane forces that determine material fracture[21].

To overcome these challenges, here we propose a strategy to identify promising 2D materials from non-van der Waals layered solids. Our strategy is based on one of the simplest experimental methods: the Mohs hardness test. The Mohs hardness scale[22-26] measures a material's resistance to scratching (Figure 5.1A), with values that range from one (talc, easy to scratch) to ten (diamond, resists scratching). The scratch resistance test combines load and shear forces to macroscopically probe bond strength and framework density during the key moments of cleavage and fracture[25]. In this way, a scratch test bears a striking similarity to mechanical exfoliation: the competition between out-of-plane cleavage and in-plane fracture are key factors in the mechanical exfoliation of 2D materials[21]. A qualitative survey of the Mohs hardness scale suggests that it may provide new insight into exfoliation: molybdenite, (MoS_2, Mohs hardness = 1.25) is a van der Waals layered solid with no interlayer bonding, gypsum ($CaSO_4 \bullet 2\ H_2O$, Mohs = 2) has water that bridges layers via hydrogen bonds, clintonite (a mica, Mohs = 2.5) has bridging calcium ions in a O-Ca-O sequence, damaraite ($Pb_3Cl(OH)O_2$, Mohs = 3), has bridging chlorides in a Pb-Cl-H sequence, lindgrenite ($Cu_3(MoO_4)_2(OH)_2$, Mohs = 4.5) has bridging oxygens in a Cu-O-Mo sequence, lepidocrocite (γ-FeO(OH), Mohs = 5) has short and very strong hydrogen bonds between layers, sogdianite ($Zr_2KLi_3Si_{12}O_{30}$, Mohs = 6) has bridging oxygens in a Si-O-Si sequence, and staurolite ($Fe_2Al_9Si_4O_{23}(OH)$, Mohs = 7) has bridging oxygens in an Al-O-Si

sequence (see Figure 5.1). This series suggests that Mohs hardness provides insight into the nature of interlayer interactions as well as the ease with which exfoliation may occur. With this strategy in mind, we have explored the utility of Mohs hardness in identifying non-van der Waals solids with good prospects for exfoliation into 2D materials.

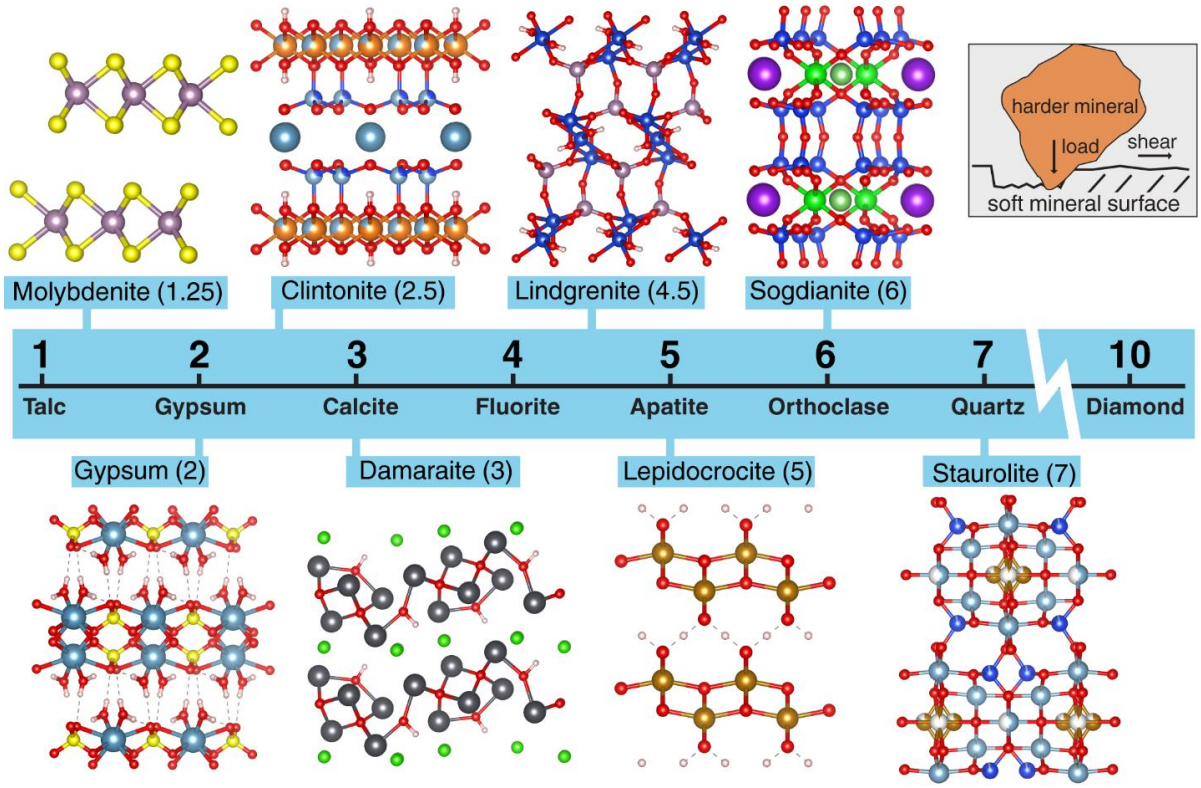

Figure 5.1 | The Mohs hardness scale. The scale is based on the scratch resistance of a series of 10 minerals, from talc (1) to diamond (10). The images show examples of layered crystals of varying Mohs hardness. The Mohs hardness appears to roughly correlate with the strength of interlayer bonds: from left to right, interlayer interactions are non-bonding (molybdenite), weak hydrogen bonding (gypsum), bridging Ca^{2+} ions (clintonite), bridging Cl^- ions (damaraite), bridging Si-O-Mo (lindgrenite), strong hydrogen bonding (lepidocrocite), bridging Si-O-Si (sogdianite), and bridging Al-O-Si (staurolite). Inset: a schematic of the Mohs hardness test, in which a harder mineral scratches a soft mineral by applying load and shear forces. Structures plotted with VESTA[27].

Mohs hardness is widely used in geology and has therefore been measured for nearly every mineral. We have therefore used the American Mineralogist Crystal Structure Database (AMCSD)[28] and the Handbook of Mineralogy (HoM)[20] to build an initial list of

2,232 minerals. We obtained most Mohs hardness values from the HoM (see supporting information in Appendix 4 for a complete list of sources,) and most crystal structures were obtained from the AMCSD and the Crystallography Open Database (COD)[29]. We randomly selected 1,000 of these minerals and classified each as layered or non-layered and described the nature of interlayer bonding (van der Waals, hydrogen bonding, ionic, or covalent, or a mixture of several types). We procured 21 natural minerals for exfoliation experiments and we measured the Mohs hardness of each, because the Mohs hardness often varies significantly because of variations in composition, microstructure, defects, and sample history. Scotch tape or Nitto tape exfoliation was used to prepare and isolate 2D nanoflakes of various minerals. The flakes were deposited on a UV-ozone cleaned silicon or aluminum oxide substrate with a 90 or 300 nm oxide layer. The substrates were first washed with acetone followed by 2-propanol and dried with a N_2 gun before placing in the UV-ozone chamber. Samples were imaged using an optical microscope and Asylum atomic force microscope.

We began our survey by exploring hydrogen-bonded layered minerals, which we expected to be easier to cleave than ionic or covalent-bonded layered materials. We divide hydrogen-bonded minerals into two types: those with water in the interlayer space, and those without water. Beginning with the water-containing minerals, we explored posnjakite (Mohs hardness = 1) and erythrite (Mohs hardness = 2.0). Posnjakite, $Cu_4(SO_4)(OH)_6 \bullet H_2O$, is a layered copper hydroxide with some hydroxides replaced by sulfates. It is remarkable for having the lowest possible Mohs hardness, which is likely a result of the size-mismatched combination of large sulfates and small hydroxides, requiring the interlayer space to be filled by water. This material cleaved very easily into few-layer flakes (Figure 5.2A). Erythrite,

$Co_3(AsO_4)_2 \cdot 8H_2O$, is a fascinating mineral in which cobalt arsenate sheets of a fluctuating thickness are capped on top and bottom by water molecules that bridge adjacent layers. Despite the higher Mohs hardness, these sheets also cleaved readily into few-layer flakes.

We next considered hydrogen bonded minerals without water. We examined two isostructural minerals, brucite ($Mg(OH)_2$) and pyrochroite ($Mn(OH)_2$). A computational screening had predicted both to be easily exfoliable[6], with an interlayer binding energy of 33 meV/Å^2 for $Mg(OH)_2$ and 24 meV/Å^2 for $Mn(OH)_2$. Despite these similarities, our sample of brucite had a Mohs hardness of 2 while the pyrochroite had a Mohs hardness of 4.5. In AFM images, we observed that the brucite cleaved into extremely large monolayer and few-layer flakes (Figure 5.2C), while the pyrochroite did not cleave into well-defined layers (Figure 5.2D). Therefore, it appears that Mohs hardness may have a greater predictive value than interlayer binding energy, since the Mohs hardness will depend not only on interlayer binding energy, but also grain boundaries, contaminants, crystal domain size, and other defects—factors that are not captured by calculations on pristine crystals.

Layered crystals with ionic interlayer interactions have been little explored as 2D materials, and these are a particularly large class of layered solids. In the case of natural crystals, these include micas, which are routinely cleaved to provide flat substrates. We selected muscovite, which had a Mohs hardness of 2-2.5, and sanbornite, which had a Mohs hardness of 5.5. We found that our muscovite sample readily cleaved down to monolayer thickness (Fig 5.2E), while sanbornite also cleaved into thick flakes, about 15-25 nm thick (Figure 5.2F). Despite repeated attempts, it was not possible to produce thinner flakes of sanbornite. It therefore appears that, just as in the case of pyrochroite, a Mohs hardness of 4.5 to 5.5 identifies samples that are difficult to cleave into 2D materials.

Our survey also included layered solids with covalent interlayer interactions. We discuss two of these here, covellite and eudidymite. Covellite, CuS, is a layered material with covalent Cu-S interlayer bonding, but the Mohs hardness of our sample was just 2.5. Although the sample appeared to produce a larger proportion of poorly defined pieces, there were, nonetheless, a significant number of few-layer flakes (Figure 5.2G). We also obtained a sample of eudidymite for which we measured a Mohs hardness between 2.5 and 4. Prior to exfoliation, the crystal morphology is somewhat fibrous; after exfoliation, the resulting flakes were elongated (Figure 5.2H). Flakes were as thin as 3 nm, which is remarkable given the likely cleavage of Si-O-Si bonds in the exfoliation process.

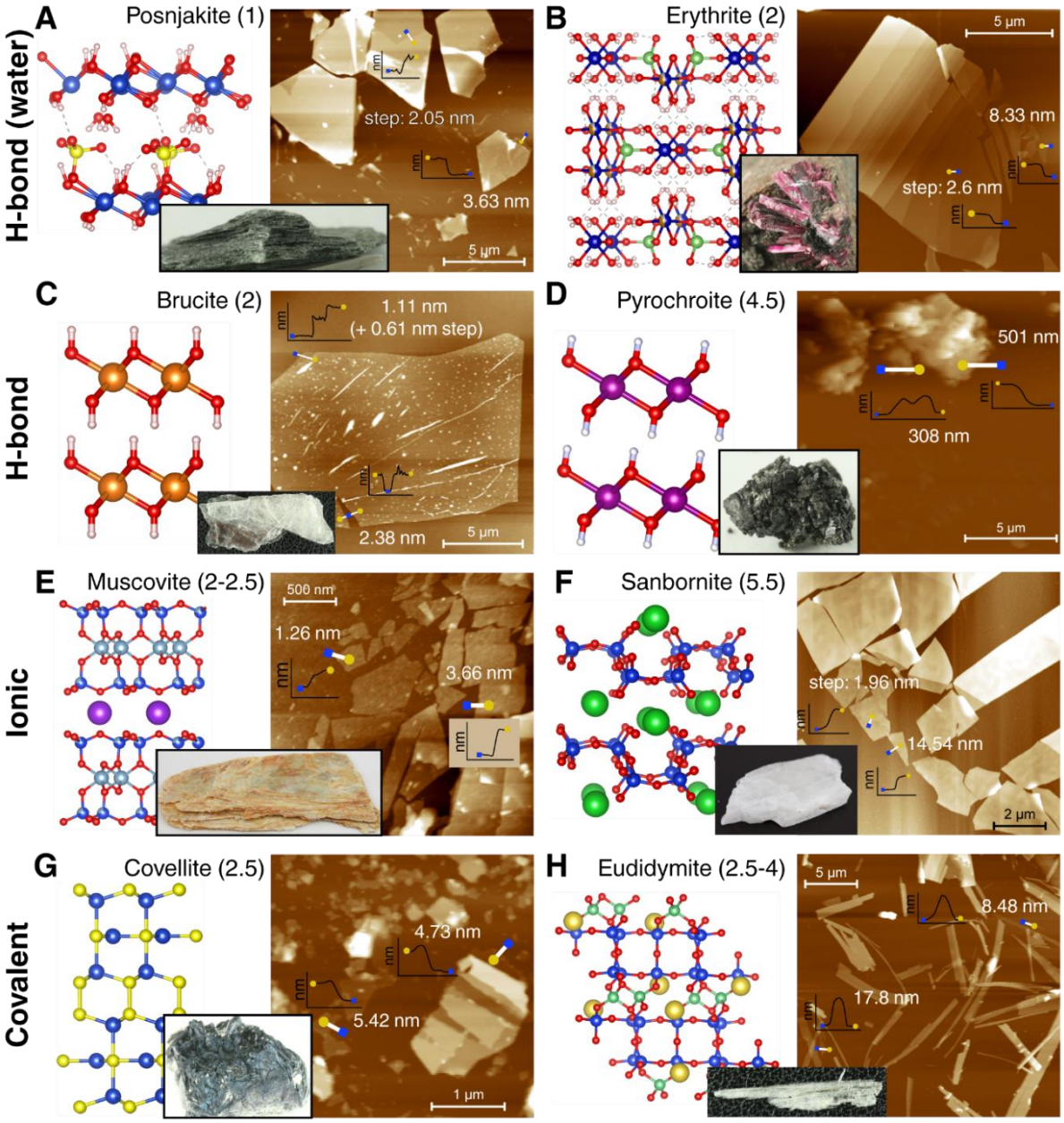

Figure 5.2 | Exfoliation of non-van der Waals layered solids. (A), Posnjakite, $Cu_4(SO_4)(OH)_6 \bullet H_2O$, Mohs hardness = 1, gave flakes 3-8 nm thick. **(B),** Erythrite, $Co_3(AsO_4)_2 \bullet 8H_2O$, Mohs = 2, gave flakes 5-19 nm thick. **(C),** Brucite, $Mg(OH)_2$, Mohs = 2, gave flakes 1-5 nm thick. **(D),** Pyrochroite, $Mn(OH)_2$, Mohs = 4.5, gave poorly defined particles. **(E),** Muscovite, $KAl_2(AlSi_3O_{10})(OH, F)_2$, Mohs = 2-2.5, gave flakes 1-2 nm thick. **(F),** Sanbornite, $BaSi_2O_5$, Mohs = 5.5, gave flakes 15-24 nm thick. **(G),** Covellite, CuS, Mohs = 2.5, gave flakes 3-5 nm thick. **(H),** Eudidymite, $NaBeSi_3O_7(OH)$, Mohs = 2.5-4, gave flakes 3-12 nm thick.

Collectively, we explored the exfoliation of 20 non-van der Waal layered solids. Regardless of the nature of the interlayer interaction, we consistently found that a Mohs hardness between 4.5 and 5.5 corresponded to the point at which few-layer (< 10 nm) flakes could no longer be obtained. To better understand this relationship, we carefully examined the crystal structures of 1,000 randomly selected minerals that were cross-listed between the AMCSD and HOM (the original set had 2,232 minerals in it). The Mohs hardness for these 1,000 minerals spans from a value of 1 to 9.5 (Figure 5.3A), with most minerals having values between 2 and 6. This distribution matches the distribution of the original set of 2,232 minerals, indicating that our subset is representative of the whole (see supporting information, Appendix 4). We analyzed these 1,000 structures according to a set of criteria (described in detail in the supporting information, Appendix 4) to identify structures as either layered on non-layered. Interestingly, the layered structures, which comprise 32% of the total (N = 322), tend to have lower Mohs hardness values than non-layered structures. For example, at a Mohs hardness between 1 and 1.5, nearly 70% of all crystals have a layered structure. This finding is consistent with the model that a fracture event (such as caused by a scratch test or exfoliation) must occur along a plane, and that crystals with a layered structure are pre-disposed to fracture on the planes that separate layers. Figure 5.3B therefore is consistent with the model that Mohs hardness is a measure of the difficulty of separating adjacent layers, with higher Mohs hardness indicating greater difficulty.

To understand this model better, we further classified the 322 layered structures according to the nature of interlayer bonding. We classified bonding as van der Waals (N = 13), hydrogen bonding (N = 49), ionic bonding (N = 51), covalent bonding (N = 39), or some combination of these types (N = 170). For greatest clarity, we focused our analysis on

layered minerals with only one interlayer bond type, and these are displayed in Figure 5.3C-F. These results reveal that van der Waals layered solids have a low Mohs hardness, while hydrogen bonded solids are harder, and that covalent and ionic bonded solids are harder yet. This series is consistent with the general trend of bond strength: that covalent and ionic bonds are stronger than most hydrogen bonds, and that hydrogen bonds are stronger than most van der Waals interactions. This intuitive trend, which emerges out of an extremely varied collection of interlayer bond compositions, bond types, and bond densities, reinforces the model that the Mohs hardness of layered solids is related to the nature of interlayer bonding. It also reveals that there are a very large proportion of layered solids —including those with covalent and ionic interlayer interactions— that can be exfoliated into 2D materials. This vastly expands the library of possible 2D materials.

To further understand the proposed model—that Mohs hardness is related to the strength of interlayer bonding—we consider a common metric of bond strength: melting point. It is widely observed that melting point increases as bond strength increases. It is also widely observed that Mohs hardness increases as bond strength increases. In Figure 5.3G, we plot melting point versus Mohs hardness for both layered and non-layered crystals. Non-layered crystals exhibit the expected linear correlation between Mohs hardness and melting point, as exemplified by diamond (strong bonds give rise to a high melting point and high Mohs hardness), while layered crystals show strikingly different behavior. In layered crystals, as melting point increases, Mohs hardness does not change significantly, remaining consistently low. In graphite, for example, the melting point exceeds 4000 °C but its Mohs hardness remains low. This relationship leads to a deeper understanding of layered materials: fracture requires that only the weakest bonds break, while melting requires that all bonds

break. These findings further illustrate that Mohs hardness provides information about the nature of interlayer interactions—i.e., the weakest bonds in a material—while melting point provides information about the nature of intra-layer interactions—i.e., the strongest bonds in a material.

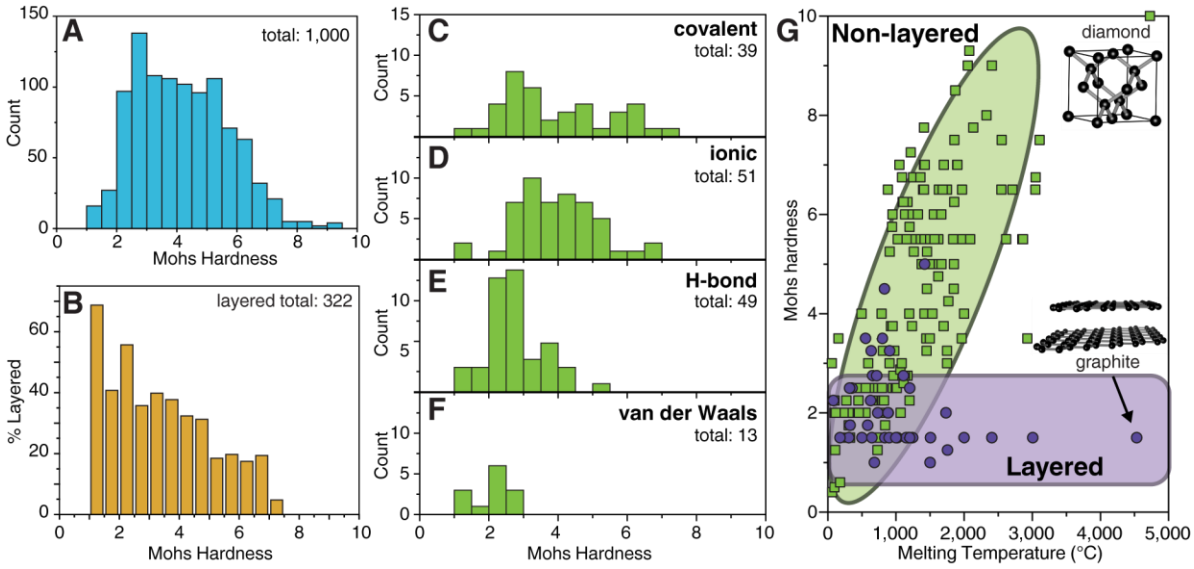

Figure 5.3 | Histograms of the layered mineral distribution. (A), distribution of minerals across Mohs hardness scale (1,000 total). (**B)**, the percentage (%) of layered minerals within the distribution of (A). (**C–F)**, layered mineral distributions from (B) categorized by bond type. **(G)**, Mohs hardness and melting point correlation for non-layered and layered crystals.

The analysis presented here has made use of nearly every Mohs hardness that has been yet reported for crystalline layered solids. Thus, we confront the question of whether the insights provided by Mohs hardness could be utilized by high-throughput computational screening to find non-van der Waals layered solids, even when Mohs hardness is not known. Fortunately, there are multiple straightforward paths to use these insights. One of the most well-established and widely used relationships connects Mohs hardness to Vickers hardness. We have tabulated and plotted this relationship for known minerals in Figure 5.4. In general, there is a very strong correlation between these properties. Because Vickers hardness is

readily calculated[30], this allows high-throughput screening to identify the non-van der Waals solids that can be exfoliated.

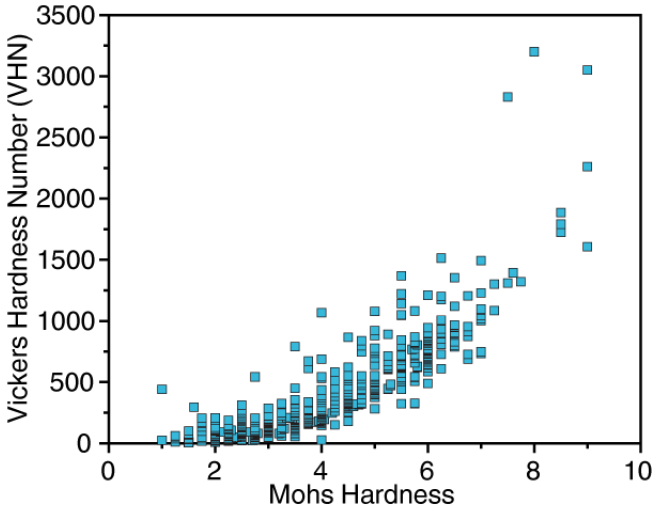

Figure 5.4 | Relationship between Mohs hardness and Vickers hardness.

In conclusion, we report here the utility of Mohs hardness to identify non-van der Waals solids for exfoliation. Remarkably, there is a very large collection of layered materials that have intralayer covalent, ionic, and hydrogen bonds that can be readily exfoliated to monolayer or few-layer materials. Our investigation suggests that most layered materials with a Mohs hardness below 4.5-5.5 can be mechanically exfoliated. Our study naturally raises a number of interesting questions, such as the nature and degree of surface reconstruction that accompanies bond cleavage. It is possible, for example, that the cleavage of interlayer bonds opens pathways for surface functionalization. It is also possible that surface reconstruction of a 2D material leads to significant changes in chemical and physical properties of the resulting 2D materials. Therefore, there is justifiably much excitement by the creation and discovery of novel non-van der Waals 2D materials.

REFERENCES

1. Deng, D.; Novoselov, K. S.; Fu, Q.; Zheng, N.; Tian, Z.; Bao, X., Catalysis with two-dimensional materials and their heterostructures. *Nat. Nanotechnol.* **2016,** *11*, 218.

2. Hua, W.; Hongbin, F.; Jinghong, L., Graphene and Graphene-like Layered Transition Metal Dichalcogenides in Energy Conversion and Storage. *Small* **2014,** *10* (11), 2165-2181.

3. Novoselov, K. S.; Geim, A. K.; Morozov, S. V.; Jiang, D.; Zhang, Y.; Dubonos, S. V.; Grigorieva, I. V.; Firsov, A. A., Electric Field Effect in Atomically Thin Carbon Films. *Science* **2004,** *306* (5696), 666-669.

4. Hu, S.; Lozada-Hidalgo, M.; Wang, F. C.; Mishchenko, A.; Schedin, F.; Nair, R. R.; Hill, E. W.; Boukhvalov, D. W.; Katsnelson, M. I.; Dryfe, R. A. W.; Grigorieva, I. V.; Wu, H. A.; Geim, A. K., Proton transport through one-atom-thick crystals. *Nature* **2014,** *516*, 227.

5. Ashton, M.; Sinnott, S. B.; Hennig, R. G., Computational discovery and characterization of polymorphic two-dimensional IV–V materials. *Appl. Phys. Lett.* **2016,** *109* (19), 192103.

6. Mounet, N.; Gibertini, M.; Schwaller, P.; Campi, D.; Merkys, A.; Marrazzo, A.; Sohier, T.; Castelli, I. E.; Cepellotti, A.; Pizzi, G.; Marzari, N., Two-dimensional materials from high-throughput computational exfoliation of experimentally known compounds. *Nat. Nanotechnol.* **2018,** *13* (3), 246-252.

7. Revard, B. C.; Tipton, W. W.; Yesypenko, A.; Hennig, R. G., Grand-canonical evolutionary algorithm for the prediction of two-dimensional materials. *Phys. Rev. B* **2016,** *93* (5).

8. Cheon, G.; Duerloo, K. N.; Sendek, A. D.; Porter, C.; Chen, Y.; Reed, E. J., Data Mining for New Two- and One-Dimensional Weakly Bonded Solids and Lattice-Commensurate Heterostructures. *Nano Lett* **2017,** *17* (3), 1915-1923.

9. Choudhary, K.; Kalish, I.; Beams, R.; Tavazza, F., High-throughput Identification and Characterization of Two-dimensional Materials using Density functional theory. *Sci Rep* **2017,** *7* (1), 5179.

10. Lebègue, S.; Björkman, T.; Klintenberg, M.; Nieminen, R. M.; Eriksson, O., Two-Dimensional Materials from Data Filtering andAb InitioCalculations. *Physical Review X* **2013,** *3* (3).

11. Wang, Y.; Miao, M.; Lv, J.; Zhu, L.; Yin, K.; Liu, H.; Ma, Y., An effective structure prediction method for layered materials based on 2D particle swarm optimization algorithm. *The Journal of Chemical Physics* **2012,** *137* (22), 224108.

12. Michael, N.; Murat, K.; Volker, P.; Jun, L.; Junjie, N.; Min, H.; Lars, H.; Yury, G.; W., B. M., Two-Dimensional Nanocrystals Produced by Exfoliation of Ti3AlC2. *Advanced Materials* **2011,** *23* (37), 4248-4253.

13. Tao, L.; Cinquanta, E.; Chiappe, D.; Grazianetti, C.; Fanciulli, M.; Dubey, M.; Molle, A.; Akinwande, D., Silicene field-effect transistors operating at room temperature. *Nat Nano* **2015,** *10* (3), 227-231.

14. Puthirath Balan, A.; Radhakrishnan, S.; Woellner, C. F.; Sinha, S. K.; Deng, L.; Reyes, C. d. l.; Rao, B. M.; Paulose, M.; Neupane, R.; Apte, A.; Kochat, V.; Vajtai, R.; Harutyunyan, A. R.; Chu, C.-W.; Costin, G.; Galvao, D. S.; Martí, A. A.; van Aken, P. A.; Varghese, O. K.; Tiwary, C. S.; Malie Madom Ramaswamy Iyer, A.; Ajayan, P. M., Exfoliation of a non-van der Waals material from iron ore hematite. *Nature Nanotechnology* **2018**.

15. Jing, Y.; Ma, Y.; Li, Y.; Heine, T., GeP3: A Small Indirect Band Gap 2D Crystal with High Carrier Mobility and Strong Interlayer Quantum Confinement. *Nano Letters* **2017,** *17* (3), 1833-1838.

16. Björkman, T.; Gulans, A.; Krasheninnikov, A. V.; Nieminen, R. M., van der Waals Bonding in Layered Compounds from Advanced Density-Functional First-Principles Calculations. *Physical Review Letters* **2012,** *108* (23), 235502.

17. Guo, H.; Barnard, A. S., Thermodynamic modelling of nanomorphologies of hematite and goethite. *Journal of Materials Chemistry* **2011,** *21* (31), 11566-11577.

18. Mackrodt, W. C., Atomistic simulation of oxide surfaces. *Physics and Chemistry of Minerals* **1988,** *15* (3), 228-237.

19. Reeves, N. J.; Mann, S., Influence of inorganic and organic additives on the tailored synthesis of iron oxides. *Journal of the Chemical Society, Faraday Transactions* **1991,** *87* (24), 3875-3880.

20. Anthony, J., W.; Bideaux, R. A.; Bladh, K., W.; Nichols, M. C., *Handbook of Mineralogy*. Mineralogical Society of America: Chantilly, VA 20151-1110, USA.

21. Guo, Y.; Liu, C.; Yin, Q.; Wei, C.; Lin, S.; Hoffman, T. B.; Zhao, Y.; Edgar, J. H.; Chen, Q.; Lau, S. P.; Dai, J.; Yao, H.; Wong, H. S. P.; Chai, Y., Distinctive in-Plane Cleavage Behaviors of Two-Dimensional Layered Materials. *ACS Nano* **2016,** *10* (9), 8980-8988.

22. Broz, M. E.; Cook, R. F.; Whitney, D. L., Microhardness, toughness, and modulus of Mohs scale minerals. *Am. Mineral.* **2006,** *91* (1), 135-142.

23. Gerberich, W. W.; Ballarini, R.; Hintsala, E. D.; Mishra, M.; Molinari, J.-F.; Szlufarska, I.; Green, D. J., Toward Demystifying the Mohs Hardness Scale. *J. Am. Ceram. Soc.* **2015,** *98* (9), 2681-2688.

24. Julg, A., An empirical relation between hardness and bond-ionicity in a crystal. *Physics and Chemistry of Minerals* **1978,** *3* (1), 45-53.

25. Meng, C. G.; Guo, J. T.; Liu, X. Y.; Hu, Z. Q., A new criterion of hardness for materials with rocksalt structure. *Materials Letters* **1993,** *17* (1), 54-58.

26. Tabor, D., Mohs's hardness scale-a physical interpretation. *Proceedings of the Physical Society. Section B* **1954,** *67* (3), 249.

27. Momma, K.; Izumi, F., VESTA 3 for three-dimensional visualization of crystal, volumetric and morphology data. *Journal of applied crystallography* **2011,** *44* (6), 1272-1276.

28. Downs, R. T.; Hall-Wallace, M., The American Mineralogist crystal structure database. *American Mineralogist* **2003,** *88*, 247-250.

29. Grazulis, S.; Chateigner, D.; Downs, R. T.; Yokochi, A. F. T.; Quiros, M.; Lutterotti, L.; Manakova, E.; Butkus, J.; Moeck, P.; Le Bail, A., Crystallography Open Database - an open-access collection of crystal structures. *Journal of Applied Crystallography* **2009,** *42* (4), 726-729.

30. Tse, J. S., Intrinsic hardness of crystalline solids. *Journal of Superhard Materials* **2010,** *32* (3), 177-191.

APPENDIX 1: CENTRIFUGE SPEED CALCULATIONS

Centrifugation is a common technique for separating a suspension of particles through a centrifugal force. The Centrifugation issue of Sigma Aldrich BioFiles[1] presents an excellent discussion and summary of the factors at play within centrifugation and this appendix draws heavily from Frei's discussion. Centrifugation is based on the spinning of a solution of particles around a center axis, enacting a centrifugal force to pull particles out of a solution. Larger particles will require greater forces to sediment out of solution than a smaller particle, and the Stokes equation[1] governs this sedimentation rate:

$$v = \frac{d^2(\rho_p - \rho_s) \times g}{18\eta} \quad \text{(A1-1)}$$

where υ = sedimentation rate or velocity of the particle (assuming a sphere geometry), d = diameter of the particle, ρ_p = particle density, ρ_s = medium (solvent) density, η = viscosity of medium (solvent), and g = gravitational force.

The time required to sediment a pellet from a dispersion is simply the inverse of the sedimentation rate (A1-1). If the angular velocity (ω) and radius of circular motion (R) of the centrifuge are considered, we can express the sedimentation time (T)[2] by equation A1-2:

$$T = \frac{9l\eta}{2r^2(\rho_p - \rho_s)\omega^2 R} = \beta \frac{4.5l}{\omega^2 R} \quad \text{(A1-2)}$$

where T = time (sec), *l* = depth of fluid (m), r = radius of suspended particles, ω = angular velocity in radians/sec, R = radius of motion in meters (m), and β = numerical simplification unit.

Angular velocity is related to the revolutions per minute (rpm) of a centrifuge by:

$$\omega = \frac{2\pi(rpm)}{60} = rad/s \quad \text{(A1-3)}$$

The simplification unit of β enables the comparison of centrifuge times of the *same* dispersion of particles at different speeds even if the radius and density of the particle are unknown. For example, if it takes 40 minutes to sediment out a dispersion of particles at 5,000 rpm, we can calculate the time to centrifuge the same dispersion at 10,000 rpm using the following ratio:

$$\frac{\mathrm{T}(10{,}000\ rpm)}{\mathrm{T}(5{,}000\ rpm)} = \frac{x}{40\ min} \tag{A1-4}$$

where T is calculated using (A1-2) and (A1-3) and the β values cancel other out to yield the new time in minutes. Note that the time to sediment out a suspension is dependent on the depth of fluid, *l*, in (A1-2) and different times will be required based on the size and volume of the centrifuge tube.

Centrifugal force is often referenced in the literature rather than rpm because the rpm is intrinsically tied to the rotor radius. The relative centrifugal force (RCF) may be calculated by equation A1-5 and is expressed in terms of the gravitational constant (*g's*).

$$RCF = 11.18 \times \mathrm{r} \times \left(\frac{RPM}{1000}\right)^2 \tag{A1-5}$$

where r = length of the centrifuge rotor (cm) and RPM = revolutions per minute.

REFERENCES

1. Frei, M. Centrifugation Basics *BioFiles* [Online], 2011, p. 4-5.

2. Clarke, P. Theory of sedimentation and centrifugation *self-published* [Online], 2009, p. 1-23.

APPENDIX 2: SUPPORTING INFORMATION FOR CHAPTER THREE

A2.1 Band gap measurement of 2D phosphorus dispersions

This section provides background information on the use of Tauc analyses and our so-called "alpha method" to measure the band gap of 2D phosphorus dispersions. This information was originally included as supporting information for the manuscript[1] in chapter 3.

In order to validate the alpha method, we first applied Tauc analyses to calculated absorption spectra[2] of bulk, trilayer, bilayer, and monolayer phosphorus. Because of the linearity of the Tauc analyses, we were able to extract accurate values of the band gap for each thickness (Figure A2-1).

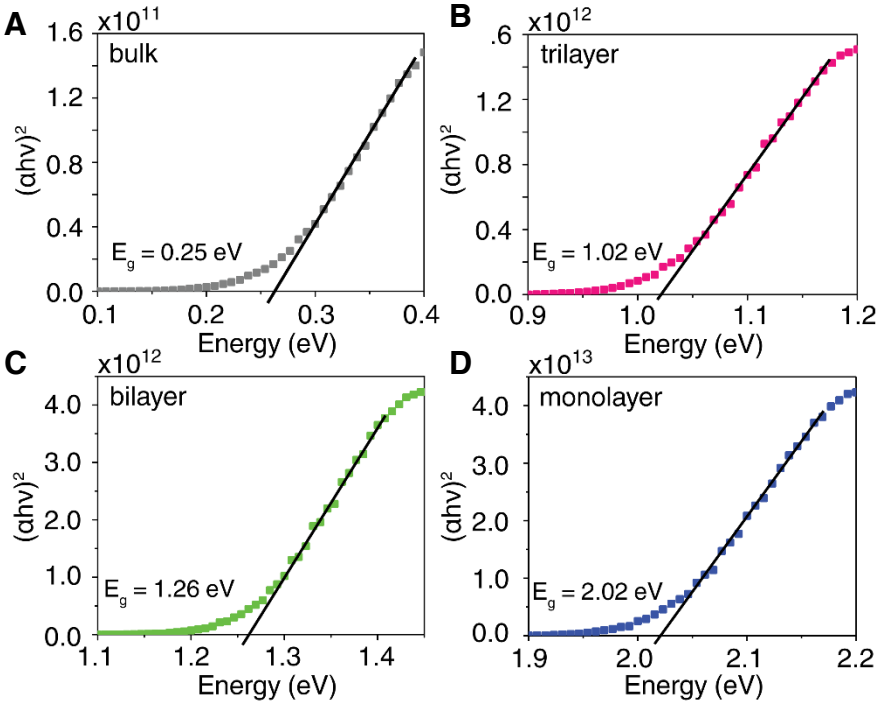

Figure A2-1 | Tauc analysis provides estimate of thickness-dependent band gap

We next applied our alpha method to the same absorption spectra to obtain a new estimate of the band gap. To do this, we measured the absorption coefficient at the theoretical bulk band gap (0.252 eV, see Figure A2-1A) and equated this value to α_{AE}. Drawing a line

across the plot from the standard α_{AE} allowed us to determine a band gap for each flake thickness (Figure A2-2). We directly compare the alpha estimates to the Tauc analysis in Table A2-1. As listed in Table A2-1, the percent difference between our alpha method of extracting the band gap and the Tauc analysis remains relatively small, with a maximum difference of just 3%. We conclude that the alpha method is likely to be as reliable as the Tauc analysis for samples that contain a single flake thickness.

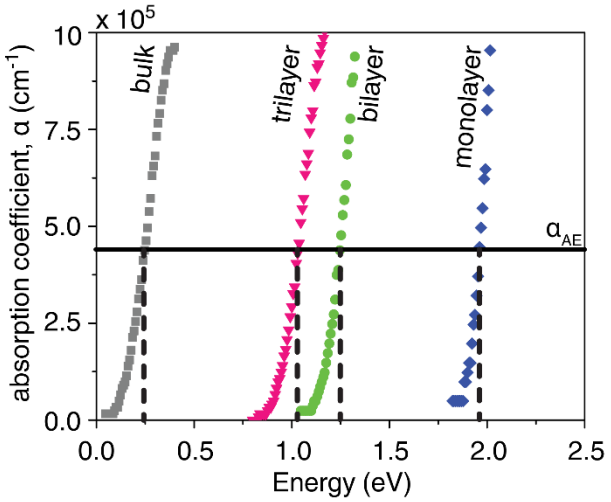

Figure A2-2 | Alpha method using same data as in Figure A2-1

Table A2-1 | Comparison of band gaps extracted using both Tauc analysis and alpha method

	Tauc Analysis (eV)	$\alpha = 4.6 \times 10^5$ cm^{-1} (eV)	Percent Error (%)
Bulk	0.25	0.25	0
Trilayer	1.02	1.04	1.96
Bilayer	1.26	1.25	0.79
Monolayer	2.02	1.96	2.97

Our samples, however, are polydisperse. In order to account for their polydispersity, we employed several statistical measures of flake thickness in these polydisperse distributions. As an initial, simple demonstration of the utility of this approach, we applied the alpha method to a series of artificial mixtures comprised of trilayer and bilayer flakes. For example, mixtures included 90:10 trilayers:bilayers; the full list is shown in Table A2-2. For each mixture, the individual absorption profile of each flake type was weighted

according to its prevalence in the mixture—for example, in the 90:10 mixture, the absorbance spectrum of the trilayer was multiplied by 0.9 and the added to the absorbance spectrum of the bilayer, which had first been multiplied by 0.1. The alpha method was then applied to each mixture to determine an effective band gap. Next, we attempted to make an estimate of flake thickness for each distribution by using either the number- or weight-averaged thickness (these are the 1st and 2nd moments of a distribution and are analogous to M_n and M_w in polymer chemistry). Returning to our example of the 90:10 mixture, the number averaged thickness is:

$$number\ averaged\ thickness = \sum_t x_t t = 0.9 \times 3 + 0.1 \times 2 = 2.9 \qquad \text{(A2-1)}$$

where x_t is the number fraction of flakes with a specific thickness and t is the thickness. The weight-averaged thickness for the 90:10 mixture is:

$$weight\ averaged\ thickness = \sum_t w_t t = 0.93 \times 3 + 0.07 \times 2 = 2.93 \qquad \text{(A2-2)}$$

where w_t is the weight fraction of flakes with a specific thickness and is calculated by

$$w_t = \frac{x_t t}{\sum_t x_t t} \qquad \text{(A2-3)}$$

which, in the case of the 90:10 trilayer:bilayer mixture, is:

$$w_3 = \frac{0.9 \times 3}{0.9 \times 3 + 0.1 \times 2} = 0.93 \qquad \text{(A2-4)}$$

and

$$w_2 = \frac{0.1 \times 2}{0.9 \times 3 + 0.1 \times 2} = 0.07 \qquad \text{(A2-5)}$$

We now have two measures of "effective thickness" which can be paired with an "effective band gap". These effective thickness-effective band gap data points can be compared to the power law fit to provide an estimate of the error associated with the effective thickness-effective band gap approach. The results of this analysis is summarized in Table A2-2 and Figure A2-3.

Table A2-2 | Monotonic increase of the effective band gap with changing sample composition. The percent errors describe the deviation of alpha-calculated band gaps from the fitted equation.

	Band gap $\alpha_{AE} = 4.6 \times 10^5$ cm^{-1} (eV)	Weight-average percent error (%)	Number-average percent error (%)
Trilayer	1.04	0.08	0.08
90:10	1.05	0.53	1.0
80:20	1.06	0.34	1.24
70:30	1.07	0.48	1.74
60:40	1.09	0.13	1.68
50:50	1.12	0.84	0.94
40:60	1.16	2.78	0.89
30:70	1.20	4.10	2.26
20:80	1.23	3.99	2.44
10:90	1.24	2.36	1.40
Bilayer	1.25	0.16	0.16

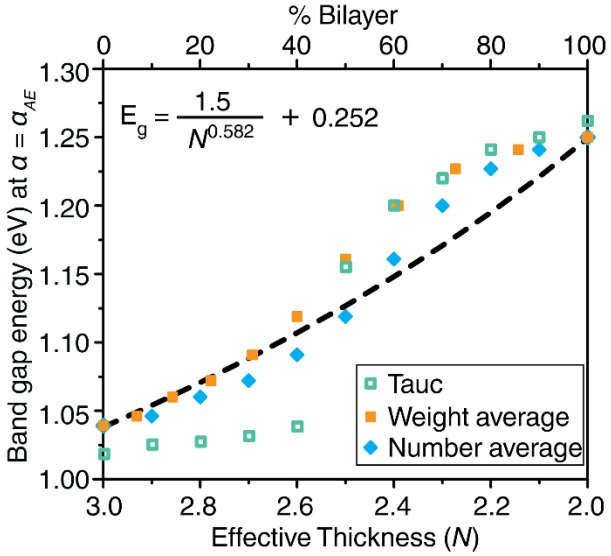

Figure A2-3 | Band gaps (determined using alpha and Tauc methods) of sequential combinations of trilayer and bilayer flakes.

Our analysis in Figure A2-3 also includes band gap estimates that come from Tauc plots. The Tauc plots of mixtures often lack linear regions and the Tauc analyses is dubious. Indeed, an extremely poor match to the power law is observed, although it should be noted that the Tauc analysis is not designed for this type of band gap analysis. In any case, the

alpha analysis provides a far better approach for band gaps that follow the expected power law.

To illustrate how number and weight averages influence the distribution, we examine two ways of plotting our real flake distributions: number and weight-averaged distributions. In some situations, a weight average is advantageous because the weighting applied for each flake thickness depends on how much of that flake is present, rather than the number of flakes of that type that are present. We will describe, below, which sorts of distributions (or, more specifically, statistical measure of the distribution) are best for pairing with the alpha method. Figure A2-4 shows a number-average thickness distribution and Figure A2-5 shows a weight-average thickness distribution for our real flake histograms.

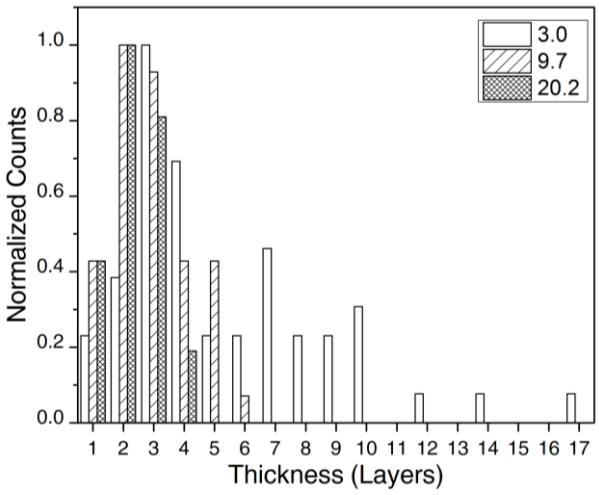

Figure A2-4 | Number-average thickness distribution of three 2D phosphorus suspensions.

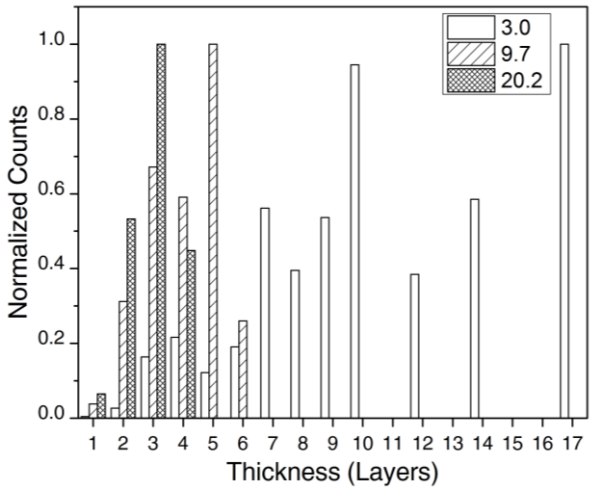

Figure A2-5. Weight-average thickness distribution of three 2D phosphorus suspensions.

In order to determine which statistical measure of thickness should be paired with the alpha analysis, we expanded our survey of statistical measures beyond number- and weight-averages to include three log-normal fittings: the log-normal mean, median, and mode. Rather than using mixtures of just two flakes, we examined mixtures of flakes of four different thicknesses, from bilayer flakes to five-layer flakes. The absorbance spectra of the bilayer and trilayer flakes came from G_0W_0 calculations[2] and the spectra of the four- and five-layer were estimated by scissoring the band gap of 3-layer flake until it had band gaps that matched those predicted by a power law. We note that the absorption coefficient (α) at energies near the band gap of the 3-layer flake is nearly the same as for the bulk material[8] so that scissoring to intermediate thicknesses is unlikely to introduce significant error in the variation of α with photon energy. The flakes were combined into 24 realistic distributions with systematically varying shapes and skewnesses (Figure A2-6). These distributions were used to weight the absorbance spectra prior to adding them to yield a total absorbance of each simulated mixture. The alpha method was applied to each mixture to obtain an effective band gap and five statistical measures were applied to analyze the distribution to obtain an

effective thickness. A table that reports the most important parameters of these distributions is shown below, Table A2-3. This table is divided into several sections, including a listing of the number fraction of each flake in the distribution (blue), the effective band gap of the distribution as determined by the application of the alpha method (yellow), a listing of the effective thicknesses as determined by the five different statistical measures (orange), and the percent error between the "true" band gap—the band gap indicated by the power law—and the effective band gap, as determined by the alpha method. These comparisons between true and effective band gaps are performed five times for each distribution—one time for each of the five estimates of effective thickness. In other words, we use the power law equation to solve for the band gap at all five of the effective thicknesses to obtain five estimated band gaps. The difference in energy between this band gap, which falls on the power law curve, and the band gap that arises from the alpha method is used to calculate the percent error.

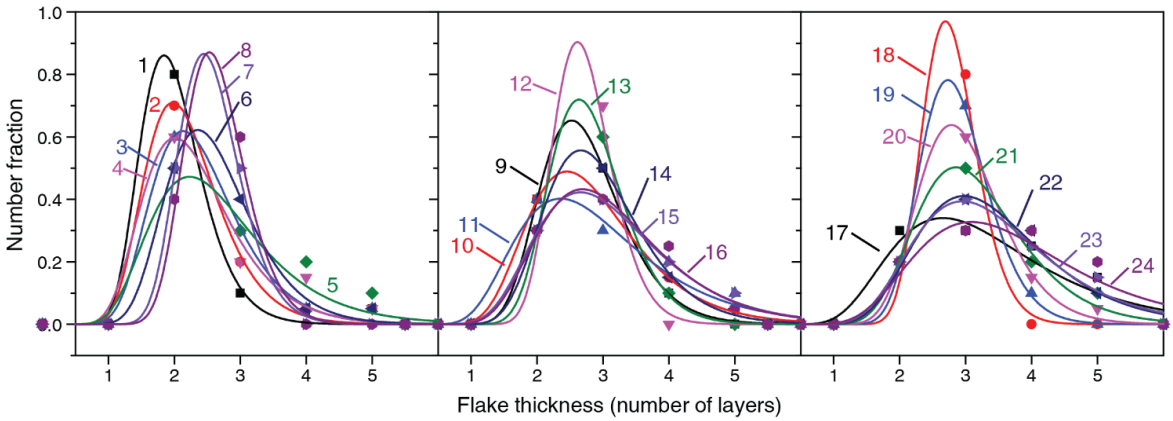

Figure A2-6 | Summary of the 24 flake thickness distributions from Table A2-3. The distributions were fitted to a log-normal curve.

Table A2-3 | Summary of 24 simulated mixtures. The individual spectra were obtained from calculated G_0W_0 spectra whose band gaps for 2- to 5-layer pieces fit a power law. The spectra were weighted according to their number fraction to determine an effective band gap and effective thickness. These values were compared to the value estimated from the power law fit to determine an error.

Number fraction of each flake (2, 3, 4, or 5 layers thick)				Effective band gap (eV)	Effective thickness of distribution					Error (% difference between power law band gap and effective (alpha) band gap)				
					Log-normal fit			No fit		Log-normal fitting			No fitting	
2	3	4	5		Mean	Median	Mode	Number-average mean	Weight-average mean	Mean	Median	Mode	Number-average mean	Weight-average mean
0.8	0.1	0.05	0.05	1.23	2.0	2.0	1.8	2.4	2.6	1.6%	3.2%	6.5%	-6.1%	-11.1%
0.7	0.2	0.05	0.05	1.20	2.2	2.1	2.0	2.5	2.7	-1.0%	1.0%	5.0%	-6.0%	-10.7%
0.6	0.3	0.05	0.05	1.15	2.4	2.3	2.1	2.6	2.8	-1.4%	0.7%	5.1%	-4.0%	-8.4%
0.6	0.2	0.15	0.05	1.15	2.3	2.2	2.0	2.7	3.0	0.1%	2.9%	9.0%	-5.8%	-10.8%
0.5	0.3	0.2	0.1	1.02	2.7	2.5	2.2	2.9	3.3	5.4%	8.7%	15.9%	1.5%	-3.7%
0.5	0.4	0.05	0.05	1.10	2.6	2.5	2.4	2.7	2.9	-0.5%	1.2%	4.8%	-1.2%	-5.3%
0.5	0.5	0	0	1.10	2.6	2.5	2.4	2.5	2.6	-0.4%	0.5%	2.2%	1.1%	-0.9%
0.4	0.6	0	0	1.07	2.7	2.6	2.5	2.6	2.7	1.1%	1.9%	3.6%	2.2%	0.4%
0.4	0.5	0.1	0	1.07	2.7	2.7	2.5	2.7	2.9	-0.1%	1.3%	4.1%	0.7%	-1.9%
0.4	0.4	0.15	0.05	1.04	2.9	2.7	2.5	2.9	3.1	0.1%	2.5%	7.8%	0.1%	-4.0%
0.4	0.3	0.2	0.1	1.02	3.0	2.7	2.4	3.0	3.3	0.4%	4.2%	12.5%	-0.2%	-5.1%
0.3	0.7	0	0	1.05	2.7	2.7	2.6	2.7	2.8	1.7%	2.4%	3.8%	2.2%	0.8%
0.3	0.6	0.1	0	1.04	2.8	2.8	2.6	2.8	2.9	1.2%	2.2%	4.4%	1.3%	-0.9%
0.3	0.5	0.15	0.05	1.02	2.9	2.8	2.7	3.0	3.2	0.6%	2.3%	5.7%	0.5%	-2.9%

0.3	0.4	0.2	0.1	1.00	3.1	3.0	2.7	3.1	3.4	-0.3%	2.4%	8.2%	0.4%	-3.7%
0.3	0.4	0.25	0.05	1.00	3.2	3.0	2.7	3.1	3.3	-0.5%	2.1%	7.5%	1.1%	-2.5%
0.3	0.3	0.25	0.15	0.97	3.4	3.1	2.7	3.3	3.6	-1.3%	2.6%	11.2%	0.8%	-3.7%
0.2	0.8	0	0	1.04	2.8	2.8	2.7	2.8	2.9	1.8%	2.3%	3.5%	1.5%	0.5%
0.2	0.7	0.1	0	1.02	2.9	2.8	2.7	2.9	3.0	1.8%	2.7%	4.4%	1.4%	-0.3%
0.2	0.6	0.15	0.05	1.01	3.0	2.9	2.8	3.1	3.2	1.2%	2.4%	4.8%	0.3%	-2.4%
0.2	0.5	0.2	0.1	0.99	3.2	3.1	2.9	3.2	3.4	0.2%	1.9%	5.5%	-0.1%	-3.4%
0.2	0.4	0.3	0.1	0.96	3.4	3.3	3.0	3.3	3.5	-0.9%	1.3%	6.1%	1.0%	-2.3%
0.2	0.4	0.25	0.15	0.96	3.5	3.3	3.0	3.4	3.6	-0.9%	1.6%	6.9%	0.6%	-3.0%
0.2	0.3	0.3	0.2	0.93	3.8	3.5	3.1	3.5	3.8	-2.1%	1.0%	7.6%	1.6%	-2.2%

From this analysis of 24 distributions, we find that the log-normal mean and the number-average mean provide, on average, the best measures of flake thickness. It is these two measures that, when paired with the effective band gap, fall closest to the power law curve. The next best measures of effective thickness come from the log-normal median and weight-average mean. In every case, the log-normal median provides an effective thickness that is too small, while in almost every case, the weight-average mean provides an effective thickness that is too large. We therefore use the log-normal median and weight-average mean to define the likely range of the band gap in Figure 3.9A and we use the log-normal mean and number-average mean to define the range of most probable band gaps.

We note that the log-normal fitting allows us to determine the skewness of the distribution. Unfortunately, there is only a weak correlation between the distribution's skewness and the % error in the band gap, which prevents us from further refining our estimates of thickness and band gap by taking into the distribution's shape (Figure A2-7).

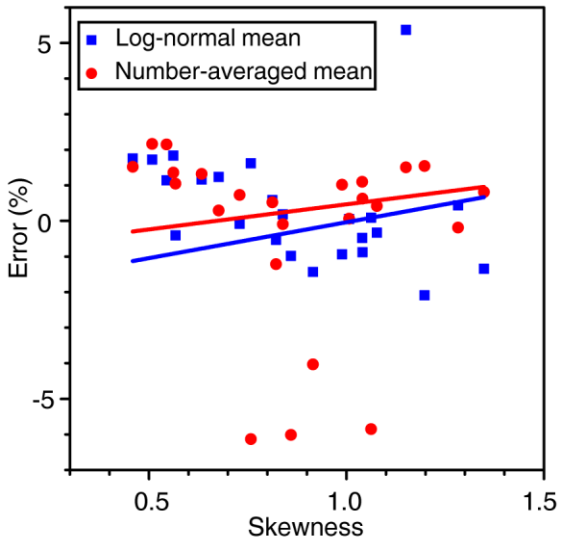

Figure A2-7 | Correlation between the flake thickness distribution's skewness (determined from the log-normal curve fit, Figure A2-6) **and % error** between the true (power law) fit and the effective band gap-effective thickness estimate.

This analysis of artificial flake distributions has allowed us to identify the best statistical measures of flake thickness to pair with the alpha method. This information has allowed us to measure and accurately analyze real samples—obtaining their thickness distribution from TEM measurements and their absorption coefficients from UV-vis-near IR spectroscopy and ICP-MS—to establish a relationship between flake thickness and band gap (These curves are constructed by making a power law fit (described in main text of Chapter to the effective thicknesses and effective band gaps of real samples. An example of the data points of effective thickness and band gap that is produced in this approach is shown below (Figure A2-8).

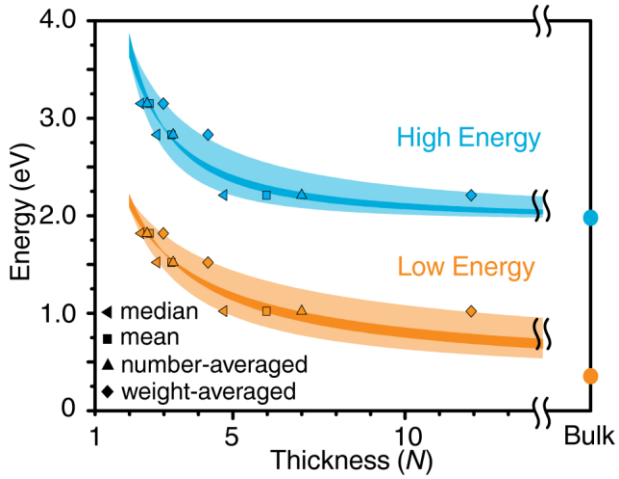

Figure A2-8 | Data points used to construct Figure 3.9. Each sample was analyzed to determine an effective band gap using the alpha method. Next, each sample was analyzed to make four different estimates of effective thickness using log-normal median, log-normal mean, a number-average mean and weight-average mean. Four different power laws were fit to each type of effective thickness, generating a most probable range (dark colors) and a maximum likely range (light colors) for the low energy transition (band gap) and the high energy transition (VB-1 → CB). The plot also shows the transitions of the bulk materials.

The power laws that are used to construct Figures 3.9 and A2-8 are shown below in Table A2-4. As mentioned previously, the best two fits to the data are the number-average mean and the log-normal mean, and these values form the boundaries of the darker regions in Figures 3.9 and A2-8. The weight-average mean and the log-normal median tend to over and

underestimate the band gaps, as described previously, and these define the boundaries of the lighter regions in Figures 3.9 and A2-8.

Table A2-4 | Fitted curves of the thickness-dependent band gap analysis

	High Energy Transition	Low Energy Transition
weight-average	$E_g = \frac{3.77934}{N^{1.03498}} + 1.95$	$E_g = \frac{2.72265}{N^{0.55884}} + 0.33$
number-average	$E_g = \frac{4.44045}{N^{1.40402}} + 1.95$	$E_g = \frac{2.96239}{N^{0.75568}} + 0.33$
log-normal mean	$E_g = \frac{6.19795}{N^{1.71072}} + 1.95$	$E_g = \frac{3.55728}{N^{0.92397}} + 0.33$
log-normal median	$E_g = \frac{6.89643}{N^{2.04329}} + 1.95$	$E_g = \frac{3.73757}{N^{1.09509}} + 0.33$

A2.2 Spectroscopy of 2D phosphorus dispersions

This section details the spectroscopic methods of chapter three that were originally included in the supporting information of the original manuscript[1]. For a more detailed discussion of light absorption and scattering and the use of an integrating sphere, see section 2.4.1.

Starna 1-mm pathlength quartz cuvettes with transparency range from 170 to 2700 nm were used in all experiments. Cuvettes were filled in a glove box and fitted with airtight PTFE stoppers to maintain an inert atmosphere.

In UV-vis-nIR transmission spectroscopy, the incident light (I) may be transmitted (T), absorbed (A), reflected (R), forward scattered (FS) or back scattered (BS). Because of the conservation of energy, $I = T + A + R + FS + BS$, where each term measures light intensity. In the solution spectroscopy of small molecules, typical approximations are that $FS \approx 0$, $BS \approx 0$, and that R is made effectively zero *via* the collection of a background spectrum that contains solvent but no analyte. Consequently, $I = T + A$, allowing a simple measurement of the transmitted light intensity with (T) and without (I) the analyte to provide accurate information about light absorption (A) by the molecule.

These approximations do not hold when performing transmission spectroscopy on objects that are larger than a few nanometers in size. As objects increase in size, so does the scattering cross section. Earlier work demonstrated that light scattering by 2D sheets that are suspended in liquids can be modeled by Mie theory[3]. A key result of Mie theory, which we used in developing an appropriate experimental approach, is that most Mie-scattered light is scattered in the forward direction, leading to the approximation that $BS \approx 0$. Consequently, if

FS light can be directed into the detector, then the 'apparent' FS ≈ 0. If achieved, this allows a straightforward use of the equation I = T + A.

To capture forward-scattered light, we made four experimental choices, summarized in Figure A2-9. First, the cuvette was placed near the detector opening. This allowed the collection of light scattered at high angles. Second, we selected a very thin (1-mm thick) cuvette rather than a 1-cm cuvette. By having the entire solution placed close to the detector opening, we could collect light scattered at very high angles. Third, by ensuring that the light that illuminated the cuvette covered a region that was smaller than the detector's entrance aperture, we were able to collect an even larger proportion of forward-scattered light. Fourth, the detector was an integrating sphere, which allowed the detector to collect and quantify light, even if it was scattered at a high angle.

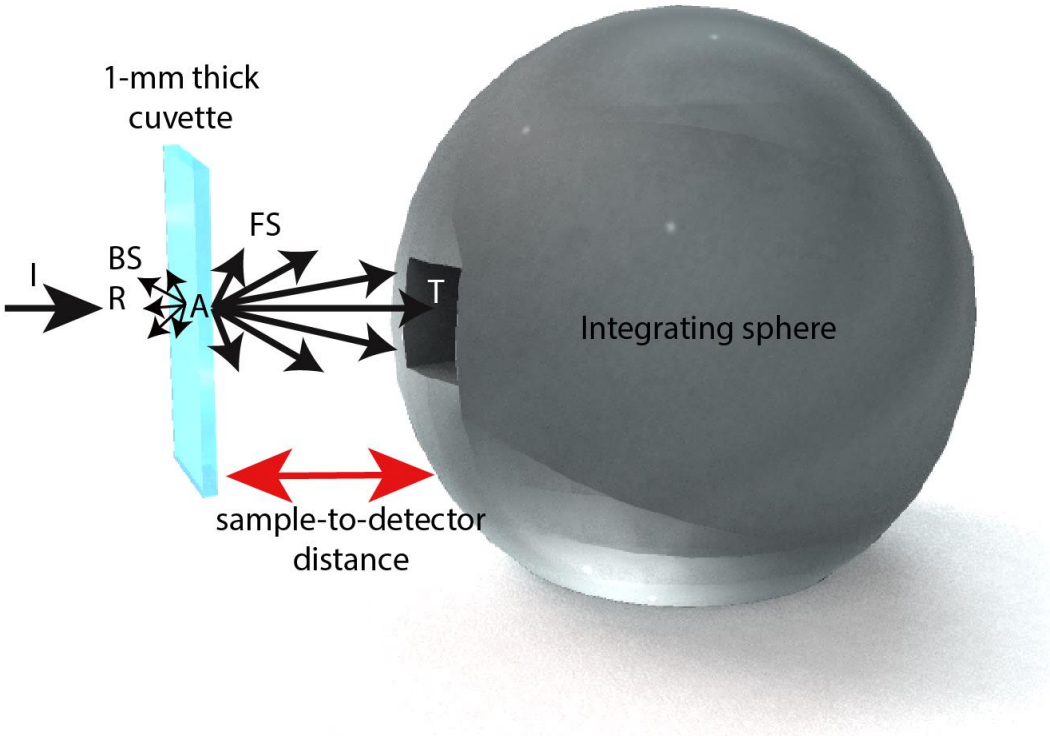

Figure A2-9 | UV-vis-nIR absorbance spectroscopy setup. By placing the 1-mm cuvette adjacent to the integrating sphere aperture and by restricting the size of the incident light beam I, we were able to capture most forward-scattered (FS) light.

In order to test the utility of our design, we systematically varied the distance between the sample and detector, collecting "absorbance" spectra at each position. The solution used for this test was comprised of thick and large flakes, which scatter light strongly. Figure A2-10 summarizes these results. In moving the sample from a position nominally labeled 5 cm (the actual sample-to-detector distance is *ca.* 5.2 cm) to 0 cm (the actual sample-to-detector distance is *ca.* 0.2 cm), the absorbance spectra changed monotonically, resulting in an apparent decrease in absorbance. We further modified the setup to remove the clamp that held the sample in place, which allowed us to position the sample directly against the opening aperture of the integrating sphere (sample-to-detector distance is 0 cm). With this change, the apparent absorbance decreased again. These changes in apparent absorbance are consistent with capturing increased amounts of forward-scattered light. These changes in apparent absorbance result in quantifiable shifts in Tauc plot analyses. We used this modified setup to collect all of our UV-vis-nIR transmission spectra.

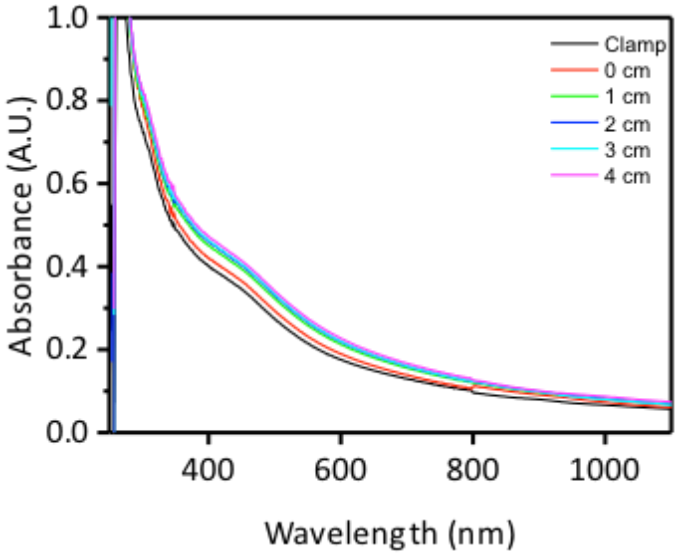

Figure A2-10 | Apparent absorbance vs. wavelength for different cuvette positions.

REFERENCES

1. Woomer, A. H.; Farnsworth, T. W.; Hu, J.; Wells, R. A.; Donley, C. L.; Warren, S. C., Phosphorene: Synthesis, Scale-Up, and Quantitative Optical Spectroscopy. *ACS Nano* **2015,** *9* (9), 8869-8884.

2. Tran, V.; Soklaski, R.; Liang, Y.; Yang, L., Layer-controlled band gap and anisotropic excitons in few-layer black phosphorus. *Physical Review B* **2014,** *89* (23).

3. Coleman, J. N.; Lotya, M.; O'Neill, A.; Bergin, S. D.; King, P. J.; Khan, U.; Young, K.; Gaucher, A.; De, S.; Smith, R. J.; Shvets, I. V.; Arora, S. K.; Stanton, G.; Kim, H. Y.; Lee, K.; Kim, G. T.; Duesberg, G. S.; Hallam, T.; Boland, J. J.; Wang, J. J.; Donegan, J. F.; Grunlan, J. C.; Moriarty, G.; Shmeliov, A.; Nicholls, R. J.; Perkins, J. M.; Grieveson, E. M.; Theuwissen, K.; McComb, D. W.; Nellist, P. D.; Nicolosi, V., Two-dimensional nanosheets produced by liquid exfoliation of layered materials. *Science* **2011,** *331* (6017), 568-71.

APPENDIX 3: SUPPORTING INFORMATION FOR CHAPTER FOUR

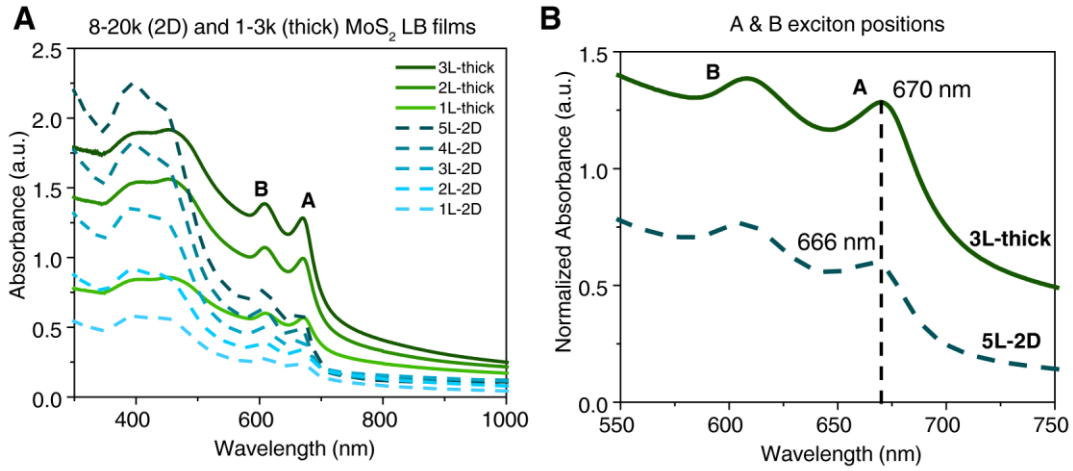

Figure A3-1 | Absorbance spectra of 2D and thick flakes of MoS_2 for sequential numbers of deposition cycles via Langmuir-Blodgett assembly **(A)**. The 2D flakes exhibit an exciton A peak that is blue-shifted with respect to the thick flakes **(B)** even after 5 deposition cycles.

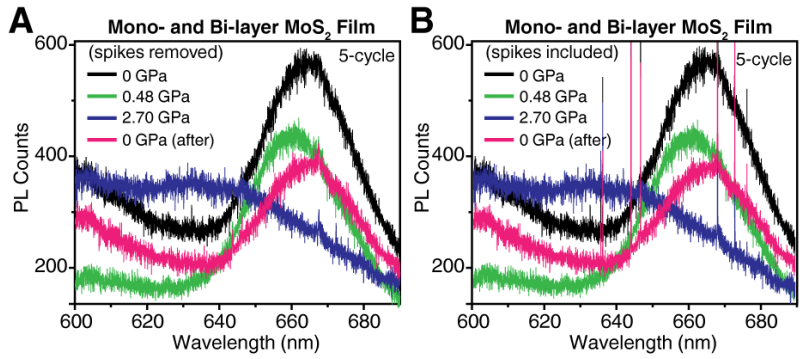

Figure A3-2 | Photoluminescence of 5-cycle LB MoS_2 film under pressure. (A) Processed data with extraneous spikes from instrument removed, **(B)** original data.

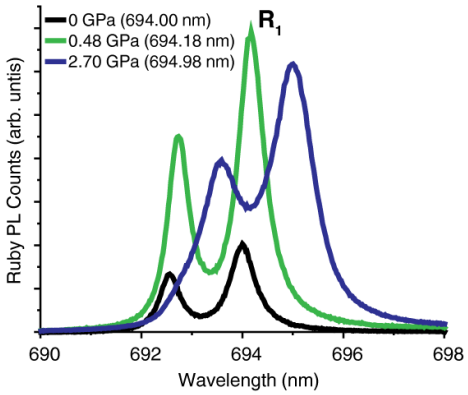

Figure A3-3 | Ruby R_1 fluorescence peak used as an in-situ pressure manometer in the diamond anvil cell. Red shift corresponds to an increase in applied pressure.

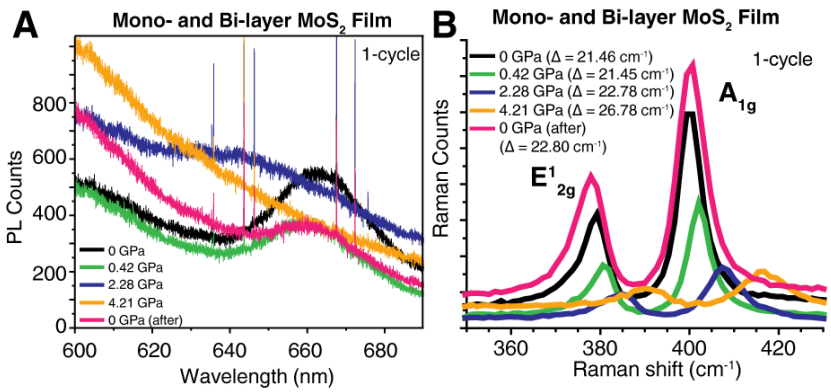

Figure A3-4 | Photoluminescence (A) and Raman shift (B) of a 1-cycle MoS_2 under pressure.

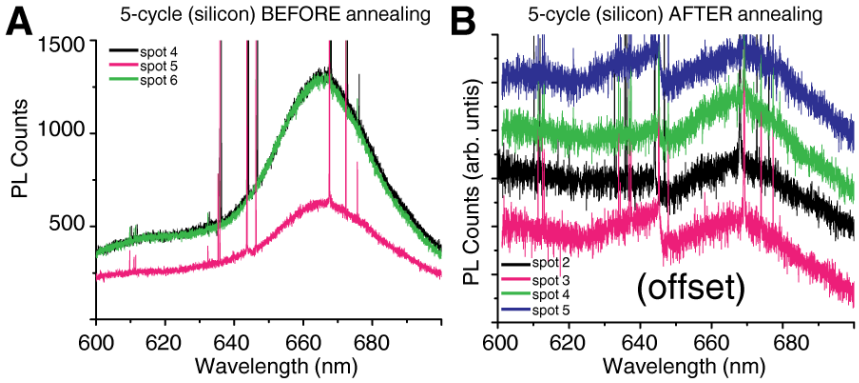

Figure A3-5 | Photoluminescence of a 5-cycle nBuLi-MoS_2 film before (A) and after (B) annealing at 300 °C under N_2 (g)

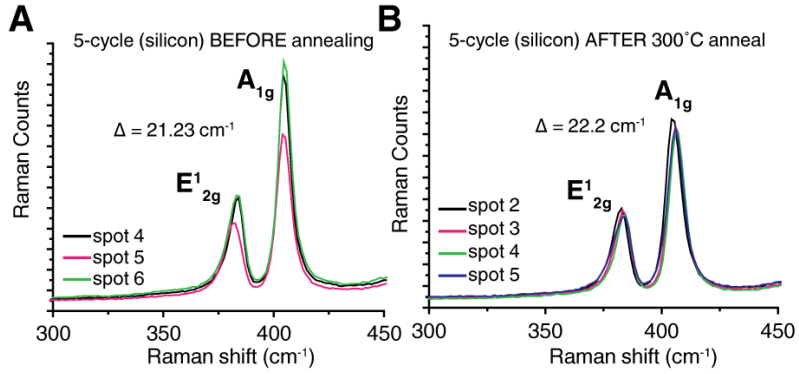

Figure A3-6 | Raman shift of a 5-cycle nBuLi-MoS_2 film before (A) and after (B) annealing at 300 °C under N_2 (g)

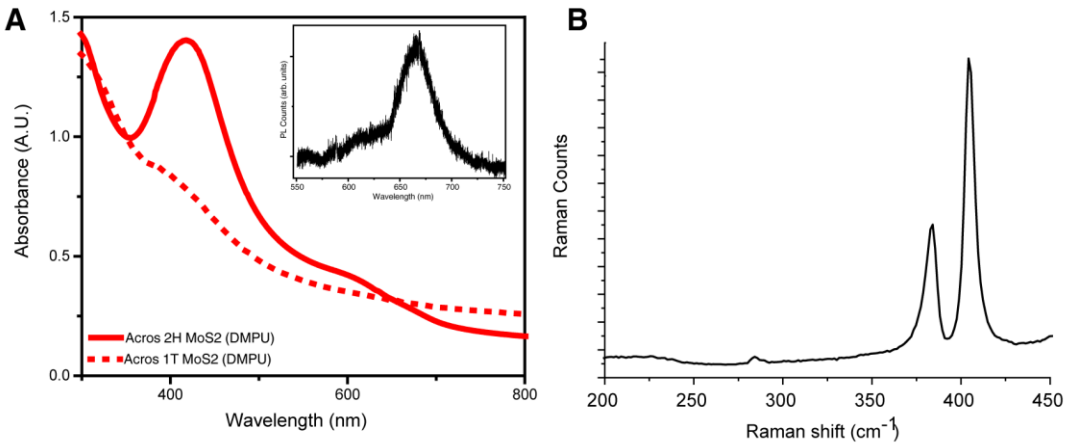

Figure A3-7 | Conversion of nBuLi-exfoliated monolayer MoS_2 from the 1T metallic phase to 2H semiconducting phase. (A) UV-vis shows emergence of C exciton peak for the 2H phase (solid line). Inset: Photoluminesence of film of exfoliated 2H flakes. **(B)** Raman spectrum confirm absence of peaks in 20 0– 275 cm^{-1} and 300 – 350 cm^{-1} to demonstrate full conversion to 2H.

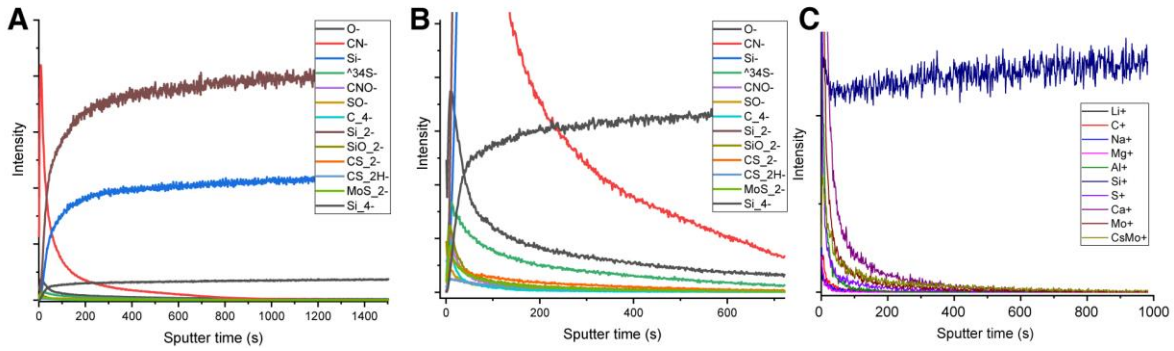

Figure A3-8 | SIMS data of a 5-cycle nBuLi-MoS_2 film on silicon with the anions (A, B [zoom]) and cations **(C)** shown as function of sputter time. This data shows the presence of the CN^- anion that is residue from the DMPU solvent used in the conversion of 1T MoS_2 to 2H phase.

Table A3-1 | Table of Raman peak frequency differences ($\Delta = A_{1g} - E^1_{2g}$) for single crystals of exfoliated MoS_2

Laser line (nm)	1L Δ cm^{-1}	2L Δ cm^{-1}	3L Δ cm^{-1}	bulk Δ cm^{-1}	Reference
325	20.7	22.7	23.5	25.3	1
488	18.1	22.2	23.3	25	1
***514.5**	18.7	21.6	23.1	25.5	2
^514 (CVD)	20.6	22.3			3
532	18	20.2	23.3	24.8	1
***532**	20	22.1	23.6	24.8	2
532 *air	19.6	22.3	23.9	24.8	2
632.8	18.8	21	21.7	25.1	1

Table A3-2 | Peak frequency differences ($\Delta = A_{1g} - E^1_{2g}$) in films of nBuLi-exfoliated MoS_2 of varying thickness

Laser line	Thickness A	Thickness B	Thickness C	Reference
442 (Silicon)	21.47 (1-cycle)	21.48 (2-cycle)	21.48 (3-cycle)	this work
514	22.1 (1.3 nm)	22.1 (1.9 nm)	23 (7.5 nm)	Ref(4)

Table A3-3 | Raman peak frequency differences ($\Delta = A_{1g} - E^1_{2g}$) for rotated bilayers of MoS_2

Rotation (°)	Laser: 532 nm[5]	Rotation (°)	Laser: 532 nm[6]
0	22.74	0	22.5–24
7.3	21.32	5	22
13.2	22	15	21.5–22
21.8	21.66	20	21.5–22.5
27.8	20.64	30	21.4–21.6
32.2	20.44	45	21.8
38.2	19.9	55	22.4
46.8	21.21	60	22.4–23
52.7	21.45		
60	22.14		

REFERENCES

1. Li, H.; Zhang, Q.; Yap, C. C. R.; Tay, B. K.; Edwin, T. H. T.; Olivier, A.; Baillargeat, D., From bulk to monolayer MoS2: evolution of Raman scattering. *Advanced Functional Materials* **2012,** *22* (7), 1385-1390.

2. Lee, C.; Yan, H.; Brus, L. E.; Heinz, T. F.; Hone, J.; Ryu, S., Anomalous lattice vibrations of single-and few-layer MoS2. *ACS nano* **2010,** *4* (5), 2695-2700.

3. Zhan, Y.; Liu, Z.; Najmaei, S.; Ajayan, P. M.; Lou, J., Large-area vapor-phase growth and characterization of MoS2 atomic layers on a SiO2 substrate. *Small* **2012,** *8* (7), 966-971.

4. Eda, G.; Yamaguchi, H.; Voiry, D.; Fujita, T.; Chen, M.; Chhowalla, M., Photoluminescence from chemically exfoliated MoS_2. *Nano Letters* **2011,** *11* (12), 5111-6.

5. Huang, S.; Liang, L.; Ling, X.; Puretzky, A. A.; Geohegan, D. B.; Sumpter, B. G.; Kong, J.; Meunier, V.; Dresselhaus, M. S., Low-frequency interlayer Raman modes to probe interface of twisted bilayer MoS2. *Nano letters* **2016,** *16* (2), 1435-1444.

6. Liu, K.; Zhang, L.; Cao, T.; Jin, C.; Qiu, D.; Zhou, Q.; Zettl, A.; Yang, P.; Louie, S. G.; Wang, F., Evolution of interlayer coupling in twisted molybdenum disulfide bilayers. *Nature communications* **2014,** *5*, 4966.

APPENDIX 4: SUPPORTING INFORMATION FOR CHAPTER FIVE

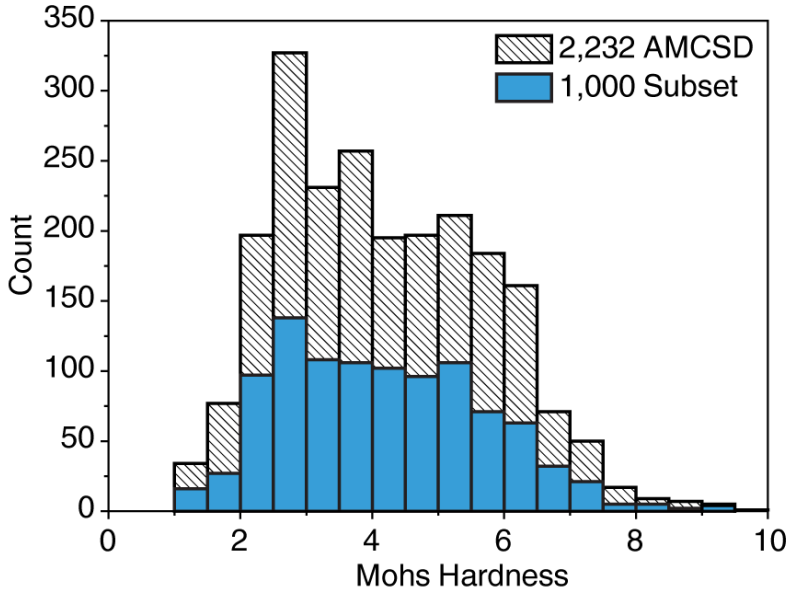

Figure A4-1 | Distribution of minerals across Mohs Hardness scale. The white patterned columns represent 2,232 minerals cross-listed between the AMCSD[1] and HoM[2] databases. The blue distribution is a 1,000 mineral subset of these minerals used in our study. Note the close resemblance between the two, indicating the subset is a good representation of the overall database.

Layered Criteria

Our identification of layered structure types is based on a bond density model. We identified a crystal structure as "layered" if it had one set of parallel planes that existed with a lower density of atoms/bonding than elsewhere. The known cleavage plane reported in the literature[2] must also coincide with the one predicted from the crystal structure (i.e. our identified plane with low bond density). However, there are also examples (faizievite, Figure A4-2A) where we classify something as layered and there is no cleavage reported in the literature. For crystals with multiple cleavage planes, there must be one that is better than others (perfect vs. good). Natrolite (Figure A4-2B) is an example of a non-layered classification because it has perfect cleavage along two different planes, (110) and (-110).

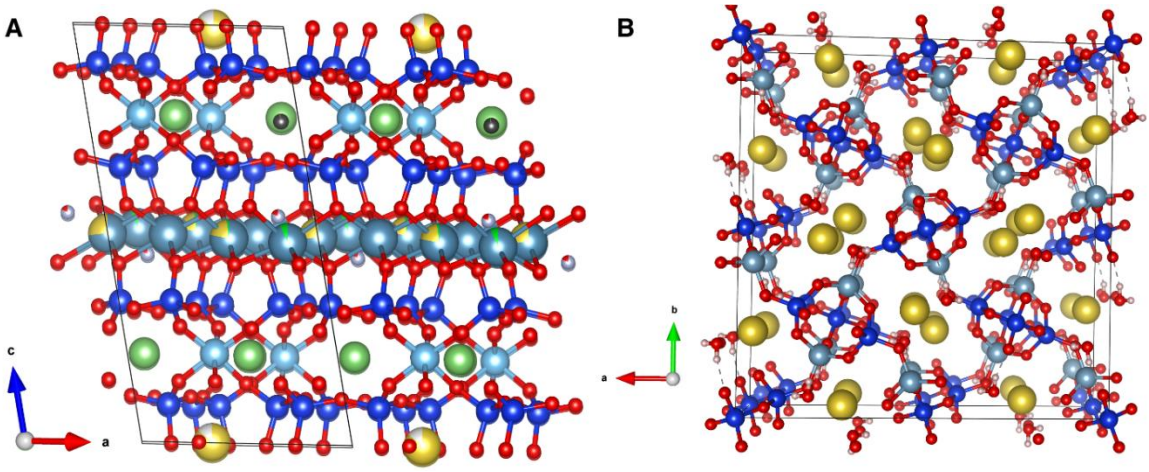

Figure A4-2 | Layered vs. non-layered assignment. (A) Faizievite (Mohs = 4.25) is an example of a layered assignment with no reported cleavage plane. We assign a cleavage plane of (001). **(B)** Natrolite (Mohs = 5.25) is an example of a non-layered assignment because of multiple perfect cleavage planes, (110) and (-110).

A few notes on the layered assignment:

- The presence of a single reported perfect cleavage plane in the literature does not necessarily lead to a layered classification. This crystal structure must be inspected for bond density considerations.
- A few cleavage planes are misreported in the literature. In several cases, this is due to a mismatch between the lattice parameters of the CIF file and the lattice parameters in the literature report. Use discretion.
- A quick visual inspection can be insufficient to determine whether a crystal is layered. Quantitative analysis of the number and type of bonds may be required with consideration of the cleavage plane of interest. For example, comparing the bond density in # bonds/surface area along the (001) vs (100) planes.

Table A4-1 | Line profiles of AFM images in Figure A4-3

Bond Type	Mineral Name	ID	Mohs: lit (*expt*)	Composition	profile 1 (nm)	profile 2 (nm)	profile 3 (nm)	profile 4 (nm)	profile 5 (nm)	profile 6 (nm)	profile 7 (nm)	profile 8 (nm)	profile 9 (nm)
van der Waals	**Pyrophyllite**	**a1**	1.5 (*1.5-2*)	$Al_2Si_4O_{10}(OH)_2$	3.52	2.81 + 1.18 step	6.22 + 1.49 step	2.57					
		a2			2.06	Steps: 1.68/1.15/ 1.77/3.36/ 1.41	Steps: 1.77/6.00	3.8					
	Orpiment	**b1**	1.75 (*1.5-2*)	As_2S_3	8.88	6.94	3.06						
		b2			4.14	step: 2.11							
		b3			6.94	12.52	step: 2.82						
		b4			4.2	6.44	steps: 1.17/2.55 /2.82						
		b5			3.83	2.29 + 0.76 step	step: 5.13						
		b6			3.43	5.91	3.7	3.55	2.43				
		b7			3.26	2.19	step: 12.57						
		b8			step: 1.81	3.84	2.04						
H-bond	**Brucite**	**c1**	2.5 (*2*)	$Mg(OH)_2$	4.31 + step: 1.00	5.25 + step: 0.96	4.04						

		c2			4.77	4.43	step: 0.95							
		c3			4.5	7.02								
		c4			1.13	2.56	step:0.864	step: 1.08						
		c5			1.22	2.37 + step: 0.98								
		c6			1.11 + step: 0.61	2.38								
		c7			3.41	3.77	step: 1.14	2.52	3.14					
		c8			2.22	step: 1.3	2.43							
	Pyrochroite	**d1**	2.5 (*4.5*)	$Mn(OH)_2$	501	239	308	483						
H-bond (water)	**Gypsum**	**e1**	1.75 (*2*)	$CaSO_4 \bullet 2H_2O$	steps: 3.79/7.25	9.67	16.54	15.99	15.33					
		e2			11.04	31.05	steps: 3.70/4.12 /8.19							
		e3			11.77	12.33	step: 1.11	11.74						
	Erythrite	**f1**	2 (*2*)	$Co_3(AsO4)_2 \bullet 8H_2O$	10.08	10.57	12.44							
		f2			steps: 3/3.4/12.2/ 8.9/3.3/2.5 /9.3/7.5/5. 1/14.9/25	step: 24.99	step: 15.04	step: 2.95	step: 3.41	21.11	step: 2.60	8.33	9.65	
		f3			6.41	6.53	25.31	32.89						

		f4			7.8	11.7	11.7	63.9	8.3 + 14.8 step	14.3 + steps: 14.8/28.3				
		f5			14.2	step: 3.64	13.3	6.93 + steps: 5.45/5.45/21.25	4.66 + 2.61 step					
		f6			18.94	32.86	steps: 4.45/4.73	19.22						
	Posnjakite	**g1**	2.25 (*1*)	$Cu_4(SO_4)(OH)_6 \cdot H_2O$	19.22	9.19	16	6.16	31.53	12.5				
		g2			10.2	10 + steps: 1.5/1.5/1.3	8.2	9.4	11.2	21.3 + steps: 4.2/10.4/14.4/8.4				
		g3			25.92 + step: 2.72	9.88	3.63	step: 2.05	12.06					
		g4			4.24	5.12	3.98	5.67						
		g5			4.64	4.84	15.11 + step: 15.51	3.84	4.57	4.37	4.37	4.51		
	Kottigite	**h1**	2.5 (*n/a*)	$Zn_3(AsO_4)_2 \cdot 8H_2O$	114.1 + step: 81.9	89	128.3	78.6	26 + step: 46.9					
Ionic	**Biotite**	**i1**	2.75 (*1.5–2*)	$K(Mg; Fe^{2+})_3(Al; Fe^{3+})Si_3O_{10}(OH; F)_2$	7.9	7.96	7.21	13.23	12.1	5.53 + 1.77 step	steps: 2.32/3.42	5.5	5.21	
		i2			step: 2.19	5.1	7.86	step: 1.93	5.73					

	i3			7.39	7.13	step:7.01	step: 1.32	5.27				
	i4			4.61	4.48	step: 4.86	4.53	4.97				
Muscovite	**j1**	2.5 (*2–2.5*)	$KAl_2(Si_3Al)O_{10}(OH; F)_2$	1.256	3.657	1.842	1.497					
	j2			1.606	1.25	2.058						
	j3			2.48	4.18	4.18 + 8.17 step	7.06					
Lepidolite	**k1**	3.25 (*2.5*)	$K(Li; Al)_3(Si; Al)_4O_{10}(F; OH)_2$	3.33 + 1.85 step	4.81	2.8	4.63					
	k2			1.73	3.91	1.60 + 1.37 step	2.11	1.45				
	k3			1.72	2.07	2.86	1.82	2.42 + 4.59 step	3.19	step: 1.72	step: 1.93	steps: 1.26/1.16
Clintonite	**l1**	3.5 (*2.5*)	$Ca(Mg; Al)_3(Al_3Si)O_{10}(OH)_2$	6.18 + 11.55 step	4.83	6.40 + 10.74 step	16.38	18.35				
	l2			1.86 + 1.86 step	3.82	step: 0.68	step: 2.41	3.81	6.7			
	l3			7.33	7.12	7.74						
	l4			4.65	5.14	4.61	4.1					
Sanbornite	**m1**	5 (*5.5*)	$BaSi_2O_5$	24.59	20.18	19.08						
	m2			16.04	step: 13.63	36.85	23.41	step: 1.96	14.52			
	m3			step: 3.5	steps: 22.4/2.8/24	23.5	52					

Covalent	**Covellite**		1.75 (2.5)	CuS									
		n1			12.01	5.42	2.73 + 8.18 step	4.66	4.89	4.73	5.23	4.69	
		n2			9.33 + 5.40 step	3.22	10.37	3.98	4.97				
	Smithite	**o1**	1.75 (*n/a*)	$AgAsS_2$	39.9 + 46.1 step	125.9	137.6	84.8	76.2	72.5	59.6 + 76.2 step		
		o2			83.7	82.4	18.4	38					
	Eudidymite	**p1**	6 (*2.5–4**)	$NaBeSi_3O_7(OH)$	51.8	9.3	7.3	9.5					
		p2			21.1 + 13.8 step	24.4 + 15.7 step	17.8	15.3	30.8 + 11.9 step	11.9 + 23.9 step	69.1	8.48	10.22
		p3			3.03 / 32.95	16.95	10.61	2.94					
	Stilpnomelane	**q1**	3.5 (*3.5*)	$K(Fe^{2+};Mg;Fe^{3+})_8(Si;Al)_{12}(O;OH)_{27}$	10.31 + 36.67 step	18.66 +26.74 step	35.37 + 24.32 step						

Figure A4-3 | AFM images with line profiles of minerals in Table A4-1

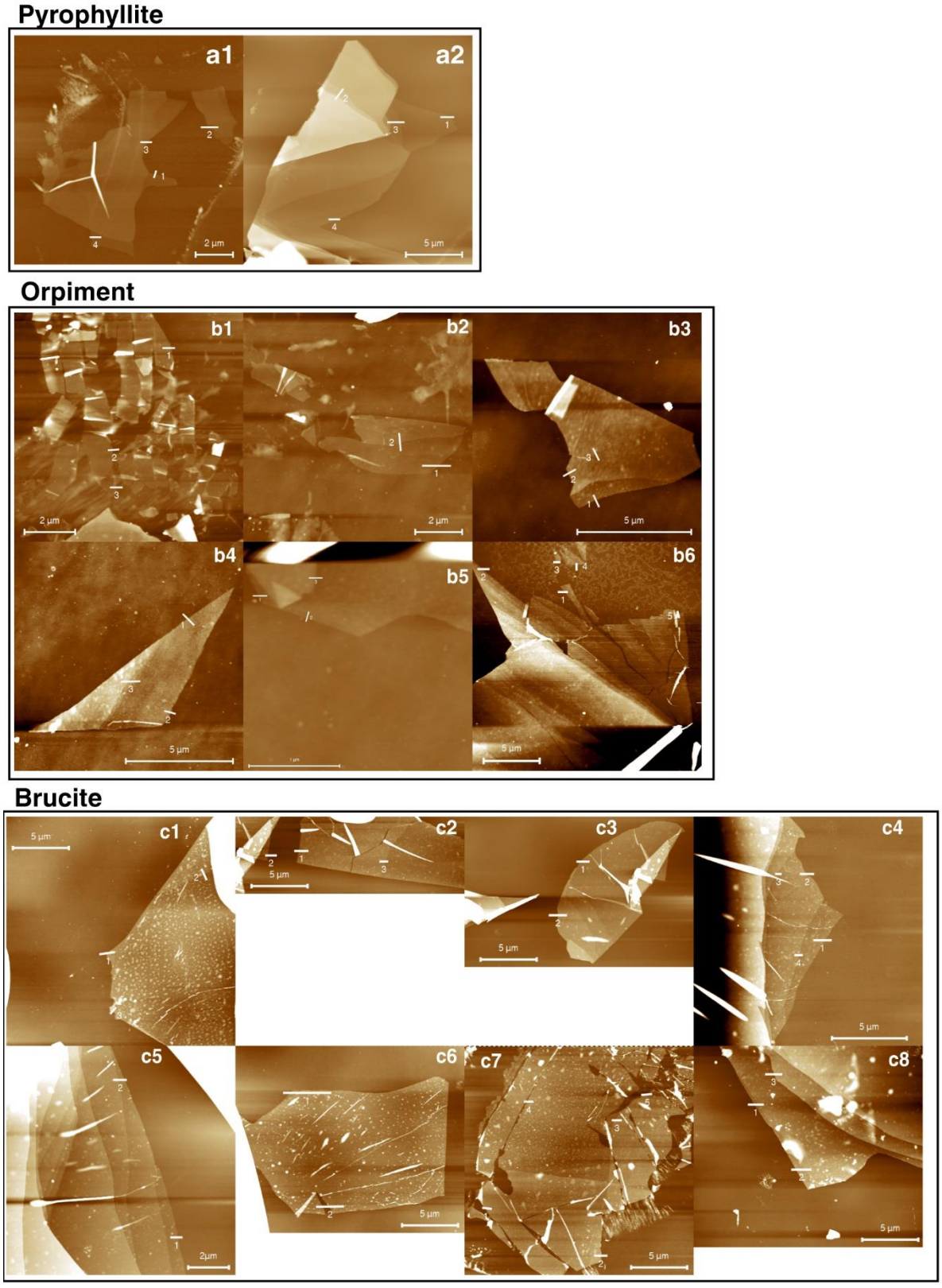

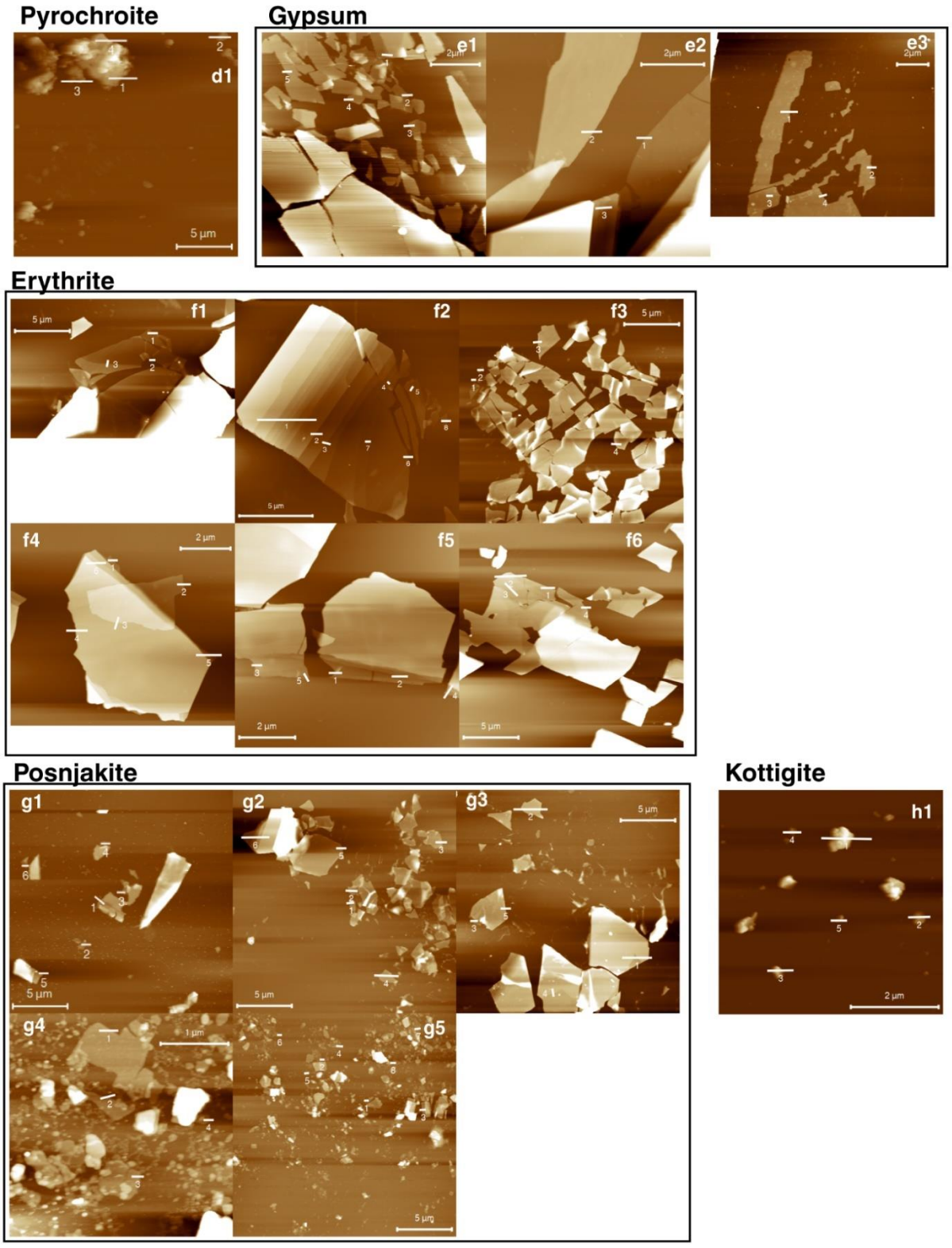
Pyrochroite
d1
5 µm
Gypsum
e1
e2
e3
Erythrite
f1
f2
f3
f4
f5
f6
Posnjakite
g1
g2
g3
g4
g5
Kottigite
h1
2 µm

Biotite

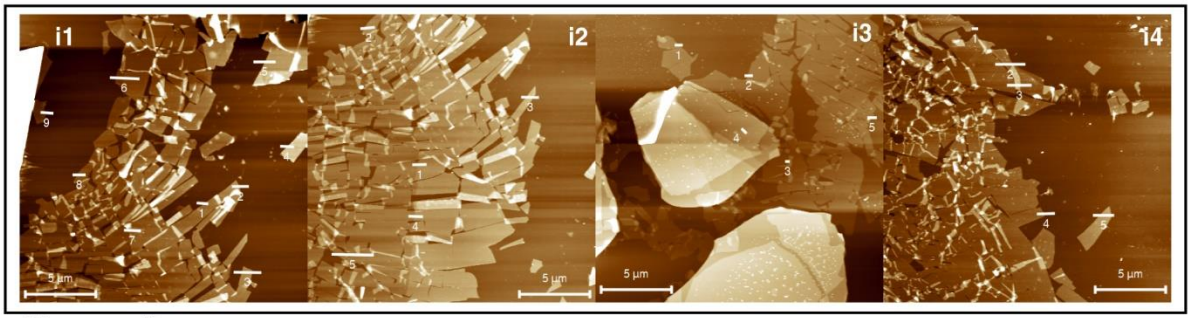

Muscovite

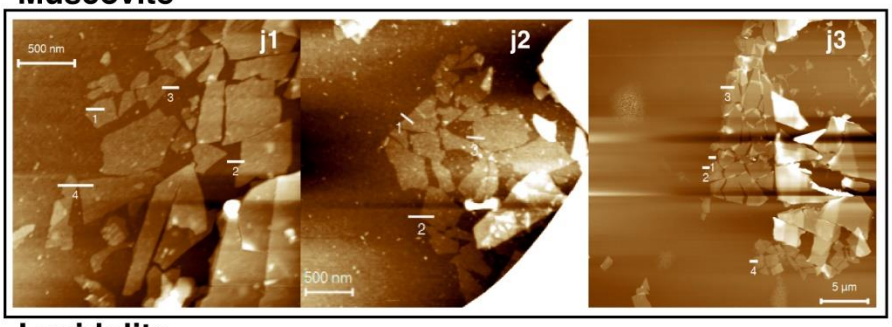

Lepidolite

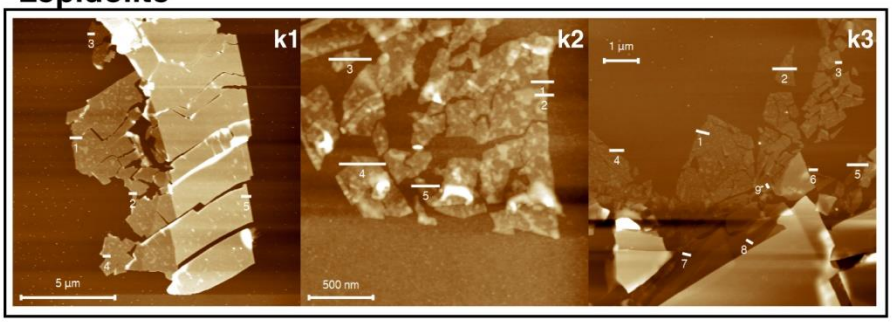

Clintonite

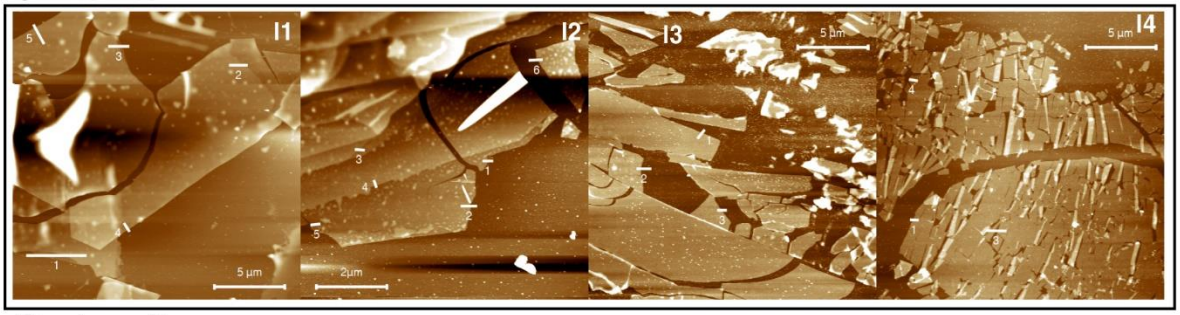

Sanbornite

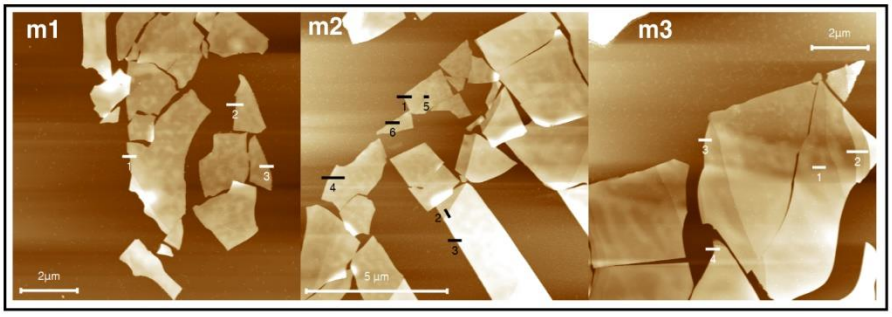

Covellite

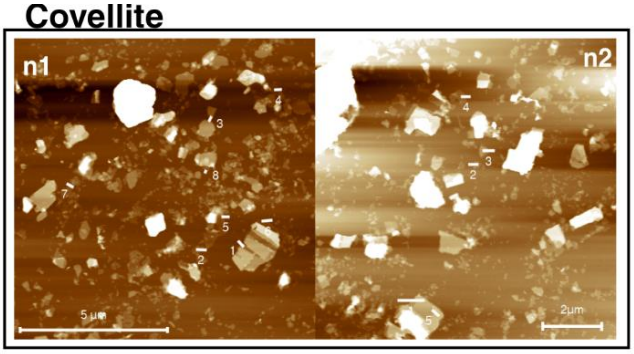

Smithite

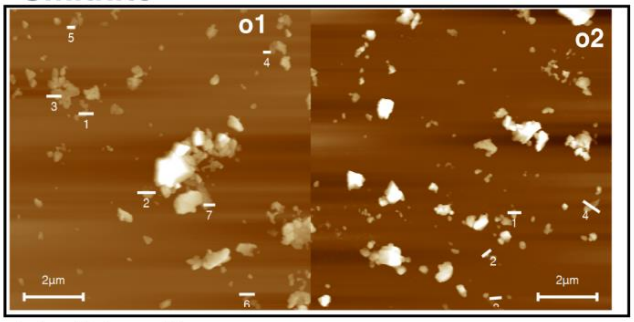

Eudidymite

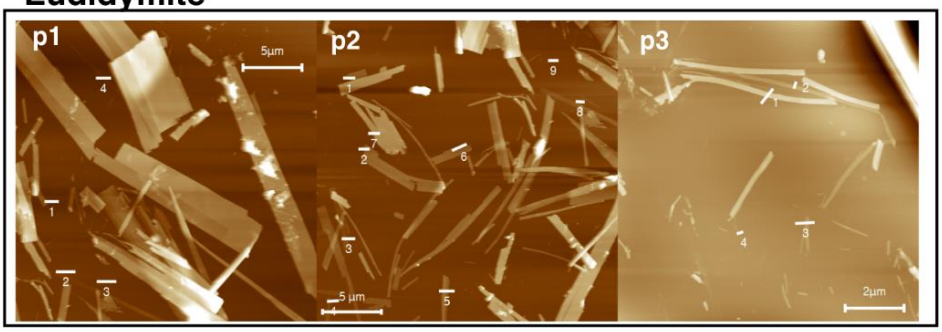

Stilpnomelane

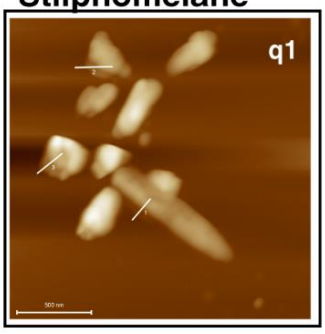

Table A4-2 | Layered minerals from 1,000 mineral subset

AMCSD Mineral Name[1]	Composition	Ave. Mohs[2]	1 vdW	2 h-bond	3 ionic	4 covalent	plane	notes
Bluebellite	Cu6[IO3)(OH)3](OH)7Cl	1		16			(001)	O-H-O = 2.60 A. Short! No interdigitation of H-bonds.
Larisaite	Na(H3O)(UO2)3(SeO3)2O2 •4(H2O)	1			3		(010)	2 Na, 1 K ions. No significant H bonds. Perfect cleavage on (010)
Carlinite	Tl2S	1	yes				(001)	Perfect cleavage on (0001)
Valleriite	4(Fe, Cu)S • 3(Mg, Al)(OH)2	1	yes				(001)	excellent cleavage on (001); broken S-S vdW interactions. Long Fe-S, Cu-S bonds in-plane
Mojaveite	Cu6[TeO4(OH)2](OH)7Cl	1		10	1			perfect cleavage on (001); 1 Cl/unit cell involved with h-bonding
Anthoinite	WAlO3(OH)3(?)	1		yes			(001)	perfect cleavage reported on "one direction"; weird bonding
Molybdenite	MoS2	1.25	yes					
Motukoreaite	Mg6Al3(OH)18[Na(H2O)6] [SO4]2 · 6H2O	1.25		9			(001)	O-H-O. Molecular interlayer. Perfect cleavage but facet not reported.
Melonite	NiTe2	1.25	1				(0001)	Perfect cleavage on (0001); 3.46 A Te-Te
Kenhsuite	γ–Hg3S2Cl2	1.25			2		(100)	excellent cleavage on (100) [Durovic]; HoM incorrectly states perfect on (001)
Sternbergite	AgFe2S3	1.25				4 or 8	(001)	perfect cleavage on (001); either Ag-S or Fe-S bonds broken; likely Ag-S (4)
Vermiculite	(Mg; Fe 3+; Al)3(Si; Al)4O10(OH)2 ² 4H2O	1.5		6			(001)	2.766 A O-H-O distance. 50% of H is used in H-bond
Simonkolleite	Zn5Cl2(OH)8 · H2O	1.5		1 + 6			(001)	1 medium H-bond (2.949 A) and 6 super weak H bonds (H-Cl)
Kuzelite	Ca4Al2(SO4)(OH)12 • 6H2O	1.5		yes	yes		(001)	Perfect cleavage on (001)
Nagyagite	(Te, Au)Pb(Pb, Sb)S2	1.5						By eye, you may expect (001); but perfect cleavage on (010) and excellent on (101) [both similar]; based on am. Miner. Paper 84, 669-676, 1999
Birnessite	(Na, Ca)0.5(Mn4+,Mn3+)2O4 • 1.5H2O	1.5		yes	yes		(001)	no cleavage listed;

Smithite	AgAsS2	1.75	yes			maybe	(100)	Ag-S interactions between cleavage plane (100) at 2.835 A. Common Ag-S is 2.7 A. Shotest Ag-S in material is 2.5 A
Covellite	CuS	1.75				1	(001)	Unclear if breaking one covalent (S-S) or ionic (Cu-S) bond per cell. Cleavage perfect on (001).
Bariosincosite	BaV2O2(PO4)2•4(H2O)	1.75		yes	yes			
Tellurobismuthite	Bi2Te3	1.75	yes				(001)	perfect cleavage on (001)
Arupite	Ni3(PO4)2 • 8H2O	1.75		4			(010)	no cleavage reported in HoM; webmineral lists "good" but no plane
Picropharmacolite	Ca4Mg(AsO4)2(HAsO3OH)2 • 11H2O	1.75		yes	yes		(100)	perfect cleavage on (100), (010); by structure analysis, (100) is obvious
Glauconite	(K; Na)(Fe 3+; Al;Mg)2(Si; Al)4O10(OH)2	2			5		(001)	K-O interaction @ 2.93A to 3.19 A… essentially interaction with O lone pair b/c O bonding is saturated
pääkkönenite	Sb2AsS2	2	yes				OFF AXIS	Sb-S distance is 3.55 A. 4 A is vdW. 2.5 is covalent.
Megacyclite	Na8KSi9O18(OH)9 ²19H2O	2		16	16		(001)	platelets connected by ionic bonding
Alfredstelznerite	Ca4(H2O)4[B4O4(OH)6]4(H2O)15	2		yes… 12?			(010)	
Cualstibite	Al Cu2 H12 O12 Sb	2		9			(001)	
Meyerhofferite -- interesting case of in-plane H-bond	Ca2B6O6(OH)10•2(H2O)	2		6			(010)	Fascinating case of chains with direction-dependent H-bond density. Cleaves on (010), which is also has a lower density of H-bonds. 2.78 A O-H-O
Bijvoetite-(Y)	Y6REE2(UO2)16O8(OH)8(CO3)16•39(H2O)	2		yes			(010)	
Takovite	Ni6Al2(OH)16[CO3] · 4H2O	2		1			(001)	2.82 A O-H-O strong bond
Livingstonite	HgSb4S8	2	yes					Perfect cleavage on (001)
Koritnigite	Zn(AsO3OH) •H2O	2		yes			(010)	Perfect cleavage on (010)
Cobaltkoritnigite	(Co, Zn)(AsO3OH) •H2O	2	may be	yes			(010)	Perfect cleavage on (010)
Abhurite	Sn2+ 21 O6Cl16(OH)14	2		yes	4		(001)	no cleavage reported; along (001), Cl ions and H-bonding; odd in-plane Sn bonds
Litharge	PbO	2	yes				(001)	literature claims distinct cleavage along (110); but long Pb-Pb bonds on (001);

								https://www.reade.com/products/litharge-lead-ii-oxide-lead-monoxide
Richelsdorfite	Ca2Cu5Sb5+(AsO4)4(OH)6Cl • 6H2O	2		yes		4	(001)	perfect cleavage on (001); breaking of Sb-O bonds (1.97 A), many water molecules
Mirabilite	Na2SO4 • 10H2O	2		12			(100)	perfect cleavage on (100)
Deliensite	Fe2+(UO2)2(SO4)2(OH)2 • 3H2O	2		yes		yes	(100)	(breaking of 2 Fe-O bonds (2.33A) and multiple water interactions (> 6)
Spangolite	Cu6Al(SO4)Cl(OH)12 • 3H2O	2		yes	1		(001)	perfect cleavage on (001)
Svenekite	Ca[AsO2(OH)2]2	2		2	yes		(010)	very good cleavage on (010)
Luneburgite	Mg3B2(PO4)2(OH)6•6H2O	2		2	maybe		(010)	fair cleavage on (010)
Scotlandite	PbS4+O3	2				yes	unclear	perfect cleavage on (100); It's not obvious to me because (001) seems much more likely; also note the S4+ charge
Paraguanajuatite	Bi2(Se, S)3	2	yes				(001)	perfect cleavage on (001)
Pyrostilpnite	Ag3SbS3	2				2	(010)	no cleavage listed; Ag-S (2.76A) linkages
sodiumzippeite (sp-natro)	Na4(UO2)6(SO4)3(OH)10 • 4H2O	2		yes	yes		(010)	perfect cleavage on (010)
Rauchite	Ni(UO2)2(AsO4)2·10H2O	2		yes	maybe		(001)	perfect cleavage on (001)
Iowaite	Mg6Fe3+ 2 Cl2(OH)16 • 4H2O	2		yes	yes		(001)	perfect cleavage on (001); Cl and/or water molecules between layers
Thomsenolite	NaCaAlF6 •H2O	2		yes	yes		(001)	perfect cleavage on (001); another example of highly ionic in-layer and out-of-plane
Peprossiite-(Ce)	(Ce,La)Al2B3O9	2	maybe		maybe		(001)	perfect cleavage on (001)
Revdite	Na16Si16O27(OH)26 ²28H2O	2		yes	4		(100)	perfect cleavage on (001)
Bazhenovite	CaS5 •CaS2O3 • 6Ca(OH)2 • 20H2O	2			yes	yes	(010)	good cleavage on (010); very strange sulfur bonding
Aravaipaite	Pb3AlF9 •H2O	2		yes	2		(001)	perfect (micaceous) cleavage on (001)
Portlandite	Ca(OH)2	2		yes			(001)	perfect cleavage on (001)
Tellurite	TeO2	2	yes				(100)	perfect cleavage on (100)
Gerhardtite	Cu2(NO3)(OH)3	2		yes			(001)	perfect cleavage on (001)...HoM misreports as (010)

Tyrolite	CaCu5(AsO4)2(CO3)(OH)4 • 6H2O	2		yes	probably	maybe	(100)	perfect, micaceous cleavage on (001) (?); appears to be incorrect, as structure clearly indicates along (100)
Bismoclite	BiOCl	2.25	yes		yes?		(001)	Perfect on (001). Interlayer Bi-Cl distance = 3.49 A, vs. typical Bi-Cl = 3.05 A, vs. vdW = 4.1 A.
Volkovskite	KCa4B6O8(OH)7Cl•4(H2O)	2.25		yes	yes		(010)	Unclear which plane cleaves but 2 are possible… pure H-bond or pure ionic. Perfect cleavage on (010).
Pharmacolite	Ca(HAsO4) · 2H2O	2.25		4			(010)	Perfect cleavage on (010). 2.740 A O-H-O bonds
Metazeunerite	Cu(UO2)2(AsO4)2 · 8H2O	2.25		yes			(001)	
Nordstromite	CuPb3Bi7(Se4S10)	2.25	borderline		yes		(10-1)	Crosslinked sheets with Bi-S distance that is between ionic and vdW (3.3 A vs. 2.8 A vs. 4.1 A)
Posnjakite	Cu4(SO4)(OH)6 · H2O	2.25		8			(001)	2.74 A, 3.27 A, 2.87, 3.18 A H-bond distances. Perfect cleavage but plane not stated.
Metauranocircite I	Ba(UO2)2(PO4)2 • 8H2O	2.25		yes	2		(010)	Bridging Ba ions; 3 Ba-O bonds ~ 2.9-2.95A
Borax	Na2B4O5(OH)4 • 8H2O	2.25		10			(100)	Perfect cleavage on (100); note in-plane ionic and h-bonding
Botryogen	MgFe3+(SO4)2(OH) • 7H2O	2.25		yes			(010)	1D ; perfect cleavage listed along (010)
Bismuthinite	Bi2S3	2.25	yes				(100)	** based on our observed crystal structure…the literature reports perfect cleavage on (010), which is consistent with labeled axes.
Uranospathite	HAl(UO2)4(PO4)4 • 40H2O	2.25		yes	yes		(100)	mislabeling of axes; different sources swap a- and c- axis; perfect cleavage on longer direction of unit cell
Barlowite	Cu4FBr(OH)6	2.25		yes	2	2	(001)	perfect cleavage on (001); 1 F ion, 1 Br/Cl, and 2 Cu-O + H-bonds
Vendidaite	Al2(SO4)(OH)3Cl •6H2O	2.25		2	2		(010)	perfect cleavage on (010)
Greifensteinite	Ca2Be4(Fe2+,Mn)5(PO4)6(OH)4 • 6H2O	2.25			1	6	(100)	parting cleavage on (100)
Haidingerite	Ca(AsO3OH) •H2O	2.25		4			(010)	perfect cleavage on (010); 1.90A H-bond

Lorandite	TlAsS2	2.25	yes			2	(100)	excellent cleavage on (100); long Tl-S bonds (3.64A) possible, shorter Tl-S (3.23A) link layers
Clinochlore	(Mg; Fe 2+)5Al(Si3Al)O10(OH)8	2.25	may be	likely			(001)	perfect cleavage on (001)
Chalcothallite	Tl2(Cu, Fe)6SbS4	2.25	yes			yes	(001)	perfect cleavage on (001)
Tangdanite	Ca2Cu9(AsO4)4(SO4)0.5(OH)9·9H2O	2.25		maybe	maybe	2	(100)	perfect cleavage on (100)
Palygorskite	(Mg; Al)2Si4O10(OH) ² 4H2O	2.25		yes	maybe	1	(110)	good cleavage on (110)
Melanovanadite	Ca(V5+, V4+)4O10 • 5H2O	2.5		5	1		(010)	5 H-bonds is a guess.
Strontioginorite	SrCaB14O20(OH)6 • 5H2O	2.5		yes, about 12		2	(010)	2 B-O-Ca or B-O-Sr bonds, the rest are h-bonds. Perfect cleavage in minearl on (010)
Preiswerkite	Na(Mg2Al)(Al2Si2)O10(OH)2	2.5		2		4	(001)	Si-O-Mg. Long H-bonds (2.42 A, 1.0A). Mineral cleaves on (001).
Zhangpeishanite	BaFCl	2.5			2		(001)	3.195 A Ba-Cl distance. This is a typical Ba-Cl distance. Mineral cleaves on (001).
Montetrisaite	Cu6(SO4)(OH)10•2H2O	2.5		8			(001)	Known to cleave on (001). H-bonding scheme confirmed from published work. Material is fragile in light.
Aramayoite	Ag3Sb2BiS6	2.5				4	(001)	4 Ag-S bonds that are slightly longer (2.93 A) than in-plane bonds (2.77-2.85 A). This is a 50% higher bond density than within the layer. Cleaves on (001).
Chesnokovite	Na2[SiO2(OH)2]•8H2O	2.5		yes			(010)	Perfect cleavage on (010)
Kottigite	Zn3(AsO4)2 · 8H2O	2.5		8			(010)	Rippled 2D layers; perfect cleavage on (010)
Pyrochroite	Mn(OH)2	2.5		2			(001)	very long H-bonding (2.41 A) for a O-H-O distance of 3.36 A (through bonds); perfect cleavage on (001)
Kobyashevite	Cu5(SO4)2(OH)6·4H2O	2.5		5?			(010)	Positions of H are unknown. Cleavage on (010)
Sjogrenite	C0.125 H8 Fe0.25 Mg0.75 O2.875	2.5		2			(001)	2 medium H-bonds (2.92 A). Cleavage on (001).
Joteite	Ca2CuAl(AsO4)[AsO3(OH)]2(OH)2 · 5H2O	2.5		yes			(001)	
Schoepite	(UO2)8O2(OH)12•12(H2O)	2.5		yes			(001)	
Nestolaite	CaSeO3·H2O	2.5		4			(100)	Cleavage on (100)

Torrecillasite	Na(As,Sb)4O6Cl	2.5	yes				(001)	Cleavage on (001). Cl sticks out a little… interdigitation. As-Cl distance = 3.219 A.
Sahlinite	Pb14(AsO4)2O9Cl4	2.5				4	(010)	As-O bond. Perfect on (010).
Uranosphaerite	Bi(UO2)O2(OH)	2.5		2	8		(101)	8 Long Bi-O interlayer bonds (2.97 A) vs. short in-plane Bi-O (2.08 A) vs. vdW (3.85 A). 2.91 A O-H interlayer bonds
Nissonite	Cu2Mg2(PO4)2(OH)2-5H2O	2.5		6			(100)	Perfect cleavage on (100). 2.74 (x2) & 2.87 (x4) A distances.
Goldichite	KFe3+(SO4)2 • 4H2O	2.5		yes			(100)	Perfect cleavage on (100). H-bonding unclear; puckered plane with K channels
Brucite	Mg(OH)2	2.5		yes			(001)	Perfect cleavage on (0001); no clear h-bond orientation of H atom
Metaschoepite	UO3 • 1−2H2O	2.5		yes	maybe		(100)	Cleavage misidentified as (001); most structures listed cations between layers
Ungemachite	K3Na8Fe3+(SO4)6(NO3)2 • 6H2O	2.5		no	yes		(001)	Perfect cleavage on (0001); Na ionic bonding; Water h-bonding is not linking
Wroewolfeite	Cu4(SO4)(OH)6 • 2H2O	2.5		yes	yes		(001)	Perfect cleavage listed as (001), (010), (100); structure indicates along (001)…depends on strength of ionic/h-bond breaking on (010)/(100) and Cu-O bond on (001)
Murmanite	Na2(Ti; Nb)2Si2O9 ² nH2O	2.5		yes	yes		(001)	perfect cleavage on (001)
Angarfite	NaFe3+ 5(PO4)4(OH)4·4H2O	2.5		2	2	4	(010)	poor cleavage on (010); 4 Fe-O, 2 Na ions, four H2O (1.84 and 2.0 A length)
Gordaite	NaZn4(S04)(OH)6CI-6H2O	2.5		yes	2		(001)	perfect cleavage on (001)
Lavendulan	NaCaCu5(AsO4)4Cl • 5H2O	2.5		yes	yes		(010)	good cleavage on (010)
Quenselite	PbMn3+O2(OH)	2.5				4	(001)	perfect cleavage on (001); "nearly micaceous"
Devilline	CaCu4(SO4)2(OH)6 • 3H2O	2.5		probably	4		(100)	perfect cleavage on (100); HoM incorrectly lists as (001) perfect; see Acta Cryst. (1972). B28, 1189
Parafransoletite	Ca3Be2(PO4)2(PO3OH)2 • 4H2O	2.5	2		1		(010)	no cleavage reported; fewer Ca ions along (010), but replaced with H-bonds
Thomasclarkite-(Y)	(Na, Ce)(Y, Ce,La, Nd)(HCO3)(OH)3 • 4H2O	2.5		yes	yes		(010)	perfect cleavage on (010)
Nanpingite	Cs(Al;Mg; Fe 2+;Li)2(Si3Al)O10(OH; F)2	2.5			2		(001)	perfect on (001)
Metavoltine	K2Na6Fe2+Fe3+ 6 O2(SO4)12 • 18H2O	2.5		yes	yes		(001)	perfect cleavage on (001)

Poughite	Fe3+ 2 (Te4+O3)2(SO4) • 3H2O	2.5		>4			(010)	perfect cleavage on (010); H-bonds 1.87, 1.92A
Norrishite	KLiMn 3+ 2 Si4O12	2.5			1		(001)	perfect cleavage on (001)
Polybasite	(Ag, Cu)16Sb2S11	2.5				24	(001)	imperfect cleavage on (001); compare bond density to fedotovite…covalent vs ionic and same Mohs
Fedotovite	K2Cu3O(SO4)3	2.5			8		(100)	perfect cleavage on (100)
Muscovite	KAl2(Si3Al)O10(OH; F)2	2.5			2		(001)	perfect cleavage on (001); Mohs = 2.5 on (001) and 4 perpen. (001)
Semseyite	Pb9Sb8S21	2.5				10	(112)	perfect cleavage on (112); 3.2 A Pb-S bonds (10)
Schultenite	Pb(AsO3OH)	2.5		yes (2?)			(010)	good cleavage on (010)
Amesite	Mg2Al(SiAl)O5(OH)4	2.75		6			(001)	1.74 to 1.8777 A long h-bond, 0.9965 to 1.06 A short h-bond, all are O-H-O
Parapierrotite	S8 Sb5 Tl	2.75	1			3	(101)	
Ankinovichite	Al4 H16 Ni0.72 O20 V1.88 Zn0.28	2.75		5			(100)	Reported to cleave on (010) but this is certainly an error.
Clinoclase	Cu3(AsO4)(OH)3	2.75	yes	maybe			(100)	Misidentified cleavage of (001)
Guanajuatite	Bi2Se3	2.75	yes			maybe	(100)	Corrugated planes with possible interlayer bonding of Bi-Se (3.41 A distance); literature distinct cleavage on (100)
Boromuscovite	KAl2(Si3B)O10(OH; F)2	2.75			yes		(001)	perfect cleavage on (001)
Valentinite	Sb2O3	2.75	3 or 4				(110)	perfect cleavage on (110); 3.9 A vdw gap Sb-Sb on (110); 2.51 Sb-O gap on (010); unclear if would form sheets
Macphersonite	Pb4(SO4)(CO3)2(OH)2	2.75	yes				(010)	perfect cleavage on (010); Pb-Pb (3.8, 3.9 A)
Paragonite	NaAl2(Si3Al)O10(OH)2	2.75			2		(001)	perfect cleavage on (001)
Namuwite	(Zn, Cu)4(SO4)(OH)6 • 4H2O	3		7			(001)	perfect cleavage on (001), 7 O-O contacts within 3.2 A across gap
Antimonpearceite	(Ag, Cu)16(Sb, As)2S11	3	yes			1	(001)	Ag-S-Ag connection. Cleavage known to be fair on (001). Now called polybasite-Tac
Antigorite	(Mg; Fe 2+)3Si2O5(OH)4	3		84		8	(001)	
Kihlmanite-(Ce)	Ce2TiO2[SiO4](HCO3)2(H2O)	3		1.6	0.5		(001)	O-Ca-O
Hydrocalumite	C H44 Al4 Ca8 Cl2 O36.6	3		yes	yes		(001)	

Perite (borderline but clear case for layered ionic)	PbBiClO2	3			yes		(001)	Long Pb-Cl distance (3.25 A). Long Bi-Cl distance (3.43 A). Not vdW (4 A), but longer than normal ionic (2.8-3A). Known to cleave on (001).
Donnayite-(Y)	Sr3NaCaY(CO3)6•3(H2O)	3			yes		(001)	Known to cleave on (001)
Francevillite	Ba(UO2)2(VO4)2 · 5H2O	3		yes	yes		(001)	
Seelite	Mg(UO2)(AsO3)0.52(AsO4)0.5•7(H2O)	3		2+4			(100)	2 short, 4 long
Schneiderhohnite	Fe24As5O13	3			2		(10-1)	Cleavage information incomplete, but claimed to be on (100)
Franklinfurnaceite	Ca2FeMn4(Zn2Si2O10)(OH)8	3		6	2		(001)	O-Ca-O (2) and H-bonds from 3.19 to 3.32 to 2.86 A. Perfect cleavage on (001)
Tarbagataite	(K,)2(Ca,Na)(Fe2+,Mn)7Ti2(Si4O12)2O2(OH)4(OH,F)	3			4		(001)	Perfect cleavage on (001), moderate on (010). Cylindrical channels within the interlayer space.
Favreauite	PbBiCu6O4(SeO3)4(OH)·H2O	3				16	(001)	Perfect cleavage on (001); Pb-O bonding
Gilmarite	Cu3(AsO4)(OH)3	3		maybe		1	(001)	Good cleavage listed on (010), but (001) seems more probable
Liveingite	Pb9As13S28	3	yes			6	(010)	As-O chains (6 bonds/cell) bridging Pb/As-O layers
Iangreyite	Ca2Al7(PO4)2(PO3OH)2(OH,F)15·8H2O	3		yes	yes	4	(001)	Perfect cleavage on (001); hydrogen locations unk.; Al-O (1.85 A) links
Paulmooreite	Pb2As3+ 2 O5	3				2	(100)	Good cleavage on (100), O-As-O (1.83A) x2
Moctezumite	Pb(UO2)(Te4+O3)2	3			6		(100)	Perfect cleavage on (100); cleaves U-O bonds
Foshagite	Ca4Si3O9(OH)2	3		yes	4	2	(001)	distinct cleavage reported on (001)
Tooeleite	Fe3+ 8 (AsO4, SO4)6(OH)6 • 5H2O	3		yes	yes		(001)	good cleavage reported on (010); doesn't make sense. Varying results in literature
Fransoletite	Ca3Be2(PO4)2(PO3OH)2 • 4H2O	3		maybe	1		(010)	imperfect cleavage on (010)
Mountainite	(Ca; Na2; K2)2Si4O10 ² 3H2O	3		yes	4		(100)	cleavage listed as "(001)(?)"
Geigerite	Mn2+ 5 (AsO4)2(AsO3OH)2 • 10H2O	3		2		1	(010)	perfect cleavage on (010)
Lalondeite	(Na,Ca)6Ca3Si16O38(F,OH)2·3H2O	3		yes		2	(001)	perfect cleavage on (001)

Bismutite	Bi2O2(CO3)	3				maybe	(001)	cleavage listed as "probable" on (001)
Laueite	Mn2+Fe3+ 2 (PO4)2(OH)2 • 8H2O	3		yes	mayb e	maybe	(010)	perfect cleavage on (010)
Johillerite	NaCu(Mg, Zn)3(AsO4)3	3			2	8	(010)	perfect cleavage on (010)
Ezcurrite	Na4B10O17 • 7H2O	3		4	2		(110)	excellent cleavage on (110); note that there are in-plane h-bonds
Roeblingite	Pb2Ca6Mn 2+Si6O18(SO4)2(OH)2 ² 4H2O	3				4	(001)	perfect cleavage on (001); long Pb-O bond (2.84A)
Dolerophanite	Cu2O(SO4)	3				1	(-101)	perfect cleavage on (-101)
Holdawayite	Mn2+ 6 (CO3)2(OH)7(Cl, OH)	3		yes	yes	4	(100)	perfect cleavage on (100): 4 Mn-O + Cl-H interactions
Barnesite	(Na, Ca)2V5+ 6 O16 • 3H2O	3			2		(001)	perfect cleavage on (001)
Zincroselite	Ca2Zn(AsO4)2• 2H2O	3		2	2		(010)	good to perfect cleavage on (010)
Tundrite-(Ce)	Na3(Ce;La)4(Ti; Nb)2(SiO4)2(CO3)3O4(OH) ² 2H2O	3			3		(010)	pronounced cleavage on (010; odd mix and water not complete
Freedite	Pb8Cu1+(As3+O3)2O3Cl5	3			10	2	(100)	perfect on (100); 10 Cl ions, 2 Cu-As
Damaraite	Pb4O3Cl2	3		maybe	4		(010)	good cleavage on (010)
Churchite-(Y)	YPO4 • 2H2O	3		yes			(010)	perfect cleavage on (???) – confusion between sources; isostructural with gypsum
Teepleite	Na2B(OH)4Cl	3.25		yes	yes	yes	(001)	Indistinct cleavage. In-plane strength is probably as strong as out-of-plane strength.
Alvanite	(Zn,Ni)Al4(V5+O3)2(OH)1 2 · 2H2O	3.25		6			(100)	2.69 A H-bond distance.
Herbertsmithite	Cu3Zn(OH)6Cl2	3.25		yes	yes	3	(10-11)	Good cleavage on (10-11); Cu-O, Cl ions, and H-bonding
Lepidolite	K(Li; Al)3(Si; Al)4O10(F; OH)2	3.25			2		(001)	perfect cleavage on (001)
Lautite	CuAsS	3.25	1			4	(001)	cleavage reported on (001)
Benjaminite	Ag2.25Cu0.75Bi5Pb2S12	3.4			2		(001)	2 2.5995 A Bi-S. 4 long Bi-S (3.4 A, vdw)
Francisite	Cu3BiO2(Se4+O3)2Cl	3.5	yes		4		(001)	Long Bi-O ionic interaction at 2.80 A (much shorter than vdW) but also 2.44 A within layer. Clear cleavage unknown

Newberyite	Mg(PO3OH)•3H2O	3.5		15			(010)	2.688 A O-H-O distance but longer ones, too Every H is used in H-bond.
Fourmarierite	Pb(UO2)4O3(OH)4 • 4H2O	3.5		16	3		(001)	O-Pb-O, with variable occupancy between natural & synthetic crystals
Volborthite	Cu3V2O7(OH)2 • 2H2O	3.5		4		2	(001)	Cleavage perfect on an unidentified facet. V-O-V covalent bond
Hematolite	Al1.89 As3 Fe0.19 H23 Mg2.53 Mn10.39 O34	3.5			1		(001)	Perfect on (001). O-Mn-O
Soddyite	U2SiOH4	3.5		yes	yes		(001)	
Girvasite	NaCa2Mg3(PO4)2[PO2(OH)2](CO3)(OH)2•4(H2O)	3.5		8			(001)	Super short H-bonds: as short as 2.548 O-H-O (v. strong symmetric bridge) to 2.822 A O-H-O (strong). Cleavage on (001)
Natisite	Na2(TiO)SiO4	3.5			4		(001)	Sheets bridged by Na ions. Perfect (001) cleavage.
Monteregianite-(Y)	K Na1.41 O23.13 Si8 Y	3.5		yes	yes		(010)	Cleavage on (010)
Antlerite	Cu3(SO4)(OH)4	3.5		4	2		(001)	Cleavage on (001).
Stibarsen	AsSb	3.5				4 (1)	(001)	Perfect cleavage. 3.28 A interlayer As-As distance vs. 2.66 A in-plane vs. 4.1 A vdW.
Dietzeite	Ca2(IO3)2(CrO4) •H2O	3.5		yes	2		(100)	Interrupted cleavage on (100)
Gillespite	BaFe 2+Si4O10	3.5			yes	yes	(001)	Either Si-O (4) or Ba-O (8) bonds broken for cleavage
Ohmilite	Sr3(Ti; Fe 3+)(Si2O6)2(O; OH) ²2¡3H2O	3.5		yes	2		(100)	Perfect cleavage on (100); Si-O,Ti-O chains held together by Sr ions in-plane
Weloganite	Na2Sr3Zr(CO3)6 • 3H2O	3.5		maybe	3		(001)	Perfect cleavage on (001); potential long H-bonds
Tikhonenkovite	SrAlF4(OH) •H2O	3.5		yes	yes		(100)	perfect cleavage on (100)
Chalcostibite	CuSbS2	3.5	yes			maybe	(001)	perfect cleavage on (001); vdW? interactions (borderline covalent) of Sb-S (3.2 A separation)
Pentagonite	Ca(V4+O)Si4O10 ² 4H2O	3.5		yes	2	4	(010)	good cleavage on (010)
Gordonite	MgAl2(PO4)2(OH)2 • 8H2O	3.5		3		1	(010)	perfect cleavage on (010)
Usovite	Ba2CaMgAl2F14	3.5			yes		(100)	Perfect cleavage listed but plane unknown; highly ionic species in mica family
Theophrastite	Ni(OH)2	3.5		yes			(001)	perfect cleavage on (001)

Messelite	Ca2(Fe2+,Mn2+)(PO4)2 • 2H2O	3.5	2		2	(001)	perfect cleavage on (001); Ca-O: ionic or covalent?
Bermanite	Mn2+Mn3+ 2 (PO4)2(OH)2 • 4H2O	3.5	yes		5	(001)	perfect cleavage on (001)
Lomonosovite	Na5Ti2O2(Si2O7)(PO4)	3.5					perfect cleavage reported as (100); could not verify citation; seems more likely to be (001) based on structure
Allochalcoselite	Cu+Cu2+ 5PbO2(SeO3)2Cl5	3.5		yes		(100)	perfect cleavage on (100); Cl interactions, notably with Cu, Se, and Pb
Ericlaxmanite	Cu4O(AsO4)2	3.5			4	(010)	distinct cleavage on one direction; Si-O bonds
Rankamaite	(Na, K, Pb,Li)3(Ta, Nb, Al)11(O, OH)30	3.5		2.5	8	(010)	no cleavage reported
Inderborite	CaMg[B3O3(OH)5]2 • 6H2O	3.5	>12	maybe		(100)	good cleavage on (100)
Walpurgite	Bi4(UO2)O4(AsO4)2 • 2H2O	3.5	yes	maybe	maybe	(010)	perfect cleavage on (010); is U-O covalent or Ionic?
Heulandite-Ba	(Ba,Ca,Sr,K,Na)5Al9Si27O72·22H2O	3.5	yes	yes	2	(010)	perfect cleavage on (010); several ionic vacancies
Overite	CaMgAl(PO4)2(OH) • 4H2O	3.75	8	4		(010)	perfect cleavage on (010)
Baratovite	KLi3Ca7(Ti; Zr)2Si12O36F2	3.75		yes ?		(001)	plane with K, Li, and Ti seems most likely to cleave but uncertain
Beta-roselite	As2 Ca2 Co0.532 H4 Mg0.468 O10	3.75	2	2		(010)	Cleavage perfect on (010). As-O-Ca linkage
Heulandite	(Ca; Na2)Al2Si7O18 ² 6H2O	3.75	yes	yes	2	(010)	Perfect cleavage on (010). Hydrated Ca or Na ions. Possible channels.
Kleinite	Hg2N(Cl, SO4) • nH2O	3.75	yes	yes	2	(0001)	Uneven cleavage on (0001)
Bornemanite	BaNa4Ti2NbSi4O17(F; OH) ²Na3PO4	3.75		yes		(001)	perfect cleavage on (001)
Ephesite	NaLiAl2(Al2Si2)O10(OH)2	3.75		2		(001)	perfect cleavage on (001)
Macdonaldite	BaCa4Si16O36(OH)2 ²10H2O	3.75	yes	2		(001)	perfect cleavage on (001) (by structure); good on (010)
Yvonite	Cu(AsO3OH) • 2H2O	3.75	yes			(100)	perfect cleavage on (100)
Fluckite	CaMn2+(AsO3OH)2 • 2H2O	3.75	2			(010)	perfect cleavage on (010); easy cleavage on (100)
Pucherite	BiVO4	4		4		(001)	2.721 Bi-O distance across gap, compared to 2.29, 2.34, 2.58 A Bi-O distances

							elsewhere in structure; cleavage perfect on (001)
Bannisterite	KCa(Mn 2+; Fe 2+; Zn;Mg)20 (Si; Al)32O76(OH)16 ² 4¡12H2O	4	yes	yes		(001)	lamellar, with Mn-O bonds
Colinowensite	BaCuSi2O6	4		16		(001)	Ba-O bond
Montgomeryite	Ca4MgAl4(PO4)6(OH)4 • 12H2O	4	YES	9		(010)	
Creedite	Ca3Al2SO4(F,OH) 10· 2(H2O)	4	YES	4		(100)	Known to cleave on (100).
Yeatmanite	(Mn, Zn)16Sb2Si4O29	4		6		(001)	6 Mn-O interactions per unit cell. Cleavage reported on different plane.
Perraultite	Ba2.5 Ca F4 Fe6.1 H8 K1.2 Mn9.4 Na3 Nb0.32 O72 Si16 Ti7.68 Zr0.3	4	4		12	(001)	8 Si-O and 4 Ti-O linkages & 4 H bonds
Kanemite	NaHSi2O5•3(H2O)	4	4			(010)	2.82 A O-H-O distance. Interdigitation. (010) cleavage reported.
Sampleite	NaCaCu5(PO4)4Cl · 5H2O	4	12	2		(010)	2 bridging waters (Ca-O(H2)-Na) and 12 H bonds. Perfect cleavage on (010).
Qingheiite-(Fe2+)	Na2Fe2+ MgAl(PO4)3	4		yes		(010)	Fascinating case. Qingheiite-Fe2+ has vacancies in a Na+ site compared to normal Qingheiite. Perfect cleavage on this plane (010) in Fe2+ but "indistinct" in normal Qingheiite. Hardness is 4 in Q-Fe but is 5.5 in normal Q. This should make a good 2D material. Shows key role of regular vacancies/defects in enabling cleavage.
Minehillite	K1.9Na0.3Fe0.1Mg0.1Mn0.1Ca27.5Zn4.8Al4.4Si39.4O112(OH)15.2	4		4.552		(001)	Perfect cleavage on (001). Defective plane of K (.948), Zr(1.604), and Al (2)
Partheite	Ag3Pb6Sb11S24	4					
Melanostibite	Mn2+(Sb5+, Fe3+)O3	4		8		(0001)	Perfect cleavage on (0001). Could occur at Mn or Fe. I chose Mn b/c of longer bond lengths
Bussyite-(Ce)	(Ce,REE,Ca)3(Na,H2O)6MnSi9Be5(O,OH)30(F,OH)4	4	yes	yes		(10-1)	Perfect cleavage on (10-1); Na-O/F bonds or water-O/F bonds at break

Ilimaussite-(Ce)	Ba2Na4CeFe 3+Nb2Si8O28 ² 5H2O	4	maybe	yes	yes	(001)	no cleavage reported in literature; Ce-O bond breaking along (001), but could also be along Ba ion
Kipushite	(Cu, Zn)6(PO4)2(OH)6 •H2O	4	maybe		4	(100)	no cleavage reported; 4 P-O bonds (1.52A)
Cupromakovickyite	Cu8Pb4Ag2Bi18S36	4			2	(001)	No cleavage; two areas within unit cell along (001) that have lower bond density (2 Bi-S bonds, 2.64 A)
Waterhouseite	Mn7(PO4)2(OH)8	4		yes	yes	(100)	perfect cleavage on (100); difficult to discern…breaking of 2 PO4 interactions and two Mn-OH bonds
Rajite	CuTe4+ 2 O5	4			5	(010)	cleavage listed as (010); along Cu linkage
Ferrowyllieite	(Na, Ca,Mn2+)2(Fe2+,Mn2+)(Fe 2+, Fe3+,Mg)Al(PO4)3	4		3 or 4	4	(010)	perfect on (010)
Segelerite	CaMgFe3+(PO4)2(OH) • 4H2O	4	yes	4		(010)	perfect on (010)
Plombierite	Ca5H2Si6O18 ² 6H2O(?)	4	yes	0.75		(001)	no cleavage reported; Ca vacancy and water molecules in cleavage plane
Deloryite	Cu4(UO2)(MoO4)2(OH)6	4			1	(100)	perfect cleavage listed as both (100) and (010); (100) is most obvious
Beudantite	PbFe3+ 3 (AsO4)(SO4)(OH)6	4		maybe	yes	(001)	good cleavage on (001); see note on hinsdalite
Symesite	Pb10(SO4)O7Cl4(H2O)	4	yes	8		(001)	perfect cleavage on (001); H atoms NOT included; Dan?
Ferrisicklerite	Li(Fe3+,Mn2+)PO4	4		~1	2	(010)	perfect cleavage on (010); partial Li vacancy; either 2 P-O or 2 Fe-O bonds
Ellingsenite	Na5Ca6Si18O38(OH)13.6H 2O	4	yes			(001)	perfect cleavage on (001); very wide gap (4.8 A) but high Mohs (4)
Ganophyllite	(K,Na,Ca)2Mn8(Si,Al)12(O, OH)32 · 8H2O	4.25	yes	yes	yes	(010)	
Bassoite	SrV3O7·4H2O	4.25	12			(001)	No cleavage observed. Rippled structure that maximizes H-bonding. 6-->3 (4 very strong H) 5-->3 (4 weak H) , 7-->5 (4 weak H)
Collinsite	MgCa2(PO4)2.2(H2O)	4.25	4	4		(010)	4 Ca-O, 4 very short h-bond (2.61 O-H-O distance). Cleavage known on (010)
Pyrosmalite-(Mn)	(Mn2+ , Fe2+)8Si6O15(OH, Cl)10	4.25	maybe	maybe	2	(001)	Perfect cleavage on (0001); linked by silicate clusters: 2 Si-O ; Potential for H-

Bityite	CaLiAl2(AlBeSi2)O10(OH)2	4.25		2 or 3		(001)	bonding between OH and O; Cl ions within pockets Perfect "micaceous" cleavage on (001)
Faizievite	K2Li6Na(Ca6Na)Ti4[Si6O18]2[Si12O30]F2	4.25		7		(001)	no cleavage reported; potential plane along Ca ions; interesting example of no cleavage but possible layered
Prosopite	CaAl2(F, OH)8	4.5	yes	yes		(111)	Ca-F or Al-F ionic bonding
Silinaite	NaLiSi2O5 ² 2H2O	4.5	2		2	(001)	Material cleaves on (001). Si-O-M. M=Na,Li
Umbite	K2ZrSi3O9•(H2O)	4.5	8	4		(010)	4 Zr-O-Si. Perfect on (010).
Roweite (borderline case for inclusion, based on cleavage)	Ca2Mn2+2B4O7(OH)6	4.5	yes	yes		(100)	Known to cleave on (001)
Haradaite	SrVSi2O7	4.5			2	(010)	Cleavage on (010). Si-O-Si bond. Interdigitation.
Chabazite-Ca	(Ca0.5,Na,K)4[Al4Si8O24]•12H2O	4.5	yes	yes	yes	(111)	Known cleavage on same plane. Interlayer Ca and water and Si-O-Al bonds.
Allactite	Mn7(AsO4)2(OH)8	4.5	very long	12		(001)	As-O and Mn-O connections
Junitoite	CaZn2Si2O7 ²H2O	4.5	yes	8	2	(100)	Good cleavage on (100)
Lawsonbauerite	(Mn2+,Mg)9Zn4(SO4)2(OH)22 • 8H2O	4.5	yes	4		(100)	Zn-O-Mn links between layers; some hydrogen bonding. No cleavage reported
Natrochalcite	NaCu2(SO4)2(OH) •H2O	4.5	6	yes		(001)	Perfect cleavage on (001); 6 h-bonds, 4 Na ions
Esperanzaite	NaCa2Al2(AsO4)2F4(OH) • 2H2O	4.5	maybe	yes	yes	(100)	Perfect cleavage listed at (001),but (100) seems more probable along As-O tetrahedra; Na-O, Al-O, As-O
Legrandite	Zn2(AsO4)(OH) •H2O	4.5	8		2	(100)	corrugated along (100); listed as fair to poor on (100); Zn-O-As bond(x2); H-O bonds: 1.81 A (x2)
Yoshimuraite	(Ba; Sr)2Mn 2+ 2 Ti(SiO4)2(PO4; SO4)(OH; Cl)	4.5		2		(010)	perfect cleavage on (010); along Ba ions
Seidozerite	(Na; Ca)2(Zr; Ti;Mn)2Si2O7(O; F)2	4.5		2	2	(001)	

Flinkite	Mn2+ 2 Mn3+(AsO4)(OH)4	4.5	4		2	(100)	no cleavage reported
Ericssonite	BaMn 2+ 2 Fe 3+OSi2O7(OH)	4.5	maybe	2		(100)	perfect on (100); H is in composition but not in structure
Synchysite-(Ce)	Ca(Ce,La)(CO3)2F	4.5		6		(001)	no cleavage reported; Ca ions between Ce/F-CO3 layers
Parisite-(Ce)	Ca(Ce,La)2(CO3)3F2	4.5		yes		(001)	"probably" a parting on (001); interesting example of ionic interactions and CO3 groups
Cafetite	Ca(Fe3+, Al)2Ti4O12 • 4H2O	4.5	yes	2		(001)	while it looks layered along (001); the Ca in the Ti-O plane may present another cleavage plane (two cleavages reported, but direction not specified)
Gerstmannite	(Mg;Mn 2+)2Zn(SiO4)(OH)2	4.5			7	(010)	good cleavage on (010); Zn-O bonds
Hinsdalite	(Pb, Sr)Al3(PO4)(SO4)(OH)6	4.5		mayb e	yes	(001)	perfect cleavage on (001); Pb vacancy may lead to cleavage along P-O bonds…
Kinoite	Ca2Cu2Si3O8(OH)4	4.5	maybe	yes	yes	(010)	excellent cleavage on (010)
Lindgrenite	Cu3(MoO4)2(OH)2	4.5			2	(010)	perfect cleavage on (010); either 2 Si-O or 2 Mo-O
Armstrongite	CaZrSi6O15•2.5H2O	4.6			10	(001)	perfect cleavage on (001); unclear if breakage plane is 10 Si-O or 10 Ca or Zr interactions
Fluorapophyllite	KCa4Si8O20(F; OH) ² 8H2O	4.75	5		4	(001)	
Vergasovaite	Cu3 Mo0.742 O9 S1.258	4.75		4		(001)	S-O-Cu (2) and Mo-O-Cu (2). No reported cleavage.
Innelite	(Na,Mg,Ca)2(Ba,K)4Ti3(Si2O7)2(SO4)2(OH,F)	4.75		yes		(100)	Multiple planes of cleavage seem possible
Namibite* barely layered… closer to 3D case	CuBi2(VO4)2O2	4.75		2		(001)	Cleavage "good" on (001) with no other cleavage reported. Layers connected by low density VO4 tetrahedra.
Wollastonite	CaSiO3	4.75		yes		(100)	Perfect cleavage on (100)
Hydroxyapophyllite	KCa4Si8O20(OH; F) ² 8H2O	4.75	yes	yes	yes	(001)	perfect cleavage on (001); either along SI-O OR Water/Ca/K ions
Bafertisite	Ba(Fe 2+;Mn 2+)2TiOSi2O7(OH; F)2	5	4 or 8	12		(001)	

Turanite *Clear case for ionic interaction in atypical layered material.	Cu5(VO4)2(OH)4	5	4	2		(011)	4 strong O-H-O bond (total dist = 2.85 A) and 2 V-O-Cu bonds per unit cell. Perfect cleavage on (011)
Harrisonite	CaFe5.4Mg0.7(PO4)2(SiO4)2	5			2	(001)	Si-O-Fe bonds. Cleavage indistinct.
Penkvilksite	Na4Ti2Si8O22 · 4H2O	5	4		2	(100)	Perfect cleavage on a plane but plane not identified.
Bergslagite	CaBe(AsO4)(OH)	5		4		(100)	Cleavage not reported. O-Ca-O linkage. Counting # Ca ions, non-directional bonding
Tilasite	CaMg(AsO4)F	5		8		(10-1)	Good cleavage listed as (10-1). Hard to distinguish
Emmonsite	Fe3+ 2 Te4+ 3 O9 • 2H2O	5	maybe		3	(01-1)	Perfect cleavage seems to be improperly identified as (010). Bridging bonds of Te-O
Batiferrite	BaFe2+ 2 Fe3+ 8 Ti2O19	5		3		(001)	Cleavage good on (001); 3 Fe-O octahedra (1.98 A)
Hilgardite	Ca2B5O9Cl •H2O	5		3	3	(010)	Perfect cleavage on (010); 2Ca-O (2.79A), 1Ca-Cl (2.81A), 3B-O (1.49A)
Yusupovite	Na2Zr(Si6O15)(H2O)3	5	yes	yes	8	(010)	literature perfect cleavage on (110); I assign as (010)
Brianroulstonite	Ca3[B5O6(OH)6](OH)Cl2 • 8H2O	5	yes	4		(010)	perfect cleavage on (010)
Arctite	Na5Ca7Ba(PO4)6F3	5		yes		(001)	perfect cleavage on (001); CIF files from AMCSD and COD are not the same as lattice parameters of HoM, poor representation of actual crystal
Wardite	NaAl3(PO4)2(OH)4 • 2H2O	5		yes	2	(001)	perfect cleavage on (001)
Lepidocrocite	γ–Fe3+O(OH)	5	likely			(100)	perfect cleavage on (100)
Sanbornite	BaSi2O5	5		2		(001)	perfect cleavage on (001); puckered silicate 2D sheets
Manaksite	KNaMn 2+Si4O10	5		2	2	(001)	perfect cleavage on (001); 2 Si-O and 2 K ions
Quadruphite	Na14CaMgTi4(Si2O7)2(PO4)4O4F2	5		3	1	(001)	perfect cleavage on (001)
Datolite	CaBSiO4(OH)	5.25	yes	yes		(001)	No cleavage known. Interesting case where ther is a layered structure but that

								out-of-plane bonding may be as strong as in-plane bonding.
Petarasite	Na5Zr2Si6O18(OH; Cl) ² 2H2O	5.25		yes	yes		(110)	Perfect cleavage on (110); very good on (010); cleavage through Na and hydroxyl ions
Clinohedrite	CaZnSiO4 •H2O	5.5		2	2		(010)	perfect cleavage on (010)
Delafossite	CuFeO2	5.5				yes	(001)	Known to cleave on other plane (1010)
Kyanite	Al2(SiO4)O	5.5				4	(100)	Perfect cleavage on (100). Mohs hardness is 5.5 when cleaved along (100) but 7 when along [100]. Al-O-Si bonds. Interesting case because it is very hard but still a clear cleavage plane.
Diegogattaite	Na2CaCu2Si8O20·H2O	5.5			5	8	(001)	Good cleavage on (001) because of lower bond density
Joaquinite-(Ce)	NaBa2Ce2Fe 2+Ti2Si8O26(OH) ²H2O	5.5		maybe	6	4	(001)	Good cleavage on (001); 4Ti-O, 6Ba-O, H2O?
Perrierite-(Ce)	(Ce;La; Ca)4(Fe 2+; Mg)2(Ti; Fe 3+)3Si4O22	5.5			11	4	(001)	No cleavage noted; long 4Ti-O(2.09 A) and Na-O (2.75A, 2.49A) bonds
Eudialyte	Na4(Ca; Ce)2(Fe 2+;Mn 2+)ZrSi8O22(OH; Cl)2(?)	5.5			7?	3?	(100)	Perfect to indistinct on (001) – very interesting way to describe cleavage; Complicated structure, but I could see it cleaving along Na ions
Lintisite	Na3LiTi2(Si2O6)2O2 ² 2H2O	5.5		yes	4		(100)	perfect cleavage on both (100) and (010); the (010) is less clear….requires breaking of covalent Ti-O and Si-O
Agrellite	NaCa2Si4O10F	5.5	yes		yes		(110)	excellent cleavage on (110); poor on (010); particular plane has no Si-O bonds
Lovdarite	K2Na6(Be; Al)4Si14O36 ² 9H2O	5.5			2	2	(100)	distinct cleavage on (100)
Byelorussite-(Ce)	NaMn 2+Ba2(Ce;La)2Ti2Si8O26(F ; OH) ²H2O	5.75		yes	4	4	(100)	perfect cleavage on (100)
Tuscanite	K(Ca; Na)6(Si; Al)10O22(SO4; CO3)2(OH)²H2O	5.75			8?		(100)	distinct cleavage on (100); 6 Ca ions and 2 SO4 ions
Kvanefjeldite	Na4(Ca;Mn)Si6O14(OH)2	5.75		4	6		(010)	
Hawthorneite	Ba(Cr4Ti3Fe2+ 2 Fe3+ 2 Mg)O19	5.8			yes	4	(001)	no cleavage reported

Oftedalite	(Sc,Ca,Mn2+)2K(Be,Al)3Si12O30	6			6	(001)	O-Si-O bonds
Sogdianite *Clear covalent case	K Li3 O30 Si12 Zr2	6			6	(001)	Perfect cleavage on (001).
Scorzalite	(Fe2+,Mg)Al2(PO4)2(OH)2	6			4	(100)	Al-O-P bond (2)
Bustamite	(Mn 2+; Ca)3Si3O9	6		8		(100)	Perfect cleavage on (100)Mn-O (2.05 A), Ca-O (2.38 A) bonds on cleavage plane
Titantaramellite	Ba4(Ti; Fe 3+; Fe 2+;Mg)4(B2Si8O27)O2Clx	6		yes	6	(100)	Perfect cleavage on (100); 4 Ti-O, 2 Si-O (or B-O) + ions
Stokesite	CaSnSi3O9 ² 2H2O	6	yes		2	(100)	perfect cleavage reported on (101); imperfect on (100)
Friedrichbeckeite	K(0.5Na0.5)2Mg2Be3[Si12O30]	6		~0.5	6	(001)	lists cleavage as "none"; (100)/(010) are nearly identical; example of bond density difference
Eudidymite	NaBeSi3O7(OH)	6	yes		yes	(001)	perfect cleavage on (001); Si-O or As-O bonds
Foordite	Sn2+(Nb, Ta)2O6	6			4	(100)	perfect cleavage on (100); 4 Sn-O bonds
Hyalophane	(K; Ba)Al(Si; Al)3O8	6.25		2	4		perfect cleavage on (001); Al/Si-O (x4) and Ba ion (x2) cleavage; good cleavage listed on (010), but smaller area/bond (13.85)
Albite	Na1:0¡0:9Ca0:0¡0:1Al1:0¡1:1Si3:0¡2:9O8	6.25		1.5?	4	(001)	perfect on (001)
Plumboferrite	Pb2Fe11O18.2	6.5		2 O-Pb-O & 1 Fe-(O,O,O)-Fe		(001)	Perfect cleavage on (001). Layer of Pb-O is disordered & could facilitate cleavage. O-Pb-O and Fe-O-Fe connections between layers. I bet the Pb could be chemically etched away. 2.44 A O-Pb distance (interlayer) vs. 2.17 A intralayer Pb-O.
Fluoro-Potassic-pargasite, HOM (sp-potassic-fluoro, AMCSD)	KCa2(Mg4Al)(Si6Al2)O22F2	6.5		4++	2	(110)	Perfect cleavage on (110); 4 Ca-O (2.60 A), 2 Si-O (1.61A); a couple other ions involved

Ardennite-(As)	Mn 2+ 4 (Al;Mg)6(SiO4)2(Si3O10)[(As; V)O4](OH)6	6.5	yes		yes	(001)	perfect cleavage along longest unit cell direction (different btw. Cif and literature); unclear if plane along Al-O or Mn-O, Si-O
Clinozoisite	Ca2Al3(SiO4)(Si2O7)O(OH)	6.5		2	2	(001)	perfect cleavage on (001); 2 Si-O and 2 Ca ions
Reedmergnerite	NaBSi3O8	6.5		4	4	(001)	perfect cleavage on (001)
Langbanite	(Mn 2+; Ca)4(Mn 3+; Fe 3+)9Sb 5+Si2O24	6.5			yes	(001)	good or parting cleavage on (001); perhaps along Sb atom plane
Staurolite	(Fe 2+;Mg)2Al9(Si; Al)4O20(O; OH)4	7.25			12	(010)	Distinct cleavage on (010). 1.90A Al-O, 1.65 A Si-O linkage

Table A4-3 | Non-layered minerals from 1,000 mineral subset

AMCSD Mineral Name[1]	Composition	Ave. Mohs[2]	notes
Hughesite	Na3Al(V10O28)·22H2O	1	
Rakovanite	Na3(H3[V10O28])·15H2O	1	
Lasalite	Na2Mg2[V10O28]·20H2O	1	
Carpathite	C24H12	1	by definition, too many perfect cleavage planes
Dorfmanite	Na2(PO3OH) • 2H2O	1.25	
Szmikite	Mn2+SO4 •H2O	1.5	
Alacranite	AsS	1.5	
Paceite	CaCu(C2H3O2)4 • 6H2O	1.5	
Wakabayashilite	As10S14	1.5	So cool! Tubes with a paddlewheel shape!
Uzonite	As4S5	1.5	
Iodargyrite	AgI	1.5	
Arangasite	Al2F(PO4)(SO4) · 9H2O	1.5	
Millosevichite	Al2(SO4)3	1.5	
Arsenolite	As2O3	1.5	0D spheres held together by vdW; cleavage noted at (111)
Dimorphite	As4S3	1.5	
Simmonsite	Na2LiAlF6	1.5	***not accurate – sources disagree***perfect cleavage on (001); multiple cleavage planes
Lead	Pb	1.5	
Aurichalcite	(Zn, Cu)5(CO3)2(OH)6	1.5	multiple perfect cleavage planes
Tetraauricupride	AuCu	1.6	
Nitratine	NaNO3	1.75	
Putnisite	SrCa4Cr8 3+(CO3)8SO4(OH)16·25H2O	1.75	
Zinc	Zn	2	
Uytenbogaardtite	Ag3AuS2	2	
Elyite	Pb4CuO2(SO4)(OH)4 •H2O	2	
Melanterite	FeSO4·7(H2O)	2	
Dundasite	PbAl2(CO3)2(OH)4 · H2O	2	
Jacquesdietrichite	Cu2BO6H5	2	1D chains
Qilianshanite	CH8BNaO8	2	1d polymer
Boussingaultite	(NH4)2Mg(SO4)2 · 6H2O	2	
Selenium	Se	2	Chiral chains
Ramdohrite	Ag3Pb6Sb11S24	2	Two "distinct" cleavage planes identified, (100) and (110). (100) is most obvious.
Bluelizardite	Na7(UO2)(SO4)4Cl(H2O)2	2	
Rorisite	CaFCl	2	
Nabaphite	NaBaPO4 • 9H2O	2	
Belakovskiite	Na7(UO2)(SO4)4(SO3OH)(H2O)3	2	
Korshunovskite	Mg2Cl(OH)3•3.5-4H2O	2	1D ribbons
Rambergite	MnS	2	
Inyoite	CaB3O3(OH)5 • 4H2O	2	several cleavage planes; h-bonded and ionic clusters
Munakataite	Pb2Cu2(Se4+O3)(SO4)(OH)4	2	

Boyleite	(Zn,Mg)SO4 • 4H2O	2	
Schneebergite	BiCo2(AsO4)2[(H2O)(OH)]	2	
Nielsbohrite	K(UO2)3(AsO4)(OH)4·H2O	2	
Cannizzarite	Pb46Bi54S127	2	
Laurelite	Pb7F12Cl2	2	
Gearksutite	CaAl(OH)F4 •H2O	2	
Hexatestibiopanickelite	(Ni, Pd)(Te, Sb) --> close to NiTe	2.1	Te-Te 3.52 A or 3.44 A Sb-Sb. But also 2.6 A Te-M distance.
Meta-autunite	Ca(UO2)2(PO4)2 • 2−6H2O	2.25	not layered
Morenosite	NiSO4 • 7H2O	2.25	
sodiummetaautunite (sp-metanatro)	Na2(UO2)2(PO4)2 • (6−8)H2O	2.25	
Nicksobolevite	Cu7(SeO3)2O2Cl6	2.25	
Kottenheimite	Ca 3Si(SO4)2(OH)6·12H2O	2.25	Calcium silicate chains.
Hielscherite	Ca3 O25 S2 Si	2.25	Calcium silicate chains
Acanthite	Ag2S	2.25	
Ahlfeldite	NiSe4+O3 • 2H2O	2.25	
Arzakite	Hg3S2(Br, Cl)2	2.25	
Fangite	Tl3AsS4	2.25	
Poyarkovite	Hg3ClO	2.25	
Jentschite	PbTlAs2SbS6	2.25	perfect cleavage on (-101)
Lecontite	(NH4, K)Na(SO4) • 2H2O	2.25	1D ionic chains held together by h-bonding
Proustite	Ag3AsS3	2.25	
Freieslebenite	AgPbSbS3	2.25	
Tellurium	Te	2.25	
Villiaumite	NaF	2.25	
Nanlingite	Na(Ca5Li)Mg12(AsO3)2[Fe2+(AsO3)6]F14	2.3	
Wiserite	(Mn 2+;Mg)14B8(Si;Mg)O22Cl(OH)10	2.5	
Zeunerite	Cu(UO2)2(AsO4)2 • 10−16H2O	2.5	
Gladite	PbCuBi5S9	2.5	
Miargyrite	AgSbS2	2.5	Sb-S distance intralayer = 2.51 A, Sb-S interlayer = 3.22 A. Ignoring Sb-S interlayer bonding.
Humberstonite	K3Na7Mg2(SO4)6(NO3)2 • 6H2O	2.5	
Heinrichite	Ba(UO2)2(AsO4)2 • 10−12H2O	2.5	
Rossite	CaV5+ 2 O6 • 4H2O	2.5	
Pascoite	Ca3V5+ 10 O28 • 17H2O	2.5	
Rosslerite	MgHAsO4 • 7H2O	2.5	
Rozenite	Fe2+SO4 • 4H2O	2.5	
Hydroniumpharmacosiderite	(H3O)Fe4(AsO4)3(OH)4•4H2O	2.5	
Berthierite	FeSb2S4	2.5	
Krennerite	AuTe2	2.5	

Admontite	B6 H22 Mg O17	2.5	
Montbrayite* interesting case to illustrate not layered	Au2Te3	2.5	
Cotunnite	PbCl2	2.5	
Nickelboussingaultite	(NH4)2(Ni,Mg)(SO4)2•6(H2O)	2.5	
Bonazziite	As4S4	2.5	
Lillianite	Pb3Bi2S6	2.5	
Mendipite	Pb3Cl2O2	2.5	
Syngenite	Ca H2 K2 O9 S2	2.5	
Artinite	Mg2(CO3)(OH)2	2.5	
Pyrargyrite	Ag3S3Sb	2.5	
Tiemannite	HgSe	2.5	
Cryptohalite	(NH4)2[SiF6]	2.5	
Billingsleyite	Ag7AsS6	2.5	
Dessauite-(Y)	(Sr,Pb)(Y,U)(Ti,Fe)20O38	2.5	
Yedlinite	Pb6CrCl6(O,OH,H2O)8	2.5	
Marshite	CuI	2.5	
Chenite	Pb4Cu(SO4)2(OH)6	2.5	
Bromargyrite	AgBr	2.5	
Muirite	Ba10 Ca2 Cl8 H12 Mn O32 Si8 Ti	2.5	
Elpasolite	K2NaAlF6	2.5	
Linarite	PbCu(SO4)(OH)2	2.5	clear plane along (100), but h-bonding in-plane which gives rise to interrupted (001) cleavage
Carmichaelite	(Ti, Cr)2O3(OH)	2.5	
Coloradoite	HgTe	2.5	
Aluminum	Al	2.5	
Evdokimovite	Tl4VO3(SO4)5(H2O)5	2.5	
Eglestonite	Hg1+ 6 HCl3O2	2.5	
Teruggite	Ca4MgAs2B12O22(OH)12 • 14H2O	2.5	good cleavage on (001); 8 Ca-O bonds 2.4, 2.44 A
Chlorargyrite	AgCl	2.5	
Nahcolite	NaHCO3	2.5	
Chlormanganokalite	K4MnCl6	2.5	
Canfieldite	Ag8SnS6	2.5	
Nantokite	CuCl	2.5	
Guildite	Cu(Fe3+, Al)(SO4)2(OH) • 4H2O	2.5	perfect on (001) AND (100); pleochroic
Machatschkiite	Ca6(AsO4)(AsO3OH)3(PO4, SO4) • 15H2O	2.5	
Magnesiohornblende	Ca2[(Mg; Fe 2+)4Al](Si7Al)O22(OH)2	2.5	perfect cleavage on (110); not immediately obvious
Darapskite	Na3(NO3)(SO4) •H2O	2.5	
Mandarinoite	Fe3+ 2 (Se4+O3)3 • 6H2O	2.5	
Changoite	Na2Zn(SO4)2 • 4H2O	2.5	

Magnesiochromite	MgCr3+ 2 O4	2.5	
Aluminium	Al	2.5	
Cryolite	Na3AlF6	2.5	
Ferrinatrite	Na3Fe3+(SO4)3 • 3H2O	2.5	perfect vs less perfect cleavage
Kamphaugite-(Y)	CaY(CO3)2(OH) •H2O	2.5	
Frankdicksonite	BaF2	2.5	
Lopezite	K2Cr2O7	2.5	
Wooldridgeite	Na2CaCu2(P2O7)2 • 10H2O	2.5	
Kernite	Na2B4O6(OH)2 • 3H2O	2.5	two perfect cleavage planes
Dreyerite	BiVO4	2.5	
Wittichenite	Cu3BiS3	2.5	
Nesquehonite	Mg(HCO3)(OH) • 2H2O	2.5	
Wulffite	K3NaCu4O2(SO4)4	2.5	
Albrechtschraufite	Ca4Mg(UO2)2(CO3)6F2 • 17H2O	2.5	
Piypite	K2Cu2O(SO4)2	2.5	1D chains along (001); cleavage parallel to elongation
Bararite	(NH4)2SiF6	2.5	
Yofortierite	(Mn 2+;Mg)5Si8O20(OH)2 ²8¡9H2O	2.5	note the major difference in Mohs hardness vs Pargasite, with similar structure, but no ions in vacancies
Whewellite	CaC2O4 •H2O	2.75	
Blodite	Na2Mg(SO4)2 • 4H2O	2.75	
Vauquelinite	Cr Cu H O9 P Pb2	2.75	
Stromeyerite… replacement of Ag in reaction with H could lead to 2D CuS material?	AgCuS	2.75	
Djurleite	Cu31S16	2.75	
Kuznetsovite	Hg3Cl(AsO4)	2.75	
Margarosanite	PbCa1.99Mn0.08Si2.88O9	2.75	
Dansite	Na21Mg(SO4)10Cl3	2.75	
Diaphorite	Pb2Ag3Sb3S8	2.75	
Boulangerite	Pb5Sb4S11	2.75	
Phurcalite	Ca2(UO2)3O2(PO4)2 • 7H2O	2.75	
Stolzite	PbWO4	2.75	Imperfect cleavage on (001); 4 Pb-O bonds in center of unit cell
Digenite	Cu9S5	2.75	
Argyrodite	Ag8GeS6	2.75	
Edenharterite	PbTlAs3S6	2.75	
Bournonite	PbCuSbS3	2.75	
Huemulite	Na4MgV5+ 10 O28 • 24H2O	2.75	
Cryolithionite	Na3Li3Al2F12	2.75	distinct on (011); reminds me of usovite
Robinsonite	Pb4Sb6S13	2.75	
Raberite	Tl5Ag4As6SbS15	2.75	
Vanadinite	Pb5(VO4)3Cl	2.75	
Cupromolybdite	Cu3O(MoO4)2	3	
Baumhauerite	Pb3As4S9	3	
Upalite	Al(UO2)3O(PO4)2(OH) • 7H2O	3	
Barstowite	Pb4(CO3)Cl6 •H2O	3	

Bideauxite	Pb2AgCl3(F, OH)2	3	
Aphthitalite	(K, Na)3Na(SO4)2	3	
Chovanite	Pb15–2xSb14+2xS36Ox (x ~ 0.2)	3	
Ojuelaite	ZnFe3+ 2 (AsO4)2(OH)2 • 4H2O	3	
Monteponite	CdO	3	
Jarosite	Fe3 H6 K O14 Se2	3	
Natroxalate	Na2C2O4	3	
Ramsdellite* a case with two equivalent planes of cleavage rather than one	MnO2	3	
Hohmannite	Fe3+2(SO4)2(OH)2•7(H2O)	3	
Zigrasite	H8 Mg O12 P2 Zr	3	
Marrite	PbAgAsS3	3	
Jordanite	Pb14(As,Sb)6S23	3	
Inderite	MgB3O3(OH)5•5(H2O)	3	
Wulfingite	Zn(OH)2	3	
Altaite	PbTe	3	
Calcite	CaCO3	3	
Cahnite	Ca2[B(OH)4](AsO4)	3	
Rimkorolgite	(Mg,Mn)5(Ba,Sr,Ca)(PO4)4 · 8H2O	3	
Zincgartrellite	PbZn0.9Fe0.6Cu0.5(AsO4)2(OH)0 .8(H2O)1.2	3	
Sodium alum	NaAl(SO4)2*12H2O	3	
Mendozite	NaAl(SO4)2.11H2O	3	
Mopungite	NaSb5+(OH)6	3	
Nabiasite	BaMn(VO4, AsO4)6(OH)2	3	
Nacaphite	Na2Ca(PO4)F	3	
Barikaite	Pb10Ag3(Sb8As11)S19S40	3	
Sonoraite	Fe3+Te4+O3(OH) •H2O	3	sim ilar bond densities along (100) and (010); interesting structure
Willhendersonite	KCaAl3Si3O12 ² 5H2O	3	multiple perfect cleavage planes: zeolite
Ganomalite	Pb9Ca5Mn 2+Si9O33	3	distinct cleavage on (100) and (001); similar bond densities per calculations on right
Rathite	(Pb, Tl)3As5S10	3	Perfect cleavage listed as (001)
Ferruccite	NaBF4	3	
Clinoatacamite	Cu2Cl(OH)3	3	perfect cleavage on (012); I would have expected (011); multiple cleavage directions… DAN
Barentsite	H2Na7Al(CO3)4F4	3	2 perfect cleavage planes (001) and (110)
Aerinite	Ca4(Al; Fe 3+;Mg; Fe 2+)10Si12O35(CO3)(OH)12 ² 12H2O	3	
ODanielite	H2Na(Zn,Mg)3(AsO4)3	3	two perfect cleavages on (010) and (100)
Pachnolite	NaCaAlF6 •H2O	3	good to indistinct on (001); row of F ions on (100)
Jamesite	Pb2ZnFe3+ 2 (Fe3+, Zn)4(AsO4)4(OH)8(OH, O)2	3	

Rickturnerite	Pb7O4[Mg(OH)4](OH)Cl3	3	indistinct cleavage reported (no plane); looks like similar bond density along (001) and (010)
Zlatogorite	CuNiSb2	3	
Vasilyevite	(Hg2) 2+ 10O6I3Br2Cl(CO3)	3	
Groatite	NaCaMn2+ 2(PO4)[PO3(OH)]2	3	no cleavage observed; but (100) and (010) look probable; I listed as "2" because both planes are similar ((100) does looks more promising b/c lower bond density)
Huntite	CaMg3(CO3)4	3	
Fornacite	Pb2Cu(AsO4)(CrO4)(OH)	3	
Pearceite	(Ag, Cu)16As2S11	3	
Olivenite	Cu2(AsO4)(OH)	3	
Penobsquisite	Ca2Fe2+B9O13Cl(OH)6 • 4H2O	3	
Petersenite-(Ce)	Na4(Ce,La, Nd)2(CO3)5	3	
Mapimite	Zn2Fe3+ 3 (AsO4)3(OH)4 • 10H2O	3	
Metavauxite	Fe2+Al2(PO4)2(OH)2 • 8H2O	3	
Ferrochiavennite	Ca1-2FeSi5Be2O13(OH)2·2H2O	3	
Chukhrovite-(Y)	Ca3(Y, Ce)Al2(SO4)F13 • 10H2O	3	distinct cleavage on (111)
Bornite	Cu5FeS4	3.125	
Eskebornite	CuFeSe2	3.25	
Szaibelyite	MgBO2(OH)	3.25	
Calciolangbeinite	Ca1.325 K2 Mg0.67 O12 S3	3.25	
Boleite	Ag9 Cl62 Cu24 H48 K O48 Pb26	3.25	
Gallite	CuGaS2	3.25	
Hanksite	KNa22(SO4)9(CO3)2Cl	3.25	
Paratacamite-(Mg)	Cu3(Mg,Cu)Cl2(OH)6	3.25	perfect cleavage on (201); I see multiple directions of cleavage (see note on clinoatacamite)
Baryte	BaSO4	3.25	
Kelyanite	Hg36Sb3O28(Cl, Br)9	3.25	
Antimonselite	Sb2Se3	3.3	Nanoribbons with nearly vdW separation
Pringleite	Ca9B26O34Cl4(OH)24 • 13H2O	3.5	
Sterryite	Ag2Pb10(Sb, As)12S29	3.5	
Spiroffite	(Mn2+, Zn)2Te4+ 3 O8	3.5	
Colusite	Cu26V2(As, Sn, Sb)6S32	3.5	
Lime	CaO	3.5	
Schairerite	Na21(SO4)7F6C	3.5	
Haineaultite	Ca0.25 H7.8 Na2.52 Nb0.2 O18.49 Si6 Ti0.925	3.5	
Renierite	(Cu1+,Zn)11Fe4(Ge4+,As5+)2S16	3.5	
Vaesite	NiS2	3.5	
Arseniopleite	As3 Ba0.01 Ca0.68 Fe0.27 Mg0.52 Mn2.21 Na1.25 O12 Pb0.06	3.5	
Georgiadesite	Pb4Cl4AsO4H	3.5	

Boggsite	Al0.76 H10 O12.247 Si3.24	3.5	
Dussertite	As2 Ba Fe2.52 O14 Sb0.48	3.5	
Hannebachite	2CaSO3•(H2O)	3.5	
Schuilingite-(Nd)	PbCuNd0.3Gd0.3Sm0.2Y0.2(CO3)3(OH)•5(H2O)	3.5	
Howlite	Ca2B5SiO9(OH)5	3.5	
Arsentsumebite	Pb2Cu(AsO4)(SO4)(OH)	3.5	
Pyrobelonite	PbMn(VO4)OH	3.5	
Molybdomenite	PbSeO3	3.5	
Zorite	Na8(Ti,Nb)5(Si6O17)2(OH,O)5 · 14H2O	3.5	
Bartonite	K3Fe10S14	3.5	
Afwillite	Ca3Si2O4(OH)6	3.5	
Famatinite	Cu3S4Sb	3.5	
Mansfieldite	AlAsO4 • 2H2O	3.5	
Vrbaite	Tl4Hg3Sb2As8S20	3.5	Good cleavage on (010) could be attributed to "soft" Hg-S bonds
Cavansite	Ca(V4+O)Si4O10 ² 4H2O	3.5	porous channels
Ruitenbergite	Ca9B26O34Cl4(OH)24 • 13H2O	3.5	
Jeanbandyite	(Fe3+,Mn2+)Sn4+(OH)6	3.5	Fair cleavage noted along (100) and (001)
Bariopharmacoalumite	Ba0.5Al4(AsO4)3(OH)4·4H2O	3.5	
Muckeite	CuNiBiS3	3.5	cleavage very good (010)
Sulphohalite	Na6(SO4)2FCl	3.5	
Kogarkoite	Na3(SO4)F	3.5	
Sulvanite	Cu3VS4	3.5	
Tenorite	CuO	3.5	
Calciborite	CaB2O4	3.5	
Vladimirite	Ca4(AsO4)2(AsO3OH)·4H2O	3.5	one good cleavage listed; bond densities too similar in (010) vs (001)
Hydroxylborite	Mg3(BO3)(OH)3	3.5	
Potarite	PdHg	3.5	
Sclarite	(Zn,Mg,Mn2+)4Zn3(CO3)2(OH)10	3.5	no cleavage reported; similar bond densities on two different axes
Tuhualite	(Na; K)Fe 2+Fe 3+Si6O15	3.5	several good cleavage planes
Komkovite	BaZrSi3O9 ² 3H2O	3.5	
Chukhrovite-(Ca)	Ca4.5Al2(SO4)F13•12H2O	3.5	
Frolovite	CaB2(OH)8	3.5	
Vauxite	Fe2+Al2(PO4)2(OH)2 • 6H2O	3.5	
Carlfriesite	CaTe4+ 2 Te6+O8	3.5	
Hashemite	Ba(Cr, S)O4	3.5	
Fluoborite	Mg3(BO3)(F, OH)3	3.5	
Arsenosulvanite	Cu3(As, V)S4	3.5	
Curetonite	Ba(Al, Ti)(PO4)(OH, O)F	3.5	
Natroalunite	NaAl3(SO4)2(OH)6	3.75	

Althausite	Mg2(PO4)(OH, F, O)	3.75	
Zaccariniite	RhNiAs	3.75	
Dolomite	CaMg(CO3)2	3.75	
Northupite	Na3Mg(CO3)2Cl	3.75	
Mimetite	Pb5(AsO4)3Cl	3.75	
Chiolite	Al3F14Na5	3.75	
Cameronite	AgCu7Te10	3.75	
Powellite	CaMoO4	3.75	
Lautarite	Ca(IO3)2	3.75	multiple cleavage planes through IO3/Ca ionic bonds
Shortite	Na2Ca2(CO3)3	3.75	
Scorodite	Fe3+AsO4 • 2H2O	3.75	
Tetrahedrite	(Cu, Fe, Ag, Zn)12Sb4S13	3.75	
Otavite	CdCO3	3.75	
Kutnohorite	Ca(Mn2+,Mg, Fe2+)(CO3)2	3.75	
Siderite	FeCO3	3.875	
Izoklakeite	Pb27(Cu, Fe)2(Sb, Bi)19S57	3.95	Good cleavage reported on (001); this is not clear
Iron	Fe	4	
Manganhumite	(Mn 2+;Mg)7(SiO4)3(OH)2	4	
Colquiriite	LiCaAlF6	4	
Krauskopfite	BaSi2O4(OH)2 ² 2H2O	4	
Rockbridgeite	(Fe2+,Mn2+)Fe3+ 4 (PO4)3(OH)5	4	
Rosemaryite	(Na, Ca,Mn2+)(Mn2+, Fe2+)(Fe3+, Fe2+,Mg)Al(PO4)3	4	
Mineevite-(Y)	C15 H4 Ba Cl Dy0.4 F2 Gd0.5 Na25 O53 S2 Y1.1	4	
Koutekite	Cu5As2	4	
Hydroxylbastnasite -(Ce)	Ce(CO3)(OH)	4	
Strontiofluorite	SrF2	4	
Fluorite	CaF2	4	
Manganite	MnO(OH)	4	
Stibivanite	Sb2VO5	4	1-D chains
Alcaparrosaite	Fe H4 K3 O19 S4 Ti	4	
Stenhuggarite	As2 Ca Fe O7 Sb	4	
Stannoidite	Cu8Fe3Sn2S12	4	
Ferrotychite	Na6Fe2(SO4)(CO3)4	4	
Heazlewoodite	Ni3S2	4	
Olympite	LiNa5(PO4)2	4	
Gainesite	Na(Na,K)(Be,Li)Zr2(PO4)4 · 1.5-2H2O	4	
Behoite	Be(OH)2	4	
Nalipoite	NaLi2PO4	4	
Kintoreite	PbFe3(PO4)2(OH)4.5(H2O)1.5	4	
Holfertite	CaxU2-xTi(O8-xOH4x) · 3H2O	4	Cleavage on (110)
Denningite	(Mn,Zn)Te2O5	4	Framework structure
Stranskiite	Zn2Cu(AsO4)2	4	

Magnesite	MgCO3	4	Perfect cleavage on (10-11); Mg-CO3 bonding
Amstallite	CaAl(Si; Al)4O8(OH)4 ² (H2O; Cl)	4	good cleavage on (100); unclear which plane of atoms. Most likely 4 Si-O rather than mix of Al-O, Ca, water/Cl; structure indicates multiple cleavage directions
Bonshtedtite	Na3(Fe2+,Mg)(PO4)(CO3)	4	perfect cleavage on both (010) and (100)
Averievite	Cu5O2(VO4)2 •CuCl2 • (Cs, K, Rb)Cl	4	
Modderite	(Co, Fe)As	4	
Mroseite	CaTe4+O2(CO3)	4	no cleavage reported; possible along (001) by breaking CO3 interactions; (010) shows promise –> ultimately too similar
Caryinite	(Na, Pb)(Ca, Na)(Ca,Mn2+)(Mn2+,Mg)2(AsO4)3	4	
Cernyite	Cu2CdSnS4	4	
Bellingerite	Cu3(IO3)6 • 2H2O	4	
Clinomimetite	Pb5(AsO4)3Cl	4	
Cannonite	Bi2O(SO4)(OH)2	4	
Wakefieldite-(La)	LaVO4	4	
Libethenite	Cu2(PO4)(OH)	4	
Fukalite	Ca4Si2O6(CO3)(OH; F)2	4	
Pyrrhotite	Fe1−xS (x = 0 to 0.17)	4	
Schoenfliesite	MgSn4+(OH)6	4	product of corrosion of a 1375 BC bronze harpoon head from shipwreck in Med. Sea
Murdochite	PbCu6O8−x(Cl, Br)2x (x ≤ 0.5)	4	
Dufrenite	Ca0.5Fe2+Fe3+ 5 (PO4)4(OH)6 • 2H2O	4	perfect vs. less perfect cleavage; not enough distinction
Weddellite	Ca(C2O4) • 2H2O	4	
Kovdorskite	Mg2(PO4)(OH) • 3H2O	4	
Jaskolskiite	Pb2+xCux(Sb, Bi)2−xS5 (x = 0.15–0.2)	4	
Hauerite	MnS2	4	
Sarcopside	(Fe2+,Mn2+,Mg)3(PO4)2	4	multiple cleavage planes
Offretite	(K2; Ca)2:5Al5Si13O36 ²15H2O	4	
Sulfoborite	Mg3B2(SO4)(OH)9F	4.25	
Hydroniumjarosite	(H3O)Fe3+ 3 (SO4)2(OH)6	4.25	
Ancylite-(Ce)	Sr(La,Ce)(CO3)2(OH)•(H2O)	4.25	
Clarkeite	NaUO4	4.25	
Rollandite	As2Cu3H8O12	4.25	
Fersmite	(Ca,Ce,Na)(Nb,Ta,Ti)2(O,OH,F)6	4.25	
Smithsonite	ZnCO3	4.25	Nearly perfect cleavage on (10-11); Zn- CO3 bonding
Paralstonite	BaCa(CO3)2	4.25	
Ancylite-(La)	Sr(La, Ce)(CO3)2(OH) •H2O	4.25	
Heterosite	(Fe3+,Mn3+)PO4	4.25	Good cleavage on (100); poor on (010); bond length is deciding factor, similar bond densities
Bastnasite-(Ce)	(Ce,La)(CO3)F	4.25	another example of CO3 lamellar structure

Calcioancylite-(Nd)	Ca(Nd, Ce, Gd, Y)3(CO3)4(OH)3•H2O	4.25	
Purpurite	(Mn3+, Fe3+)PO4	4.25	good cleavage on (001); imperfect on (010); hard to distinguish
Anatacamite	Cu2(OH)3Cl	4.25	good cleavage on (11-1); I see multiple cleavage planes; Cl structure may be interesting to Dan
Borcarite	Ca4MgB4O6(CO3)2(OH)6	4.25	
Bastnasite-(La)	(La, Ce)(CO3)F	4.25	
Austinite	CaZn(AsO4)(OH)	4.25	good cleavage on (011); along Ca ions, Zr-O bonds
Jarlite	Na(Sr, Na)7MgAl6F32(OH, H2O)2	4.25	
Ferberite	Fe2+WO4	4.25	
Stottite	Fe2+Ge4+(OH)6	4.5	
Lithiophilite	Li(Mn2+, Fe2+)PO4	4.5	
Cornetite	Cu3(PO4)(OH)3	4.5	
Olgite	Na(Sr, Ba)PO4	4.5	
Frondelite	(Mn2+, Fe2+)Fe3+ 4 (PO4)3(OH)5	4.5	
Kosnarite	KZr2(PO4)3	4.5	
Medenbachite	Bi2Fe3+(Cu, Fe2+)(O, OH)2(AsO4)2(OH)2	4.5	
Roscherite	Ca(Mn++,Fe++)5Be4(PO4)6(OH)4•6(H2O)	4.5	
Sabelliite	Cu2Zn(As,Sb)O4(OH)3	4.5	
Kasolite	PbSiUO6	4.5	
Fluorellestadite	Ca5(SiO4)1.5(SO4)1.5F	4.5	
Caracolite	Na3Pb2(SO4)3Cl	4.5	
Arsenbrackebuschite	Pb2F3.75Z.25(AsO4)2-H2O	4.5	
Tsumcorite	PbZnFe+(AsO4)2•(H2O)	4.5	
Curite	Pb3(UO2)8O8(OH)6 · 3H2O	4.5	
Bultfonteinite	Ca2(HSiO4)F · H2O	4.5	
Chalcosiderite	CuFe6(PO4)4(OH)8 · 4H2O *borderline case, cleavage on (001)	4.5	
Philipsbornite	PbAl3(AsO4)2(OH)5•(H2O)	4.5	
Kesterite	Cu2S4SnZn	4.5	
Sarkinite	Mn2AsHO5	4.5	
Huttonite	ThSiO4	4.5	
Koksharovite	CaMg2Fe4(VO4)6	4.5	
Helmutwinklerite	PbZn2(AsO4)2•2(H2O)	4.5	
Phosphoferrite	(Fe,Mn)3(PO4)2•3(H2O)	4.5	
Cerchiaraite-(Fe)	Ba4Fe3+4(Si4O12)O2(OH)4Cl2[Si2O3(OH)4]	4.5	
Shimazakiite	Ca2B2O5	4.5	
Svabite	Ca5(AsO4)3(F,OH)	4.5	F ion channels
Stanekite	Fe3+(Mn, Fe2+,Mg)O(PO4)	4.5	
Cooperite	(Pt, Pd)S	4.5	
Hydroxylellestadite	Ca10(SiO4)3(SO4)3(OH; F)2	4.5	
Tornebohmite-(Ce)	(Ce;La)2Al(SiO4)2(OH)	4.5	
Nickel	Ni	4.5	
Kusachiite	CuBi2O4	4.5	perfect cleavage on (110)
Variscite	AlPO4 • 2H2O	4.5	(001) and (100) are too similar
Rinkite	(Ca; Ce)4Na(Na; Ca)2Ti(Si2O7)2F2(O; F)2	4.5	

Triphylite	Li(Fe2+,Mn2+)PO4	4.5	perfect cleavage on (001); 7.13 area/bond on (010)
Kolicite	Mn 2+ 7 Zn4(AsO4)2(SiO4)2(OH)8	4.5	
Cerchiaraite-(Mn)	Ba4Mn4(Si4O12)O2(OH)4Cl2[Si2 O3(OH)4]	4.5	Cl ion framework (Dan?)
Milotaite	PdSbSe	4.5	
Cornwallite	Cu5(AsO4)2(OH)4	4.5	no cleavage reported
Wairauite	CoFe	4.5	
Hechtsbergite	Bi2O(VO4)(OH)	4.5	
Fluocerite-(La)	(La, Ce)F3	4.5	
Gartrellite	PbCu(Fe3+, Cu)(AsO4)2(OH, H2O)2	4.5	
Nefedovite	Na5Ca4(PO4)4F	4.5	
Vitusite-(Ce)	Na3(Ce,La, Nd)(PO4)2	4.5	
Satterlyite	(Fe2+,Mg, Fe3+)2(PO4)(OH)	4.75	
Safflorite	(Co, Fe)As2	4.75	
Pectolite	NaCa2Si3O8(OH)	4.75	
Bariopyrochlore	Ba20 Nb16 O53 Ti2	4.75	
Isokite	CaMg(PO4)F	4.75	
Pseudomalachite	Cu5P2O12H4	4.75	
Holtedahlite	H7 Mg12 O30 P6	4.75	
Cebaite-(Ce)	Ba3Ce2(CO3)5F2	4.75	
Manganberzeliite	NaCa2(Mn2+,Mg)2(AsO4)3	4.75	
Triploidite	(Mn2+, Fe2+)2(PO4)(OH)	4.75	
Wolfeite	(Fe2+,Mn2+)2(PO4)(OH)	4.75	
Coulsonite	Fe2+V3+ 2 O4	4.75	
Wakefieldite-(Ce)	(Ce,La, Nd, Pb)VO4	4.75	good cleavage on (100); I think (100) and (010) are too similar
Thorite	(Th; U)SiO4	4.75	
Calcium catapleiite	CaZrSi3O9 ² 2H2O	4.75	cleavage is "present"
Wicksite	NaCa2(Fe2+,Mn2+)4MgFe3+(PO4)6 • 2H2O	4.75	
Cechite	Pb(Fe ˇ 2+,Mn)(VO4)(OH)	4.75	
Plumbogummite	PbAl3(PO4)2(OH)5 •H2O	4.75	
Natrophilite	NaMn2+PO4	4.75	good cleavage on (001), indistinct on (100)
Palladium	Pd	4.75	
Nioboaeschynite-(Ce)	(Ce, Ca, Th)(Nb, Ti)2(O, OH)6	5	
Freudenbergite	Na2(Ti, Fe3+)8O16	5	
Hauchecornite	Ni9Bi(Sb, Bi)S8	5	
Siegenite	(Ni, Co)3S4	5	
Britholite-(Ce)	(Ce; Ca)5(SiO4; PO4)3(OH; F)	5	
Dioptase	CuSiO2(OH)2	5	
Westerveldite	(Fe, Ni)As	5	
Eosphorite	Mn2+Al(PO4)(OH)2 •H2O	5	
Vonsenite	Fe2+ 2 Fe3+BO5	5	
Beusite	(Mn2+, Fe2+, Ca,Mg)3(PO4)2	5	
Poldervaartite	(Ca;Mn 2+)2(SiO3OH)(OH)	5	
Deanesmithite *another close case… (110)? I think not	(Hg+2)Hg2+3(CrO4)S2O	5	
Terskite	Na4 O18 Si6 Zr	5	
Moskvinite-(Y)	K Na2 O15 Si6 Y	5	

Bearthite	Al Ca2 H O9 P2	5	
Polydymite	Ni3S4	5	
Chrisstanleyite	Ag2Pd3Se4	5	
Armalcolite* Another instructive case. Want to call it layered but no cleavage info known.	Mg O5 Ti2	5	
Ikranite	Ca3.3 Ce0.33 Cl0.74 Fe2.1 H18.453 K0.3 La0.132 Mn1.398 Na9.627 Nb0.1 Nd0.036 O79.661 Si24.3 Sr0.504 Ti0.1 Zr3.4	5	
Georgechaoite	H4 K Na O11 Si3 Zr	5	
Gonnardite	(Na,Ca)2(Si,Al)5O10 · 3H2O	5	
Tinsleyite	KAl2(PO4)2(OH)-2H2O	5	
Sakhaite	Ca3Mg(BO3)2(CO3)•0.36(H2O)	5	
Polyphite	Na5(Na4Ca2)Ti2(Si2O7)(PO4)3O 2F2	5	
Arrojadite	KNa4CaMn4Fe10Al(PO4)12(OH) 1.5F0.5	5	
Attakolite	CaMnAl4(HSiO4)(PO4)3(OH)4	5	
Cheralite	CaTh(PO4)2	5	
Gugiaite	Ca2Be(Si2O7)	5	
Perloffite	Ba(Mn,Fe)2Fe2(PO4)3(OH)3	5	
Ruizite	CaMnSi2O6(OH)•2(H2O)	5	
Samuelsonite	(Ca,Ba)Ca8(Fe,Mn)4Al2(PO4)10(OH)2	5	
Derbylite	Fe3Fe2Ti2SbO13(OH)	5	
Galuskinite	Ca7(SiO4)3(CO3)	5	
Fluornatromicrolite	(Na,Ca,Bi)2Ta2O6F	5	
Ferroalluaudite	NaCaFe2+(Fe3+,Mn2+, Fe2+)2(PO4)3	5	
Angelellite	Fe(3+)4O3(AsO4)2	5	There are two possible cleavage directions that break As-O and Fe-O bonds
Childrenite	Fe2+Al(PO4)(OH)2 •H2O	5	
Svanbergite	SrAl3(PO4)(SO4)(OH)6	5	Distinct cleavage known as (0001)
Fetiasite	(Fe2+, Fe3+, Ti)3O2(As3+ 2 O5)	5	Perfect cleavage on (100), but (001) looks identical
Carbonate-fluorapatite	Ca5(PO4, CO3)3F	5	
Liottite	(Ca; Na; K)8(Si; Al)12O24[(SO4); Cl; (CO3); OH]4 ²H2O	5	
Stilleite	ZnSe	5	
Homilite	Ca2(Fe 2+;Mg)B2Si2O10	5	
Carnallite	KMgCl3 •6H2O	5	
Kentrolite	Pb2Mn 3+ 2 O2Si2O7	5	distinct cleavage on (110); but I also observe (010) through the similar low bond density
Carrollite	Cu(Co, Ni)2S4	5	
Violarite	Fe2+Ni3+ 2 S4	5	
Talmessite	Ca2Mg(AsO4)2 • 2H2O	5	potential 1D
Arrojadite-(KNa)	KNa4Ca(Fe2+,Mn2+)14Al(PO4)1 2(OH)2	5	

Pumpellyite-(Fe2+)	Ca2(Fe 2+; Fe 3+;Mg)Al2(SiO4)(Si2O7)(OH)2 ²H2O	5	
Melonjosephite	CaFe2+Fe3+(PO4)2(OH)	5	
Fluorapatite	Ca5(PO4)3F	5	
Belovite-(Ce)	NaSr3(Ce,La)(PO4)3(F, OH)	5	cleavage: Prismatic and pinacoidal, imperfect; is Sr-O covalent or ionic? Also see (100); (001) is too similar bond density to (100)/(010)
Gladiusite	(Fe2+,Mg)4Fe3+ 2 (PO4)(OH)11 •H2O	5	
Janhaugite	Na3Mn 2+ 3 Ti2Si4O15(OH; F; O)3	5	
Trevorite	NiFe3+ 2 O4	5	
Hydroxylapatite	Ca5(PO4)3(OH)	5	
Plumbopyrochlore	(Pb, Y, U, Ca)2−xNb2O6(OH)	5	
Billwiseite	Sb3+ 5(Nb,Ta)3WO18	5	
Turneaureite	Ca5(AsO4)3Cl	5	
Petewilliamsite	(Ni,Co)30(As2O7)15	5	
Wopmayite	Ca6Na3 Mn(PO4)3(PO3OH)4	5	
Ishiharaite	(Cu,Ga,Fe,In,Zn)S	5	
Traskite	Ba9Fe 2+ 2 Ti2(SiO3)12(OH; Cl; F)6 ² 6H2O	5	
Jasmundite	Ca11(SiO4)4O2S	5	
Wagnerite	(Mg, Fe2+)2(PO4)F	5.25	
Nickeline	NiAs	5.25	
Bismutotantalite	BiTa0.8Nb0.2O4	5.25	
Pyrochlore	(Na,Ca)2Nb2O6(OH,F)	5.25	
Esperite	PbCa2(ZnSiO4)3	5.25	
Cerite-(Ce)	Ce9Fe(SiO4)6(SiO3)(OH)4	5.25	
Chlorkyuygenite	Ca12Al14O32[(H2O)4Cl2]	5.25	
Durangite	NaAl(AsO4)F	5.25	
Fabriesite	Na3Al3Si3O12·2H2O	5.25	H atoms not in .cif; cage-structure
Lollingite	FeAs2	5.25	
Trinepheline	NaAlSiO4	5.25	
Ludwigite	Mg2Fe3+BO5	5.25	
Palenzonaite	NaCa2Mn2+ 2 (VO4)3	5.25	
Hyalotekite	(Ba; Pb; Ca)6(B; Si; Al)2(Si; Be)10O28(F; Cl)	5.25	
Natrolite	Na2Al2Si3O10 ² 2H2O	5.25	perfect cleavage on (110); but also consider (-110)…multiple cleavage directions in structure
Alluaudite	(Na, Ca)Mn2+(Fe3+,Mn2+, Fe2+,Mg)2(PO4)3	5.25	three good cleavage planes
Sorensenite	Na4SnBe2Si6O18 ² 2H2O	5.25	
Zwieselite	(Fe2+,Mn2+)2(PO4)F	5.25	
Monazite-(Ce)	(Ce,La, Nd, Th)PO4	5.25	distinct cleavage on (100); probably cleaves along Ce-O bonds; see also Monazite-Nd
Monazite-(Nd)	(Nd,La, Ce)PO4	5.25	distinct cleavage on (100); probably cleaves along Nd-O bonds (2.4, 2.6A); border case
Monazite-(La)	(La, Ce, Nd)PO4	5.25	compare this analysis with the other monazite species
Qingheiite	Na2(Mn2+,Mg, Fe2+)2(Al, Fe3+)(PO4)3	5.45	see note on qingheiite-Fe2+

Waimirite-(Y)	YF3	5.5	
Nosean	Na8Al6Si6O24(SO4)•H2O	5.5	
Tschermakite	Ca2[(Mg; Fe 2+)3Al2](Si6Al2)O22(OH)2	5.5	
Arfvedsonite	NaNa2[(Fe 2+;Mg)4Fe 3+]Si8O22(OH)2	5.5	
Strontio-orthojoaquinite	Sr2Ba2(Na; Fe 2+)2Ti2Si8O24(O; OH)2 •H2O	5.5	
Wodginite	Mn2+(Sn4+, Ta)Ta2O8	5.5	
Zangboite	TiFeSi2	5.5	
Ferropargasite	NaCa2[(Fe 2+;Mg)4Al](Si6Al2)O22(OH)2	5.5	
Lithosite	K6Al4Si8O25 ² 2H2O	5.5	
Hillebrandite	Ca3 H2 O7.5 Si1.5	5.5	
Srebrodolskite	Ca2Fe2O5	5.5	
Willemite	O4 Si Zn2	5.5	
Bunsenite	NiO	5.5	
Coffinite	USiO4	5.5	
Hydroxycalciopyrochlore	(Ca,Na,U,□)2(Nb,Ti)2O6(OH)	5.5	
Hastingsite	Al3.31 Ca1.74 Fe3 H1.44 K0.3 Mg1.17 Na0.82 O24 Si5.27 Ti0.39	5.5	
Ferrocarpholite	Al2 Fe H4 O10 Si2	5.5	
Pseudorutile	Fe2Ti3O9	5.5	
Uraninite	UO2	5.5	
Karlite	Mg7(BO3)3(OH)4Cl	5.5	Perfect cleavage claimed on (001); note the cylindrical channels containing Cl
Geikielite	MgTiO3	5.5	
Uedaite-(Ce)	Mn2+CeAl2Fe(Si2O7)(SiO4)O(OH)	5.5	
Cobaltite	CoAsS	5.5	perfect cleavage on (001)
Alleghanyite	Mn 2+ 5 (SiO4)2(OH)2	5.5	
Manganogrunerite	Mn2(Fe 2+;Mg)5Si8O22(OH)2	5.5	perfect cleavage on (110)
Pargasite	NaCa2[(Mg; Fe 2+)4Al](Si6Al2)O22(OH)2	5.5	perfect cleavage on (110); very similar to magnesiohornblende; there are actually several examples.
Omphacite	(Ca; Na)(Mg; Fe; Al)Si2O6	5.5	
Winchite	NaCa][(Mg; Fe 2+)4Al]Si8O22(OH)2	5.5	perfect on (110); see note on pargasite
Emeleusite	Na4Li2Fe 3+ 2 Si12O30	5.5	
Hausmannite	Mn2+Mn3+ 2 O4	5.5	
Parwelite	(Mn 2+;Mg)5Sb 5+As 5+SiO12	5.5	
Holmquistite	Li2[(Mg; Fe 2+)3Al2]Si8O22(OH)2	5.5	see note on pargasite
Magnesiotaramite	Na[NaCa][(Mg; Fe 2+)3Al2](Si6Al2)O22(OH)2	5.5	see note on pargasite
Andremeyerite	BaFe 2+ 2 Si2O7	5.5	two perfect cleavage planes
Rhonite	Ca2(Mg; Fe 2+; Fe 3+; Ti)6(Si; Al)6O20	5.5	
Vishnevite	(Na; Ca; K)6(Si; Al)12O24[(SO4); (CO3); Cl2]2¡4 ² nH2O	5.5	
Meionite	3CaAl2Si2O8 ²CaCO3	5.5	
Manganosite	Mn2+O	5.5	
Romanechite	(Ba, H2O)2(Mn4+,Mn3+)5O10	5.5	

Actinolite	Ca2(Mg; Fe 2+)5Si8O22(OH)2	5.5	good cleavage on (110); see note on pargasite
Palermoite	(Li, Na)2(Sr, Ca)Al4(PO4)4(OH)4	5.5	
Cafarsite	Ca8(Ti, Fe2+, Fe3+,Mn)6−7(As3+O3)12 • 4H2O	5.75	
Danalite	Fe 2+ 4 Be3(SiO4)3S	5.75	
Arapovite	(U,Th)(Ca,Na)2(K1-x x)Si8O20•H2O	5.75	
Anatase	TiO2	5.75	
Macedonite	PbTiO3	5.75	
Bavenite	Ca4.1Be2.9Al1.2Si9.2O26(OH)2	5.75	
Anthophyllite	□(Mg2)(Mg5)(Si8O22)(OH)2	5.75	Multiple cleavage planes.
Studenitsite	NaCa2B9O14(OH)4 • 2H2O	5.75	
Awaruite	Ni2Fe to Ni3Fe	5.75	
Loparite-(Ce)	(Ce, Na, Ca)(Ti, Nb)O3	5.75	
Amblygonite	LiAl(PO4)(F, OH)	5.75	Claimed perfect cleavage through (100). Not obvious, based on crystal structure. Requires breaking of H-bonds and ionic/covalent. Multiple directions as well (100) vs (010)
Hauyne	(Na; Ca)4¡8Al6Si6(O; S)24(SO4; Cl)1¡2	5.75	distinct cleavage on (110)
Brookite	TiO2	5.75	
Manganilvaite	CaFe2+Fe3+(Mn,Fe2+)(Si2O7)O(OH)	5.75	
Natronambulite	(Na;Li)Mn 2+ 4 Si5O14(OH)	5.75	
Leucophoenicite	Mn 2+ 7 (SiO4)3(OH)2	5.75	
Lawsonite	CaAl2Si2O7(OH)2 •H2O	6	
Wenkite	Ba4Ca6(Si; Al)20O39(OH)2(SO4)3 • nH2O(?)	6	
Polycrase-(Y)	(Y, Ca, Ce, U, Th)(Ti, Nb, Ta)2O6	6	
Chiappinoite-(Y)	Y2Mn(Si3O7)4	6	
Microsommite	(Na; Ca; K)7¡8(Si; Al)12O24(Cl; SO4)2¡3	6	
Baghdadite	Ca3(Zr; Ti)Si2O9	6	
Magnocolumbite	(Mg, Fe2+,Mn2+)(Nb, Ta)2O6	6	
Plumbomicrolite	(Pb, Ca)2(Ta, Nb)2O6(OH)	6	
Pseudobrookite	(Fe3+, Fe2+)2(Ti, Fe3+)O5	6	
Kalsilite	AlKO4Si	6	
Kosmochlor	Cr Na O6 Si2	6	
Davidite-(La)	La0.7Ce0.2Ca0.1Y0.75U0.25Ti15Fe5O38	6	
Kalborsite	K6Al4Si6B1.4O22.5(OH)4Cl	6	
Ferrocolumbite	(Fe2+,Mn2+)(Nb, Ta)2O6	6	
Yafsoanite	Ca3Zn3(Te6+O6)2	6	
Chromio-pargasite	NaCa2Mg4CrSi6Al2O22(OH)2	6	Perfect cleavage on (110); similar to fluoro-potassic pargasite
Ferroglaucophane	Na2[(Fe 2+;Mg)3Al2]Si8O22(OH)2	6	perfect on (110); breaking 2 Si-O bonds and 2 Na ion interactions
Svyatoslavite	CaAl2Si2O8	6	similar cleavage plane on (100)) vs (010)
Orthopinakiolite	(Mg,Mn2+)2Mn3+BO5	6	no cleavage reported; potential breaking point along (100) Mg-O bonds; note partial vacancies of

			Mn in place of Mg, which could indicate 3D covalent linkages
Batisite	(Na; K)2BaTi2(Si2O7)2	6	
Romeite	(Ca, Fe2+,Mn2+, Na)2(Sb, Ti)2O6(O, OH, F)	6	
Chkalovite	Na2BeSi2O6	6	Fair cleavage along "one direction"; requires breaking of Be-O bonds and possible Na-O interactions
Welshite	Ca2Mg4Fe 3+Sb 5+Si4Be2O20	6	multiple cleavage planes are possible; considered similar bonding between alkaline earth metals
Neltnerite	CaMn 3+ 6 SiO12	6	
Hibschite	Ca3Al2(SiO4)3¡x(OH)4x (x = 0.2 to 1.5)	6	
Aegirine	NaFe 3+Si2O6	6	
Jacobsite	(Mn2+, Fe2+,Mg)(Fe3+,Mn3+)2O4	6	
Lorenzenite	Na2Ti2Si2O9	6	
Mapiquiroite	(Sr,Pb)(U,Y)Fe2(Ti,Fe3+)18O38	6	
Slawsonite	(Sr; Ca)Al2Si2O8	6	
Kudryavtsevaite	Na3MgFe3+Ti4O12	6	
Hurlbutite	CaBe2(PO4)2	6	
Celsian	BaAl2Si2O8	6.25	
Prehnite	Ca2Al2Si3O10(OH)2	6.25	
Leucosphenite	BaNa4Ti2B2Si10O30	6.25	
Narsarsukite	Na2(Ti; Fe 3+)Si4(O; F)11	6.25	
Norbergite	Mg3(SiO4)(F; OH)2	6.25	Instructive example of a borderline case that we classified as being not layered. Looks lamellar on (010) with partial F occupancy on a plane but not a significant variation in bond density in F plane.
Andesine	Na0:7¡0:5Ca0:3¡0:5Al1:3¡1:5Si2:7¡2:5O8	6.25	Several cleavage planes identified
Lithiotantite	Li(Ta, Nb)3O8	6.25	
Wohlerite	NaCa2(Zr; Nb)Si2O7(O; OH; F)2	6.25	
Oligoclase	Na0:9¡0:7Ca0:1¡0:3Al1:1¡1:3Si2:9¡2:7O8	6.25	perfect on (001) vs less perfect on (010); not enough distinction
Helvine	Mn 2+ 4 Be3(SiO4)3S	6.25	
Iwakiite	Mn2+(Fe3+, Mn3+)2O4	6.25	
Grandaite	Sr2Al(AsO4)2(OH)	6.25	
Chondrodite	(Mg; Fe 2+)5(SiO4)2(F; OH)2	6.25	
Rutile	TiO2	6.25	
Stibiconite	Sb3+Sb5+ 2 O6(OH)	6.25	
Braunite	Mn 2+Mn 3+ 6 SiO12	6.25	perfect cleavage on (112); example of perfect cleavage, but non-layered (Growth vs cleavage plane??)
Microcline	KAlSi3O8	6.25	
Thalenite-(Y)	Y3Si3O10(F; OH)	6.25	
Wadeite	K2ZrSi3O9	6.25	
Isolueshite	(Na,La, Ca)(Nb, Ti)O3	6.25	
Naquite	FeSi	6.5	
Linzhiite	FeSi2	6.5	

Eucryptite	LiAlSiO4	6.5	
Genthelvite	Zn4Be3(SiO4)3S	6.5	
Sverigeite	NaMn 2+MgSn 4+Be2Si3O12(OH)	6.5	
Stillwellite-(Ce)	(Ce; La; Ca)BSiO5	6.5	
Kotoite	B2Mg3O6	6.5	
Hingganite-(Yb)	YbY0.5Be2Si2O8(OH)2	6.5	
Hancockite	(CaPb)(Al2Fe)(Si2O7)(SiO4)O(OH)	6.5	
Sperrylite	PtAs2	6.5	
Trimerite	CaMn2Be3(SiO4)3	6.5	
Cassiterite	SnO2	6.5	
Redledgeite	BaTi6Cr3+ 2 O16 •H2O	6.5	
Thortveitite	(Sc; Y)2Si2O7	6.5	
Bertrandite	Be4Si2O7(OH)2	6.5	example of bond density analysis breakdown? Perfect cleavage on (001) but structure looks better on (100) or (010)…(001) requires breaking of Si-O and Be-O
Ferro-axinite	Ca2Fe 2+Al2BSi4O15(OH)	6.75	
Schreibersite	(Fe, Ni)3P	6.75	
Manganaxinite	Ca2Mn 2+Al2BSi4O15(OH)	6.75	
Pollucite	(Cs; Na)(AlSi2)O6 ² nH2O	6.75	
Uvarovite	Ca3 Cr2 O12 Si3	6.75	
Manganbabingtonite	Ca2(Mn,Fe)FeSi5O14(OH)	6.75	
Melanophlogite	SiO2 ²n(C; H; O; S)	6.75	Cage-like structure
Serendibite	Ca2(Mg; Al)6(Si; Al; B)6O20	6.75	Repeating pattern obvious along (011); good cleavage reported on both (010) and (001)
Sinhalite	MgAlBO4	6.75	No reported cleavage plane. Mg-O (2.2A/2.12/2.04A) bridging
Gadolinite-(Y)	Y2Fe 2+Be2Si2O10	6.75	
Grossular	Ca3Al2(SiO4)3	6.75	
Fluor-tsilaisite	Na(Mn2+)3Al6(Si6O18)(BO3)3(OH)3F	7	
Dravite	Na(Mg3)Al6(Si6O18)(BO3)3(OH)3(OH)	7	
Zunyite	Al13Si5O20(OH,F)18Cl	7	
Goldmanite	Ca3(V3+; Al; Fe 3+)2(SiO4)3	7	
Luobusaite	FeSi2	7	bonding is not clear; no cleavage listed
Foitite	Nax[Fe 2+ 2 (Al; Fe 3+)]Al6(BO3)3Si6O18(OH)4	7	
Qandilite	(Mg, Fe2+)2(Ti, Fe3+, Al)O4	7	
Fluor-schorl	NaFe2+ 3Al6Si6O18(BO3)3(OH)3F	7	
Forsterite	Mg2SiO4	7	
Tridymite	SiO2	7	
Ferroindialite	(Fe2+,Mg)2Al4Si5O18	7	
Feruvite	(Ca; Na)(Fe 2+;Mg)3(Al;Mg)6(BO3)3Si6O18(OH)4	7	
Majorite	Mg3(Fe; Al; Si)2(SiO4)3	7.25	
Schorlomite	Ca3(Ti 4+; Fe 3+)2(Si; Fe 3+)3O12	7.25	

Boracite	Mg3B7O13Cl	7.25	
Behierite	(Ta, Nb)BO4	7.25	
Spessartine	Mn 2+ 3 Al2(SiO4)3	7.25	
Pyrope	Mg3Al2(SiO4)3	7.25	
Cordierite	(Mg; Fe 2+)2Al4Si5O18	7.25	cool porous framework
Akdalaite	4Al2O3 •H2O	7.25	
Sapphirine	Al2O3	7.5	
Galaxite	(Mn2+, Fe2+,Mg)(Al, Fe3+)2O4	7.5	
Dalyite	K2ZrSi6O15	7.5	
Phenakite	Be2SiO4	7.75	
Dumortierite	Al6.79 B O18 Si3	7.75	
Londonite	(Cs, K, Rb)Al4Be4(B, Be)12O28	8	
Eskolaite	Cr2O3	8	
Painite	CaZrAl9O15(BO3)	8	
Swedenborgite	NaBe4SbO7	8	distinct cleavage listed as (001); likely listed as "distinct" because strong bonds (Be-O = 1.65 A)? (mohs = 8)
Schiavinatoite	(Nb, Ta)BO4	8	
Ferronigerite-2N1S	(Fe2+, Zn,Mg)(Sn, Zn)2(Al, Fe3+)12O22(OH)2	8.5	both AMCSD and COD CIF would not open in VESTA
Mariinskite	(Cr,Al)2BeO4	8.5	

Table A4-4 | Layered mineral melting points

Mineral Name	Composition	MP (°C)	Ave. Mohs	MP ref/ Handbook ID Hdbk: ref. ([3]); USGS: ref. ([4])	Mohs ref. HoM: ref. ([2]); MED:[5]
Borax	$Na_2B_4O_5(OH)_4 \bullet 8H_2O$	75	2.25	Hdbk-2717	HoM
Sinjarite	$CaCl_2 \bullet 2H_2O$	172	1.5	6	HoM
Calomel	HgCl	302	1.5	Hdbk-1816	HoM
Claudetite	As_2O_3	313	2.5	Hdbk-288	HoM
Orpiment	As_2S_3	320	1.75	Hdbk-290	HoM
Brucite	$Mg(OH)_2$	350 (decomposes)	2.5	Hdbk-1697	HoM
Pyrophyllite	$Al_2Si_4O_{10}(OH)_2$	500-960 (dehydrates)	1.5	7	HoM
Chalcostibite	$CuSbS_2$	552.9	3.5	USGS	HoM
Tetradymite	Bi_2Te_2S	585	1.75	Hdbk-473	HoM
Tellurantimony	Sb_2Te_3	629	2.25	Hdbk-265	HoM
Antimony	Sb	630.7	3.25	Hdbk-246	HoM
Synthetic	$SnSe_2$	647	1.5	8	9
Valentinite	Sb_2O_3	656	2.75	Hdbk-257	HoM
Lawrencite	$(Fe^{2+},Ni)Cl_2$	676.9	1	USGS	10
Guanajuatite	Bi_2Se_3	710	2.75	Hdbk-464	HoM
Tellurite	TeO_2	733	2	Hdbk-2864	HoM
Molybdite	MoO_3	800.9	3.5	USGS	5
Bismite	α–Bi_2O_3	824.9	4.5	USGS	HoM
Berndtite	SnS_2	837	1.5	11	12
Herzenbergite	SnS	879.9	2	USGS	HoM
Mirabilite	$Na_2SO_4 \bullet 10H_2O$	884	2	Hdbk-2704	HoM
Massicot	PbO	888	2	Hdbk-1529	HoM
Lepidolite	$K(Li;Al)_3(Si;Al)_4O_{10}(F;OH)_2$	900	3.25	13	HoM
Synthetic	$NbTe_2$	900	1.5	8	9
Synthetic	TaS_2	1000	1.5	14	9
Synthetic	$NbSe_2$	1000	1.5	8	9
Synthetic	TiS_2	1000	1.5	8	9

Biotite	$K(Mg;Fe^{2+})3(Al;Fe^{3+})Si_3O_{10}(OH;F)_2$	1110-1115	2.75	13	HoM
Synthetic	WTe_2	1020	1.5	14	9
Synthetic	$MoSe_2$	1150	1.5	8	9
Synthetic	$MoTe_2$	1180	1.5	8	9
Synthetic	$TiTe_2$	1200	1.5	8	9
Muscovite	$KAl_2(Si_3Al)O_{10}(OH;F)_2$	1202-1208	2.5	13	HoM
Vermiculite	$(Mg;Fe^{3+};Al)_3(Si;Al)_4O_{10}(OH)_2•4H_2O$	1240-1430	1.5	15	HoM
Sanbornite	$BaSi_2O_5$	1420	5	Hdbk-373	HoM
Talc	$Mg_3Si_4O_{10}(OH)_2$	1500	1	16	HoM
Synthetic	WSe_2	1500	1.5	14	9
Carnotite	$K_2(UO_2)_2(VO_4)_2•3H_2O$	1728	2	17	12
Molybdenite	MoS_2	1750	1.25	Hdbk-1868	HoM
Synthetic	$TaSe_2$	2000	1.5	18	9
Tungstenite	WS_2	2400	1.5	8	9
Synthetic	NbS_2	3000	1.5	8	9
Graphite	C	4526	1.5	19	HoM

Table A4-5 | Non-layered mineral melting points

Mineral Name	**Composition**	**MP (°C)**	**MP Ref/ Handbook ID** Hdbk: ref. ([3]); USGS: ref. ([4])	**Ave. Mohs**	**Mohs Ref.** HoM: ref. (2); MED: ref. (5)
Sodium alum	NaAl(SO4)2*12H2O	60	Hdbk-2558	3	HoM
potassium	K	63	USGS	0.4	MED
Bieberite	CoSO4 • 7H2O	96.8	Hdbk-903	2	HoM
sodium	Na	98	USGS	0.5	MED
Goslarite	ZnSO4 • 7H2O	100	Hdbk-3279	2.25	HoM
Thermonatrite	Na2CO3 •H2O	109	Hdbk-2573	1.25	HoM
sulfur	S	115	USGS	2	MED
Indium	In	156.6	Hdbk-1390	3.5	HoM
lithium	Li	180	USGS	0.6	MED
Selenium	Se	217	Hdbk-2464	2	HoM

Tin	Sn	231.9	Hdbk-2990	2	HoM
Bismuth	Bi	271.4	Hdbk-436	2.25	HoM
Arsenolite	As2O3	275	Hdbk-287	1.5	HoM
realgar		307	USGS	1.75	HoM
Niter	KNO3	307	Hdbk-2665	2	HoM
Cadmium	Cd	321.07	Hdbk-508	1.5	HoM
lead	Pb	328	USGS	1.5	MED
Zinc	Zn	419.5	Hdbk-3219	2	HoM
bromargyrite		430	USGS	2.5	HoM
Nantokite	CuCl	430	Hdbk-935	2.5	HoM
Tellurium	Te	449.8	Hdbk-2860	2.25	HoM
chlorargyrite		455	USGS	2	HoM
cotunnite		495	USGS	4	HoM
stibnite		556	USGS	2	HoM
iodargylite		558	USGS	2.5	HoM
Nitrobarite	Ba(NO3)2	592	Hdbk-356	3	HoM
Marshite	CuI	605	Hdbk-938	2.5	HoM
magnesium	Mg	650	USGS	2.5	MED
Senarmontite	Sb2O3	656	Hdbk-259	2.25	HoM
Aluminum	Al	660	USGS	2.5	HoM
barium	Ba	729	USGS	1.25	MED
chiolite		737	USGS	1.5	HoM
Sylvite	KCl	776	Hdbk-2147	2	HoM
strontium	Sr	777	USGS	1.5	MED
Heazlewoodite	Ni3S2	790	Hdbk-1974	4	HoM
cerium	Ce	798	USGS	2.5	MED
Halite	NaCl	800.7	Hdbk-2576	2.25	HoM
Witherite	BaCO3	811	Hdbk-319	3.25	HoM
Acanthite	Ag2S	825	Hdbk-2546	2.25	HoM
calcium	Ca	842	USGS	1.75	MED
thenardite		882	USGS	6.5	HoM

Altaite	PbTe	905	Hdbk-1542	3	HoM
Natrolite		910	USGS	5.25	HoM
Langbeinite	K2Mg2(SO4)3	927	Hdbk-2212	3.75	HoM
Skutterudite	CoAs2−3	942	Hdbk-840	5.75	HoM
germanium	Ge	948	USGS	6	MED
Chalcopyrite	CuFeS2	950	Hdbk-972	3.75	HoM
Hessite	Ag2Te	955	Hdbk-2547	2.5	HoM
Silver	Ag	961.93	Hdbk-2504	2.75	HoM
Millerite	NiS	976	Hdbk-1978	3.25	HoM
villiaumite		996	USGS	2.5	HoM
Cryolite	Na3AlF6	1012	Hdbk-2611	2.5	HoM
Hornblende		1025	USGS	5.5	https://geology.com/minerals/hornblende.shtml
Jeremejevite	Al6(BO3)5(F, OH)3	1050	Hdbk-21	7	HoM
Gold	Au	1064.43	Hdbk-1283	2.75	HoM
Clausthalite	PbSe	1065	Hdbk-1534	2.75	HoM
Wulfenite	PbMoO4	1065	Hdbk-1525	2.875	HoM
Arcanite	K2SO4	1069	Hdbk-2251	2	HoM
copper	Cu	1085	USGS	3	MED
Grossular		1090	USGS	6.75	mohs-https://geology.com/minerals/olivine.shtml
Albite		1099.5	USGS	6.25	HoM
Chalcocite	Cu2S	1100	Hdbk-942	2.75	HoM
Oligoclase		1110	USGS	6.25	HoM
Galena	PbS	1113	Hdbk-1539	2.6	HoM
Raspite	PbWO4	1123	Hdbk-1549	2.75	HoM
Stolzite	PbWO4	1130	Hdbk-1550	2.75	HoM
uranium		1135	USGS	6	MED
Microcline		1147	USGS	6.25	HoM
Meionite		1156	USGS	5.5	HoM
Breithauptite	NiSb	1158	Hdbk-1933	5.5	HoM

Anglesite	PbSO4	1170	Hdbk-1538	2.75	HoM
Pyrite	FeS2	1171	Hdbk-1446	6.25	HoM
Troilite	FeS	1194	Hdbk-1194	4	HoM
sanidine		1200	USGS	5.75	HoM
Meta-autunite		1200.0	USGS	2.25	HoM
fayalite		1217	USGS	7.25	HoM
Actinolite		1230	USGS	5.5	HoM
cuprite		1236	USGS	3.75	HoM
manganese		1244	USGS	6	MED
Olivine		1250	USGS	6.75	HoM
tephroite		1251	USGS	6	HoM
Sellaite	MgF2	1263	Hdbk-1690	5.25	HoM
beryllium	Be	1287	USGS	5.5	MED
pyrope		1297	USGS	6	HoM
Rhodonite	(Mn2+; Fe 2+;Mg; Ca)SiO3	1323	Hdbk-1762	6	HoM
rankinite		1360	USGS	6.75	HoM
Wustite	Fe2+O	1377	Hdbk-1186	5	HoM
diopside		1395	USGS	5.5	HoM
titanite (sphene)		1397	USGS	5.5	HoM
eucryptite		1397	USGS	6.5	HoM
almandine		1410	USGS	7	HoM
Beryl	Be3Al2Si6O18	1410	Hdbk-410	7.75	HoM
silicon	Si	1412	USGS	6.5	MED
Fluorite	CaF2	1418	Hdbk-595	4	HoM
Quartz	SiO2	1423	Hdbk-2492	7	HoM
Tenorite	CuO	1446	Hdbk-992	3.5	HoM
Anhydrite	CaSO4	1450	Hdbk-644	3.25	HoM
Nickel	Ni	1453	Hdbk-1929	4.5	HoM
akermanite		1458	USGS	5.25	HoM
cobalt	Co	1495	USGS	5	MED
Strontianite	SrCO3	1497	Hdbk-2775	3.5	HoM

Gehlenite	Ca2Al(AlSi)O7	1500	Hdbk-565	5.5	HoM
Stilleite	ZnSe	1517	Hdbk-3274	5	HoM
Iron	Fe	1535	Hdbk-1440	4	HoM
clinoenstatite		1557	USGS	6	HoM
anorthite		1557	USGS	6	HoM
Hausmannite	Mn2+Mn3+ 2 O4	1564	Hdbk-1801	5.5	HoM
Maghemite	γ–Fe2O3	1565	Hdbk-1148	5	HoM
Magnetite	Fe(2+)Fe2(3+)O4	1597	Hdbk-1455	6	HoM
Scheelite	CaWO4	1620	Hdbk-655	4.75	HoM
hematite		1622	USGS	5.5	HoM
Cassiterite	SnO2	1630	Hdbk-2745	6.5	HoM
titanium	Ti	1666	USGS	6	MED
Whitlockite	Ca9(Mg, Fe2+)(PO4)6(PO3OH)	1670	Hdbk-630	5	HoM
leucite		1686	USGS	6.5	HoM
Sphalerite	(Zn, Fe)S	1700	Hdbk-3283	3.75	HoM
Wurtzite	(Zn, Fe)S	1700	Hdbk-3282	3.75	HoM
Tridymite	SiO2	1703	Hdbk-2491	7	HoM
Cristobalite	SiO2	1713	Hdbk-2493	6.5	HoM
thorium		1750	USGS	3	MED
Mullite	Al6Si2O13	1750	Hdbk-80	6.5	HoM
Greenockite	CdS	1750	Hdbk-548	3.25	HoM
Platinum	Pt	1768.4	Hdbk-2105	4.25	HoM
Manganosite	Mn2+O	1840	Hdbk-1787	5.5	HoM
Variscite	AlPO4 • 2H2O	1850	Hdbk-73	4.5	HoM
zirconium	Zr	1852	USGS	5	MED
Rutile	Fe2Ti3O9	1855	Hdbk-3003	6.25	HoM
Chromium	Cr	1857	Hdbk-779	7.5	HoM
Chrysoberyl	BeAl2O4	1870	Hdbk-409	8.5	HoM
Forsterite	Mg2SiO4	1898	Hdbk-1728	7	HoM
vanadium	V	1902	USGS	7	MED

Rhodium	Rh	1966	Hdbk-2360	3.5	HoM
zincite		1969	USGS	6.5	HoM
Perovskite	CaTiO3	1975	Hdbk-654	5.5	HoM
Oldhamite	(Ca,Mg)S	2000	Hdbk-647	4	HoM
Corundum	Al2O3	2054	Hdbk-63	9	HoM
boron	B	2077	USGS	9.3	MED
Bunsenite	NiO	2090	Hdbk-1964	5.5	HoM
Spinel	MgAl2O4	2135	Hdbk-1659	7.75	HoM
Eskolaite	Cr2O3	2330	Hdbk-819	8	HoM
bromellite		2408	USGS	9	HoM
Ruthenium	Ru	2546	Hdbk-2414	6.5	HoM
Zircon	ZrSiO4	2550	Hdbk-3313	7.5	HoM
molybdenum	Mo	2617	USGS	5.5	MED
Baddeleyite	ZrO2	2710	Hdbk-3306	6.5	HoM
Periclase	MgO	2852	Hdbk-1712	5.5	HoM
Uraninite	UO2	2865	Hdbk-3081	5.5	HoM
Lime	CaO	2927	Hdbk-622	3.5	HoM
Osmium	(Os, Ir, Ru)	3045	Hdbk-2033	6.5	HoM
Thorianite	ThO2	3050	Hdbk-2964	6.75	HoM
tungsten	W	3107	USGS	7.5	MED
Diamond	C	4726	Ref: [20]	10	HoM

REFERENCES

1. Downs, R. T.; Hall-Wallace, M., The American Mineralogist crystal structure database. *American Mineralogist* **2003,** *88*, 247-250.

2. Anthony, J., W.; Bideaux, R. A.; Bladh, K., W.; Nichols, M. C., *Handbook of Mineralogy*. Mineralogical Society of America: Chantilly, VA 20151-1110, USA.

3. Perry, D. L., *Handbook of inorganic compounds [electronic resource]*. CRC Press: Boca Raton, 2011.

4. Robie, R.; Hemingway, B., US Geological Survey Bulletin 2131. *US Geological Survey: Reston, VA* **1995**.

5. Wolfram|Alpha Knowledgebase. 2018.

6. Aljbouri, Z.; Aldabbagh, S. M., Sinjarite, a new mineral from Iraq. *Mineralogical Magazine* **1980,** *43* (329), 643-645.

7. Zhang, Z.; Wang, L., X-ray powder diffraction analysis on characteristics of heating phase transformation of pyrophyllite. *J. Chin. Ceram. Soc.* **1998,** *26* (5), 618-623.

8. Okamoto, H., Phase diagrams for binary alloys. *ASM International* **2000,** *314*.

9. Geuehring, J.; Cselle, T.; Rechberger, J. Cutting tool. 1996.

10. Barthelmy, D. Mineralogy Database.

11. Tōhoku, D., Mineralogy, petrology, economic geology: Tōhoku Daigaku rika hōkoku dai 3-shū (gansekigaku, kōgaku, kōshōgaku). *Science reports of the Tohoku University* **1921,** *3*.

12. mindat.org. Hudson Institute of Mineralogy: http://www.mindat.org.

13. The determination of the melting points of minerals and rocks [machine translation]. *Tschermaks Mineralogische und Petrographische Mitteilungen* **1901,** *20*, 210-32.

14. Walker, P.; Tarn, W. H., *CRC handbook of metal etchants*. CRC press: 1990.

15. Suvorov, S. A.; Skurikhin, V. V., Vermiculite — a Promising Material for High-Temperature Heat Insulators. *Refractories and Industrial Ceramics* **2003,** *44* (3), 186-193.

16. What is talc? http://www.ima-na.org/page/what_is_talc (accessed May 8).

17. Poerschke, D. L.; Barth, T. L.; Fabrichnaya, O.; Levi, C. G., Phase equilibria and crystal chemistry in the calcia–silica–yttria system. *Journal of the European Ceramic Society* **2016,** *36* (7), 1743-1754.

18. www.americanelements.com. www.americanelements.com (accessed May 13).

19. Savvatimskiy, A. I., Measurements of the melting point of graphite and the properties of liquid carbon (a review for 1963–2003). *Carbon* **2005,** *43* (6), 1115-1142.

20. Oganov, A. R.; Hemley, R. J.; Hazen, R. M.; Jones, A. P., Structure, bonding, and mineralogy of carbon at extreme conditions. *Reviews in Mineralogy and Geochemistry* **2013,** *75* (1), 47-77.